HUNGARIAN

Journal of

INDUSTRIAL CHEMISTRY

Edited by

the Hungarian Oil & Gas Research Institute (MÁFKI),
the Research Institute for Heavy Chemical Industries (NEVIKI),
the Research Institute for Technical Chemistry of the
Hungarian Academy of Sciences (MÜKKI),
the Veszprém University of Chemical Engineering (VVE).
Veszprém (Hungary)

Volume 17. **1989.** **Number 3.**

HU ISSN: 0133-0276
CODEN: HJICAI

The "Hungarian Journal of Industrial Chemistry" is a joint publication of the Veszprém scientific institutions of the chemical industry that deals with the results of applied and fundamental research in the field of chemical processes, unit operations and chemical engineering. The papers are published in four numbers at irregular intervals in one annual volume, in English.

Editorial Office:
Veszprémi Vegyipari Egyetem
"Hungarian Journal of Industrial Chemistry"
H-8201 Veszprém, P.O. Box: 158.
Hungary

Distributor:
KULTÚRA Foreign Trading Co. H-1389, BUDAPEST, P.O. Box 149. Hungary.

FELELŐS SZERKESZTŐ: DR. BODOR ENDRE H-8201 Veszprém. P.O. Box: 158
KIADJA AZ IDEGENNYELVŰ FOLYÓIRAT KIADÓ LEÁNYVÁLLALAT 1052 BUDAPEST, ALPÁRI GYULA U. 2.
TELEFON: 1189-895
A KIADÁSÉRT FELELŐS: ROÓZ FERENC IGAZGATÓ

HUNGARIAN JOURNAL
OF INDUSTRIAL CHEMISTRY
VESZPRÉM
Vol. 17. pp. 289–294 (1989)

SOLVENT DEMETALIZATION OF HEAVY OIL RESIDUE

A. S. FARAG, O. I. SIF EL-DIN, M. H. YOUSSEF,
S. I. HASSAN and S. FARMAWY

(Egyptian Petroleum Research Institute, Nasr City, Cairo, Egypt)

Received: March 28, 1988

A description of the application of various precipitating solvents for the removal of heavy metals, particulary vanadium and nickal via the removal of asphaltene from atmospheric petroleum residue. The solvent deasphalting processes were carried out at ambient temperature. Hydrocarbons of relatively high molecular weight were tried together with some nonconventianol solvents. The precipitation variables were studied. The degree of refining was studied by evaluating the properties of the refined residue.

Introduction

There is a strong demand for economical conversion processes, which upgrade heavy hydrocarbons into more valuable light hydrocarbons. Hydrocracking processes are widely used for this purpose. But the high content of heteroatoms in the residue prevents an economical application of processes where catalysts are involved.

Direct hydrodesulphurization of petroleum residues either atmospheric or vacuum, presents problems that are difficult to resolve due to the concentration in these fractions of impurities contained in the crude-asphaltenes (C_7 insolubles); metals (Ni, V); and nitrogen compounds. These compounds can severely limit the performance of the catalysts used in the processes.

The main objective of deasphalting is to produce deasphalted oil containing a minimum amount of asphaltenes and metals compatible with downstream processes. Various methods have been applied [1–4].

Meanwhile, crude quality has always been an important factor in considering coking for maximum diesel product. High metals and sulphur content crude could not be used economically because of the low value of the coke obtained. Thus, treating the coker feedstock with solvent before coking, allows the production of high quality coke from virtually any feed. Besides, a very small

amount of vanadium and sodium found in some oils may lead to extreme corrosion when such fuels are burned in boilers or are used as gas turbine fuel [5].

The present work aims to evaluate new solvents as a precipitating agent for deasphalting and demetalization of Egyptian atmospheric petroleum residue.

Experimental

Atmospheric petroleum residue was subjected to bench scale, solvent deasphalting at 25 °C. A mixer settler apparatus was used.

The main variables were the type of solvent (hydrocarbon solvents ranging from nC_5–nC_8, ethyl acetate and butyl acetate), and solvent to feed ratio.

The properties of the feed residue and the deasphalted products were determined according to standard methods for analysis, unless otherwise stated.

Resins and oils were determined for the feed residue and the deasphalted residue by component analysis using activated alumina [6].

Results and Discussion

The properties of petroleum residue are shown in *Table 1.*

Deasphalted residues made by treating the atmospheric petroleum residue with various solvents are reported in *Table 2.* Analyzing the data in *Table 2,* the dissolving capacity for the hydrocarbon solvents decreases with the increase in the number of carbon atoms (nC_5–nC_8), while it decreases with the increase in the molecular weight of the acetate solvents. Ethyl acetate exhibits the highest efficiency for the removal of vanadium and nickel.

Table 1.

Properties of Petroleum Residue

Density, 70 °C, kg/dm^3	0.9226
Conradson carbon residue, wt%	13.20
Ash content, wt%	0.079
Vanadium content, ppm.	214
Nickel content, ppm.	64
Composition:	
Oil, wt%	49.56
Resins, wt%	38.55
Asphaltene, wt% (heptane Insol.)	11.89

The efficiency of the hydrocarbon solvents for the removal of asphaltene and metals (V and Ni) are presented graphically *(Figs. 1, 2).* It is obvious from the Figures that solvents of lower molecular weights have better efficiency than the

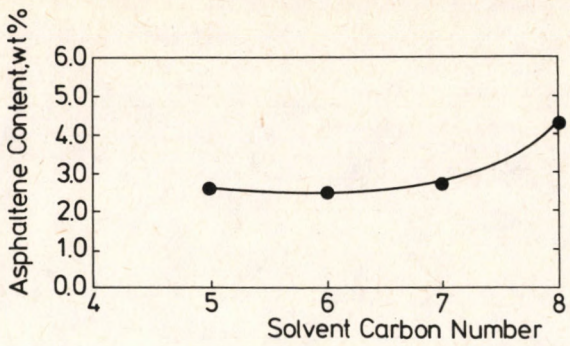

Fig. 1.
Effect of Solvent Carbon Number on the Asphaltene content of deasphalted residues

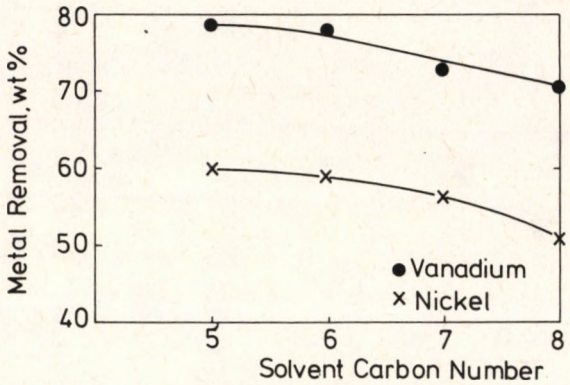

Fig. 2.
Effect of Solvent Carbon Number on the percentage of Metal Removal

higher ones. Irrespective of their carbon numbers, the studied solvents show better efficiency for vanadium removal than nickel removal.

More extensive studies were performed on the petroleum residue using petroleum ether (40–60 °C), ethyl acetate and butyl acetate at various solvent feed ratios keeping the other variables unchanged. The results are shown in *Table 3*.

The efficiency of the examined solvents can be evaluated by measuring the quality index of the deasphalted residue in terms of asphaltene and/or metal removal. For example, vanadium removal (R_v) is expressed as follows:

$$R_v = (100 - E_{wt}) \frac{V_A}{V_F}$$

Where:

E_{wt} = yield of the deasphalted residue, wt%
V_A = vanadium in asphaltene residue, ppm.
V_F = vanadium in feed, ppm.

Table 2.

Properties of the Deasphalted Residues
Extraction temperature = 25 °C; Solvent: Feed ratio = 6 : 1

Solvent	Yield, wt%	Conradson carbon residue, wt%	Ash content, wt%	Vanadium content, ppm.	Nickel content, ppm.	Composition, wt%		
						Oil	resin	asphaltene
Pentane	68.7	7.72	0.021	66	32	60.25	37.16	2.59
Hexane	70.4	8.32	0.023	66	37	59.08	38.44	2.48
Heptane	73.7	8.41	0.027	78	38	58.20	39.12	2.68
Octane	76.6	8.80	0.028	82	41	54.88	40.87	4.25
Petroleum ether, (40–60 °C)	68.9	9.77	0.054	104	34	50.46	43.98	5.56
Ethyl acetate	75.2	8.10	0.025	34	24	63.51	34.31	2.18
Butyl acetate	80.7	10.65	0.039	125	49	54.05	41.53	4.42

Table 3.

Effect of Solvent Ratio on the Properties of the
Deasphalted Residues; Extraction Temp. = 25 °C

Solvent ratio	Yield, wt%	Conradson carbon residue, wt%	Ash content, wt%	Vanadium content, ppm.	Nickel content, ppm.	Composition, wt%		
						Oil	resin	asphaltene
Ethyl acetate								
4 : 1	72.6	8.64	0.031	49	26	61.75	34.97	3.28
6 : 1	75.2	8.10	0.025	34	24	63.51	34.31	2.18
8 : 1	72.5	7.04	0.019	31	24	66.89	31.20	1.91
10.1	71.3	6.72	0.012	33	24	67.20	31.30	1.50
Butyl acetate								
4 : 1	79.5	11.45	0.045	155	51	50.62	43.71	5.67
6 : 1	80.7	10.65	0.039	124	49	54.05	41.53	4.42
8 : 1	81.2	10.19	0.038	111	43	55.55	41.45	3.00
10.1	80.2	10.11	0.015	90	42	57.35	39.85	2.80
Petroleum ether (40–60 °C)								
4 : 1	67.0	9.80	0.061	110	49	41.87	51.81	6.32
6 : 1	68.9	9.77	0.054	104	34	50.46	43.98	5.56
8 : 1	72.3	8.67	0.042	72	34	57.99	37.76	4.25

Data deduced from *Table 3* show that ethyl acetate gives the highest removal of vanadium and nickel. Correlating the vanadium and nickel removals with asphaltene removal *(Fig. 3)*, indicates that the heavy metals particularly vanadium, are mainly concentrated in asphaltene precipitate. For the studied solvents, the rate of removal of vanadium precedes that of nickel irrespective of the solvent used and at all solvent feed ratios.

Demetalization is higher for ethyl acetate than that for petroleum ether. For

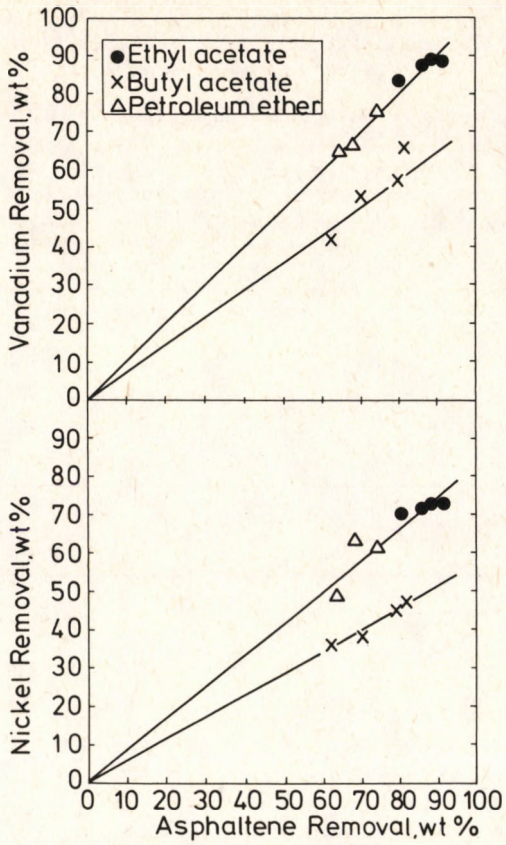

Fig. 3.
Correlation between Asphaltene Removal and Metal Removal

instance, for the same yield of deasphalted product, the vanadium removal is 89.5 wt% for ethyl acetate and 75.7 wt% for petroleum ether at a solvent feed ratio of 8 : 1.

It may be concluded that treating atmospheric petroleum residue with precipitating solvents results in a residue with reduced amounts of heavy metals (V & Ni). Such deasphalted, demetalized residue may be ecnomically used as a feedstock for a delayed coking process with the production of an appreciable quantity of metallurgical coke (13–21 wt%). Such a figure is estimated from the following correlation [7].

$$W_c = 2.0 + 1.66k$$

Where:

W_c = yield of delayed coke, wt%
k = feed conradson carbon residue, wt%

REFERENCES

1. GEARHART, J. A., and GARWIN, L.: Oil & Gas J., *1976,* 74, June 14, 63.
2. BILLON, A., PERIES, J. P., FEHR, E., LORENZ, E. and BASF, A. G.: Oil & Gas J., *1977,* 75, Jan. 24, 43.
3. VILORIA, D. A., KRASUK, J. H., RODRIGUEX, O., BUENAFAMA, H., and LUBKOWITZ, J.: Hydroc. Process., *1977,* 56 (3), 109.
4. SIKONIA, J. G., STOLFA, F., BURTON, V. P. and HUTCHINGS, L. E.: Oil & Gas J., *1978,* 76, March 20, 94.
5. NELSON, W. L.: Petroleum Refining Engineering, 4th Ed., McGraw-Hill, New York, 1958.
6. TAMAN, A. R. M., SHALABY, A. A., and ROUSHDY, M. I.: Bull. NRC, Egypt, *1980, 6,* 490–501.
7. NELSON, W. L.: Oil & Gas J., *1955,* Dec. 19, 99.

HUNGARIAN JOURNAL
OF INDUSTRIAL CHEMISTRY
VESZPRÉM
Vol. 17. pp. 295–310 (1989)

THE MODIFIED TEMPERATURE INTERVAL METHOD FOR HEAT EXCHANGER NETWORK SYNTHESIS

J. JEZOWSKI

(Institute of Chemical Engineering and Heating Equipment, Wrocław Technical University, Wrocław, Poland)

Received: June 13, 1988

Significant progress is noted in solving the problem of heat exchange network (HEN) synthesis. Linear programming (LP), mixed-integer linear programming (MILP) and nonlinear programming (NLP) methods were developed, but they are complex and based on a simplified model of a heat exchanger.

Industrial practice requires rather simple approaches, which offer flexibility and the possibility of including specific features of the task at hand. The pinch design method (PDM) of Linnhoff and Hindmarsh with certain heuristics of matching streams meets such conditions, but the approach is frequently fallible.

In order to make it more reliable, it is necessary to include a model of matches with stream splittings in heuristic rules, i.e. to allow for parallel or serial-parallel sequences of matches. To date a few methods offered such an option, but they are not general or are unreliable. This paper deals with a general strategy of synthesizing the networks with the minimum use of utilities and with a number of matches close to the minimum. The networks can include parallel, serial-parallel and serial sequences. The application of the synthesis approach is demonstrated on several examples.

Introduction

The paper deals with the heat exchanger network (HEN) synthesis problem formulated as follows:

Design HEN in which NH hot streams ($h_i : i = 1, \ldots, \mathrm{NH}$) are to be cooled down from T^1_{hi} to T^2_{hi} and NC cold streams are to be heated up from T^1_{cj} to T^2_{cj}.

Mass flowrates of these streams are given and proper heating utilities (hu) and cooling media (cu) are available. The HEN should ensure minimum cost (or heat) of the utilities to be used in it and should contain a minimum number of matches.

Many problem-solving approaches have been suggested to date, but only a few of them have attracted general attention. Among them the pinch design method (P D M) of LINNHOFF and HINDMARSH [1] is probably the most widely used approach in industrial practice. Simplicity, flexibility and elegance are the major advantages of the P D M. However, the PDM is not the algorithmic approach of synthesis for the entire HEN, since it gives the rules on how to match streams at the pinch only and does not determine how to design a network away from the pinch. Therefore, the PDM has to be connected with another approach, usually heuristic rules and both these approaches together give the method of synthesizing entire network (we will refer to such a combined strategy as the pinch and heuristic design method – the PHDM).

REV and FONYO [2] gave more details on the PHDM and they also pointed out two basic drawbacks of the PHDM:

1. the possibility that the designed network will use excess heat of utilitics, higher than the minimum value (Q_u^{min}),
2. the possibility of obtaining many matches, i.e. the number of matches in the HEN may be higher than the minimum number (N^{min}).

The main reason for these drawbacks is the heuristic method of calculating matches, that is the determination of the heat duty (Q) and temperatures of streams (t_c^1 , t_c^2, t_h^1, t_h^2) in a match. Those calculations are based on the heuristic QMAX: "recover as much heat as possible" or on the tick-off rule of LINNHOFF, HINDMARSH [1]: "obtain one residual stream in a match" (author [3] suggested the rule "minimum number of residuals and maximum heat load" which is the combination of QMAX and tick-off). Such rules have been adapted to minimize the heat transfer area of the apparatus (see e.g. [4]) or to minimize the number of matches (see discussion in [5]), but they are still only heuristics. Moreover, the heuristics of match calculation are usually applied in such a way that only the serial sequences of matches can be created (the approach suggested in [6] is the exception, but it yields unnecessary splits). Thus, the inclusion of stream splittings in heuristics may eliminate their disadvantages and this modification is expected to ensure that the PHDM will give networks with Q_u^{min} and N^{min}. Such an idea was the basis of the approach of REV and FONYO [2] who tried to connect rules of streams splitting at the pinch from the PDM with heuristics of matching streams. This method consists of creating pinch situations in course of synthesis. To obtain pinches, REV and FONYO [2] applied the heuristic called MAHL (maximum allowable heat in a match) to determine the heat load of a match. The use of MAHL also ensures that the synthesized network reaches a minimum enthalpy of utilities, on the other hand, the MAHL rule means that the network has a lot of matches, usually many more than N^{min}. It is necessary to add that the computation of the MAHL value is very complex.

Moreover, the use of MAHL in synthesis creates pinch-like situations in a limited number of cases (tasks) described by authors [2] as hidden pinch situations. For other tasks (called in [2] pseudopinch situations of explicit or implicit type) pinch situations cannot be created. To overcome this problem, REV and FONYO [2] applied the lower bound on the MAHL, the so-called minimum heat

load (MHL) and this forces the splittings in pseudopinch situations. (The lower bound on the heat load was also used in the other works, e.g. [7] but it resulted from economic and manufacture constraints and was in no way connected with the required structure of the HEN). There arises the question about the value for the MHL, and REV and FONYO [2] did not answer it. There is probably the unique value of the MHL for the task at hand an the application of the higher MHL gives an excess use of utilities (compare networks in Fig. *19, 20, 21* and *22* in [2] calculated for various values of the MHL). On the other hand, the lower value of the MHL does not force necessary splitting.

Concluding, it is possible to state that the method of the authors [2] does not ensure that synthesized HEN will reach bot targets: Q_u^{min} and N^{min}. Nevertheless, their paper gives a proper insight into the disadvantages of the PHDM, and suggests the correct, general way of eliminating them – by including the necessary splittings of streams.

Modified Temperature Interval Method for the Tasks Consisting of a Single Interval

At first, let us note that situations where stream splittings may be necessary to obtain Q_u^{min} and/or N^{min} in the HEN are of the following type: in a certain temperature interval (I) the number of hot NH(I) or cold streams NC(I) differs largely from the number of cold or hot streams, respectively – in a simple case: $NH(I) = 1$ and $NC(I) > 1$ or $NC(I) = 1$ and $NH(I) > 1$. The examples given in [5] and [8] support this statement. Having selected the interval of potential stream splitting it is necessary to consider the necessity of a split in such the way as to obtain the HEN with Q_u^{min} and N^{min}. On this basis, as well as on the well known results from the analysis of the HEN synthesis problem, let us formulate rules and conclusions, which form the framework of the suggested method.

Rule 1. Stream splittings may be neccessary in such a temperature interval where there is a large difference between the number of hot and cold streams. Hot stream(s) is likely to be split in the case of $NH(I) > NC(I)$ and cold stream/s in the opposite case.

Conclusion 1. To simplify the calculations it is advisable to select temperature intervals, which contain one hot (cold) stream and at least two cold (hot) streams (these intervals will be referred to as the intervals of potential stream splittings – the PSS intervals).

Rule 2. To obtain Q_u^{min} in the HEN, heat loads of matches in the PSS intervals have to be such that the heat flow in and out of the PSS intervals equal $\Delta Q(I)_k$ ($\Delta Q(I)_1$ – flow in, $\Delta Q(I)_2$ – flow out). The values of $\Delta Q(I)_k$ are determined from the problem – table method of LINNHOFF, FLOWER [9].

The proof for rule 2 results from the problem – table method.

Conclusion 2. Having determined the values of $\Delta Q(I)_k$ it is possible to determine for each stream in the interval its inlet temperature to the first match and its

outlet temperature from the last match in the interval. Thus, if a stream is matched only once in the interval, its outlet and inlet temperature in this match can be calculated.

Remark – in cases (a), (b) there is an infinite number of temperature values, but one is able to choose the temperatures.

(a) $Q(\mathrm{I})_1 > 0$ *and* $NC(\mathrm{I}) > 1$ $(NH(\mathrm{I}) = 1)$

(b) $Q(\mathrm{I})_2 > 0$ *and* $NH(\mathrm{I}) > 1$ $(NC(\mathrm{I}) = 1)$

Rule 3. To approach $N^{\min}$ matches in the HEN, the number of matches in the PSS interval should not exceed $N(\mathrm{I})$.

$$N(\mathrm{I}) = NH(\mathrm{I}) + NC(\mathrm{I}) - 1 \tag{1}$$

Conclusion 3. Having known value of $N(\mathrm{I})$ it is possible to determine which streams will not be split and will be matched once in the I-th interval. For $NH(\mathrm{I}) = 1$; $N(\mathrm{I}) = NC(\mathrm{I})$ and cold streams have to be matched once, for $NC(\mathrm{I}) = 1$; $N(\mathrm{I}) = NH(\mathrm{I})$ and hot streams have to matched once.

Rules and Conclusions 2 and 3 determine number of matches in the PSS interval, heat load of each match and for the stream which is likely to be split, its inlet temperature for the first match and its outlet temperature from the last match.

Rule 4. The sequence of matches in the PSS interval that meets the conditions of conclusions 2, 3 as well as thermodynamical constraints (relationships 2, 3) is involved in the so-called "superstructure" introduced by authors [10] (the superstructures for $NH(\mathrm{I}) = 1$, $NC(\mathrm{I}) = 2$ and $NH(\mathrm{I}) = 1$, $NC(\mathrm{I}) = 3$ are shown in the Appendix, more details on superstructures are given in [10]).

$$t_{\mathrm{h}}^1 - t_{\mathrm{c}}^2 \geqq \Delta \mathrm{T}^{\min} \tag{2}$$

$$t_{\mathrm{h}}^2 - t_{\mathrm{c}}^1 \geqq \Delta \mathrm{T}^{\min} \tag{3}$$

Discussion of rule 4:

a) Rules and conclusions 2, 3 make the estimation of the heat loads of the matches possible. Therefore, the proof for rule 4 is identical to the proof given in Appendix A in the paper [10].

b) there may be more than one feasible sequence in the superstructure and its selection as well as its parameters (mass flowrates of the split streams) can be carried out by optimization (see [10]). However, it is possible to reduce the computations using such heuristics as:

b1. while selecting sequence to be checked at first choose serial sequences since they are simplier and easier to control than parallel sequences,

b2. first check this serial sequence for feasibility, which follows the heuristics of stream matching e.g. those of PONTON, DONALDSON [11],

b3. avoid bypasses introduced by WOOD et al. [12] since they usually increase the investment cost,

b4. use as many specific constraints for the HEN problem at hand as possible (see example 6).

In the Appendix the feasibility conditions are given for all the sequences involved in the superstructure for $NH(I) = 1$ and $NC(I) = 2$. The 1, 2, 3 and 4 rules and conclusions yield the method of solving the synthesis problem for tasks consisting of a single PSS interval. To illustrate the application of these rules, let us solve the following examples.

Example 1 – according to REV, FONYO [2] (Table 5 in [2], pseudopinch situation of explicit type).

The task is shown in *Fig. 1a*. The application of the rules is as follows:

ad. Rule 1. Single PSS interval within temperatures 130/110 and 100/80, with one hot stream and two cold streams.

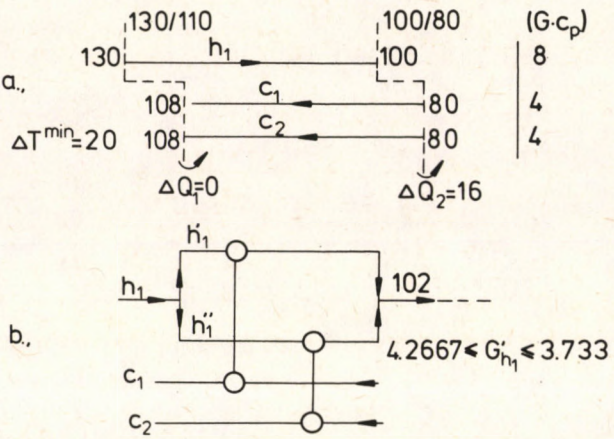

Fig. 1.
Example 1
1a Representation of the data
1b Sequence calculated by the MTI method

ad. Rule 2. Heat flow into the interval equals zero and flow out of it 16. Thus, the outlet temperature of the hot stream can be calculated from Eq. 4.

$$t_h^2 = T_h^1 - \frac{\Delta Q_2}{G_h \cdot c_{ph}} \tag{4}$$

Outlet temperatures of cold streams have to be equal to a lower temperature bound (80).

ad. Rule 3. Minimum number of matches for the interval is two. Therefore, cold streams c_1 and c_2 have to reach their target temperatures in matches and heat loads of these matches can be determined.

ad. Rule 4. The superstructure involves two matches, where the heat loads are known. The temperature of the cold and hot streams at the inlet and outlet of the superstructure is also known. With the help of the feasibility relation-

ships from the Appendix it is easy to check that no serial connection is feasible, but a parallel sequence is (see *Fig. 1b*).

Example 2 – according to REV, FONYO [2] (Table 6 in [2], pseudopinch situation of implicit type).

The task is shown in *Fig. 2a* together with temperature bounds of the PSS interval and values of heat flows. The application of the rules is identical as in Example 1. The feasible parallel sequence is shown in *Fig. 2b*.

Example 3 – according to REV, FONYO [2] (*Table 4* in [2], hidden pinch situation). *Fig. 3a* shows the task together with bounds of the PSS interval and values of heat flows. Outlet temperatures of streams are calculated in the same way as in the above examples.

From the superstructure for three cold streams and one hot (*Fig. A2* in Appendix) it is possible to check that no serial sequence is feasible and a parallel connection has to be used *(Fig. 3b)*. For comparison, *Fig. 3c* shows the network designed by the method of REV and FONYO [2] which consists of one apparatus more than the minimum number.

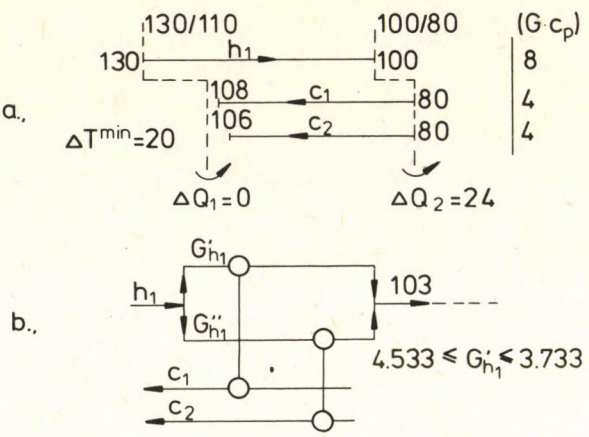

Fig. 2.
Example 2
2a Representation of the data
2b Sequence calculated by the MTI method

On the basis of the above examples, it is possible to note that:

(i) it is unnecessary to distinguish in the suggested method various pseudo- or hidden pinch situations as it was necessary in the method suggested in [2],

(ii) the suggested method ensures that for all the above examples the networks with N^{min} and Q_u^{min} have been obtained.

Example 4 – task 4SP2 according to [6] (data shown in *Fig. 4a*). This task differs from the previous examples since there is one cold stream and three hot streams, and heating not cooling utility is to be used. Heat outflow from the PSS interval

equals zero and the flow in it is equal to Q_{hu}^{min} (336,67). Therefore, the outlet temperature of cold stream is equal to:

$$t_c^2 = T_c^2 - \frac{\Delta Q_1}{(G_{cp})_c} \tag{5}$$

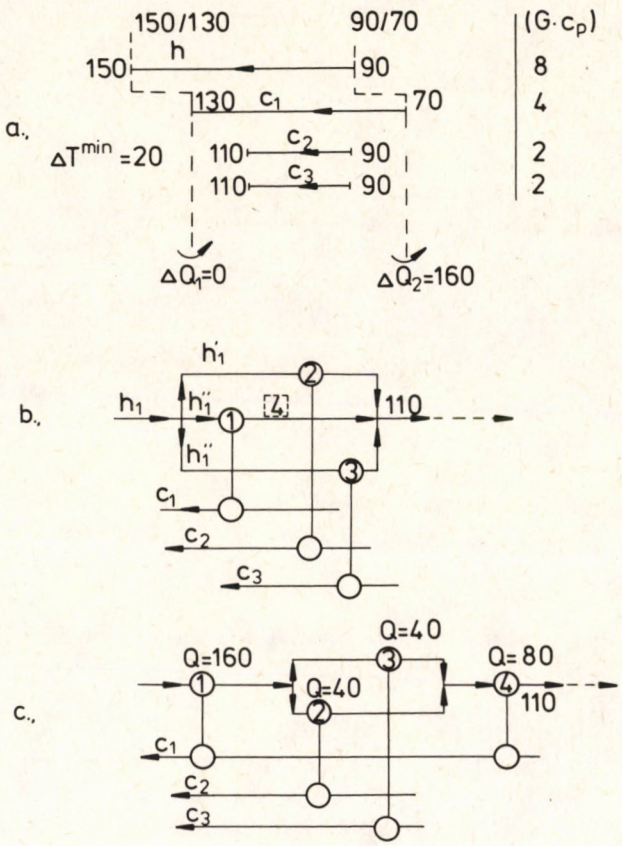

Fig. 3.
Example 3
3a Representation of the data
3b Sequence calculated by the MTI method
3c Sequence calculated by the method of Rev, Fonyo [2]

Outlet temperatures of hot streams in the matches have to be equal to their target temperatures, since there must be three matches in the interval. No serial sequence in the superstructure is feasible and it is necessary to use a parallel sequence *(Fig. 4b)* (no exhaustive search for other parallel or serial-parallel sequences was carried out).

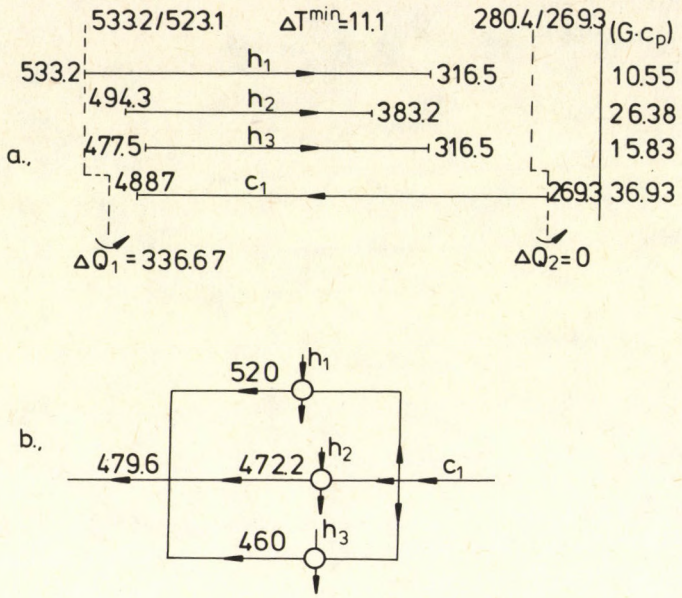

Fig. 4.
Example 4
4a Representation of the data
4b Sequence calculated by the MTI method

Modified Temperature Interval Method for Tasks Consisting of Several Intervals

The examples calculated in the previous section consisted of a single PSS interval and, therefore, they did not show the interrelation among intervals. As mentioned in Rule 3, sequences with N(I) matches for each interval do not necessarily create the HEN with a minimum number of matches (N^{min}). Certain streams may exist in k intervals and they are counted k – times in the calculation of the number of matches in the HEN – the situation is identical as in the case of tasks with several pinches. However, in the opposite to a pinched task there is some freedom since the heat flow from the previous interval to the next one is larger than zero. Therefore, it is possible to decide how to use these heat flows and this decision should take the number of matches in the HEN into account. Let us formulate Rule 5 which determines the use of the heat flow between the intervals in order to reduce the number of matches in the HEN.

Rule 5. To reduce the number of matches in the HEN use the heat flow to the I-th interval to obtain in this interval the same matches as designed for the previous interval. Each pair of such matches can be lumped immediately into the single match.

At first match those cold streams in the I-th interval which enthalpy changes are lower than the heat inflow (or equal).

The application of Rule 5 is shown in *Fig. 5*. From Rules 2 and 3 it is possible to suppose that in the first interval there should be the following matches: h_1–c_1, h_1–c_2, h_1–c_3 (shown in the form of a graph in *Fig. 5a*). Without Rule 5 one may use heat flow $\Delta Q1$ to heat up, e.g. cold streams c_2 and c_4 and thus obtain a network with seven matches (case A in *Fig. 5*). Applying Rule 5 it is possible

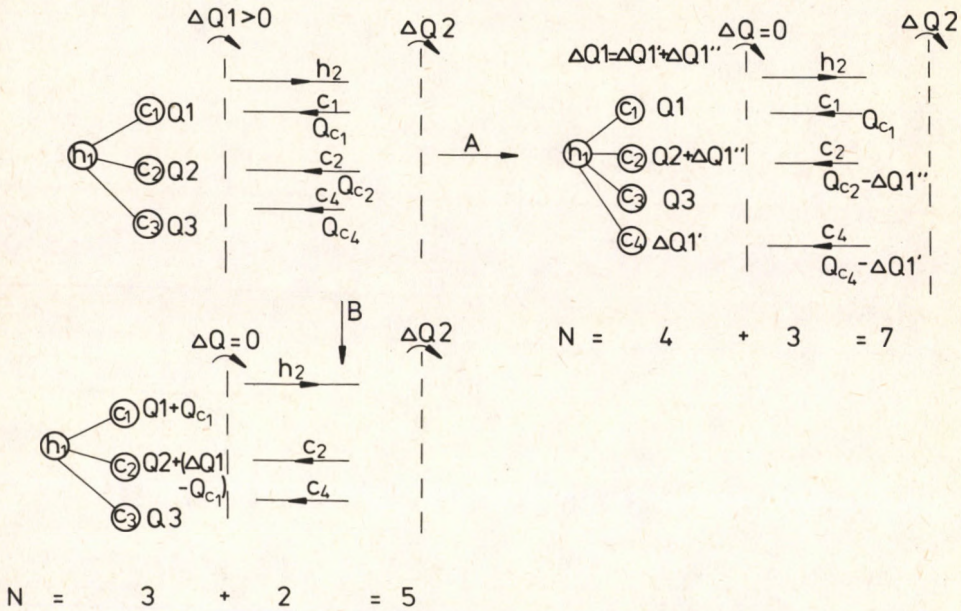

Fig. 5.
Illustration for application of Rule 5 in the MTI method

to reach a network with five matches (case B in *Fig.5*). Thus, the suggested synthesis method for tasks consisting of several PSS intervals is based on five rules (and conclusions) which form the following sequence of operations:

1. selection of PSS intervals according to rule 1,
2. calculation of values of N(I) and $\Delta Q(\mathrm{I})_1$, $\Delta Q(\mathrm{I})_2$ for selected intervals ($I = 1$, ...),
3. determination of stream temperatures in matches within intervals and matches between intervals – that is the superstructure for intervals (rules 2, 3 and 5),
4. selection of feasible sequence/s from each superstructure (rule 4).

Since the above approach bears a certain resemblance to the temperature interval (TI) method of LINNHOFF and FLOWER [9] it has been called the modified temperature interval (MTI) method.

It is necessary to note that the MTI method is aimed at threshold tasks or synthesis away from pinch, therefore the PDM has to be used first in case of pinched problems. Let us now illustrate the application of the MTI method on examples.

Example 5 – according to REV, FONYO [2] (*Table 7* in [2]).

The data for the example are given in *Fig. 6a*. According to the PDM it is necessary to divide the task into two subtasks: hot subtask (above the pinch) and cold subtask (below the pinch).

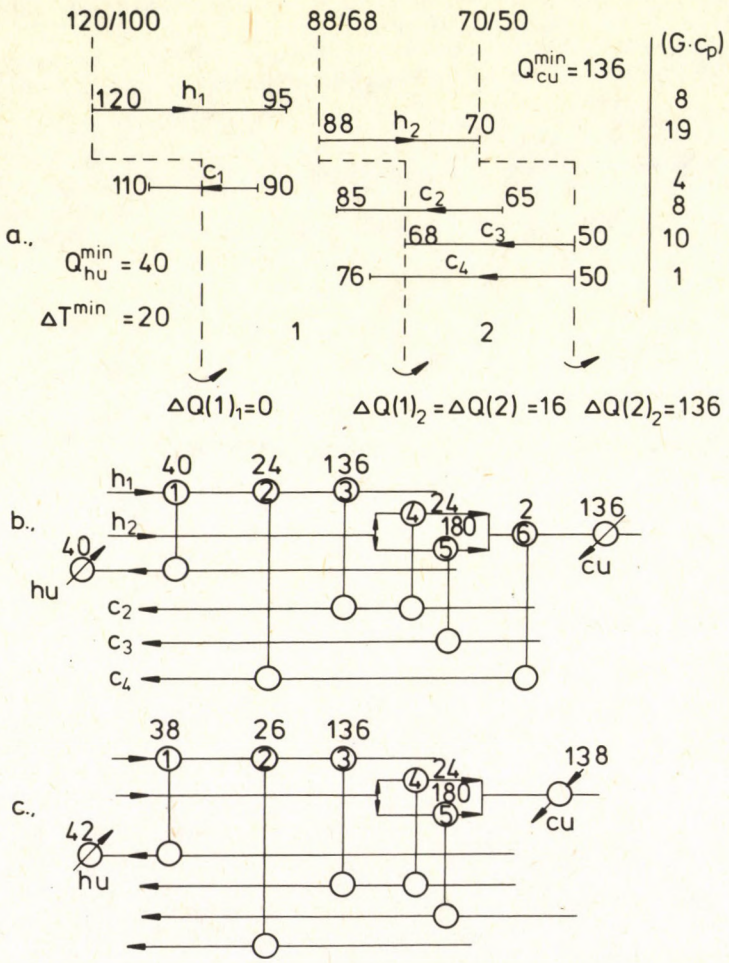

Fig. 6.
Example 5
6a Representation of the data
6b Network with Q_u^{min} synthesized by the MTI method
6c Network with N^{min} synthesized by the MTI method

The former is trivial – the only solution is to match c_1 with hu. For the cold subtask, the PDM does not determine any splittings at the pinch. It is possible to start synthesis applying heuristic rules of matching streams, i.e. for this case "match the hottest hot with the hottest cold" (according to [11]). It is easy to check that this heuristic does not yield the optimal solution.

The application of the two first steps of the MTI method gives PSS intervals and heat flow values shown in *Fig. 6a*. In the first interval, there are three matches and the heat flow is through hot stream h_1. According to Rule 5 it is necessary to use this heat to heat up cold stream c_2 or cold stream c_4 in the second interval. For both options, there will be three matches in interval 1 and three in interval 2, together with the cooler and heater, the HEN will consist of eight matches, while N^{min} equals seven.

To reach N^{min} it is necessary to move more heat than $\Delta Q(1)_2$ to the second interval and this possibility will be discussed in the following. For the option where $\Delta Q(1)_2$ is used to heat up cold stream c_4 it is possible to determine superstructures for both intervals. The feasible sequences derived from both superstructures are shown in *Fig. 6b* – it is the solution with 8 matches for this example. It is worthwhile noting that serial connection is feasible for the first interval, though it could not be obtained from the heuristic of PONTON and DONALDSON [11]. As for a reduction of the number of matches it is easy to note that by moving an additional two units of heat to interval 2 (two units more than $\Delta Q(1)_2$) we can heat up cold stream c_4 to its target temperature, thus reducing the number of matches to the minimum (the solution with 7 matches and higher use of utilities is shown in *Fig. 6c*).

This operation is equivalent to the relaxation from pinch according to REV, FONYO [2]. It is possible, of course, to move the additional heat through pinch basing on the network with 8 matches, but the MTI method gives the possibility of making such decisions *during* synthesis.

For comparison, the best network for this task obtained by REV and FONYO [2] used 8 heat units more of both Q_{cu} and Q_{hu} than the solution from *Fig. 6b*.

Example 6 – according to [13] (simplified crude oil preheating train). Data for this task are given in *Fig. 7a*. It is evident from this Figure that cold streams are likely to be splited and it is impossible to find PSS intervals with one cold stream only. If we place intervals as in *Fig. 7a,* we will have one cold stream in the first interval and two cold streams in the second.

However, it is obvious that part of the heat flow from the first interval ($\Delta Q(1)_2$) has to be used to heat up stream c_2 from 398° to 408°. Thus, we can state that the entire c_2 is in the superstructure for the first interval, but then we have to reduce $\Delta Q(1)_2$ by enthalpy of c_2 from 398° to 408° to obtain the real heat flow $\Delta Q(1)_2^R$. In this way, we obtained two PSS intervals each with a single cold stream and the values of the heat flows. There are a minimum of three matches in each interval. It is now possible to construct superstructures for the intervals. The sequence for the first interval cannot be serial (parallel sequence is shown

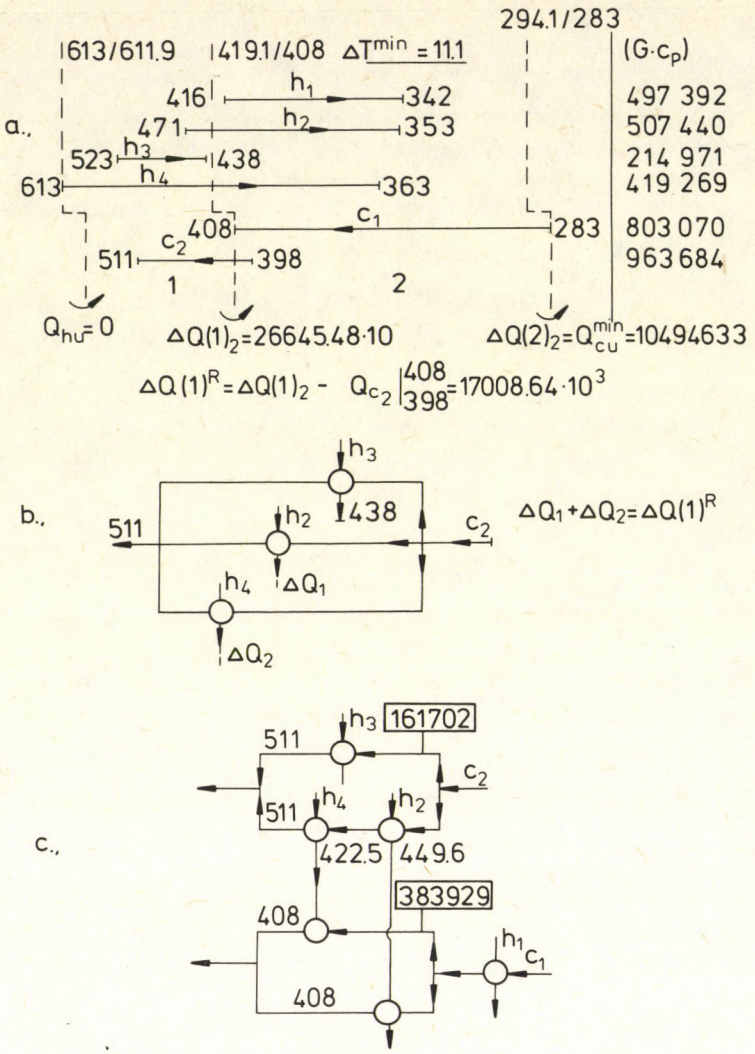

Fig. 7.
Example 6
7a Representation of the data
7b Parallel sequence for interval 1
7c Network synthesized by the MTI method

in *Fig. 7b*). In this case there is a spectrum of values of temperatures t^2_{h2}, t^2_{h4} for which:

$$\Delta Q_1 + \Delta Q_2 = \Delta Q(1)^R_2 \tag{6}$$

where: ΔQ_1 (ΔQ_2) – enthalpy change of h_2 (h_4) from t^2_{h2} (t^2_{h4}) to target temperature $T^2_{h_2}$ ($T^2_{h_4}$)

Let us assume that an additional constraint of using isothermic mixing has been imposed in this task. The network synthesized for this condition is shown in *Fig. 7c*.
It is worthwhile noting that the network designed by heuristic approach contains eight matches.

Summary and Conclusions

The modified temperature interval method described here is aimed at solving tasks without pinches (threshold tasks) or the synthesis of the network structure away from pinches. In the later case, the PDM of LINNHOFF and HINDMARSH [1] has to be applied to determine the necessary splits at pinches and to divide the task into threshold subtasks. The application of the MTI method does not necessarily exclude the use of the heuristic approach, e.g. of the PONTON, DONALDSON [11] type.

In the author's opinion, the heuristic rules can be used till their failure (which is easy to detect) and then the MTI method should be applied. The MTI method does not form the fully algorithmic approach of HEN synthesis. This is rather the general strategy of synthesis that allows the user to investigate several options – thus its philosophy is close to that of the PDM or of the evolutionary approach of GRIMES et al. [14].

The MTI method can be considered a simplification of the synthesis approach based on mathematical programming suggested in papers [8] and [9].

This approach consists of two basic steps:

1. calculation of heat load distribution (HLD) that minimizes enthalpy of utilities and number of matches,
2. optimization (or determination) of HEN structure.

In the MTI method, 1, 2, 3 and 5 rules (and conclusions) are used to determine HLD and these rules are based on well known conclusions from thermoeconomic analysis of HEN synthesis problem. The results of the MTI method may not be so reliable as those from LP or MILP methods, but complex computer programs are unnecessary.
Moreover, to devise the structure of the HEN on the basis of rules 1, 2, 3 and 5, the designer can use his intuition and skill and can also consider factors specific for the task at hand – this is difficult or even impossible in strict mathametical approaches. For instance, Example 5 illustrates the possibility of selecting the solution with Q_u^{min} and number of matches higher than N^{min} or the solution with N^{min}, but the use of utilities higher than Q_u^{min}. The determination of the network structure from superstructures can be carried out in the MTI method with the use of NLP too.
However, in the author's opinion it is not necessary to optimize the HEN at the initial stage of design since the model of the heat exchanger is simplified to a large extent. Therefore, it is enough to check which sequence from the super-

structure is feasible and the optimization of feasible sequences can be carried out later using the detailed model of the apparatus.
Concluding, it is possible to state that the modified temperature interval method described here forms together with the rules of the PDM a reliable, simple approach for the initial stage of HEN design to generate feasible networks with Q_u^{min} and a number of matches equal or close to N^{min}.

SYMBOLS

c_j	j-th cold stream
c_p	average heat capacity of a stream
cu	cooling utility
h_i	i-th hot stream
hu	heating utility
I	number of the PSS interval
N^{min}	minimum number of matches in the HEN
NC	number of cold streams in the HEN
NC(I)	number of cold streams in *I*-th interval
NH	number of hot streams in the HEN
NH(I)	number of hot streams in *I*-th interval
Q	heat load of a match
Q_{cu}^{min}	minimum enthalpy of cooling utilities to be used in the HEN
Q_{hu}^{min}	minimum enthalpy of heating utilies to be used in the HEN
Q_u^{min}	minimum enthalpy of heating and cooling utilities to be used in the HEN
$t^1(t^2)$	inlet (outlet) temperature of a stream in a match
$T^1(T^2)$	initial (target) temperature of a stream in the HEN
$Q(I)_1$, $Q(I)_2$	inlet (outlet) heat flow to (from) the *I*-th PSS interval

Abbreviations

HEN	heat exchanger network
LP	linear programming
MAHL	maximum allowable heat load (according to [2])
MHL	minimum heat load (according to [2])
MILP	mixed-integer linear programming
MTI method	modified temperature interval method
NLP	nonlinear programming
PDM	the pinch design method of authors [1]
PHDM	the pinch-and-heuristic design method
PSS (interval)	the potential stream aplitting (interval)
TI (method)	the temperature interval method of the authors [9]

Appendix

The superstructure for one hot stream and two cold streams *(Fig. A1)* involves two heat exchangers (HE1, HE2), three mixers (M1, M2, M3) and three splitters (S1, S2, S3). The mathematical model of this superstructure consists of:
a). heat balances for heat exchangers,
b). heat balances for mixers,
c). mass balances for splitters,
d). mass balances for mixers,
e). thermodynamic constraints for each end of each heat exchanger (see in Eq. 2, 3),

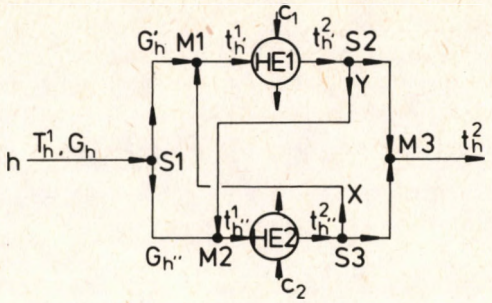

Fig. A1.
Superstructure with two cold streams and one hot stream

f). additional constraints specific for the task.
From data of the task and rules 1, 2, 3, 5 of the MTI method, the values of following parameters are known or are calculated: T_h^1, t_h^2, t_{c1}^1, t_{c1}^2, t_{c2}^1, G_h, G_c, ΔT^{min}.
From the set of model equations, it is necessary to find a feasible sequence of matches and to determine the values of $G_{h'}$, $G_{h''}$, X, Y, $t_{h'}^2$, $t_{h''}^2$.

1. Serial sequences:

1a) h_1–c_1, h_1–c_2 for $G_{h''}=0$, $Y=G_{h'}$, $X=0$
1b) h_1–c_2, h_1–c_1 for $G_{h'}=0$, $X=G_{h''}$, $Y=0$

Serial sequences (1a, 1b) are feasible if:

$$t_x - t_{ci}^1 \geqq \Delta T^{min} \text{ and } t_x - t_{cj}^2 \geqq \Delta T^{min} \text{ and } t_h^2 - t_{cj}^1 \geqq \Delta T^{min} \tag{A1}$$

where: $i=1, j=2$, $t_x = t_{h'}^2$ for case 1a
$i=2, j=1$, $t_x = t_{h''}^2$ for case 1b
$t_{h'}^2$, $t_{h''}^2$ are calculated from heat balances for HE1, HE2.

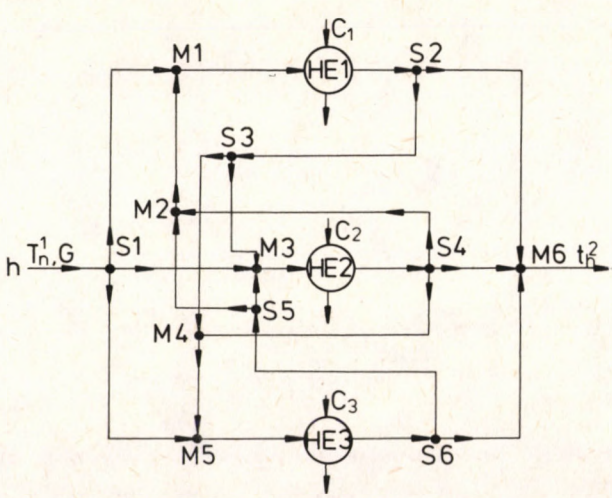

Fig. A2.
Superstructure with three cold streams and one hot stream

2. Parallel sequence with $S1$ and $M1$: $G_{h'} \neq 0$, $G_{h''} \neq 0$ and $Y = X = 0$.

Assumptions: a) c_p = const. for each stream,
b) adiabatic mixers.

The parallel sequence is feasible if for $G_{h'}$ from the range given in Eq. A2 constraints A3 and A4 are met.

$$\frac{Q1}{c_{ph}\,(T_h^1 - t_{c1}^1 - \Delta T^{min})} \leqq G_{h'} \leqq G_h - \frac{Q2}{(T_h^1 - t_{c2}^1 - \Delta T^{min})\,c_{ph}} \tag{A2}$$

$$t_h^2 - t_{c1}^1 \geqq \Delta T^{min} \tag{A3}$$

$$t_{h''}^2 - t_{c2}^1 \geqq \Delta T^{min} \tag{A4}$$

where: $Q1 = (G \cdot c_p)c_1 \cdot (t_{c1}^2 - t_{c2}^1)$

$Q2 = (G \cdot c_p)c_2 \cdot (t_{c2}^2 - t_{c2}^1)$

3. Parallel sequences of Wood's type (see [11]):

$G_{h'} \neq 0$, $G_{h''} \neq 0$ and

$$Y \neq 0,\ X = 0,\ Y < G_{h'} \quad \text{(3a)}$$

or

$$X \neq 0,\ Y = 0,\ X < G_{h''} \quad \text{(3b)}$$

WOOD's splitting (3a) is feasible if for $G_{h'}$ from the range given by relationship (A5) value of Y is within the range determined by relationship (A6) (for assumptions (a), (b) point 2).

$$G_h > G_{h'} \geqq \frac{Q1}{c_{ph}(T_h^1 - t_{c1}^1 - \Delta T^{min})} \tag{a5}$$

$$\frac{G_h - G_{h'})\,(T_h^1 - t_{c2}^2 - \Delta T^{min})}{\Delta T^{min} + t_{c2}^2 - t_{h'}^2} \geqq Y \geqq \frac{(G_h - G_{h'})\,(\Delta T^{min} + t_{c2}^1) - G_h t_h^2 - G_{h'} \cdot t_{h'}^2}{t_{h'}^2 - \Delta T^{min} - t_{c2}^1} \tag{A6}$$

where: $Q_1 = (G_{cp})_{c1} \cdot (t_{c1}^2 - t_{c1}^1)$

$t_{h'}^2$ is determined from the heat balance for HE1

The superstructure for one hot and three cold streams is shown in *Fig. A2*. The mathematical model is more complex, but consists of the same type of equations and inequalities. Moreover, in order not to consider complicated sequences of no practical use it is e.g. possible to reject beforehand such structures which involve mixers and splitters working at more than one branch of the hot stream at the same time.

REFERENCES

1. LINNHOFF, B. and HINDMARSH, E.: Chem. Eng. Sci., *1983,* 38 (5) 745.
2. REV, E. and FONYO, Z.: Hung. J. Ind. Chem., *1986,* 14 (2) 181.
3. JEZOWSKI, J.: Inz. Chem. Proc., *1985,* 6 (2) 249 (in Polish).
4. NISHIDA, N., KOBAYASHI, S. and ICHIKAWA, A.: Chem. Eng. Sci., *1971,* 26 1841.
5. CERDA, J. and WESTERBERG, A. W.: Chem. Eng. Sci., *1983,* 38 (10) 1723.
6. NISHIDA, N., LIU Y. A. and LAPIDUS, L.: AICHEJ, *1977,* 23 (1) 77.
7. GROSSMANN, I. E. and SARGENT, R. W. H.: Comp. Chem. Engng., *1978,* 2 (1) 1.
8. PAPOULIAS, S. A. and GROSSMANN, I. E.: Comp. Chem. Engng., *1983,* 7 (6) 707.
9. LINNHOFF, B. and FLOWER, J. R.: AICHEJ., *1978,* 24 (4) 633.
10. FLOUDAS, C. A., CIRIC, A. R. and GROSSMANN, I. E.: AICHEJ., *1986,* 32 (2) 278.
11. PONTON, J. W. and DONALDSON, R. A. B.: Chem. Eng. Sci., *1974,* 29 (12) 2375.
12. WOOD, R. M., WILCOX, R. J. and GROSSMANN, I. E.: Chem. Eng. Comm., *1985,* 39, 371.
13. KAFAROV, V. V., MESHALKIN, V. P. and KHOANG AN FYONG: Khim. Khim. Tekhn., *1980,* 23 (6) 782 (in Russian).
14. GRIMES, A. E., RYCHENER, M. D. and WESTERBERG, A. W.: Chem. Eng. Comm., *1982,* 14, 339.

HUNGARIAN JOURNAL
OF INDUSTRIAL CHEMISTRY
VESZPRÉM
Vol. 17. pp. 311–318 (1989)

SYNTHESIS AND EVALUATION OF SOME LUBE OIL ADDITIVES FROM LOCAL COAL TAR PHENOLS

M. H. AHMED, F. M. GHUIBA, O. M. O. HABIB* and H. KH. GHARIEB

(Egyptian Petroleum Research Institute, Nasr City, Cairo and *Chemistry Department, Faculty of Science, Mansoura University, Mansoura, Egypt.)

Received: October 14, 1988

Coal tar phenols mixture was separated and analyzed. It was alkylated with n-dodecene to give dodecyl coal tar phenols, then condensed with different molar ratios of formaldehyde and triethylenetetramine to give Mannich bases (I–III) with different structures. The physico-chemical characteristics of the prepared compounds were determined and evaluated as lube oil additives. The products gave promising results as antioxidants, dispersants, pour point depressants and viscosity index improvers.

Introduction

Among the ashless lube oil additives that have been prepared from olefins and ployethylenepolyamines, the best are the alkenyl succinimides and high molecular weight Mannich bases. The latter are usually prepared by alkylating phenols with olefinic hydrocarbons and subsequently condensing the formed alkylphenols with formaldehyde and aliphatic amines in accordance with the Mannich reaction [12]. These Mannich bases are recommended for the improvement of the antioxidant, anticorrosive and detergent properties of certain petroleum products including lube oils [11]. They are also used as jet fuel antioxidants [7], rust inhibitors for greases [1] and railway lube oils [13] providing excellent protection for the lead and copper parts of railway engines.

The present work concerns with the use of a local coal tar phenols mixture as a raw material for preparing some Mannich bases with different structures via its alkylation with *n*-dodecene then condensing the prepared alkylated coal tar phenols mixture with different molar ratios of formaldehyde and triethylenetetramine. The prepared products were evaluated as multifunctional lube oil additives using standard laboratory methods.

Experimental

Separation of the crude coal tar phenols mixture:

The crude coal tar phenols mixture (kindly provided by Al-Nasr Co. for Manufacturing Coke and Chemicals) was dried over anhydrous magnesium sulphate, distilled and the fraction of boiling range 180–230 °C was collected. The specifications and composition of the distillate are given in *Tables 1* and *2*, respectively.

Preparation of n-dodecene:

n-Dodecene was prepared via dehydrating *n*-dodecanol using sulphuric acid as a dehydrating agent [6].

Commercial concentrated sulphuric acid (300 ml) was added to water (200 ml) then cooled. *n*-Dodecanol (250 ml) was added and the mixture was then distilled at 100 °C. The upper layer of the product was separated and shaken with sodium hydroxide solution (5%), washed several times with cold water, dried and redistilled to give *n*-dodecene. The physico-chemical characteristics of the prepared *n*-dodecene are given in *Table 3*.

Preparation of dodecyl coal tar phenols:

Alkylation of the coal tar phenols distillate with *n*-dodecene was carried out using sulphuric acid as a catalyst [10].

Coal tar phenols distillate (1.0 gmol) was dissolved in *n*-octane (100 ml) and was charged in a three-necked round-bottomed flask fitted with a condenser, a thermometer and a mechanical stirrer. Concentrated sulphuric acid (25 ml) was added and the temperature was raised to 50 °C, then *n*-dodecene (1.0 gmol) was added dropwisely over a period of two hours, after which the temperature was again raised to 120 °C for a further four hours with stirring. The reaction product was cooled, washed with alcoholic potassium hydroxide, then with water several times till neutrality and finally dried over anhydrous magnesium sulphate. The solvent was evaporated and the residue was fractionally distilled at 10 mm.Hg. to give the product. The physicochemical characteristics of dodecyl coal tar phenols are given in *Table 4*.

Preparation of the Mannich bases (I–III):

Three Mannich bases (I–III) with different structures were prepared in the present work via the condensation of dodecyl coal tar phenols, formaldehyde and triethylenetetramine in the ratios 1 : 1 : 1, 2 : 2 : 1 and 1 : 2 : 2, respectively.

The appropriate amount of dodecyl coal tar phenols in methanol (100 ml) and aqueous solution of triethylenetetramine (40%) were charged in a 4-necked round bottomed flask fitted with a condenser, a mechanical stirrer, a thermometer and a dropping funnel. A formaldehyde solution (37%) was then added dropwisely at 23–30 °C, the reaction mixture was refluxed for three hours, cooled and the lower layer of the mixture was separated, dissolved in benzene, washed several times with water, dried and distilled. The physico-chemical characteristics of the prepared Mannich bases are given in *Table 5*.

Evaluation of the prepared Mannich bases as lube oil additives:

Table 1.
Specifications of the coal tar phenols distillate

Test	Value
Boiling range, °C	180–230
Specific gravity at 15.6/15.6 °C	1.0667
Refractive index at 40 °C	1.5350
Average molecular weight*	110
Carbon, wt%	76.29
Hydrogen, wt%	7.81
Oxygen**, wt%	15.90

* Average molecular weights were determined as described in literature [14].
** By difference

Table 2.
Composition of the coal tar phenol distillate*

Component	wt%
Phenol	46.0
o-Cresol	10.3
m-Cresol	25.0
p-Cresol	9.4
Xylenols	9.3

* Analysis is given by the company

Table 3.
Physico-chemical characteristics of the prepared *n*-dodecene

Test	Value	
	determined	Literature [6]
Boiling range, °C	211–214	213
Molecular weight	172	168
Density at 30 °C, g/cm^3	0.7580	0.7583
Refractive index at 20 °C	1.4309	1.4300

A) *As antioxidants:*

The lube oil sample as well as its blends with 5% by weight of each of the three prepared Mannich bases (I–III) were subjected to severe oxidation conditions in the presence of copper and iron strips at 165.5 °C for 72 hours using the Indiana test method of oxidation [9]. The oxidation stabilities of the lube oil blends were determined by taking samples at 12 hour intervals up to 72 hours. These samples were tested for:

1. Viscosity at 37.8 °C, according to IP method 71/75.
2. Total acid number, according to IP 177/64.

The results are given in *Table 6.*

Table 4.
Physico-chemical characteristics of the prepared dodecyl coal tar phenols

Test	Value
Boiling range, °C	360–440
Kinematic viscosity at 70 °C, cSt	7.9247
Refractive index at 40 °C	1.4986
Density at 40 °C, g/cm^3	0.8983
Mean molecular weight	278
carbon, wt%	82.35
Hydrogen, wt%	11.38
Oxygen*, wt%	6.27
Mean number of carbon atoms/mol.	18
Mean number of hydrogen atoms/mol.	30
Mean number of oxygen atoms/mol.	1

* By difference

Table 5.
Physico-chemical characteristics of the prepared Mannich bases (I–III)

Characteristic	Mannich base		
	I	II	III
Kinematic viscosity at 37.8 °C, cSt	70.18	251.8	115.0
Refractive index at 40 °C	1.516	1.515	1.5175
Density at 40 °C, g/cm^3	0.9362	0.9565	0.9552
Mean molecular weight	435	698	584
Carbon, wt%	72.21	77.14	76.13
Hydrogen, wt%	11.36	10.85	10.86
Nitrogen*, wt%	13.27	7.40	18.97
Oxygen, wt%	3.16	4.73	3.04
Mean number of carbon atoms/mol.	25	45	32
Mean number of hydrogen atoms/mol.	48	75	63
Mean number of nitrogen atoms/mol.	4	4	8
Mean number of oxygen atoms/mol.	1	2	1
Total base number, mg KOH/g sample	133.56	116.87	144.69

* Determined by Kjeldahl method as described in literature [2]

B) *As detergents/dispersants:*
Spot method [5]:

Drops were taken from the samples being oxidised in the Indiana test after 12 hour intervals of oxidation and up to 72 hours to make spots on special filter paper (Durieux 122) and the dispersancy of the samples was measured as follows:

Table 6.
Oxidation stability expressed in terms of the changes in both of viscosity ratios (V_{oxid}/V_o) and of the total acid number (ΔT.A.N.) of the lube oil samples with and without 5% of the Mannich bases (I–III) before and after the oxidation periods

Sample	Oxidation time hr					
	12	24	36	48	60	72
V_{oxid}/V_o						
Lube oil only	1.0	1.15	1.34	1.60	2.00	2.74
Lube oil + M. B. (I)	1.0	1.05	1.10	1.14	1.18	1.29
Lube oil + M. B. (II)	1.0	1.07	1.14	1.19	1.23	1.25
Lube oil + M. B. (III)	1.0	1.15	1.34	1.60	2.00	2.74
ΔT.A.N.						
Lube oil only	6.04	10.13	17.31	18.12	19.34	19.52
Lube oil + M. B. (I)	0.00	0.54	1.15	1.63	1.97	2.75
Lube oil + M. B. (II)	0.00	0.42	0.93	1.41	1.74	2.62
Lube oil + M. B. (III)	0.00	0.24	0.62	1.03	1.46	1.57

M. B. = Mannich base

$$\% \text{ Dispersancy} = \frac{\text{diameter of the black spot}}{\text{diameter of the total spot}} \times 100$$

The results are given in *Table 7*.

C) *As pour point depressants [8]:*

The pour points were measured according to IP method 15, and the results are given in *Table 8*.

D) *As viscosity index improvers [8]:*

The viscosity index was measured according to IP method 226, and the results are also given in *Table 8*.

Results and Discussion

Characterisation of coal tar phenols mixture:

The data given in *Tables 1* and *2* clearly show that the coal tar phenols mixture has a boiling range (180–230 °C) and an average molecular weight of 110. It is composed of phenol, *o-*, *m-* and *p*-cresols and xylenols.

Its infra-red absorption spectrum (recorded on a Perkin-Elmer Spectrophotometer Model 598) indicates the appearance of a broad band at 3600–3100 cm^{-1} and a band at 1600–1580 cm^{1} characteristic for the phenolic OH group and the aromatic ring, respectively [3].

Preparation of the olefin:

Results given in *Table 3* indicate that the prepared *n*-dodecene is of high purity giving a density and refractive index almost as given in literature [6].

Preparation of alkyl phenols from coal tar phenols mixture:

Table 7.
Dispersancy of lube oil sample and its blends containing Mannich bases (I–III, 5 wt%) after different oxidation periods

Sample	% Dispersancy					
Time, hr	12	24	36	48	60	72
Lube oil	48	40	38	35	35	34
Lube oil + M. B. (I)	33	34	61	64	62	63
Lube oil + M. B. (II)	34	37	64	62	62	63
Lube oil + M. B. (III)	34	36	62	70	77	75

M. B. = Mannich base

Table 8.
Effect of the prepared Mannich bases (I–III; 5 wt%) on the pour point and viscosity index of the lube oil sample

Sample	Pour point, °C	Viscosity index
Lube oil	−3	95
Lube oil + M. B. (I)	−7	102
Lube oil + M. B. (II)	−7	103
Lube oil + M. B. (III)	−10	112

Data given in *Table 4* indicate that the mean molecular weight and the elemental analysis provide an idea about the structure of the prepared compounds. The mean molecular weight is higher than the calculated value for dodecyl phenol. This may be due to the presence of a mixture of phenol, cresols and xylenols in the sample.

Preparation and characterisation of the prepared Mannich bases (I–III):

The physico-chemical characteristics of the prepared Mannich bases (I–III) are given in *Table 5*. It may be concluded that the mean molecular weights as well as the elemental analysis may approximately give an idea about the mean number of the carbon, hydrogen, nitrogen and oxygen atoms per mole, since the alkyl phenols used in the preparation of these compounds are not pure products. The mean number of nitrogen atoms per mole of the Mannich bases (I and II) is four. This is as expected, since one molecule of triethylenetetramine, which contains four atoms of nitrogen, was used in their preparations. However, in the case of the Mannich base (III) the mean number of nitrogen atoms per mole is eight since two molecules of triethylenetetramine were used in its preparation. Thus, it has a total base number greater than that of the other two Mannich bases. However, the presence of two phenolic groups in the Mannich base (II) is responsible for lowering its basicity.

The infra-red spectra indicate that the bands characteristic for the carbonyl group of formaldehyde molecule are completely absent in all prepared Mannich bases.

The above deducations point to the possible formation of the following expected structures for the three Mannich bases (I–III):

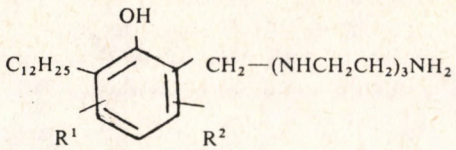

Mannich base (I)

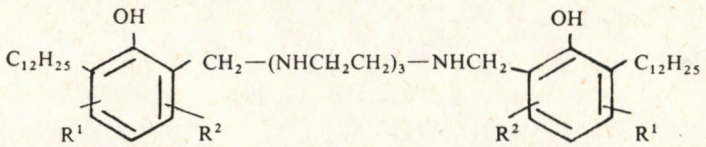

Mannich base (II)

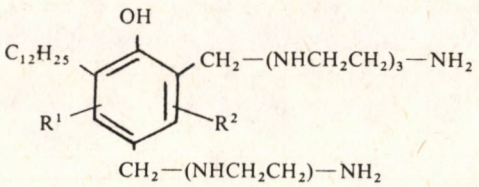

Mannich base (III)
$R^1 = R^2 = H$ or CH_3

Evalutation of the prepared Mannich bases (I–III) as lube oil additives:

A) *As lube oil antioxidants:*

The results given in *Table 6* for the Mannich bases (I–III) indicate that they impart better oxidation inhibition to the lube oils. This may be attributed to the presence of phenolic and amino groups in their structures. The efficiency of phenolic compounds as antioxidants is attributed to the fact that they are chain breaking inhibitors. The phenolic and aromatic amines inhibitors function by donation of a labile hydrogen from such groups as OH or NH to stabilize the chain radicals, i.e. these inhibitors destroy the peroxide radicals, and thus the oxidation chain is broken [4]. The presence of the amino group in the structure of the prepared compounds neutralizes some of the acidic products of the lube oil oxidation. It has been found that compound (III) is the best as a lube oil antioxidant, followed by compound (II), then compound (I) comes later. The high efficiency of Mannich base (II) is due to the presence of two phenolic groups in its structure, which play an important role as an antioxidant in these compounds. The higher efficiency of compound (III) compared with the other Mannich bases is due to the fact that it contains nearly double the number of NH groups in its structure. The presence of two terminal NH_2 groups also enables it to react with some of the acidic oxidation products.

B) *As lube oil dispersants:*

Results given in *Table 7* for the Mannich bases (I–III) clearly show that they have good dispersancy (63–75) for the sludge and solid particles formed during the lube oil oxidation for 72 hours. Their efficiency as detergents/dispersants becomes clear after 36 hours of oxidation. Data also show that compound (III) gives excellent dispersancy power during the lube oil oxidation. It is clear that the addition of such Mannich bases not only disperses solid particles in the oil and thus prevents their agglomeration and precipitation on metallic parts of engines that can cause damage, but also neutralizes some of the acidic products of oxidation due to their basic nature. Increasing the NH groups in the structure of the prepared Mannich bases promotes their capacity in dispersing sludge and solid particles in lube oils. This may be explained by the fact that the NH groups form hydrogen bonds with polar groups of oxidation products such as alcohols, aldehydes, ketones, and acids, etc.

C) *As pour point depressants and viscosity index improvers for lube oils:*

Inspection of results given in *Table 8* indicates that the prepared compounds slightly improve other properties of the lube oils, such as the pour point and viscosity index.

REFERENCES

1. ABBOTT, A. D.: US. Pat. 3, 983, 041 (1976); Chem. Abstr. 86, 109 042 (1977).
2. BATTLES, W. R. et al.: Inst. Petrol., *(1963)*, 49 (479), 340.
3. BELLAMY, L. J.: The infra-red spectra of complex molecules. Third eddition, John Wiley and Sons Inc., New York (1975).
4. BOLLAND, J. L. and TEN, H. P.: Discussion Faraday Soc. *(1947)*, 2, 252.
5. GATES, V. A., BERGSTROM, R. F. and WENDT, L. A.: Society of Automative Engineers (SAE), No. 572 (1955).
6. GILMAN, H.: Org. Synth., Collective vol. *(1948)*, 1, 430.
7. GUREEV, A. A. and CHERTKOVA, YA.: Khim. Tekhnol. Topl. Masel. *(1977)*, 6, 9; Chem. Abstr. 87, 120 219 (1977).
8. I. P. Standard for petroleum and its products. Published by the Institute of Petroleum, London 15/67 and 266/68 (1976).
9. LAMB, G. G., LOANCE, C. M. and GAYNOR, J. W.: Ind. Eng. Chem. Anal. Ed., *(1941)*, 13, 317.
10. LAPPIN, G. R., THOLSTRUP, C. E. and KELLY, C. A.: Advan. Chem. Ser *(1968)*, 85, 155.
11. PLONSKER, L. and MALEC, R. E.: US. Pat. 4, 025, 451 (1977); Chem. Abstr. 87. 70 809 (1977).
12. Standard Oil Co., (Indiana)., Neth. Appl. 6, 613, 298 (1967); Chem. Abstr. 67, 75 168 (1967).
13. THOMPSON, J. L., DELUGA, S. S., HARNACH, J. W. and SHAMAH, E. (Standard Oil Co., Indiana), US. Pat. 4, 131, 551 (1978); Chem. Abstr. 90, 124 421 (1979).
14. VAN NES, K. and VAN WESTEN, H. H., Aspect of the Constitution of mineral oils. Elsevier Publ. New York (1951).

HUNGARIAN JOURNAL
OF INDUSTRIAL CHEMISTRY
VESZPRÉM
Vol. 17. pp. 319–327 (1989)

SOME STUDIES ON IMPROVING LOW TEMPERATURE HANDLING OF EGYPTIAN WAXY CRUDES AND LOCAL FUEL OILS

H. Kh. Gharieb, O. M. O. Habib* and I. M. I. El-Gamal

(Egyptian Petroleum Research Institute and *Chemistry Department, Faculty of Science, Mansoura University, Egypt.)

Received: October 19, 1988

Fluidity and viscosity of Egyptian residual fuel oil were improved by subjecting it to some physical treatments. These involve preheating the oil samples under investigation to temperatures ranging from 70–120 °C, followed by cooling to temperatures in the range 18–0 °C, then changing the temperature at which the rate of cooling must be varied (85–35 °C) and finally altering the rate of cooling from 5.5 °C/min. to 0.7 °C/min. The optimum conditions were attained at preheating to 110 °C, then cooling to 85 °C at a rate of 5.5 °C/min then altering the rate of cooling to 0.7 °C/min. till 15 °C. The upper pour point of the treated samples was not affected by the above treatments. The optimum conditions were applied to three Egyptian waxy crude oils and improved their fluidity. The storage of the treated samples for six months does not affect their improved fluidity.

Introduction

Transportation of waxy crudes and residual fuel oils from well to refinery, and from refinery to places where they are used, presents a number of problems due to wax separation, resulting in hindering their flow at low temperatures [1]. It was found that physical treatment of the crude oils by shearing before pumping lowers their viscosities and thus results in improving their flow properties at low temperatures [2, 3]. In a previous work in this area, the fluidity of some Egyptian waxy crudes and residual fuel oils was improved by subjecting them to chemical treatments using some ashless flow improver additives [4]. The present investigation concerns with the application of some physical treatments of some Egyptian residual fuel and crude oils aimed at improving their flow characteristics at low temperatures.

Experimental, Results and Discussion

In the present work, trials were made to solve the problem of wax coagulation from some local waxy crudes and residual fuel oils during their transportation through pipelines at low temperatures. The samples under consideration were previously characterised [4] and were subjected to some physical treatments in order to improve their flow characteristics at such temperatures. Fluidity was evaluated in terms of maximum fluidity temperature (M.F.T.) and viscosity [5].

The samples used were subjected to several cycles of heating and cooling at different rates. These cycles were classified in terms of four independent factors controlling the whole process:

Effect of Preheating the Samples to Different Temperatures

It is well known that the fluidity of waxy fuel oils is dependent on their previous thermal history [6]. Therefore, the samples under evaluation were thermally treated as follows: six portions of the sample were preheated to 120, 110, 100, 90, 80 and 70 °C, respectively. They were then cooled at a rate of 5.5 °C/min. till 65 °C when the rate of cooling was changed to 0.7 °C/min. till 12 °C. After such treatment, the M.F.T. was evaluated and the results are given in *Table 1* and *Figure 1*.

It could be concluded from these results that the optimum M.F.T. was achieved by preheating the sample to 110 °C. This improvement in M.F.T. may be attributed to the modification of the wax crystal structure caused by the adsorption of a small amount of asphaltenes and resins on the surface of the growing crystals, thus preventing the formation of a waxy network that hinders the liquid flow [7].

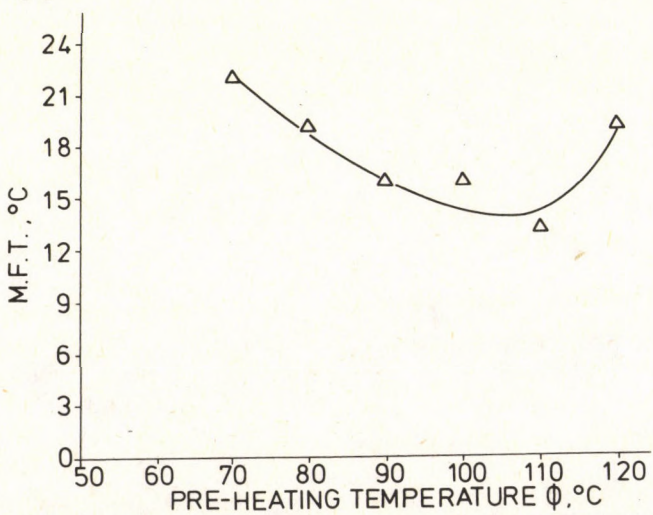

Fig. 1.
Effect of pre-heating on the MFT of residual fuel oil

Table 1.
Effect of pre-heating temperature on the fluidity of residual fuel oil using the ASTM method

θ, °C \ T, °C	38	49	60	71	82	93	M.F.T. °C
70	22	22	22	19	22	19	22
80	19	19	16	19	19	19	19
90	16	16	16	16	13	13	16
100	16	16	16	13	16	16	16
110	13	13	10	13	13	13	13
120	19	19	19	16	19	19	19

Where: θ = Pre-heating Temperature, °C; T = Fluidity Test Temperature, °C; M.F.T. = Maximum Fluidity Temperature, °C

Effect of Cooling the Samples to Different Temperatures

After heating the six portions of the sample to the favourable preheating temperature (110 °C), they were cooled to 65 °C at a rate of 5.5 °C/min., then the rate of cooling was altered to 0.7 °C/min. till 18, 15, 12, 9, 6 and 3 °C, respectively. The M.F.T. was evaluated for each portion and the results are given in *Table 2* and in *Figure 2*.

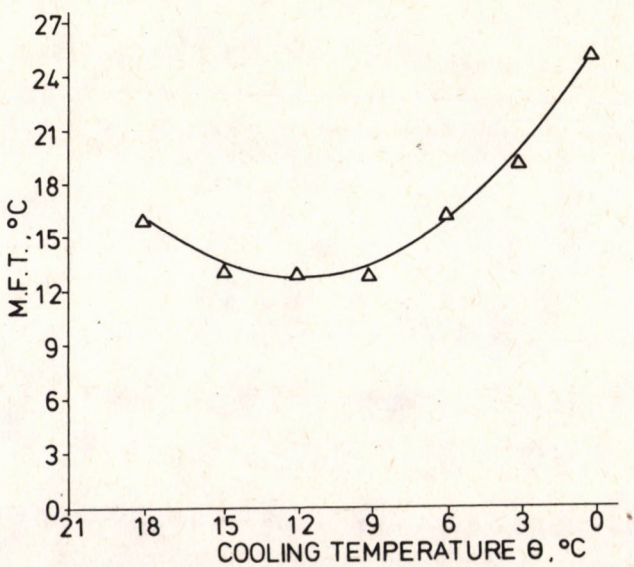

Fig. 2.
Effect of cooling on the MFT of residual fuel oil

Table 2.
Effect of cooling temperature on the fluidity of residual fuel oil pre-heated to 110 °C using the ASTM method

θ, °C \ T, °C	38	49	60	71	82	93	M.F.T. °C
18	16	16	16	13	13	16	16
15	13	13	13	10	13	10	13
12	13	13	13	13	10	13	13
9	13	13	10	13	13	10	13
6	16	16	16	13	16	16	16
3	19	16	19	19	16	19	19
0	25	25	25	25	22	25	25

Where: θ, Cooling temperature, °C

It is obvious that the preferable M.F.T. was reached by cooling to either 15, 12, or 9 °C. From an economic point of view, the cooling temperature 15 °C is considered the most favourable temperature to which the fuel oil must be cooled. Further cooling below 9 °C was accompanied by decreasing the fluidity. This may be due to the fact that at low temperatures the rate of wax precipitation increases, thus affecting the morphology of the precipitated wax crystals.

Selection of the Temperature at which the Rate of Cooling Must be Changed

In order to select the temperature at which the rate of cooling should be changed, six portions of the oil sample were preheated to 110 °C, then cooled at a rate of 5.5 °C/min. to 95, 85, 75, 55, 45 and 35 °C, respectively. After each of these temperatures was attained, the rate of cooling was altered to 0.7 °C/min., till 15 °C. The M.F.T. was evaluated and the results are given in *Table 3* and *Figure 3*.

Table 3.
Selection of temperature at which the rate of cooling is varied using the ASTM method

θ, °C \ T, °C	38	49	60	71	82	93	M.F.T. °C
95	19	19	19	19	16	16	19
85	10	7	7	10	7	7	10
75	7	10	10	10	7	10	10
65	10	10	13	13	10	13	13
55	13	13	13	10	13	13	13
45	19	16	19	19	19	19	19
35	22	22	19	22	22	22	22

Where: θ = Temperature at which the rate of cooling is varied, °C

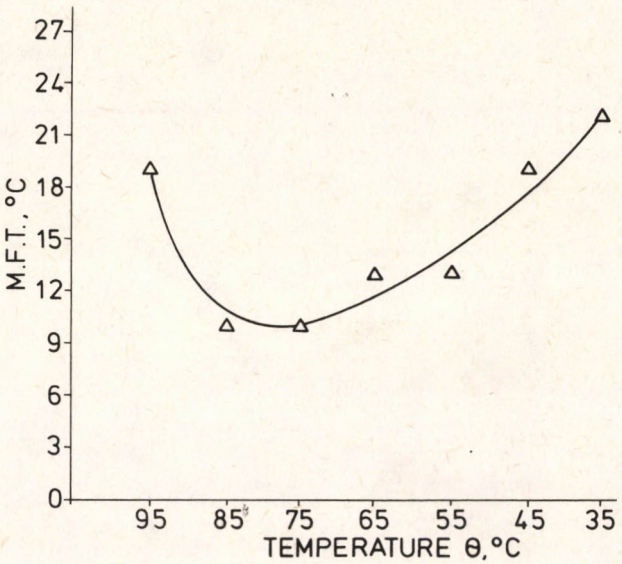

Fig. 3.
Selection of temperature at which the rate of cooling is varied

It is clear that the optimum M.F.T. was attained at either 85 or 75 °C. This may be attributed to the fact that cooling the oil sample at a rate of 5.5 °C/min. leads to shock chilling of the fuel resulting in the formation of small waxy crystals thus improving its fluidity. Further cooling below 75 °C results in increasing the rate of precipitation of these small waxy crystals more rapidly to an extent that inversely affects the fluidity as a result of re-altering the morphology of the precipitated wax crystals. Therefore, the rate of cooling has to be changed at the preferable temperature (85 °C) to the optimum cooling temperature previously concluded (15 °C).

Effect of Changing the Rate of Cooling

Five samples of the fuel oil were heated to 110 °C then cooled at a rate of 5.5 °C/min. till 85 °C, then the rate of cooling was changed to 3.8, 2.7, 1.6 and 0.7 °C/min., respectively till 15 °C. The M.F.T. was evaluated after such treatment and the results are given in *Table 4* and *Figure 4*.

It can be concluded that decreasing the rate of cooling was accompanied by improving the fluidity of the treated sample. The optimum fluidity was attained using a rate of cooling of 0.7 °C/min. Such an improvement may be attributed to the change in the rate of precipitation of the wax crystals, which leads to an alteration in their size and growth at each rate of cooling individually. It was

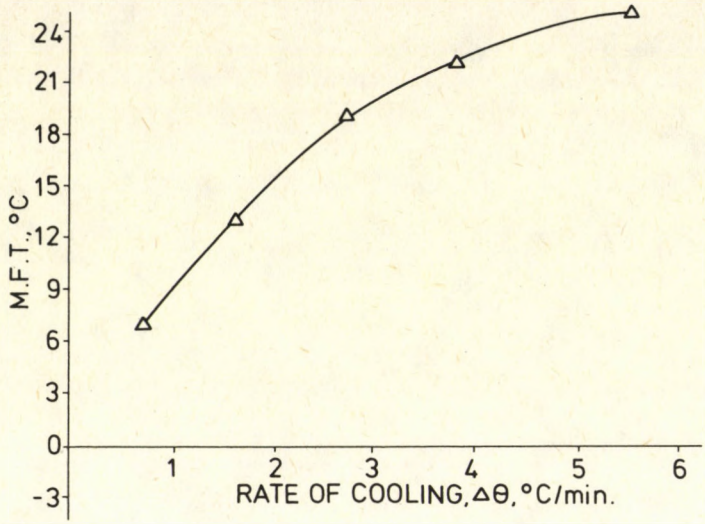

Fig. 4.
Effect of rate of cooling on the MFT of residual fuel oil

Table 4.
Effect of rate of cooling on the fluidity temperature of residual fuel oil using the ASTM method

T, °C / Δθ °C/min	38	49	60	71	82	93	M.F.T. °C
5.5	25	25	22	25	22	25	25
3.8	22	22	19	19	22	22	22
2.7	19	19	19	16	19	19	19
1.6	13	13	13	10	13	13	13
0.7	7	7	7	7	4	7	7

Δθ = Rate of cooling, °C/min.

previously stated that decreasing the cooling rate below 0.7 °C/min. did not very much affect the morphology of the wax crystals [8]. The only noticeable effect was the formation of some large, but very thin waxy plates leading to a slight improvement of fluidity in an uneconomic way.

On the other hand, the effect of the above physical treatments on the upper pour point and viscosity, of the residual fuel oil under consideration was also studied. The results are given in *Tables 5* and *6* and in *Figure 5*. It is obvious that such treatment does not in any way affect the upper pour point of the samples. This result agrees with that reported in literature [9], which states that the pour point test cannot measure the operability of residual fuel oils or waxy crudes at low temperatures.

Table 5.
Effect of physical treatment on the upper pour point and maximum fluidity temperature of residual fuel oil

Sample No.	Upper pour point °C	M.F.T. °C	
		ASTM	DIRECT
(A)	30	25	22
(B)	30	16	7
(C)	30	13	4
(D)	30	7	−2

Where (A) Untreated residual fuel oil sample.
(B) Oil sample pre-heated to 110 °C, cooled at 5.5 °C/min. till 15 °C.
(C) Oil sample pre-heated to 110 °C, cooled at 0.7 °C/min. till 15 °C.
(D) Optimum physically treated oil sample.

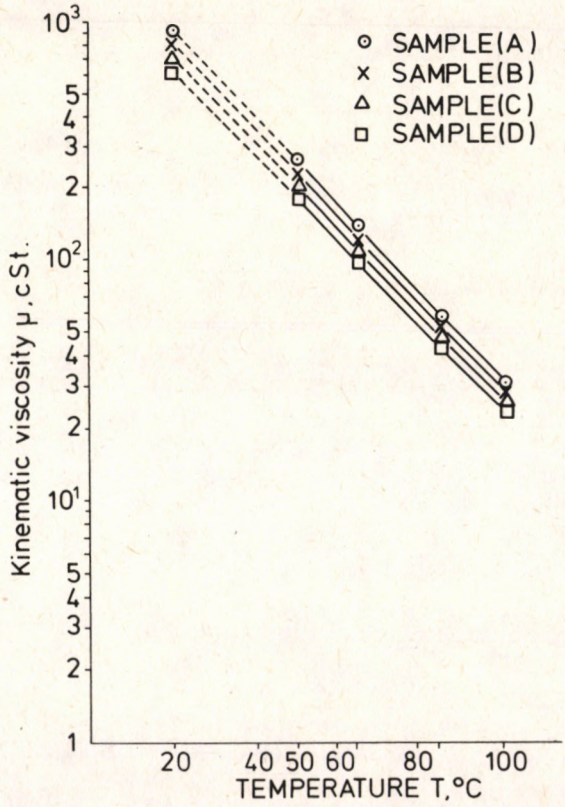

Fig. 5.
Effect of temperature on viscosity of residual fuel oil at low temperatures

Table 6.
Effect of temperature on viscosity of different treated oil samples

Sample No / T, °C	(A)	(B)	(C)	(D)
100	31.75	28.60	26.00	23.70
85	58.80	52.15	47.50	43.15
65	138.00	121.25	107.10	96.50
50	265.00	223.00	198.50	177.00
20	900	795	700	610

Where: μ = Kinematic viscosity, cSt; T = Temperature, °C

Kinematic viscosity, of the above treated samples was determined at 50, 65, 85 and 100 °C. Extrapolation of the straight lines resulting from plotting the viscosity against the temperature gave the kinematic viscosity at 20 °C *(Table 6* and *Figure 5)*. It could be concluded that the viscosities were reduced to a large extent at low temperature (20 °C). As a result of the above treatments, the viscosity was reduced from 900 cSt for the untreated sample (A) to 610 cSt for sample (D), which was subjected to the optimum conditions of treatment. In all cases there was a decrease in viscosity of the treated samples compared with that untreated.

The previous method of viscosity evaluation was carried out according to literature [10] stating that Bingham plastic viscosities at low temperatures can be obtained by extrapolating high temperature kinematic viscosity measurements to lower temperatures.

Physical treatment of local waxy crudes

Three local waxy crudes, namely Ras-Gharah, Morgan and Ramadan were subjected to the optimum conditions of physical treatment obtained for local residual fuel oil. The M.F.T. was estimated before and after treatment, and the results are given in *Table 7*. It is clear that the M.F.T. of the treated crudes was improved and that the improvment was much more noticeable with Ras-Gharah crude oil sample, which containes the highest wax content. This result is in good agreement with that reported in literature [1].

Table 7.
Effect of physical treatment on the M.F.T. of local Crude oils with different wax content

Crude oil	Wax wt%	M.F.T. °C	
		Before treatment	After physical treatment
Morgan	9.8	−4	−16
Ramadan	7.6	−7	−16
Ras-Gharah	10	13	−2

Effect of physical treatment on storage of the samples

Samples corresponding to the optimum conditions were stored at room temperature and their M.F.T. was estimated after two, four and six months, respectively. The results showed that storage up to six months does not affect the improved fluidity of the treated samples. This period is considered as a sufficient period as the problem is encountered only during the winter season.

REFERENCES

1. TOWELL, A. J. B.: *1st.* International Seminar on "Performance, Testing and Developments of Lube Oils, Fuels and Chemicals", Misr Petroleum Co., Research Centre, p. 318–336, 4–7 June (1977).
2. CHANDRASEKHARAN, K. P. and SIKDAR, P. K.: J. Oil and Gas International, *1970* 10 (10).
3. DYTYUK, L. T.: Neft. Khaz., *1969* 47 (8), 38–42.
4. GHARIEB, H. KH., HABIB, O. M. O. and EL-GAMAL, I. M.: Egyptian J. Chem., accepted for publication.
5. ASTM Designation; D-1659, Annual Book of ASTM Standards, part 18 (1965) (Reapproved 1970).
6. HARRIS, J.: J. Rheological Acta., *1968* 7 (3), 228–33.
7. KALICHEVESKY, V. A. and KOBE, K. A.: Petroleum Refining with Chemicals Elsevier, p. 525 (1965).
8. DAVENPORT, T. C. and SOMPER, R. S. H.: J. Inst. Petrol, *1971* 57, 554.
9. MORDUCHOWITZ, A. and BAILY, J. J.: US. Patent 4, 022, 590 (1977).
10. BILLINGTON, E. W.: Proc. Phys. Soc., *1960* 75, 40.

HUNGARIAN JOURNAL
OF INDUSTRIAL CHEMISTRY
VESZPRÉM
Vol. 17. pp. 329–335 (1989)

MODELLING CUBIC AUTOCATALYSIS BY SUCCESSIVE BIMOLECULAR STEPS: IMPLICATIONS ON THE PERIODIC OPERATION OF ISOTHERMAL TUBULAR REACTORS

M. CHIDAMBARAM
(Department of Chemical Engineering, Indian Institute of Technology, Bombay Powai, Bombay 400 076, India)

Received: October 29, 1988

The performance of the periodic operation of isothermal plug flow reactors for autocatalytic reactions are compared for the two variables: cubic rate kinetic model ($A+2B \rightarrow 3B$) and for the three variables: bimolecular successive second order reactions kinetic model ($A+B \rightleftharpoons X$, $X+B \rightarrow 3B$). For smaller values of the two parameters ε and K of a three variables scheme, similar behaviour to that of a two variables scheme (that is from a negligible yield at usual steady-state to a hundred percent yield under periodic operation) is obtained. For larger values of ε and K the three variables scheme gives a lower yield.

Introduction

Recently ARIS et al. [1] analyzed the performance of a steady-state CSTR for autocatalytic reactions. They considered two different modellings of autocatalytic reactions. The first model considers only two-variables, but requires a third-order kinetic model:

$$A+2B \xrightarrow{k_1} 3B \qquad r = -k_1 ab^2 \tag{1}$$

and the second model considers a 3-variables scheme with consecutive second-order reactions:

$$A+B \underset{k_{-2}}{\overset{k_2}{\rightleftarrows}} X \qquad r = -k_2 ab + k_{-2} x$$

$$X+B \xrightarrow{k_3} 3B \qquad r = -k_3 xb \tag{2}$$

Keywords: Periodie operation, Autocatalytic reactions, Tubular reactors, bimolecular and termolecular schemes.

ARIS et al. [1] primarily analyzed whether the steady-state multiplicity features arising from a cubic rate law [Eq. (1)] can also arise for a series of successive bimolecular reactions [Eq. (2)]. ARIS et al. [1] showed that the steady-state equations of a CSTR with bimolecular reactions reduce to that with a cubic reaction when the two parameters $\varepsilon(=k_3a_0/k_{-2})$ and $K(=k_2a_0/k_{-2})$ arising in system equations for the bimolecular reactions tend to zero. ARIS et al. (1988) showed that the general steady-state multiplicity features of the CSTR for bimolecular reaction is similar to that with termolecular reactions [Eq. (1)] only at smaller values of ε and K. The behaviour is considerably different at larger values of ε and K.

CHIDAMBARAM [4] recently analyzed the periodic operation (in feed concentration) of isothermal plug-flow tubular reactors for autocatalytic reactions involving a cubic from [Eq. (1)]. He showed that the periodic operation improves the average yield of the product from a negligible yield at usual steady-state to a hundred percent yield under periodic operation. The objectives of the present work are:

(i) to theoretically analyze whether bimolecular reactions [Eq. (2)] also give a similar improvement in yield under periodic operation and

(ii) to evaluate the effect of the parameters ε and K on the reactor performance under periodic operation.

Model Equations

We consider here isothermal, homogeneous autocatalytic reactions in a plug-flow reactor. The model equations for steady-state conditions are:

$$U\frac{da}{dz} = -k_2ab+k_{-2}x \tag{3}$$

$$U\frac{db}{dz} = -k_2ab+k_{-2}x+2k_3bx \tag{4}$$

$$U\frac{dx}{dz} = k_2ab-k_{-2}x-k_3bx \tag{5}$$

$$\text{at } z=0, \quad a=a_f, \quad b=b_f \quad \text{and} \quad x=0 \tag{6}$$

The dimensionless equations are:

$$\frac{1}{q}\frac{d\alpha}{dZ} = -\frac{1}{\varepsilon}\left(\alpha\beta-\frac{\xi}{K}\right) \tag{7}$$

$$\frac{1}{q}\frac{d\beta}{dZ} = -\frac{1}{\varepsilon}\left(\alpha\beta-\frac{\xi}{K}\right)+\frac{2\beta\xi}{K} \tag{8}$$

$$\frac{1}{q}\frac{d\xi}{dZ} = \frac{1}{\varepsilon}\left(\alpha\beta-\frac{\xi}{K}\right)-\frac{\beta\xi}{K} \tag{9}$$

$$\text{at } Z=0, \quad \alpha=\alpha_f, \quad \beta=\beta_f, \quad \xi=0 \tag{10}$$

In a similar manner to that as shown by ARIS et al. [1] for CSTR, the above equations [Eq. (7)–(10)] can be written as:

$$\frac{1}{q}\frac{d\alpha}{dZ} = -\alpha\beta^2 - K\alpha\beta^2(\alpha-\beta)+\varepsilon\alpha\beta^3+\ldots \tag{11}$$

$$\frac{1}{q}\frac{d\beta}{dZ} = \alpha\beta^2 - K\alpha\beta^2(\alpha-\beta)-\varepsilon\alpha\beta^3+\ldots \tag{12}$$

$$\text{at } Z=0, \quad \alpha=\alpha_f, \quad \beta=\beta_f \tag{13}$$

These equations clearly reduce to the original model equations for a cubic rate form [for Eq. (1)] in the limit both $\varepsilon \to 0$ and $K \to 0$.

Periodic Operation

Continuous periodic forcing (in feed concentration) of a wide variety of non-linear chemical processes has been shown to be superior in time-average performance to that obtained under conventional time-invariant operation (BAILEY, [3]; RENKEN, [5]; SILVESTON and HUDGINS, [7]). One important class of periodic operation as classified by BAILEY [3] and RENKEN [5] is that in which the steady-state condition is chosen arbitrarily and the mean value of the periodic input is the same as the steady-state input. Then the time average performance of the process under periodic operation is compared with that obtianed under steady-state operation. The present paper refers to this type of operation. The periodic forcing function assumed here is a rectangular pulse (bang-bang type) in the inlet concentration of both α_f and β_f as shown in *Figure 1*. It is assumed that the feed contains the components *A* and *B* and an inert. In *Figure 1*, α_f and β_f are the dimensionless amplitude of the inlet concentration pulse and γ is the cyclic split (i.e. pulse width expressed as a fraction of the dimensionless period). The condition of $\gamma = 1$ represents the usual steady-state operation and that of $\gamma < 1$ represents the periodic operation. If the dimensionless steady state input

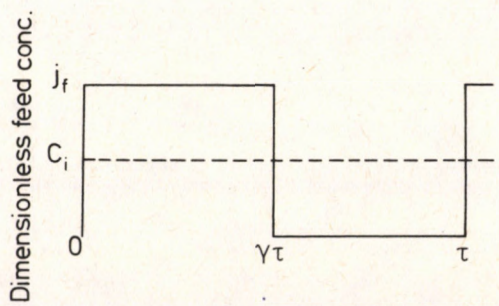

Fig. 1.
Inlet feed concentration of reactants *A* and *B*
$i = A, B, \quad j = \alpha, \beta$
——— Periodic operation; – – – – Steady-state operation

is fixed as C_A and C_B, then the following expressions can be obtained by averaging the inlet pulse over the period, τ:

$$\alpha_f = C_A/\gamma, \quad \beta_f = C_B/\gamma \tag{14}$$

To evaluate the average yield of B under periodic operation, we have to consider the transient equations of the tubular reactors [adding accumulation terms in the left side of the equations, Eq. (3) to (6)]. But for isothermal homogeneous plug flow reactors that we consider here, the average yield can easily be obtained by solving the steady-state equations [Eq. (7)–(10)] for two levels of inlet feed concentrations separately and we get the average of these yields (BAILEY, [3]). Steady-states of two different outputs for two different inputs, i.e. one for Eq. (14) and another for $\alpha_f = 0$ and $\beta_f = 0$ are mixed to gain the average exit state given:

$$(\beta)_{out} = \gamma(\beta)_{Z=1} \tag{15}$$

where $(\beta)_{Z=1}$ is the output for the input α_f and β_f as for Eq. (14). The average yield is given by:

$$\begin{aligned} Y &= (\beta)_{out} - C_B \\ &= \gamma(\beta)_{Z=1} - C_B \end{aligned} \tag{16}$$

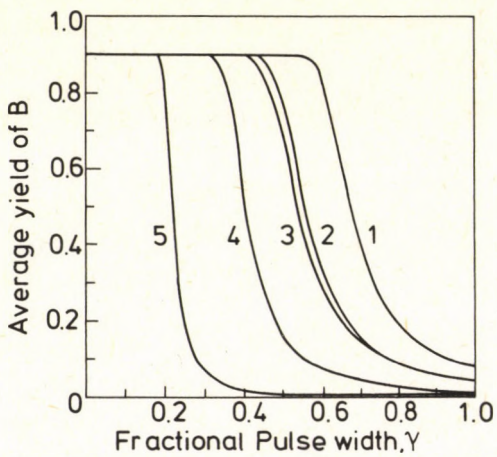

Fig. 2.
Average yield of B obtained under periodic operation.
$C_A = 0.9$, $C_B = 0.1$, feed concentration as for Eq. (14)

Curve No.	ε	K
1	0.0	0.0
2	0.3	0.1
3	0.5	0.1
4	0.3	0.3
5	0.3	0.6

We now evaluate the average yield of B of the three-variables scheme [Eq. (7)–(10)] and that of the two-variables scheme [$\varepsilon = 0$, $K = 0$ in Eq. (11) and (12)] and compare the behaviour of these two systems. The results are shown in *Figure 2* as an average yield, a function of fractional pulse width, γ. The two-variables model gives a hundred percent yield under periodic operation. For smaller values of ε and K, the 3-variables model also gives a hundred percent yield, but only at lower values of γ. For larger values of ε and K, the three-variables scheme gives a lower average yield. In other words, for a given value of γ, the two-variables scheme gives a higher yield. This difference in the average yield increases as ε and K increase. *Figure 2* also shows that K is more sensitive.

As stated earlier, the feed is assumed to contain the reactants A, B and an inert. Instead of periodically changing the feed concentration of A and B simultaneously as for Eq. (14), we need change only the feed concentration of A and keep the concentration of B at a constant value. That is:

$$\alpha_f = C_A/\gamma \quad \text{and} \quad \beta_f = C_B \tag{17}$$

The average yield of B is calculated as:

$$Y = \gamma(B)_{Z=1} + (1-\gamma)C_B - C_B \tag{18}$$

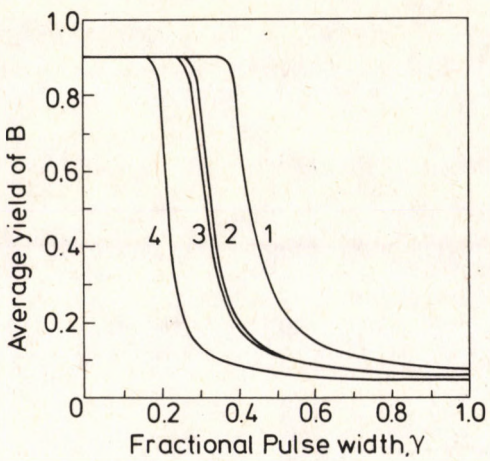

Fig. 3.
Average yield of B obtained under periodic operation.
$C_A = 0.9$, $C_B = 0.1$, feed concentration as for Eq. (17)

Curve No.	ε	K
1	0.0	0.0
2	0.1	0.05
3	0.2	0.05
4	0.1	0.1

The effect of this type of periodic operation on the average yield of B is shown in *Figure 3*. The curves shift towards the left when compared to those in *Figure 2*. For a given value of γ, the average yield of B is higher under periodically varying both A and B in the feed rather than varying only the concentration of A. The general effect of the parameters ε and K is similar to that shown in *Figure 2*.

It is known that under finite dispersion and at steady-state isothermal conditions, autocatalytic reactions may exibit oscillations, isolas and other multiplicity features (SCOTT, [6]). It will be interesting to study these multiplicity features for the two models discussed here under periodic operation. This will be reported in future.

Conclusion

The periodic operation of tubular reactors for three variables bimolecular successive second order reactions give a similar trend in average yield as that for two variables third order kinetic model only for small values of ε and K. For larger values of these parameters, the three variables scheme gives a lower average yield.

SYMBOLS

A, B	reactant and autocatalyst respectively
a	concentration of reactant A, gmol/cc
a_0	base value of concentration to which dimensionless concentration is obtained, gmol/cc.
b	concentration of product B, gmol/cc
C_A, C_B	dimensionless feed concentration of reactant A and B respectively at usual steady-state operation.
K	$k_2 a_0/k_{-2}$
k_1	reaction rate constant for Eq. (1), $(\text{gmol/cc})^{-2}$ (1/sec)
k_{+2}	forward reaction rate constant for Eq. (2), $(\text{gmol/cc})^{-1}$ (1/sec)
k_{-2}	backward reaction rate constant for Eq. (2), (1/sec)
k_3	reaction rate constant for the reaction $B+X \rightarrow 3B$, $(\text{gmol/cc})^{-1}$ (1/sec)
L	reactor length, cm
q	$k_1 a_0^2 L/U = (k_2 k_3/k_{-2}) a_0^2 L/U$
U	velocity of the fluid, cm/sec
X	intermediate product
x	concentration of intermediate product, gmol/cc
Y	average yield of B
Z	normalized distance, z/L
z	reactor axial distance, cm

Greek Letters

α	a/a_0, dimensionless concentration of reactant A.
β	b/a_0, dimensionless concentration of product B.
ε	$k_3 a_0/k_{-2}$
γ	pulse width expressed as a fraction of the dimensionless period, τ
ξ	x/a_0, dimensionless concentration of the intermediate product.
τ	dimensionless period.

Subscripts

f	feed
i	A or B

REFERENCES

1. ARIS, R., GRAY P., and SCOTT S. K.: Chem. Eng. Sci., *1988,* 43, 207.
2. BAILEY, J. E.: Can. J. Chem. Eng. *1972,* 50, 108.
3. BAILEY, J. E.: Periodic Phenomena, in *Chemical Reactor Theory: A Review,* L. Lapidus and N. R. Amundson (eds), pp. 758, Prentice Hall, New Jersey (1977).
4. CHIDAMBARAM, M., Chem. Eng. Comm., 1988, 69, 219.
5. RENKEN, A.: Int. J. Chem. Eng., *1984,* 24, 202.
6. SCOTT, S. K., Chem. Eng. Sci., *1987,* 42, 307.
7. SILVESTON, R. R. and HUDGINS, P. L., "Review of the Excitation of Chemical Reactors by Periodic Operation", in *Recent Trends in Chemical Reaction Eng.* (Ed.) B. D. Kulkarni et al. Wiley Eastern Ltd. Vol. I, 235 (1987).

HUNGARIAN JOURNAL
OF INDUSTRIAL CHEMISTRY
VESZPRÉM
Vol. 17. pp. 337–353 (1989)

LIQUID-PHASE DISPROPORTIONATION OF TOLUENE

S. N. VYAS, S. R. PATWARDHAN and M. G. GHARPURE

(Department of Chemical Engineering, Indian Institute of Technology, Powai, Bombay 400 076, India)

Received: November 11, 1988

Liquid phase disproportionation of toluene on zeolite catalysts, on which the available literature information is scanty, was studied in a high pressure, high temperature batch as well as in a continuous reactor. The first measurable conversion in the batch autoclave could be achieved at a 175 kg/cm^2, 346 °C, and SiO_2/Al_2O_3 ratio of 13.5 on a zeolite catalyst, whereas in the continuous flow reactor the conditions were: 50 kg/cm^2, 300 °C and SiO_2/Al_2O_3 ratio of 19.8 for the first conversion. Though near equilibrium conversion with high selectivity with respect to disproportionation could be obtained for 1.5 h of batch time, it was only about 15% maximum in the case of the continuous reactor study, due to space time limitation in the experimental work. A second order reversible rate model with exponential deactivation was found to fit the experimental data at 315 °C. The deactivation of the zeolite catalyst was of a temporary nature.

Introduction

Disproportionation of toluene has been established as an effective method for commercially converting toluene, which is being overproduced at present, to benzene and xylenes. It is well known that industrial outlets, mainly in the fields of rubber, plastics, fibres and solvents for benzene and xylenes (p-xylene to be precise) are far more than toluene-based ones. Obviously the demand for benzene and *p*-xylene is mounting and in India net short fall of about 250,000 and 167,000 tonnes each per annum [1, 2], respectively, is expected by the end of 1988. Conversion of toluene to benzene and *p*-xylene could be an appropriate method in order to augment the supply position of these two petrochemical base materials in India. Hydrodealkylation is another method to eliminate toluene at the expense of benzene. These two routes can be integrated along with downstream xylene isomerization so that any desired ratio of benzene to *p*-xylene can be obtained. The economic comparison of the two processes was

given by RUDD and coauthors [3] in terms of fuel oil equivalent tonnes of benzene produced. Disproportionation is seen to have an advantage over hydrodealkylation in this regard.

Disproportionation of toluene was first carried out by ANCHUTZ [4] using a $AlCl_3$ catalyst. Later on, solid acid catalysts, such as silica, alumina, alumina-boria, metal oxides, etc., were developed [5, 6]. After 1970, the scenario changed completely with the advent of synthetic zeolites, amongst which *X*, *Y*, mordenites, and ZSM were prominent ones. The shape and size selectivity of these synthetic zeolites are responsible for high selectivity towards disproportionation reactions.

There is exhaustive literature available on toluene disproportionation in a vapour phase. Only a few relevant reports are cited here. Studies on six membered ring structures, i.e. *x* and *y* were reported [7]. On a five membered base or hydrogen exchanged zeolites, namely mordenite and ZSM, the investigations were conducted at 30–70 kg/cm^2 hydrogen pressure and 400–500 °C [8, 9]. The change in catalytic behaviour with respect to charge, an increase in Bronsted acidity and pore size could be brought about by modifications of original zeolites, such as dealumination and cation-exchange. It is well established that the specificity of the reaction, and the resistance to coke formation could be improved by such techniques. Mordenite is far more amenable to such modifications than any other zeolite. Not surprisingly, there was a spate of reports on modified zeolites. HALGERI did considerable work on the reaction by using dealuminated *X*, *Y*, and mordenite catalysts. NAKNO and coworkers [10] and THAKUR and coworkers [11] reported their work on dealuminated mordenites. Likewise a considerable amount of work was reported on cation-exchanged zeolites [12–21], where elements from practically all the groups were used for cation-exchange.

In spite of the above mentioned modifications, zeolites were only partly successful as catalysts for a toluene disproportionation reaction, in the sense that though they had higher initial activity and good selectivity, their resistance to deactivation was poor. Composite catalysts [12, 22, 23] were tried to solve this problem, but there was not much headway.

From the foregoing discussion it is quite clear that the major thrust, as far as catalyst and process development aspects are concerned, is on vapour phase disproportionation (VPD) using synthetic zeolites as such or in modified forms. A wide range of pressures from 1 to 70 kg/cm^2 and temperatures in the range 350–550 °C were used for the study. However, successful commercial processes are based on liquid phase disproportionation (LPD). Some details of two such processes, namely Mobil's LTD and TATORAY's are available [24].

If toluene disproportionation is carried out in a liquid phase, the following advantages over VPD are envisaged: (1) Liquid toluene acts as a solvent for coke precursors [25], thereby keeping the catalyst surface free from deactivators all the time; (2) High hydrogen pressure favours the hydrogenation reactions for coke-like molecules [26]; (3) Capillary action and better utilization of the catalyst surface because of surface tension of the liquid is possible [27]; (4)

Higher adsorption capacity for toluene at the active sites at high pressure is exhibited [28], (5) The catalyst has a higher service life, because of the lower reaction temperature [29].

Hardly any work was reported in the published literature on the LPD of toluene. Therefore, the present work was undertaken, both for the collection of the process data, and the development of a suitable kinetic expression.

Experiments

Two commercially available grades of mordenite obtained from M/s. Norton Company, U.S.A. namely Zeolon 100 and Zeolon 900 in Na form, were converted to H form for the studies. They were characterized by *X*-ray diffraction. Both the samples had a surface area of 400 m^2/g, and particle porosity of 0.244.

Zeolon 900 H was mainly used for continuous flow reactor studies, whereas Zeolon 100 in H form was used for the batch reactor experiments. The two mordenite samples were subjected to dealumination by HCl leaching, Nickel exchange, and Nickel impregnation. Nickel salt was used for the latter modifications on the basis of our successful past experience in the vapour phase reaction [30].

The ranges of parameters studied in the two modes of operation are given in *Table 1:*

Table 1.

Ranges of variables studied

Variable	Batch reactor	Continuous reactor
SiO_2/AlO_3 ratio in mordenite	12–49	12–49
Temperature, °C	200–390	300–380
Pressure, kg/cm^2	50–230	20–70
Volumetric flow rate of gas at atmospheric pressure, ml/h	–	360–720
Initial toluene charge, ml	100–150	–
Reaction time, h	0.5–5	–
Weight of catalyst, g	10–30	20–50

Nickel exchanged mordenite contained 0.2% Ni by weight. For nickel impregnation the slurry of 10 : 1 (by wt) catalyst: $Ni(NO_3)_2$ was heated to dryness and then calcined at 500 °C for 3 hours.

Preliminary screening of the catalyst was done by carrying out experiments in a horizontal rotary type high pressure-high temperature autoclave of 0.5 l capacity.

Catalyst activity and kinetic experiments were conducted in a flow reactor, 25 mm i.d. and 900 mm length, made of alloy steel and capable of operating up to a pressure of 150 kg/cm^2 and temperature of 500 °C. The reactor, made by the Institute of Petrochemical Institute, Moscow, had a trisectional heating arrangement. Product samples were collected after cooling and condensing the

outlet vapours. The analysis of the liquid product was done by using GC at 116 °C on 4 mm column of celite 545 with 7 parts of Bentone 34 and 5 parts of divinyl phthalate per 100 parts of the solid support. Injection port temperature was maintained at 150 °C. The flow of hydrogen was kept at 60 ml/min and its analysis was done on a TCD block. Another HP 3 mm column containing 10% OV-17 on chromosorb-*W* was used for confirmation of the results at similar conditions.

Results and Discussion

Since no systematic study has been published on LPD, the results of the present work are discussed and compared with respect to those obtained in VPD by other workers.

In batch reactor studies, the powder form of mordenite was used so as to get a good dispersion in the reacting media. Batch studies also provided good operational flexibility and sufficient reaction time so that all possible side reactions could proceed.

No conversion could be detected in the absence of the catalyst, or with binder alone at 40–100 kg/cm^2 in a temperature range of 250–300 °C. It was also observed that no conversion of toluene could be achieved below 340 °C, when the initial pressure, with both hydrogen and nitrogen as pressuring agents, was varied in a range 46–225 kg/cm^2 with all mordenite samples, though the lowest temperature for the onset of LPD is reported to be 250 °C. The conversion was first observed at 346 °C with corresponding pressure of 175 kg/cm^2. At these conditions, the effect of SiO_2/Al_2O_3 ratio in mordenite on toluene conversion was studied and the data are presented in *Fig. 1*.

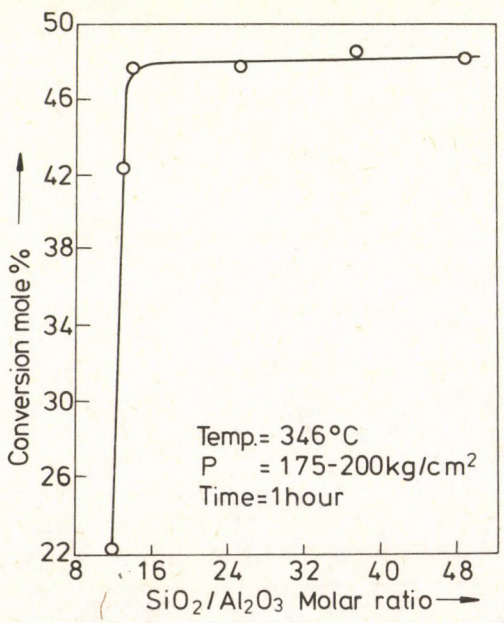

Fig. 1. Effect of SiO_2/Al_2O_3 ratio on conversion

Effect of Dealumination

Dealumination leads to the creation of stronger acid sites [31] and hence higher initial activity and better dispersion of active sites on the catalyst surface [32].

After an initial sharp rise with a small change in SiO_2/Al_2O_3 ratio, when the conversion actually jumped from 22 to 47%, the conversion became stabilized at around 47% (equilibrium conversion is around 55%), contrary to the present observation in VPD, where the activity was found to decrease with an increase in the SiO_2/Al_2O_3 ratio.

Fig. 2 shows the effect of the SiO_2/Al_2O_3 ratio on benzene to the xylenes molar ratio in the product stream. The plot indicates the occurrence of a dealkylation reaction on stronger acid sites, which confirms with VPD reports [33].

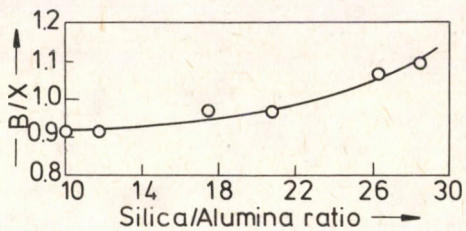

Fig. 2.
Effect of silica/alumina ratio on benzene/xylene ratio

The batch experiments indicated a choice towards the catalyst with a SiO_2/Al_2O_3 ratio of 13.5 and therefore it was selected for further experimentation.

Effect of Batch Time

The effect of batch time on the conversion and the disproportionation reaction selectivity is shown in *Fig. 3*. Here the batch time is taken from the time after attaining 346 °C. Liquid toluene and the catalyst powder were taken in the autoclave and pressurized with nitrogen or hydrogen to 60 kg/cm^2. Heaters were then switched on till the temperature of 346 °C was reached. The pressure developed at this stage was taken as the reactor pressure, which was substantially steady in the range of 175–200 kg/cm^2. Samples were drawn after the run after cooling the reactor to ambient temperature ($\sim$30 °C). The conversion did not change significantly, but the selectivity of the reaction worsened with an increase in the batch time. It was concluded that the successful batch process can be conducted for about 1.5 h at the conditions mentioned.

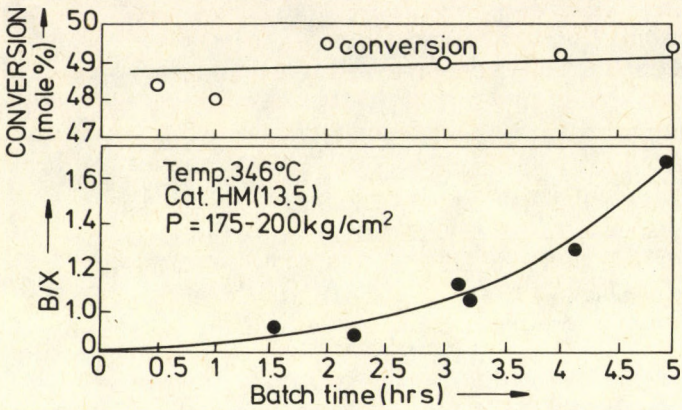

Fig. 3.
Effect of batch time on conversion and benzene/xylene ratio

In a continuous reactor, the conversion was first observed at 300 °C on H-mordenite with SiO_2/Al_2O_3 ratio of 19.8 and hydrogen pressure of 45 kg/cm^2. The plot of pressure vs conversion *(Fig. 4)* showed a maximum at 50 kg/cm^2 with corresponding conversion of about 12% at space time (W/F) of 8.931 kg cat.h/kg mole. The initial increase in the conversion may be attributed to the increase in the adsorption of toluene on the active sites, and the falling region may be due to overcrowding of toluene molecules at the catalyst surface coupled with increased residence of the products decreasing their back diffusion. This phenomenon was also indicated in one of the reports [34].

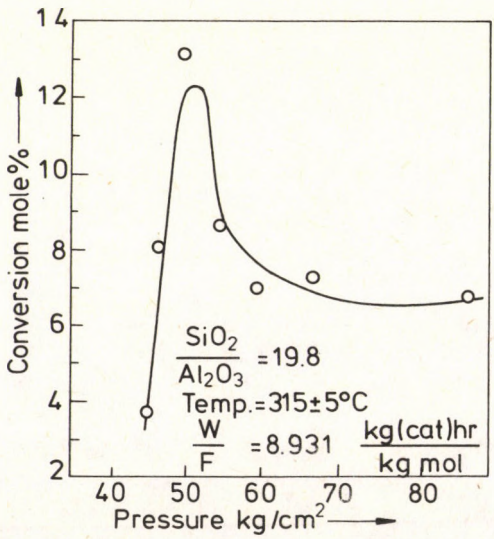

Fig. 4.
Effect of pressure on conversion

Effect of Calcination Temperature

The calcination of catalyst HM (19.8) was carried out in the flow reactor in hydrogen and air atmosphere at different temperatures. A consistant increase in the conversion was observed with an increase in the calcination temperature, irrespective of the type of gas used *(Fig. 5)*. However, alkylation took over from disproportionation at higher calcination temperature. From the point of view of operational convenience (in situ regeneration), it was decided to carry out the calcination of the used catalyst at 450 °C, at which disproportionation selectivity was quite high.

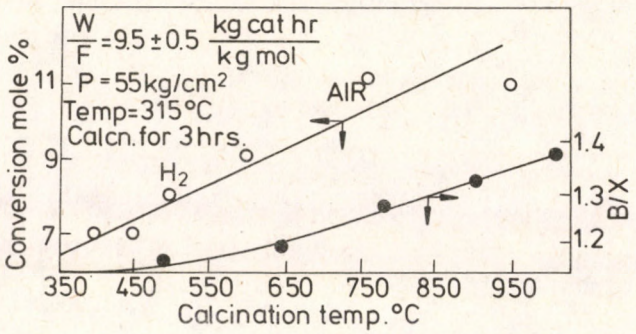

Fig. 5.
Effect of calcination temperature on conversion and benzene/xylene ratio

Effect of Carrier Gas

The results of using N_2 and H_2 as carrier gases on a deactivation pattern are given *Fig. 6*. The plot is self-explanatory. Here the temperature being of the order of 300–315 °C, hydrogen may not reactivate the catalyst by hydrogenating

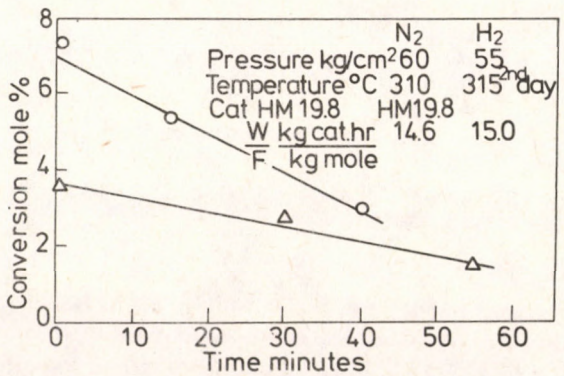

Fig. 6.
Effect of carrier gas on conversion

coke precursors or the coke formed on the catalyst. At this temperature, predominant reactions would also be xylene isomerization and disproportionation, in which H_2 may not participate. Due to possible neutrality and higher initial activity, hydrogen was used as the carrier gas in the further studies.

Effect of the Introduction of Metal in the Catalyst

The introduction of nickel yielded interesting results. The trend *(Fig. 7)* shows the clear advantage of incorporating Ni as ions or metal deposition on the catalyst. The reverse trend in the case of an impregnated catalyst indicates that different mechanisms must prevail for impregnated and cation-exchanged mordenites. Further experimentation on this aspect was not undertaken.

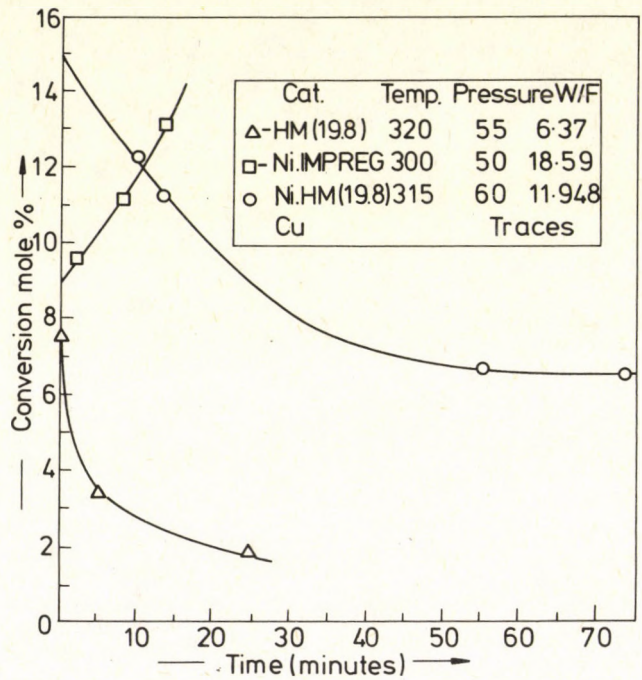

Fig. 7.
Catalyst modification and deactivation pattern

Collection of the Kinetic Data

LPD of toluene at high pressure and high temperature in the presence of gaseous H_2 takes place in a thermodynamically critical region and hence a prior knowledge of the nature and the flow stability is necessary.

The charts given by SICARDI and coworkers [35] were used to characterize the flow, which corresponded to one in a steady continuum region. The porous catalyst is expected to hold some of the fluid particles for a much longer time due to preferential adsorption. Some stagnant pockets and backmixing are also likely to be encountered. All these parameters were lumped into an axial dispersion model and quantified in terms of the Peclet number for axial mixing of liquid. The equation used for the calculation [36] was:

$$Pe_L = 0.034\ \mathrm{Re}^{0.5} \cdot 10^{0.0003\ \mathrm{Re}_G} \tag{1}$$

In order to experimentally find the values of the Peclet number (Pe_L), or dispersion number, tracer studies were conducted with *p*, *m*, *o*-xylene, and ethylbenzene tracers in the toluene-hydrogen pressurized flow at different pressures ranging from 45 to 76 kg/cm^2. The hydrocarbon flow rate was varied from 360 to 720 m/h, whereas the H_2 flow rate was kept at 5 l/min. A sample RTD plot for *o*-xylene tracer is shown in *Fig. 8*. For estimating the axial dispersion, a Gaussian distribution was assumed, which in a true sense is not correct as humps in the tailings were observed. However, the values calculated by Eq. (1), and experimentally determined values, considering dimensionless variance equation;

$$\sigma_\theta^2 = 2(D/uL) \tag{2}$$

matched well within ± 10%. The average value of the dispersion number was 0.12. In order to confirm that the axial dispersion depended on the reactor

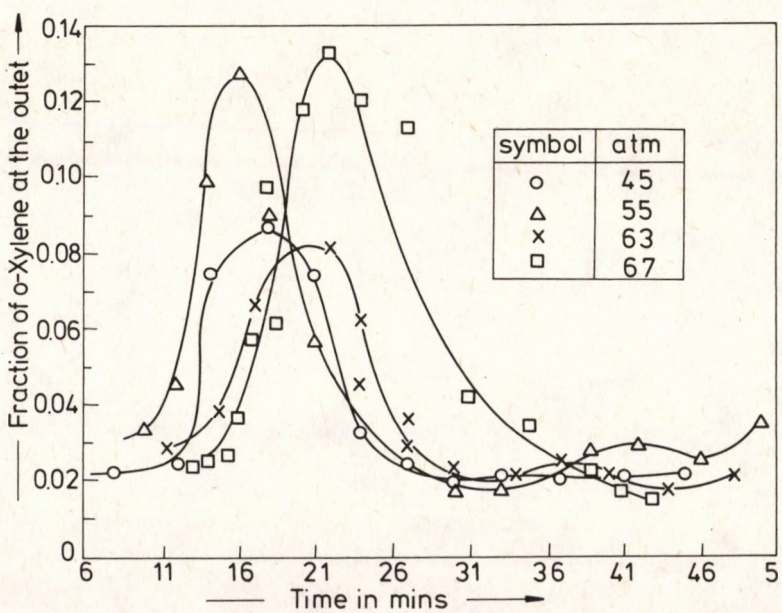

Fig. 8.
RTD with *o*-xylene tracer

geometry and not on the porous catalyst bed, experiments were conducted with iron turnings of similar geometric characteristics as those of catalyst particles. The RTD results were identical.

The dimensionless parameter ($d_p \cdot \varrho_L \cdot L/\mu_L$) was found to vary between 0.72 to 3.25, thus indicating the complete wetting of the particles, where the d_p, i.e. particle diameter was 0.3 cm.

The absence of liquid film resistance, expected due to high pressure operation was confirmed both by finding out the Biot number and by experimentation at different flow rates, but with identical W/F values. The change in conversion from 8 to 8.1% for a change in the particle size in the range of 1.5–12 mm at 315 °C, 55 kg/cm^2 and W/F of 8.9 confirmed the absence of pore diffusional resistance. This was further confirmed by checking the value of the parameter $(-r_T)_{obsd.} L^2/D_e \cdot C_{TL}$ which was estimated to be 3×10^{-6}. The value of D_e is taken from literature [27].

Having eliminated the possibility of liquid film and pore diffusion resistance interference, attempts were made to develop the intrinsic rate equation. Considering the complex nature of the system consisting of toluene and hydrogen at high pressure and high temperature, nonideality indicated by somewhat high value of the dispersion number is neglected. The usual Langmuir–Hinshelwood approach for getting the rate equation cannot be used here, because of multilayer filling and desorption difficulties experienced by benzene, due to the presence of high pressure toluene at the pore mouth.

The reversible nature of the reaction was confirmed by carrying out experiments with pure toluene, mixtures of toluene and 1 : 1 benzene-xylene components, and with only 1 : 1 benzene-xylene mixture in a differential reactor. The conversion was restricted to a maximum of 10%. It was confirmed that at 315 °C and 55 kg/cm^2 pressure all the three hydrocarbons existed as liquids, somewhat below the critical level. The liquid phase density is taken as 0.46 g/ml at these

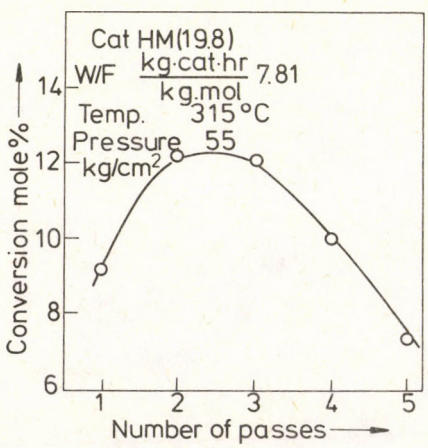

Fig. 9.
Effect of product circulation on conversion

conditions, which corresponds to 5 kg moles/m^3 of the liquid phase. The following rate values were obtained for different compositions:

Table 2. – Initial Rate Values for LPD

Initial rate, kg moles toluene consumed per kg cat h	Ratio of toluene to the equimolar mixture of benzene and m-xylene
0.396	100% Toluene
0.264	80 : 20
0.165	60 : 40
−0.132	50 : 50
−0.231	40 : 60
−0.596	20 : 80
−0.903	100% benzene-m-xylene mixture

As a first estimate, a simple elementary second order equation was assumed, i.e.:

$$-r_T = k_f \cdot C_T^2 - k_b \cdot C_B \cdot C_x \tag{3}$$

The values of k_f and k_b were calculated for a 100% toluene and 100% equimolar mixture of benzene and *m*-xylene, and then calculated rates were compared against the experimental values. A similar procedure was also followed for the first order test. The data are presented in *Table 3*.

Table 3.

Testing of the data for kinetic models

Experimental rate of toluene consumption	Rate as per the first order reversible model	Rate as per the second order reversible model
0.396	0.396	0.396
0.264	0.136	0.220
0.165	−0.123	0.000
−0.132	−0.252	−0.125
−0.231	−0.380	−0.260
−0.596	−0.640	−0.560
−0.903	−0.903	−0.903

It can be seen that except for the 60 : 40 composition, the estimated second order rate values were in good agreement with the experimental rate values. The previous work on VPD [30] reported the second order reversible mechanism.

The reversible nature of the reaction was confirmed by recirculating the reaction products after every eight minutes of the run after charging the initial load of the catalyst. All other reaction conditions were maintained constant during each run. The data shown in *Fig. 9* support the reaction reversibility.

The effect of temperature on the reaction was difficult to study because below 300 °C, no reaction was possible, whereas above 325 °C, the liquid phase could not be maintained at 55 kg/cm^2 pressure. Any increase in the pressure (for getting a higher reaction temperature) was not advantageous.

The rate expression based on the initial rate studies obtained by the differential operation of the reactor can be given as:

$$-r_T = 0.016C_T^2 - 0.036C_B \cdot C_x \quad (4)$$

The value of equilibrium conversion from these rate constants comes out to be 0.57, which is quite close to the thermodynamic equilibrium conversion of 0.55.

Catalyst Deactivation

Deactivation of zeolite catalysts in VPD is quite rapid and has been a topic of sustained investigation over the last decade or so. Many reports were published on the VPD, but there is hardly any quantitative information available in case of the the LPD. Deactivation plays a major role in kinetic expressions.

In the present work, the deactivation characteristics are shown at 315 °C in *Fig. 10* on HM (19.8). The trend is similar to that reported earlier [14, 33, 30] in VPD studies. It was observed that by cooling down the system to ambient temperature (~30 °C) and restarting the run, some gain in catalyst activity could be obtained. In order to conduct the systematic study of this behaviour, the run was discontinued after 45 minutes and, after cooling and pressure releasing, was restarted again on the same catalyst at similar conditions of temperature, pressure and W/F on the second, third, and fourth day, etc.

In normal cases of deactivation, the activity once lost cannot be restored unless the operating conditions are drastically changed or the catalyst is regenerated. In the present case, however, considerable initial activity (higher than the activity at the end of the operation on the previous day) and similar deactivation patterns were obtained on the successive days *(Fig. 11)*. Such a deactivation mode is rather unusual, and can be termed as 'temperory deactivation'.

It is known that toluene disproportionation proceeds through a diphenyl alkane intermediate, which being quite large in size gets adsorbed on the surface

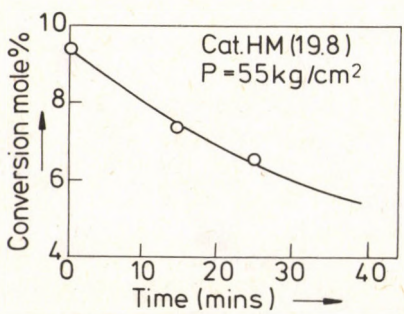

Fig. 10.
Deactivation pattern at W/F = 19 kg · cat · h/kg mole and 315 °C

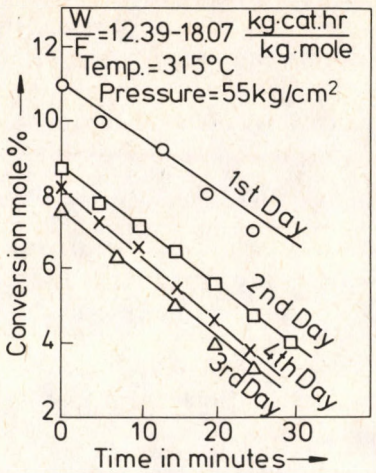

Fig. 11.
Deactivation pattern on successive days of operation

of the catalyst. The slow rate of desorption of these species causes catalyst deactivation. However, on releasing the pressure, they get desorbed.

Some experiments were conducted by using a temperature step increase method. When reaction temperature was increased in steps of 10 °C each after every 10 minutes, a significant increase in catalyst activity of deactivated catalyst was obtained. Original activity could thus be achieved in just four steps, i.e. with a 40 °C temperature rise *(Fig. 12)*. Such a stepwise increase in operating temperature was indicated earlier. This supports the theory of enhancement of the rate of desorption of weakly adsorbed bulky intermediate species.

Deactivation patterns for the forward reaction (starting from toluene) and the backward reaction (starting from the equimolar mixture of benzene and m-xy-

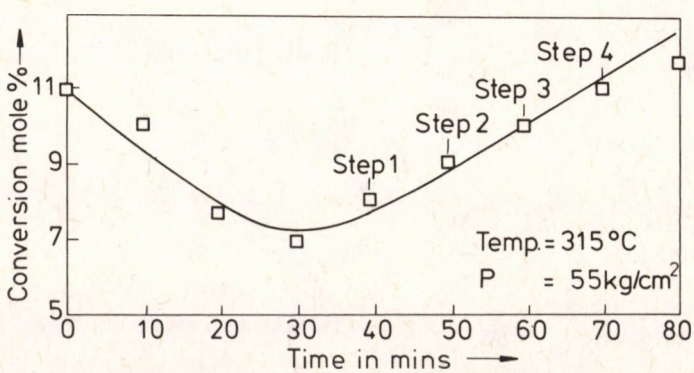

Fig. 12.
Effect of temperature rise on forward reaction at W/F = 16.7 kg · cat · h/kg mole

lene) are shown in *Fig. 13* at 315 °C. Due to severe temperature limitations stated earlier, the deactivation was studied only at 315 °C.

Two separate activity coefficients were introduced for the overall rate expression, i.e. a_F for the forward reaction and a_B for the backward reaction. Exponential decay of a_F and a_B was related through the relationship:

$$-\frac{da_F}{dt} = k_{dF} \times a_F \quad or \quad -\frac{da_B}{dt} = k_{dB} \times a_B \tag{5}$$

where k_{dF} and k_{dB} are constants. a_F or a_B is taken as the ratio of the initial rate to the rate at time, t, for forward or backward reaction as the case may be. Initial rates were calculated by extrapolating the rate to the zero time. The linearity

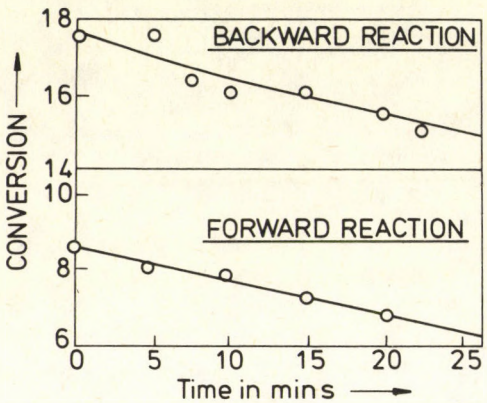

Fig. 13.
Deactivation pattern at 315 °C and W/F = 13 kg · cat · h/kg mole

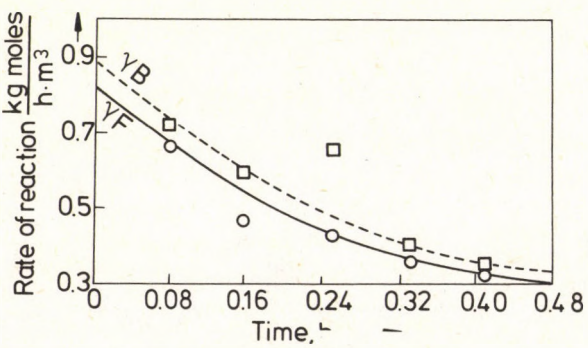

Fig. 14.
Rate of reaction vs. time plot

of ln a_F vs. t and ln a_B vs. t confirms the exponential deactivation model. The respective plots are shown in *Fig. 14 and 15*.

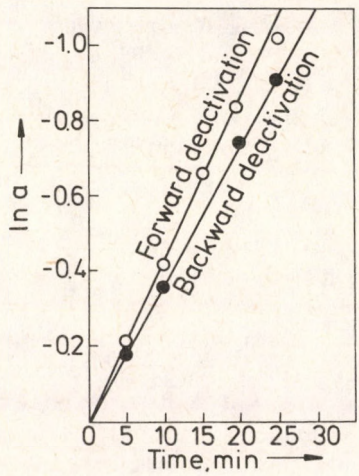

Fig. 15.
Fitting of exponential deactivation model for forward and backward reactions

The overall rate expression, taking into account the deactivation can thus be given as:

$$-r_T = 0.016C_T^2 \times a_F - 0.036C_B C_x a_B \tag{6}$$

$$\text{and } -\frac{da_F}{dt} = 2.57 \times a_F \tag{8}$$

$$\text{and } -\frac{da_B}{dt} = 2.20a_B \tag{9}$$

The rate equation developed was used to find out the conversion in the batch reactor. The value of the rate constant obtained in the continuous reactor was expressed in units of $m^6/(kg\ mole\ liq\ kg\ cat.\ h)$. In batch experiments, the catalyst concentration was 100 kg/m^3 liq. Hence the rate constants were multiplied by 100 to make the units of the constants compatible with the batch experimets. Then the conversion-time data calculated by the model

$$\frac{X_{Ae} - (2X_{Ae} - 1)X_A}{X_{Ae} - X_A} = 2k_g \times a_F \left(\frac{1}{X_{Ae}} - 1\right) \times C_{To} \tag{10}$$

was compared with the experimental data *(Fig. 4)* up to 2 hours duration, i.e. when the disproportionation reaction was predominant. The values agreed with $\pm 10\%$ error, thereby confirming the validity of the model. The values of a_F were taken as integral average values in the calculation range.

Conclusions

Based on the experiments conducted on the batch and the continuous reaction systems, the following conclusions are drawn for LPD of toluene:

1. The conversion was first observed at 175 kg/cm^2 and 346 °C in the autoclave in the presence of a mordenite catalyst.
2. Stronger acid sites (dealumination deeper than SiO_2/Al_2O_3 ratio of 13.5) and for reaction periods more than 1.5 h favour dealkylation.
3. In the continuous reactor the conversion was first obtained at 300 °C on H-mordenite with SiO_2/Al_2O_3 ratio of 19.8 and hydrogen pressure of 50 kg/cm^2.
4. For calcination temperatures higher than 450 °C, the selectivity towards disproportionation was adversely affected.
5. In comparison to nitrogen as the carrier gas, hydrogen offered a higher initial activity of the catalyst.
6. A second order reversible rate model appears to satisfactorily fit the experimental data, collected in a continuous flow reactor.
7. The catalyst deactivation was of a 'temporary' nature and the initial activity could be regained to a considerable extent by simply cooling and releasing the pressure or by applying a small tremperature step increase. Within a 40 °C rise, complete initial activity could be restored.
8. An exponential decay model equation fitted the deactivation pattern well. The activity drop over a long period was not significant, but the reaction selectivity suffered.

SYMBOLS

P_{eL}	Axial Peclet number
R_{eL}, R_{eG}	Reynold's number for liquid and gas respectively
σ_θ	Variance around the mean value
D	Diffusivity of toluene, cm^2/s
u	Flow velocity of toluene, cm/s
L	Particle area, cm^2
d_p	Particle diameter, cm
L	Density of the liquid phase, g/cm^3
μ_L	viscosity of toluene, g cm/s at 275 °C 80 kg/cm^2/pressure
W/F	Space time, g cat h/g mole
$(-r_T)_{obsd}$	rate of toluene disproportionation g mole/h cm^3 (cat.)
D_e	Effective diffusivity of toluene into mordenite pores at 25 °C, cm^3/h cm (cat)
C_{TL}	Concentration of toluene in liquid phase at the pore mouth, g mole
$-r_T$	intrinsic rate of toluene disproportionation, g moles/h cm^3 (cat.)
k_f, k_b	Forward and backward second order reaction rate constant respectively.
C_{To}	Initial concentration of toluene in liquid phase, g mole
C_T, C_B, C_X	Concentration of toluene, benzene and xylene in liquid phase, g mole/l
a_f, a_b	Activity coefficients for forward and backward deactivation reactions.
t	time, seconds
k_{dF}, k_{dB}	Forward and backward deactivation reaction rate constants.
X_{Ae}	Equilibrium conversion.

REFERENCES

1. KRISHNAMURTHY, V. A., MUKHERJEE, D. K. and NAIR C. S. B., Ind. Chem. Manufacturer: *1976* 14 (3).
2. Editorial Introduction, Chem. Age of India, *1979* 30, 4B.
3. RUDD, D. F., SEED FATH AFSHAR, ANDRAEST, STADTHERR M. A.: "Petrochemical Technology Assessment". A. Wiley Interscience Publication, New York, (1981).
4. ANEKE, L. E., GEERITSEN, L. A., VANDEN BERG, P. J. and DE JONG, W. A.: J. Catal. *1979* 59, 26.
5. BRENTSEVIG, V. V., RUDENKO, A. P., i SOLODUKHA, N. I.: Neftekhimiya *1973* 13 (2), 185–90.
6. FERINO, I.: Rend. Semin. Far. Sc. Univ. Cagliari *1977* 47 (3–4) 235–53.
7. HALGERI. A. B.: React. Kinet. Catal. Lett., *1978* 9 (4), 365–69.
8. HOLLAND, J. M., and JONES, D. W.: J. Chem. Soc. *1970* (2) D, 122.
9. CHEN. N. Y., KAEDING, W. E. and DWYER, F. G.: J. Am. Chem. Soc. *1979* 101 (22) 6783–85.
10. NAKNO NOVIKI, NISHIMURA, Y., and TAKHASHI, H.: Bulletin Japan Petrol Instituta *1971* 13 (2), 205–9.
11. THAKUR, D. K. and WELLER, S. W.: Advan. Chem. Ser., 1973, 121 (Mol. Sieres Int. Conf., 3rd.), 596–604
12. ANEKE, L. E., GERRITSEN, L. A., EILERS, J. and TRION, R.: J. Catalysis *1979* 59, 37–44.
13. YASHIMA, T., MOSLEHI, H. and NARA, N.: Bull. Japan Petrol. Inst. *1970* 12, 106–11.
14. BAWA, J. S., SHANKAR, U., RAWAT, D. S. DABROL, R. P., and BHATTACHARYA, K. K.: Proc. Ind. Natl. Sci., Acad. Part A *1975* 41 (1), 55–62.
15. KAEDING, W. W. and YOUNG, L. B.: U.S. 4,034,053 from C.A. *87* 134 438.
16. MATSUMOTO, H. and MORITTA, Y.: International. Chem. Engg., *1968* 8 (2), 364–7.
17. DAVIDOVA, N. and PESHAV, N.: J. Catal. *1979* 58 (2), 198–205.
18. ISAKO, YA. I. i MINACHEV, KH. M.: Neftekhimiya, *1973* 13 (2), 185.
19. NARAYANAN, S. and COUGHLAN, B.: Chem. and Ind. *1977* 18, 765–6.
20. WALLACE, R. C. and SUGGITT, R. M.: Can. Pat 1,019,353 from C.A. *88* 22332d.
21. SZAKACS, S., PAPP, J., LEJTOVICZ, J. and KALLÓ, D.: Reaction Kinet. Catal. Letters *1982* 21 (3), 365–70.
22. MORTIKOV, E. S. i MINACHEV, KH. M.: Naftepererabotki Neftekhimiyi (Moscow) *1972* 2, 31–3.
23. BURSIAN, N. R. i SHAVANDI, Y. A.: Khim. Tekhnol. Topl., Masel. *1974* 5, 8–10.
24. KIRK and OTHMER, "Encyclopedia of Chemical Technology", 3rd Edition, Vol. 23, Wiley International Publication, New York, pp 25–267 (1981).
25. GENDY, T. S. and KERRY, C. P.: Chem. Engg. Sci., *1982* 37 (1), 37–43.
26. GNEP, N. S. and MARTIN DE AROMANDO, M. L.: React. Kinet. Catal. Letters, *1980* 13 (3), 183–9 from C.A. *100* 51 157.
27. AVINOM, N. and LEONID, M. P.: Chem. Engg. Sci., *1977* 32 (2), 35–41.
28. PAUL, E. E. (JR.): Ind. Engg. Chem. Prod. Res. and Dev., *1971* 10, 433.
29. GRANDIO, P., SCHNEIDER, F. M., SCHWARTZ., A. H. and WISE, J. J.: Hydrocarbon Processing *1972* 51 (8), 85–86.
30. BHAVIKATTI, S.: 'Disproportionation of toluene over aluminium deficient and metal loaded mordenite catalysts; Ph. D., Thesis, I.I.T. Bombay (1980).
31. KAZUO, T., HISAO, K. and HIROSHI, T.: Bull. of Chem. Soc. Japan, *1974* 47 (4), 801–805.
32. BIERENBAUM, H. S., PARTRIDGE, R. D., and WEISS, A. H.: Adv. Chem. Ser. *1973* 121, 605.
33. MINACHEV KH. M., ISAKOV YA I., ISAGULYANTS G. V. i USOCHOV N.: Izv. Adkad. Nauki. USSR Ser. Khim. *1974* (1), 42–7.
34. SATTERFIELD, C. N., KATZER, J., and WOLF, R. V.: Ind. Engg. Chem. *1971* 10, 478.
35. SICARDI, S., BALDI, G. and SPECHIA, V.: Chem. Engg. Sci., *1980* 35, 1775–1782.
36. FROMENT, G. F. and BISCHOFF, K. B.: "Chemical Reactor Analysis and Design", John Wiley and Sons, New York, (1979).

HUNGARIAN JOURNAL
OF INDUSTRIAL CHEMISTRY
VESZPRÉM
Vol. 17. pp. 355–363 (1989)

STUDIES ON PURIFICATION OF YTTRIUM FROM HEAVY LANTHANIDES USING CHELATING ION-EXCHANGERS OF AMINO ACID AND PHOSPHONIC TYPES

H. HUBICKA

(Institute of Chemistry, Maria Curie-Skłodowska University, 20-031 Lublin, Poland)

Received: November 16, 1988

Chelating ion-exchangers of amino acid type: Amberlite IRC-718, Diaion CR–10, Lewatit TP–207, Lewatit TP-208 and Wofatit MCT-50, the aminophosphonic type: Duolite ES-467, Lewatit OC-1060 and the phosphonic type Bio-Rex 63 were used in purification of about 98% yttrium concentrate from dysprosium, holmium, erbium and ytterbium. Purification was conducted from the acetate solution of pH 5.9–6.1 by frontal analysis. The polyfunctional ion-exchanger of amino acid type Wofatit MC-50 proved to be the most effective in yttrium purification from heavy lanthanides particularly from ytterbium. The ion-exchangers of the amino acid type Amberlite IRC-718 and Lewatit TP-207 also showed high selectivity for ytterbium.

Introduction

Growing applicability of rare-earth elements makes their separation in a pure form necessary. Ion-exchange chromatography is one of the methods allowing for their preparation in a high state of purity. Applicability of the eluents such as polyaminopolycarboxylic acids, hydroxy-carboxylic acids or simple aliphatic carboxyl acids is known in the ion-exchange method to obtain rare earth elements [1, 2, 3, 4]. In most cases, ion-exchange separation of rare-earth elements was carried out using polystyrenesulfone cation exchangers of various grain sizes, crosslinking, and matrix porosity, etc. [1, 2, 3, 4]. The factors influencing the separation are differentiated values of stabilitity constants of rare-earth element complexing combinations with the eluents and complexing kinetics, but not their ion-exchange affinity for the ion-exchanger, which is only slightly differentiated. Separation of rare-earth element complexes on anion exchangers was studied to a less extent [3, 5, 6]. However, as shown from literature [7–11], chelating ion-exchangers commercially available and those synthesized by various authors have not been largely examined as far as rare

earth element separation is concerned. In most cases, the papers dealt with sorption or complexing mechanisms (as well as the structure of rare earth element complexing combinations) by ion-exchanger functional groups [11, 15], distribution coefficient determination [7, 9, 12, 15], and the separation of each pair of rare earth elements by elution, etc. [9, 11, 17, 18, 19, 20]. Recently an attempt was made to determine optimal separation conditions of the pair Pr(III)–Nd(III) on the synthesized chelating ion exchangers of amino acid type using the computer simulation method based on newly introduced equations [17]. Most of these papers are of a physicochemical or analytical character. Only chaleting ion-exchangers of phosphonic functional groups and of amino acid type found their application in the purification of rare-earth elements from the impurities of thorium (IV) and uranium (IV, VI) [15, 21–28]. The aim of this paper is to examine the possibilities of purification of the commercial about 98% yttrium (III) concentrate from Dy(III), Ho(III), Er(III) and Yb(III) on various chelating ion-exchangers by frontal analysis. For this reason, amino acid type, aminophosphonic and phosphonic ion exchangers were examined.

Experimental

The chelating ion-exchangers: Amberlite IRC-718 of amino acid type produced by Rohm and Haas USA, phosphonic Bio-Rex 63 by Bio-Rad Laboratories USA, iminodiacetic Diaion CR-10 by Mitsubishi Chemical Industry Japan, aminophosphonic Duolite ES-467 by Dia-Prosim France, aminophosphonic Lewatit OC-1060, iminodiacetate Lewatit TP-207 and iminodiacetate Lewatit TP-208 by Bayer FRG and polyfunctional Wofatit MC-50 of aminoacetic and iminoacetic groups by Wolfen GDR were used. All ion-exchangers used had grains of 20–50 mesh except Wofatit MC-50 whose grains were of 50-100 mesh. Y_2O_3 – about 98% (Yb_2O_3 – 0.32%, Er_2O_3 – 0.50%, Dy_2O_3 – 0.42% and Ho_2O_3 – 0.13%) by Reachim USSR. Purification of yttrium (III) from Dy(III), Ho(III), Er(III) and Yb(III) was carried out in glass columns of 2-cm diameter filled with a chelating ion-exchanger in an ammonium form of 25-cm bed height. Purification was carried out from acetate solutions of pH 5.9–6.1 and concentration of about 2 g Ln_2O_3/dm^3 by frontal analysis with a flow rate of about 0.2 $cm^3/cm^2 \times$ min. The effluent was collected in fractions of 200 and 250 cm^3 from which oxalates were precipitated and converted to oxides.

The percentage of dysprosium, holmium, erbium and ytterbium in yttrium in each fraction was determined by *X*-ray fluorescence using the *X*-ray fluorescent Spectrometer VRA-2 produced by Carl Zeiss Jena.

Component grinding and homogenization were carried out in an electric corundum mill of Fritsch type for 45 min. To make a tablet, 1 g of the mixture prepared from 400 mg of the sample, 200 mg of H_3BO_3 and 400 mg of ground SiO_2 (H_3BO_3 was used as a binder) was used. Two layer tablets were made from the prepared samples. The substrate with H_3BO_3 was pressed under 20 MPa, then the homogenized mixtures were spread and suitable tablets were pressed

under 200 MPa. The tablets for standard samples of 0.05% and 0.20% of Dy, Ho, Er and Yb in yttrium were made in the same way. The standard samples were prepared adding a suitable amount of $DyCl_3$, $HoCl_3$, $ErCl_3$ and $YbCl_3$ solutions into YCl_3 solution (prepared from Y_2O_3 of purity 5N produced by Fluck), then oxalates were precipitated and roasted to oxides. Concentration of each element was determined measuring line intensities of $DyL\alpha_1$, $HoL\alpha_1$, $ErL\alpha_1$ and $YbL\alpha_1$.

Conclusions

Based on literature data concerning values of stability constants of rare-earth element complex combinations with chelating ion functional groups [29, 30] and rare-earth element partition coefficients (determined for the chelating iminodiacetate ion-exchanger – Chelex 100 and phosphonic ion-exchanger – Duolite ES-63) [9], the possibility of Y(III) purification from Dy(III), Ho(III), Er(III) and Yb(III) by ion-exchange frontal analysis was examined. The results of yttrium (III) purification from heavy lanthanides on the aminophosphonic ion-exchanger – Duolite ES-467 are presented in *Table 1*, on the aminophosphonic ion-exchanger – Lewatit OC-1060 in *Table 2*, on the phosphonic ion-exchanger – Bio-Rex 63 in *Table 3*, on the amino acid type ion-exchanger – Amberlite IRC-718 in *Table 4*, on the iminodiacetate ion-exchanger – Diaion CR-10 in *Table 5*, on the iminodiacetate ion-exchanger – Lewatit TP-207 in *Table 6*, on the iminodiacetate ion-exchanger Lewatit TP-208 in *Table 7* and on the polyfunctional ion-exchanger of iminodiacetate and aminodiacetate functional groups – Wofatit MC-50 in *Table 8*.

Table 1.
Separation of Yttrium from Yb(III), Er(III), Dy(III) and Ho(III) on Chelating Ion Exchanger Duolite ES–467

Matrix structure	Functional group type	Fraction number	V dm^3	Mass of fractions Ln_2O_3 g	Impurity in Y_2O_3 after purification				Heavy lanthanides + Y_2O_3 absorbed on ion exchanger g
					Yb %	Er %	Dy %	Ho %	
Copolimer of styrene with divinylbenzene of macroporous structure	amino–	1	1.600	–					
	phos–	2	0.800	0.475	0.090	0.410	0.355	0.115	
	phonic	3	0.400	0.541	0.130	0.428	0.365	0.120	
		4	0.400	0.586	0.144	0.430	0.370	0.126	
		5	0.400	0.675	0.160	0.435	0.375	0.130	
		6	0.400	0.721	0.174	0.440	0.378	0.130	
		7	0.400	0.771	0.190	0.450	0.380	0.130	
		8	0.250	0.482	0.195	0.455	0.410	0.130	
		9	0.250	0.490	0.205	0.460	0.415	0.132	
		10	0.250	0.492	0.223	0.463	0.416	0.133	
									4.811

Out of the examined ion-exchangers, the chelating ion-exchangers of amino acid type proved to be the most effective in yttrium (III) purification from heavy lanthanides.

The affinity range of the examined rare-earth elements for the above mentioned ion-exchanger is as follows: Yb(III) > Er(III) > Dy(III) > Ho(III) > Y(III) and corresponds to the values of stability constants of rare-earth elements with iminodiacetic acid (IDA) or to N-benzyliminodiacetic acid (BIMDA) and to distribution coefficients determined for the ion-exchanger Chelex 100 [9]. Out of this type of ion-exchangers, the polyfunctional Wofatit MC-50 of amin – acetate and iminodiacetate functional groups appears to be the best. Using it, the contents of Yb(III), Er(III), Dy(III) and Ho(III) were diminished to below 0.01% in the eluate first fraction *(Table 8)*.

Out of the examined chelating ion exchangers, aminophosphonic *(Table 1* and *2)* and phosphonic ion-exchangers *(Table 3)* proved to be less useful to purify yttrium from heavy lanthanides. Moreover, the HCl solution of 6M concentration should be used for their complete regeneration, whereas other chelating ion-exchangers of amino acid type could be regenerated using 0.5M HCl solution.

Detailed physicochemical characteristics of chelating ion-exchangers and methods of their synthesis are not given by the producers. The different behav-

Table 2.
Separation of Yttrium from Yb(III), Er(III), Dy(III) and Ho(III) on Chelating Ion Exchanger Lewatit OC 1060

Matrix structure	Functional group type	Fraction number	V dm^3	Mass of fractions Ln_2O_3 g	Impurity in Y_2O_3 after purification				Heavy lanthanides + Y_2O_3 absorbed on ion exchanger g
					Yb %	Er %	Dy %	Ho %	
Copolimer of styrene with divinyl-benzene of macroporous structure	amino–phos–phonic	1	2.070	–					
		2	0.800	0.586	0.025	0.300	0.320	0.110	
		3	0.410	0.548	0.046	0.340	0.370	0.112	
		4	0.400	0.649	0.050	0.350	0.375	0.114	
		5	0.400	0.723	0.060	0.365	0.376	0.115	
		6	0.400	0.765	0.062	0.375	0.377	0.115	
		7	0.400	0.774	0.078	0.385	0.378	0.116	
		8	0.250	0.465	0.085	0.398	0.379	0.117	
		9	0.250	0.471	0.090	0.405	0.380	0.119	
		10	0.250	0.481	0.098	0.411	0.382	0.120	
		11	0.250	0.487	0.106	0.420	0.385	0.120	
		12	0.250	0.490	0.140	0.452	0.389	0.121	
		13	0.250	0.492	0.152	0.458	0.390	0.123	
		14	0.250	0.493	0.165	0.461	0.400	0.125	5.255

Table 3.
Separation of Yttrium from Yb(III), Er(III), Dy(III) and Ho(III) on Chelating Ion Exchanger Bio–Rex 63

Matrix structure	Functional group type	Fraction number	V dm^3	Mass of fractions Ln_2O_3 g	Impurity in Y_2O_3 after purification				Heavy lanthanides + Y_2O_3 absorbed on ion exchanger g
					Yb %	Er %	Dy %	Ho %	
Copolimer of styrene with divinyl–benzene of gel structure	phos–pho–nic	1	2.300	–					
		2	0.750	0.502	0.042	0.370	0.370	0.117	
		3	0.500	0.658	0.047	0.375	0.375	0.118	
		4	0.250	0.428	0.070	0.395	0.384	0.126	
		5	0.250	0.441	0.075	0.408	0.386	0.127	
		6	0.250	0.456	0.081	0.420	0.388	0.128	
		7	0.250	0.460	0.084	0.425	0.389	0.129	
		8	0.250	0.462	0.088	0.430	0.390	0.129	
		9	0.250	0.464	0.089	0.433	0.396	0.130	
		10	0.250	0.466	0.090	0.435	0.400	0.130	
		11	0.250	0.469	0.092	0.437	0.403	0.131	
		12	0.250	0.471	0.093	0.438	0.405	0.132	
		13	0.250	0.473	0.100	0.439	0.407	0.132	
		14	0.250	0.475	0.108	0.440	0.408	0.133	
		15	0.250	0.478	0.118	0.445	0.410	0.134	
		16	0.250	0.480	0.128	0.450	0.412	0.135	
		17	0.250	0.481	0.135	0.456	0.414	0.135	
		18	0.250	0.482	0.143	0.460	0.415	0.136	
		19	0.250	0.483	0.145	0.462	0.416	0.137	
		20	0.250	0.484	0.147	0.465	0.417	0.137	
									4.863

Table 4.
Separation of Yttrium from Yb(III), Er(III), Dy(III) and Ho(III) on Chelating Ion Exchanger Am berlite IRC-718

Matrix structure	Functional group type	Fraction number	V dm^3	Mass of fractions Ln_2O_3 g	Impurity in Y_2O_3 after purification				Heavy lanthanides + Y_2O_3 absorbed on ion exchanger g
					Yb %	Er %	Dy %	Ho %	
Copolimer of styrene with divinyl-benzene of macroporous structure	amino-acid	1	1.015	–					
		2	0.450	0.486	<0.01	0.044	0.059	0.023	
		3	0.400	0.677	~0.01	0.074	0.100	0.031	
		4	0.200	0.366	0.015	0.098	0.142	0.045	
		5	0.250	0.461	0.032	0.154	0.186	0.062	
		6	0.250	0.468	0.046	0.198	0.222	0.076	
		7	0.250	0.469	0.074	0.246	0.261	0.086	
		8	0.250	0.478	0.086	0.270	0.279	0.088	
		9	0.250	0.479	0.100	0.302	0.297	0.090	
		10	0.250	0.482	0.116	0.320	0.310	0.092	
		11	0.250	0.484	0.135	0.341	0.323	0.094	
		12	0.250	0.485	0.160	0.365	0.341	0.100	
		13	0.250	0.486	0.182	0.396	0.360	0.106	
		14	0.250	0.487	0.186	0.409	0.366	0.111	
		15	0.250	0.488	0.192	0.423	0.373	0.116	
		16	0.250	0.489	0.199	0.426	0.374	0.120	
		17	0.250	0.490	0.208	0.430	0.375	0.122	
		18	0.250	0.492	0.217	0.446	0.380	0.125	
		19	0.250	0.494	0.227	0.464	0.384	0.127	
		20	0.250	0.496	0.231	0.465	0.385	0.127	
		21	0.250	0.497	0.246	0.467	0.386	0.128	
									2.958

Table 5.
Separation of Yttrium from Yb(III), Er(III), Dy(III) and Ho(III) on Chelating Ion Exchanger Diaion CR-10

Matrix structure	Functional group type	Fraction number	V dm^3	Mass of fractions Ln_2O_3 g	Impurity in Y_2O_3 after purification				Heavy lanthanides + Y_2O_3 absorbed on ion exchanger g
					Yb %	Er %	Dy %	Ho %	
Copolimer of styrene with divinyl-benzene of macroporous structure	imino-diace-tic	1	1.515	–					
		2	0.610	0.488	0.030	0.140	0.150	0.040	
		3	0.410	0.733	0.050	0.180	0.181	0.055	
		4	0.200	0.363	0.071	0.200	0.190	0.060	
		5	0.250	0.458	0.075	0.214	0.203	0.064	
		6	0.250	0.480	0.080	0.230	0.220	0.070	
		7	0.250	0.482	0.089	0.251	0.239	0.075	
		8	0.250	0.484	0.100	0.280	0.260	0.081	
		9	0.250	0.486	0.116	0.284	0.267	0.085	
		10	0.250	0.487	0.125	0.290	0.275	0.090	
		11	0.250	0.488	0.130	0.302	0.282	0.091	
		12	0.250	0.489	0.135	0.320	0.290	0.092	
		13	0.250	0.490	0.141	0.334	0.301	0.096	
		14	0.250	0.491	0.160	0.350	0.310	0.100	
		15	0.250	0.491	0.165	0.354	0.315	0.101	
		16	0.250	0.492	0.170	0.360	0.320	0.102	
		17	0.250	0.493	0.174	0.365	0.322	0.103	
		18	0.250	0.493	0.180	0.370	0.325	0.104	
		19	0.250	0.494	0.187	0.380	0.325	0.105	
		20	0.250	0.494	0.195	0.390	0.326	0.106	
		21	0.250	0.495	0.198	0.395	0.327	0.108	4.829

Table 6.
Separation of Yttrium from Yb(III), Er(III), Dy(III) and Ho(III) on Chelating Ion Exchanger Lewatit TP 207

Matrix structure	Functional group type	Fraction number	V dm^3	Mass of fractions Ln_2O_3 g	Impurity in Y_2O_3 after purification				Heavy lanthanides + Y_2O_3 absorbed on ion exchanger g
					Yb %	Er %	Dy %	Ho %	
Copolimer of styrene with divinyl-benzene of macroporous structure	imino-di acetic	1	2.040	–					
		2	0.620	0.498	<0.01	0.080	0.130	0.040	
		3	0.400	0.556	0.015	0.120	0.161	0.051	
		4	0.250	0.445	0.021	0.141	0.170	0.055	
		5	0.250	0.463	0.027	0.160	0.192	0.062	
		6	0.250	0.467	0.042	0.180	0.211	0.066	
		7	0.250	0.472	0.058	0.210	0.230	0.070	
		8	0.250	0.483	0.063	0.233	0.251	0.080	
		9	0.250	0.484	0.074	0.260	0.270	0.090	
		10	0.250	0.485	0.081	0.292	0.290	0.091	
		11	0.250	0.486	0.090	0.310	0.313	0.093	
		12	0.250	0.487	0.105	0.324	0.316	0.095	
		13	0.250	0.488	0.122	0.331	0.320	0.101	
		14	0.250	0.489	0.126	0.343	0.330	0.105	
		15	0.250	0.490	0.131	0.362	0.341	0.110	
		16	0.250	0.491	0.143	0.370	0.342	0.111	
		17	0.250	0.492	0.157	0.381	0.343	0.112	
		18	0.250	0.493	0.160	0.388	0.344	0.113	
		19	0.250	0.494	0.163	0.390	0.344	0.114	
		20	0.250	0.495	0.164	0.392	0.345	0.115	
		21	0.250	0.496	0.164	0.394	0.345	0.115	5.399

Table 7.
Separation of Yttrium from Yb(III), Er(III), Dy(III) and Ho(III) on Chelating Ion Exchanger Lewatit TP 208

Matrix structure	Functional group type	Fraction number	V dm^3	Mass of fractions Ln_2O_3 g	Impurity in Y_2O_3 after purification				Heavy lanthanides + Y_2O_3 absorbed on ion exchanger g
					Yb %	Er %	Dy %	Ho %	
Copolimer of styrene with divinylbenzene of macroporous structure	imino-diacetic	1	1.900	–					
		2	0.750	0.437	0.015	0.085	0.130	0.040	
		3	0.415	0.450	0.020	0.100	0.155	0.042	
		4	0.400	0.459	0.023	0.110	0.160	0.045	
		5	0.400	0.607	0.030	0.130	0.190	0.050	
		6	0.400	0.706	0.042	0.150	0.200	0.060	
		7	0.400	0.750	0.045	0.180	0.230	0.065	
		8	0.400	0.761	0.048	0.200	0.255	0.070	
		9	0.250	0.484	0.049	0.206	0.257	0.074	
		10	0.250	0.489	0.050	0.210	0.259	0.077	
		11	0.250	0.490	0.052	0.215	0.265	0.080	
		12	0.250	0.491	0.055	0.236	0.281	0.083	
		13	0.250	0.492	0.067	0.260	0.298	0.089	
		14	0.250	0.493	0.075	0.272	0.302	0.094	
		15	0.250	0.494	0.086	0.280	0.310	0.098	
		16	0.250	0.495	0.099	0.285	0.321	0.105	
		17	0.250	0.496	0.117	0.298	0.332	0.112	5.696

Table 8.
Separation of Yttrium from Yb(III), Er(III), Dy(III) and Ho(III) on Chelating Ion Exchanger Wofatit MC-50

Matrix structure	Functional group type	Fraction number	V dm^3	Mass of fractions Ln_2O_3 g	Impurity in Y_2O_3 after purification				Heavy lanthanides + Y_2O_3 absorbed on ion exchanger g
					Yb %	Er %	Dy %	Ho %	
Copolimer of styrene with divinylbenzene of macroporous structure	imino-diacetic and amino-acetic	1	1.710	–					
		2	0.565	0.506	<0.015	<0.01	<0.01	<0.01	
		3	0.500	0.768	<0.015	0.023	0.073	0.018	
		4	0.250	0.390	0.015	0.069	0.098	0.040	
		5	0.250	0.448	0.017	0.120	0.200	0.062	
		6	0.250	0.472	0.030	0.180	0.260	0.081	
		7	0.250	0.477	0.039	0.238	0.290	0.094	
		8	0.250	0.479	0.050	0.300	0.310	0.100	
		9	0.250	0.480	0.076	0.339	0.320	0.109	
		10	0.250	0.481	0.083	0.380	0.325	0.115	
		11	0.250	0.482	0.104	0.398	0.336	0.118	
		12	0.250	0.483	0.129	0.420	0.340	0.123	
		13	0.250	0.484	0.148	0.429	0.345	0.124	
		14	0.250	0.485	0.167	0.440	0.350	0.125	
		15	0.250	0.486	0.185	0.445	0.354	0.126	
		16	0.250	0.487	0.203	0.450	0.356	0.126	
		17	0.250	0.488	0.216	0.456	0.358	0.127	
		18	0.250	0.488	0.230	0.460	0.360	0.127	
		19	0.250	0.488	0.241	0.472	0.362	0.128	
		20	0.250	0.488	0.250	0.485	0.364	0.128	2.961

iour of amino acid type ion-exchangers (selectivity differences) in relation to rare-earth elements can be explained by a different proportion of iminodiacetate and aminoacetate groups (or by presence of other functional groups) [11]. In the ion-exchanger phase, there exists the possibility of a formation of mixed complexes having a greater stability than iminodiacetic group complexes [31]. Moreover, chelating ion-exchanger selectivity is effected by the acidic-basic character of the functional groups, their reciprocal spatial position, configuration, steric effects, and in some cases the distance of the functional groups from the matrix, the kind of matrix, and its porosity, etc.

1. POWELL, J. E.: in The Rare Earths, eds. SPEDDING, F. H. and DAANE, A. H., John Wiley Sons, New York and London, 1961, pp. 55–73.
2. POWELL, J. E.: in Progress in the Science and Technology of Rare Earths, Vol. 1, ed. Le ROY EYRING, Pergamon Press, Oxford, London, New York, Paris, 1965, pp. 81–109.
3. POWELL, J. E.: in Handbook on the Physics and Chemistry of Rare-Earths, Vol. 3, eds. GSCHNEIDNER, K. A. and LE ROY EYRING, North–Holland Publishing Company, Amsterdam, New York, Oxford, 1977, pp. 89–93.
4. GSCHNEIDNER, K. A.: in Speciality Inorganic Chemicals, ed. THOMPSON, R., The Royal Society of Chemistry, Burlington House, London, 1981, pp. 403–443.
5. MINCZEWSKI, J., CHWASTOWSKA, J. and DYBCZYŃSKI, R.: Separation and Preconcentration Methods in Inorganic Trace Analysis. John Wiley Sons, New York, 1982, pp. 382–396.
6. HUBICKA, H. and HUBICKI, Z.: Solvent Extraction and Ion Exchange, *1986,* 4 (2), 383–399.
7. CHRISTELL, R., FORBERG, S. and WESTERMARK, T.: J. Inorg. Nucl. Chem. *1961,* 17, 187–189.
8. HERING, R.: J. Inorg. Nucl. Chem. *1962,* 24, 1399–1405.
9. WINGET, J. O.: Separation of the Lanthanide Series and Yttrium Using Phosphonic and Iminodiacetic Acid Resins, BuMines Report 6510, U.S. Department of The Interior, Washington, 1964.
10. SCHROBILGEN, C. J. and LANG, C. E.: J. Inorg. Nucl. Chem. *1968,* 30, 3127–3133.
11. HERING, R.: Chelatbildende Ionenaustauscher, Akademie Verlag, Berlin, 1967.
12. BÀLINT–AMBRÒ, J.: The Behaviour of Some Light Rare Earths on Varion CH Complex Forming Ion–Exchange Resins, 3rd Analytical Conference, Budapest, 1970, pp. 45–50.
13. MARHOL, M., BERANOVA, H. and CHENG, K. L.: J. Radioanal. Chem. *1967,* 21, 177–181.
14. MATORINA, N. N., KAGIYANTS, S. M., KRYUCKOVA, O. V. and CHMUTOV, K. V.: J. Phys. Chem. 1978, 52, 1155–1160.
15. MARHOL, M.: Ion Exchangers in Analytical Chemistry, Academia, Prague, 1982, pp. 377–388.
16. BARSUKOVA, K. V. i KREMLYAKOVA, N.: Radiokhimiya, *1981,* 23, 306–311.
17. TAKEDA, K., AKIYAMA, M., KAWAKAMI, F. and SASAKI, M.: Bull. Chem. Soc. Jpn. *1986,* 59, 2225–2232.
18. HUBICKI, Z., HUBICKA, H. and JUSIAK, S.: Prace Naukowe Instytutu Chemii Nieorganicznej i Metalurgii Pierwiastków Rzadkich Politechniki Wrocławskiej, 1975, 30, 95–113.
19. HUBICKA, H. and HUBICKI, Z.: Materials Science, *1977,* 3, 101–104.
20. HUBICKA, H. and Hubicki, Z.: Materials Science, *1978,* 4, 39–41.
21. HEITNER WIRGUIN, C. and URBACH, V.: J. Phys. Chem. *1965,* 69, 3400–3404.
22. MARHOL, M. and CHMELIČEK, I.: J. Chromatog. *1974,* 102, 89–94.
23. MARHOL, M. and CHENG, K. L.: Talanta, *1974,* 21, 751–762.
24. KAZANCEV, E. A. and KAZANCEV, E. J.: Ž. Prikł. Chim. *1975,* 48, 1670–1673.
25. KUŽACHMETOV, E. J.: Radiokhimiya, *1976,* 18, 197–199.
26. IYER, S. G. and PODMANABHAN, P. K.: Sep. Sci. *1977,* 12, 205–210.
27. HUBICKI, Z., HUBICKA, H. and JUSIAK, S.: Materials Science, *1977,* 3, 53–56.

28. SOZAŃSKI, A.: Industrial methods for separation of thorium from rare earth elements, Wydawnictwo Politechniki Wrocławskiej, Wrocław, 1981.
29. INCZEDY, J.: Analytical Applications of Complex Equilibria, Akadémiai Kiadó, Budapest, 1976, pp. 328–368.
30. PERRIN, D. D.: Stability Constants of Metal–Ion Complexes, Part B. JUPAC Chemical Data Series, No 22, Pergamon Press, Oxford, 1979.
31. KOSTROMINA, N. A.: Kompleksonaty Redkoziemielnych Elementow, Nauka, Moscow, 1980, pp. 46–59.

HUNGARIAN JOURNAL
OF INDUSTRIAL CHEMISTRY
VESZPRÉM
Vol. 17. pp. 365–370 (1989)

VOLTAMMETRIC INVESTIGATION OF THE CADMIUM ANODE IN POTASSIUM HYDROXIDE SOLUTIONS

V. N. VARIPAEV, F. ÓVÁRI* and A. E. GABRIKOVA

(Electrochemical Technological Department of the Technological Institute of Leningrad, USSR,
Received: December 9, 1988

An examination of the behaviour of cadmium anode with the voltammetric method in 0.4–10.0 mol/l concentration potassium-hydroxide solutions. The anodic passivation currents were determined as the function of the velocity of the potential change, the rotation velocity of the rotating electrode and temperature of the electrolite. The examined temperature range was between 20–55 °C. It was proved that the transition between the active solution and passivation range of cadmium can be determined by the conditions of diffusion and activation polarization control.

Introduction

The investigation of anodic behaviour of cadmium in alkaline solutions is significant on the one hand from the point of view of corrosion, and on the other hand because of the production technology of the cadmium-nickel alkaline storage battery (1) and other electrochemical technologies (2). Quick information can be gained from the active solution range of cadmium and the following passive range by the determination of the voltammetric polarization curves (3). Meanwhile, the effects of several factors can be studied, such as the solvent composition, concentration, temperature of the electrolite, intensity of stirring, and velocity of potential change, etc.

Method of Measurement

The investigations were performed in a tempered glass cell in which the anode field was separated from the two cathode fields by taps. The anode was a rotating or fixed cadmium electrode (99.95% Cd). The rotating electrode was

* Technological Institute of Inorganic Chemistry, Veszprém University of Chemical Engineering, Veszprém, Hungary

protected by teflon insulation from the side and from above. The electrolite was made of analytically pure KOH, its concentriation changed from 0.4–10.0 M/l. A platinum auxiliary electrode was used. The reference electrode was Hg/HgO in a KOH solution being adequate to the electrolite.

After delubrication with ethyl-alcohol, the even cadmium electrode was submitted to chemical polishing in a 1:1 ratio mixture of HNO_3 and HCl.

Just before the registration of the polarization curves, the electrode was submitted to cathodic reduction at a cathode potential of -1.00 V in the measuring solution. This made it possible to get reproducible results.

The voltammetric polarization curves were measured by a potentiostat at different velocities (from 0.8 to 40 mV/s). Most of the work was performed at 20 °C. Temperature dependence was investigated in the range of 20–55 °C.

Results

Firstly the effect of the velocity of the potential change (v) on the passivation current of cadmium (i_p) was investigated in the range of 0.8 mV/s–8 mV/s. Concentration of potassium hydroxide was investigated in the range of 0.4–10.0 M/l. *Figure 1* shows the results obtained in a logarithmic coordination system. Increasing the velocity of the potential change, the passivation current of cadmium increases, which refers to the diffusion control of the solution of active cadmium. The effects of other factors on the velocity of the potential change could be eliminated, it is practical to perform the measurements at higher velocities.

The next set of measurements clarified the effect of mixing the solution. According to this, it is the kinetics that limits the anodic solution of cadmium. Lubrication was carried out by a rotating disc electrode.

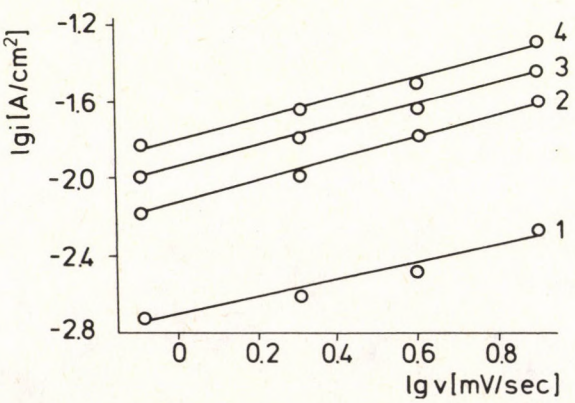

Fig. 1.
Relationship between passivation current and velocity of potential change. KOH concentrations (M/l) 1.–0.4, 2.–4.0, 3.–6.8, 4.–10.0. Temperature: 20 °C.

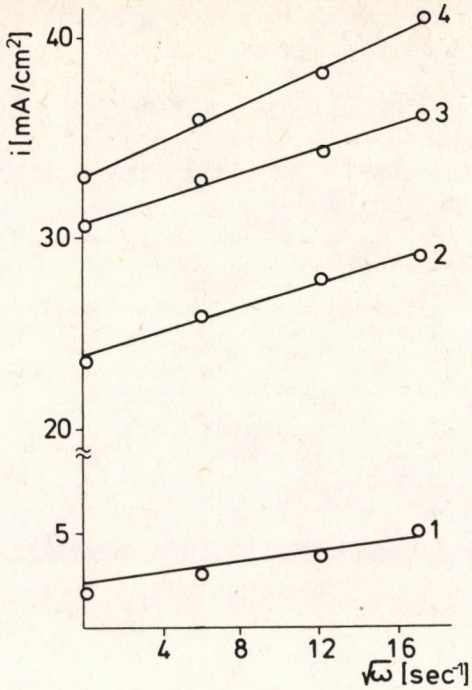

Fig. 2.
Voltammetric polarization curves at different rotation velocities of the disc electrode (ω). 1.–33, 2.–55, 3.–150, (s^{-1}). KOH concentration: 0.4 M/l. Velocity of potential change is 40 mV/s. Temperature: 20 °C.

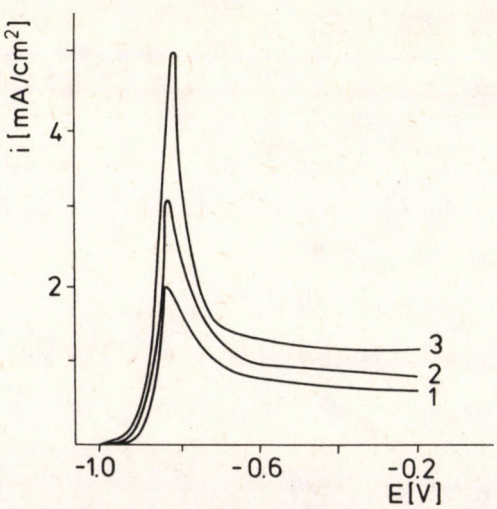

Fig. 3.
Relationship between passivation current and rotation velocity of the disc electrode. Conditions are the same as shown in *Figure 1.*

Figure 2 shows some typical voltammetric passivation curves in a 0.4 M/l KOH solution. The velocity of the potential change was 40 mV/s, at different rotation velocities.

Analogous curves to this can be gained in the case of potassium hydroxide solutions of higher concentration. Curves in *Figure 2* show how far the active solution range of cadmium gets to, then behind the peak current reduces quickly and the anode turns into the passive range.

Figure 3 shows the relationship between the anodic current peaks (i_p) and the rotation velocity of the rotating electrode at the potential change of $v = 40$ mV/s and in a wide KOH concentration interval.

The relationship is linear in the $i_p - \sqrt{\omega}$ co-ordinate system, but at the same time it cannot be extrapolated to the zero point as demanded by the theory of diffusion kinetics. This refers to the fact that the passivation process of cadmium not only has a diffusion character, that is a combined kinetic mechanism can be observed, which corresponds to the activation–diffusion control of the solution process of cadmium. Stages of the anodic polarization process of cadmium can be imagined in the following way [5, 6, 7]. Primary is the solution reaction of cadmium, during this cadmium complexes are formed:

$$Cd + 3\,OH^- \rightarrow [Cd(OH)_3]^- + 2\,e \qquad (1)$$

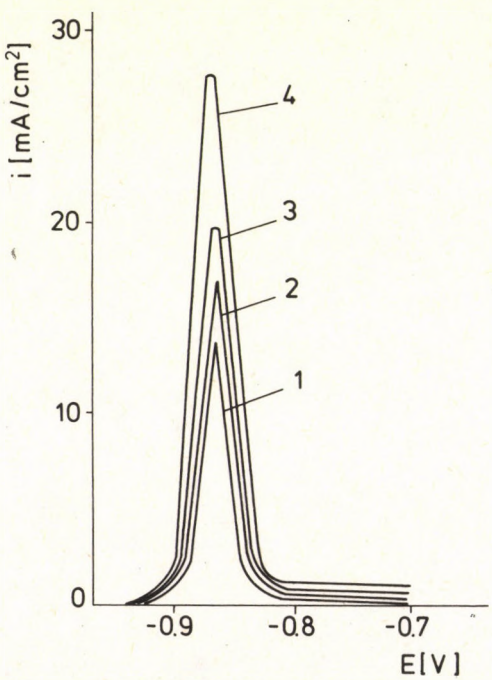

Fig. 4.
Anodic polarization curves of cadmium electrode at different temperatures (°C). 1.–20, 2.–35, 3.–45, 4.–55. KOH concentration: 10 M/l. Velocity of potential change: 0.8 mV/s.

After the anode field becomes oversaturated with $Cd(OH)_3^-$ solution, the complex decomposes and the solid state $Cd(OH)_2$ precipitates:

$$[Cd(OH)_3]^- \rightarrow Cd(OH)_2 + OH^- \quad (2)$$

When a solid – rather compact – layer from cadmium hydroxide is formed on the surface of the anode, passivation of the electrode takes place.

The higher is the concentration of KOH, the higher the solubility of cadmium and the higher the i_p which indicates the end of the active period. This is followed by the passive period. The higher the rotating velocity of cadmium anode, the later the critical oversaturated state sets in on the surface of the anode and so the passivation current density will be higher. According to our opinion, in this case diffusion control is connected with the transport of OH^- ions as they have to get through the porous and amorphous $Cd(OH)_2$ layer so that the reaction (1) could take place.

Solution of cadmium in an alkaline solution depends on the temperature as well, therefore, the increase of temperature increases the value of i_p. This can be observed on the set of i–E curves in KOH solutions of 4.0–10.0 M/l concentration. Increasing the temperature from 20 to 50 °C, the passivation current essentially increases linearly even at a small potential change velocity *(Figure 4)*.

A linear relationship can be established between the passivation current of the even electrode and the velocity of the potential change, the rotation velocity and temperature change in the KOH solution.

REFERENCES

1. Tenkovcev V. V. and Center B. I.: Theoretical Basis and Application of Hermetic Cadmium-Nickel Batteries. Moscow. Energoizdat 1985. pp. 96.
2. Óvári F., Karbasov B. G. i Rotinyan A. L.: Zhur. Prikl. Khim. *1985* 58 (3) 543–47.
3. Croft O.: J. Electrochem. Soc. *1959* 10 (4) 278–84.
4. Rotinjan A. L.–Tihonov K. I.–Sosina I. A.: Theoretical Electrochemistry. Leningrad. Khimiya 1981. 421. old.
5. Barnard R.–Edwards G. S.–Holloway I.–Tye F. L.: J. Appl. Electrochem. *13*, 751 (1983)
6. Barnard R.–Holloway I.–Randell C. F.–Tye F. L.: J. Appl. Electrochem. *14*, 187 (1984)
7. Barnard R.–Edwards G. S.–Holloway I.–Tye F. L.: J. Appl. Electrochem. *13*, 765 (1983)

HUNGARIAN JOURNAL
OF INDUSTRIAL CHEMISTRY
VESZPRÉM
Vol. 17. pp. 371–382 (1989)

CORROSION INHIBITION OF MILD STEEL IN ACIDIC SOLUTION BY ALKYLARYLAMINES

M. STUDNICKI AND MS. B. TRZEBICKA

(Institute of Carbochemistry Polish Academy of Sciences, 44–100 Gliwice ul. 1–go Maja 62)

Received: December 20, 1988

On the basis of theoretical considerations, an application of a new adsorption isotherm in approximation of the dependence logarithm of the coefficient of corrosion inhibition as a function of concentration of inhibitor is described. Correlations between parameters a, c_{00} of the isotherm, degree of protection z, and indices of molecular connectivity were found.

Introduction

The selection of proper inhibitors of corrosion in acidic solutions requires knowledge of the inhibition mechanism and the structure – properties relationship of the inhibitors. The inhibitor action depends on its adsorption on the metal surface. The knowledge of the degree of surface coverage θ is necessary for the determination of the adsorption isotherm. The values of θ on solid electrodes can be measured by the method of differential capacitance, the accuracy of this method and its applicability being limited by the presence of crevices, surface roughness, hydrogen overvoltage, oxygen formation, anodic metal dissolution, and aging of the surface, etc. [1]. A computer aided fit of the experimental data and determination of the adsorption isotherm of the inhibitors is therefore often the only way to get information on the adsorption. This determined the base of the dependence of the logarithm of the coefficient of inhibition or degree of protection on $\log c$ (inhibitor concentration in mol/dm^3) [2] and the mechanism of inhibition. The adsorption isotherm and paramters related to the inhibition mechanism are then numerically fitted to the theoretically assumed mechanism.

Mechanism of Inhibitor Action

In order to determine the dependence of log γ or z on the inhibitor concentration, equations suitable for the computer aided evaluation of the experimental data were derived based on literature references [3, 4]. The coefficient of corrosion inhibition γ was determined from the equation:

$$\gamma = \frac{i_{ok}}{i_k} \tag{1}$$

where i_{ok} is the corrosion rate without inhibitor, calculated from the mass loss of the metal sample during exposure in acidic solution, i_k is the corrosion rate with inhibitor present calculated from the mass loss of the metal.

On the basis of the theoretical considerations [3] an equation that described the dependence on log γ and θ (degree of coverage) was found for $\theta < 0.2$:

$$\log \gamma = \beta_1\theta + \beta_2\theta^\beta + y_0 \tag{2}$$

where:

$$\beta_1 = 0.43(\alpha nF\Delta\Psi_1/RT + 1)$$
$$\beta_2 = 0.43\Delta G/RT$$
$$y_0 = 0.43\alpha nF\Psi_2/RT$$

Equation (2) is valid if the mechanism of the inhibitor action is energetical, which means that the adsorption potential in the presence of the inhibitor depends on θ linearly, and the rate of the electrochemical reaction during corrosion depends on θ^β [3]. These assumptions are valid for alkylarylamines [5–9].

Adsorption of Inhibitors on a Metal Surface

HACKERMAN and coworkers [10, 11] stated that the adsorption of fatty acids, nitrils, and esters, etc., on steel or iron powder is partially irreversible, because the adsorbed substances cannot be completely removed by solvents. Such a stable adsorption is described by the Langmuir isotherm with the degree of surface coverage at saturation. SMITH and ALLEN [12] observed that the adsorption of n-nonadecane acid on copper, nickel, iron and aluminum proceeds in a very different way. It depends on the treatment of the metal surface with air or in a solvent with the exclusion of air. In the first case, the adsorption increased continuously, in the second case, saturation was reached very fast. The maximal adsorption values in the absence of air decreased in the order: copper – iron – aluminum. No evidence of permanent or irreversible adsorption was found.

In most cases, only one of many kinds of ions present in the solution is adsorbed, therefore, a charge collects on the surface of the adsorbent. This charge is compensated either by the opposite ions gathered in the solution close to the adsorbent surface (specific adsorption) or by a transfer of an equivalent amount of ions from the adsorbent to the solution (exchange adsorption) [13].

Adsorptive and protective properties of inhibitors may be related to each other by means of Langmuir and Temkin isotherms [3] and Equation (2). The Langmuir and Temkin isotherms do not take this into account for inhibitor concentration c_{00} $\theta = 1$ [3].

The new adsorption isotherm derived, based upon thermodynamic considerations and Gibbs equation, describes this behaviour. This isotherm describes the complexation of the inhibitor by the ions of the corroded metal.

The adhesion potential A on the surface of a solid is defined [14] as the difference between the thermodynamic potential of the pure solid surface γ_S and the interphase potential between the solid and the liquid γ_{SL}.

If the liquid wets very well the metal surface then:

$$\pi = \gamma_S - \gamma_{SV} \neq 0 \tag{3}$$

where γ_{SV} is the thermodynamic potential of the gas – solid interphase surface.

On the other hand, if the wetting angle α_1 goes to 0, therefore $\cos \alpha_1 \rightarrow 1$. The adhesion potential is then given by Eq. [14]:

$$A = \gamma_{LV_0} \cos \alpha_1 + \pi \cong \gamma_{LV_0} \cdot K' \tag{4}$$

where γ_{LV_0} is the surface tension of the liquid being in equilibrium with its vapour, and K' is a constant.

The surface tension of the solutions of organic substances can be found by the semi empirical equation [14]:

$$\gamma_{LV_0} = \gamma_0 - \gamma_0 B_1 \ln (1 + c_1/a) \tag{5}$$

where γ_0 is the surface tension of pure solvent, B_1 is a constant valid for homologous substances, a is a constant for a given inhibitor and c_1 is the concentration of an uncomplexed inhibitor. c_1 can be calculated from the known stability constant K of the complexes of the metal ions with the inhibitor:

$$c_1 = Kc/(K + c_{Fe}) \tag{6}$$

$$K = \frac{c_1 \cdot c_{Fe}}{c_2} \tag{7}$$

$$c_1 = c - c_2 \tag{8}$$

c_2 is the concentration of the complexed inhibitor molecules.

Equation (5) together with Gibbs Equation [14] permits the calculation of the surface excess Γ in the double layer:

$$\Gamma = -\frac{1}{RT} \frac{\partial A}{\partial \ln c} = -\frac{K'}{RT} \frac{\partial (\gamma_{LV_0})}{\partial \ln c} \tag{9}$$

The degree of the surface coverage is given by [1]:

$$\theta = \Gamma/\Gamma_\infty \tag{10}$$

where Γ is the surface excess of the inhibitor of concentration c and Γ_∞ is the surface excess of the inhibitor concentration c_{00}.

After differentiation and algebraic transformations Equations (4), (5), (6), (7), (8) and (9) yield a new adsorption isotherm:

$$\theta = \frac{(r/c_{00}+K)}{(r/c+K)}; \quad r = a(K+c_{Fe}) \tag{11}$$

or in a different form:

$$1/\theta = (1/(r/c_{00}+K))\,(r/c+K) \tag{12}$$

It can be seen that the new isotherm is an extension of the Langmuir isotherm. For $c_{Fe}=0$ we obtain the Langmuir isotherm:

$$1/\theta = \frac{c_{00}}{a+c_{00}}(a/c+1) \tag{13}$$

It can be concluded from Equation (11) that the term a describes the ability of the inhibitor to adsorb on the interphase surface. High value of a corresponds to a low inhibitor adsorption and therefore a too low degree of surface coverage. The isotherm given by Equation (11) and Equation (2) permits the connection of the inhibition properties of the compound with the saturation concentration c_{00}. For this reason, the isotherm given by Equation (11) was used to calculate the correlation parameters $\log \gamma(c)$ [Equation (2)]. The value c_{00} obtained numerically permitted the calculation of the dimension of the geometric cube occupied by the molecule adsorbed on the metal surface at saturation.

Indices of Molecular Connectivity

The measurements of the corrosion inhibition provide data on the adsorption of the inhibitors and allow the correlation of the inhibitor structure determined by the molecular connectivity indices with parameters a, c_{00} and degree of protection z.

A complex description of the electron and geometric structure of a molecule is available only through quantum mechanical methods [16]. For many purposes, however, a simplified description of the structure is sufficient, i.e. a description accounting for the ways and the order of the atomic connections and for the shape and dimensions of the molecule. Such a description is possible using the indices of molecular connectivity developed by KIER and HALL [15]: ${}^1\chi$ and ${}^1\chi^v$.

The indice ${}^1\chi$ contains information on the chain length, ring size and branching, while the indice ${}^1\chi^v$ is related to polarizability [15].

Experimental

Syntheses of alkylarylamines were described in works [5–9].

Gravimetric Measurements of Inhibition Coefficient

Sheets ($13 \times 27 \times 1$ mm) of StO steel (mild steel) were treated with acid to remove the oxide layer, washed with acetone and dried. The weighted sheets were treated for 24 hours with 15 cm^3 of 1 m HCl or 1 m H_2SO_4 with or without inhibitor.

The experiments were repeated twice for each of 10 inhibitors concentrations applied. The sheets were washed with CCl_4, water and dried. The dry sheets were weighed. The inhibition coefficient was calculated from the mass loss of the sheets according to Equation (1). The corrosion rate was calculated from:

$$i_{ok} = \Delta m_0 / F\tau \quad (14)$$

$$i_k = \Delta m / F\tau \quad (15)$$

where:

Δm_0 mass loss without inhibitor (g)
Δm mass loss in the presence of the inhibitor (g)
F surface of the sheet (m^2)
τ time (h)

Results, Discussion and Conclusions

Equations (2) and (11) were applied for the determination of the dependence of $\log \gamma$ upon c. The parameters in these equations: a, K, β_1, β_2, β, y_0 and c_{00} were chosen to obtain least square deviation between the theoretical and experimental values of $\log \gamma(c)$. A numerical procedure developed by OPFERMANN [17] was used.

Figures 1. and 2. present examples of the computer estimated fit of theoretical equations to experimental data. In *Table 1.* gravimetrical measurements are presented for 12 inhibitors (alkylarylamines). It can be seen that theoretical assumptions, together with the iterative procedure chosen, yield a good fit in

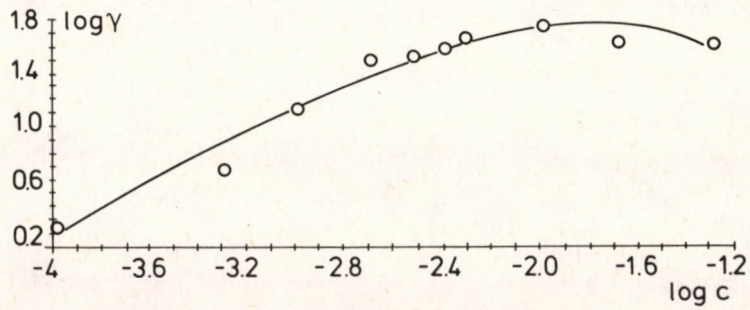

Fig. 1.
Numerical approximation of the dependence of $\log \gamma$ on c [Equations (2) and (11)] for the inhibitor 2S (1 m/dm^3 H_2SO_4, StO steel, 20 °C).

Table 1.
Gravimetrical measurements of log γ as a function of the concentration of alkylarylamine inhibitors

inhibitor	2A	3A	4A	5A	6A	8A	7A	1A	2S[1]	7B	5C	6N
c	1.2E−02	1.3E−02	2.3E−02	1.4E−02	1.2E−02	4.3E−02	2E−02	6.5E−02	5.2E−02	2.7E−02	2.6E−02	8.2E−04
log γ	1.14	1.18	1.2	1.08	1.37	1.43	1.18	1.36	1.62	0.89	0.67	0.89
c	6E−03	6.6E−03	1.2E−02	7.2E−03	6.2E−03	1.7E−02	1.1E−02	2.6E−02	2.1E−02	1.1E−02	1E−02	6.8E−04
log γ	0.91	0.94	1.03	0.88	1.19	0.83	1.02	1.06	1.62	0.86	0.78	0.8
c	4.6E−03	5E−03	8.8E−03	5.5E−03	4.7E−03	4.2E−03	7.6E−03	6.3E−03	5E−03	2.6E−03	2.5E−03	4.2E−04
log γ	0.93	0.88	1.00	0.87	1.05	0.78	1.00	0.9	1.67	0.57	0.84	0.72
c	5.1E−03	5.6E−03	9.8E−03	6.2E−03	5.3E−03	8.7E−03	8.5E−03	1.4E−02	1E−02	5.3E−03	5.2E−03	5.5E−04
log γ	0.94	0.93	1.03	0.94	1.17	0.93	1.07	1.04	1.74	0.83	0.82	0.99
c	4.1E−03	4.4E−03	7.7E−03	4.8E−03	4.2E−03	3.4E−03	6.7E−03	5.1E−03	4.1E−03	2.1E−03	2E−03	2.8E−04
log γ	0.65	0.46	0.78	0.62	0.74	0.74	0.8	0.52	1.59	0.21	0.68	0.58
c	3.5E−03	3.8E−03	6.7E−03	4.2E−03	3.6E−03	2.6E−03	5.8E−03	3.8E−03	3.1E−03	1.6E−03	1.5E−03	1.4E−04
log γ	0.65	0.47	0.71	0.61	0.72	0.69	0.95	0.57	1.52	0.17	0.7	0.59
c	2.9E−03	3.2E−03	5.6E−03	3.5E−03	3E−03	1.7E−03	4.8E−03	2.6E−03	2.1E−03	1E−03	1E−03	1.3E−04
log γ	0.65	0.42	0.67	0.71	0.64	0.52	0.77	0.52	1.49	0.18	0.5	0.46
c	2.4E−03	2.6E−03	4.5E−03	2.8E−03	2.4E−03	8.6E−04	3.9E−03	1.3E−03	1E−03	5.3E−04	5.1E−04	1.1E−04
log γ	0.69	0.38	0.68	0.7	0.64	0.1	0.69	0.26	1.14	0.05	0.12	0.61
c	1.8E−03	1.9E−03	3.4E−03	2.1E−03	1.8E−03	4.3E−04	2.9E−03	6.3E−04	5.2E−04	2.7E−04	2.6E−04	9.9E−05
log g	0.62	0.38	0.63	0.69	0.61	−0.17	0.59	0.22	0.68	0.003	−0.17	0.4
c	1.2E−03	1.3E−03	2.3E−03	1.4E−03	1.2E−03	8.7E−05	2E−03	1.3E−04	1E−04	5.3E−05	5.2E−05	8.5E−05
log γ	0.49	0.24	0.51	0.56	0.46	−0.21	0.43	0.07	0.25	−0.03	−0.26	0.2

[1] 1 m/dm^3 H_2SO_4

a wide range of concentration. A faster convergence of the iteration was reached when the initial values were estimated based upon a calculation of two parameter correlation coefficients r_{y12}. The parameters obtained for 13 inhibitors on the surface of StO steel for a computer fit of Equations (2) and (11) are given in *Table 2.*

There is a linear correlation between log a and log β:

$$\log \beta = 0.218 \log a + 0.538 \tag{16}$$

with a correlation coefficient of 0.945 for 160 measurements. The confidence interval for the correlation coefficient was calculated:

$$P\{0.915 < r < 0.964\} = 0.99$$

The probability that the correlation coefficient lies within this interval, equals 0.99.

The correlation coefficient of log $\gamma(c)$ for StO steel varies from 0.881 to 0.993. For 5 inhibitors it exceeded 0.97 and for further 5 it was greater then 0.95.

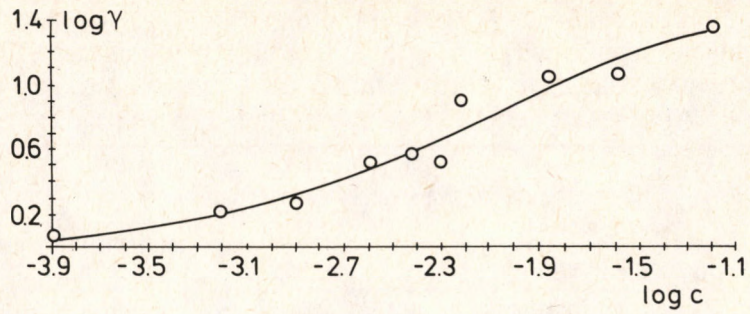

Fig. 2.
Numerical approximation of the dependence of log γ on c for the inhibitor 1 A (1 m/dm^3 HCl, StO steel).

Table 2.
Statistically fitted parameters in Equations (2) and (11) and correlation coefficients for alkylarylamine inhibitors on the surface of StO steel

Inhibitor	a	K	beta1	beta2	beta	y_0	c_{00}	correlation coefficent r_{y12}
2A	11.29512	1	133.4278	−9.223449E+12	6.4	0.4184021	1.746677	0.928
3A	4.1	1E+06	104.9191	−2.881124E+16	0.5	2.347E−02	0.9	0.950
4A	31.16998	0.59	84.87276	−1.510919E+11	6.4	0.379272	1.472646	0.966
5A	53.9	1E−03	31.30365	−2.244039E+16	10.6	0.5088088	0.5891281	0.881
6A	1000	4E+04	76.78883	−6.482597E+14	9.3	0.2480653	0.5	0.965
8A	5.1E−04	1E+05	28.18462	−27.57191	0.9	0.5603543	0.7	0.965
7A	1E−03	1E+06	15.85306	−23.21684	0.51	8.746311	0.8034946	0.973
1A	1E−02	9E+04	−5.04491	6.462047	0.93	2.266E−02	0.8408147	0.979
2S[1]	7E−03	0.4	−3.661265	5.574007	5E−01	−0.407022	0.6	0.993
7B	3E−04	100	8.518E−03	1.068941	7.7	−1.88E−02	0.5	0.968
5C	1.1E−03	9.9	123.0167	−121.5333	1.01	−0.6476059	1.088685	0.966
6N	10.2	1	−14.73.003	131.4801	4.3E−03	−125.6757	1.781	0.971
4N	11000	0.1	382.0148	−382.9333	1.01	8.08E−02	0.071	0.992

[1] 1 m/dm^3 H_2SO_4

Some relationship between the values of parameters a and K may be observed. When the constant K is low, the inhibitor is weakly adsorbed on the metal surface, because of the thermodynamic equilibrium between the amount of complexed and the amount of adsorbed inhibitor. The higher value of K means a weaker complexation of the inhibitor by the ions of the corroded metal, which means that a greater amount of inhibitor molecules may be adsorbed on the metal surface. High values of K often relate to low values of a.

Parameters β_1 and β_2 generally are of opposite sign.

It is difficult to quantitatively correlate the structure of the inhibitor with these parameters, however, qualitatively it may be stated that molecules of similar structure influence these parameters in a similar way. The inhibitor molecules containing $-NHCH_2Cl$ groups are characterised by large positive values of the parameter $\beta_1 \cdot \beta_2$ for such inhibitors have a negative value. The

exponent β is greater than 1. Parameter β_1 is negative for polymetric inhibitors containing a bifunctional –NHCHClNH– group, but of smaller absolute value, while parameter β_2 is small, but positive. Exponent β is smaller than 1.

The calculated saturation concentration c_{00} was converted to the value of d_c [10^{-10} m = 1 Å], the side length of a cube occupied by the molecule by total surface coverage ($\theta = 1$).

$$d_c = (Nc_{00})^{-1/3} = 11.84c_{00}^{-1/3} \quad [10^{-10}\ \text{m}] \tag{17}$$

The values of d_c are comparable with the d_g geometric dimensions of the inhibitor molecules *(Table 3)*.

Table 4 contains the values of $^1\chi$ and $^1\chi^v$ calculated from equations described in literature [15]. There is a two parameter correlation between parameters a, c_{00} and the molecular connectivity indices $^1\chi$ and $^1\chi^v$:

$$a = 2033.995\,{}^1\chi - 1132.657\,{}^1\chi^v - 5722.134 \tag{18}$$
$$r_{y12} = 0.903 \text{ for } 160 \text{ measurements}$$
$$c_{00} = -2.172\,{}^1\chi + 2.157\,{}^1\chi^v + 3.763$$
$$r_{y12} = 0.943 \text{ for } 160 \text{ measurements} \tag{19}$$

Although the computer aided fit of the parameters of the adsorption isotherm and of the log $\gamma(c)$ correlation parameters cannot replace their direct measurements, it can nevertheless yield important data on the corrosion inhibition mechanism and on the adsorption isotherm. The interpretation of

Table 3.

Comparison of d_g values calculated from geometrical data of the molecule of inhibitor and calculated from the saturation concentration on the surface d_{00} [Equation (17)]

	Inhibitor structure of inhibitor	$d_g\ 10^{-10}$ m	$d_c\ 10^{-10}$ m
2A	3,4-diCl—C_6H_4NHCH$_2$Cl	8.42	9.83
3A	C_6H_5NHCH$_2$Cl	6.78	12.26
4A	m—Cl—C_6H_5NHCH$_2$Cl	8.42	10.41
5A	m—HO—C_6H_5NHCH$_2$Cl	8.48	14.13
6A	m—CH_3O—C_6H_5NHCH$_2$Cl	10.04	14.91
8A	—p—C_6H_4—NHCHCl—NH—	7.88	13.34
7A	—m—C_6H_4—NHCHCl—NH—	7.88	12.74
1A	O—C_6H_4=(NH)$_2$CHCl	6.92	12.55
2S	—m—C_6H_4NHCH(IT)NH—		14.04
7B	O—C_6H_4=(NH)$_2$CHNH$_2$	7.66	14.9
5C	O—C_6H_4=(NH)$_2$CH—DBA		11.5
6N	C_6H_5NHCH$_2$NHNH$_2$	8.97	9.77
4N	m—CH_3O—C_6H_5NHCH$_2$NHNH$_2$		28.6

IT = —SC(NH)NH$_2$; DBA = —NHCH$_2$NHC$_6$H$_5$

Table 4.

Molecular connectivity indices $^1\chi$ and $^1\chi^v$ [15] for alkylarylamine inhibitors

Inhibitor	2A	3A	4A	5A	6A	8A	7A	1A
$^1\chi$	5.236	4.432	4.826	4.826	5.37	4.843	4.843	4.860
$^1\chi^v$	4.293	3.026	3.792	3.449	3.838	3.552	3.552	3.558

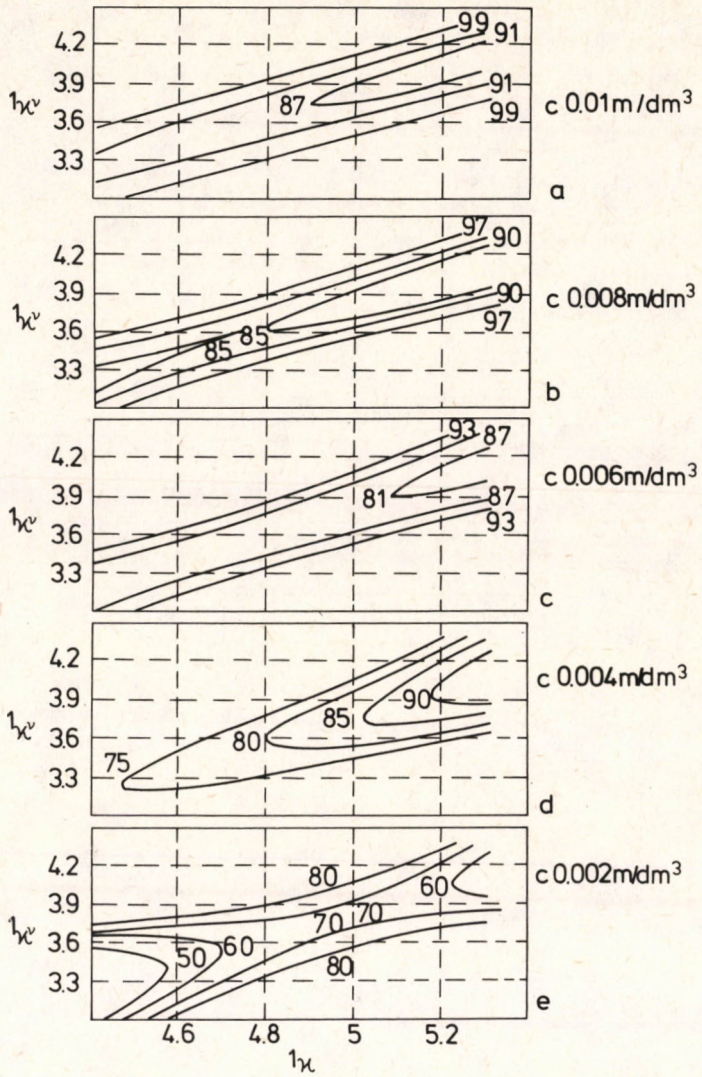

Fig. 3.
Contour map plot of z [Equations (21), (22), (23), (24)] as a function of indices of molecular connectivity: $^1\chi$, $^1\chi^v$: 0.01–0.002 mol/dm^3 of alkylarylamines, StO steel, 1 m/dm^3 HCl, 20 °C.

the measured function $\log \gamma = f(c)$ allows for their better utilization and for the determination of the statistical quality of the measurements. The determination of the characteristic inhibitor constants a, K, β_1, β_2, β, y_0, c_{00} permit the correlation of the mechanism of the inhibitor action with its chemical structure.

It is possible to use indices of molecular connectivity for the interpolation values of z:

$$z = 100(1 - 1/\gamma) \tag{20}$$

Table 5.
Statistically fitted parameters in Equations (21), (22), (23), (24) and correlation coefficients for for alkylarylamine inhibitors in concentrations: 0.01, 0.008, 0.006, 0.004, 0.002 m/dm^3

parameter	β'_1	β'_2	β'_3	y'_0	a_1	a_2	a_3	a_4	a_5	a_6	a_7	a_8	a_9	r_{y123}
concentration														
0.01	44.46839	114.9195	−79.30963	−231.6841	1	0.0118	0.2	2.11	0.11	0.111	1	0.1	0.1	0.997
0.008	126.7222	160.1042	−110.4653	−582.5081	1	0.0118	0.09	2.12	0.1	0.111	1	0.1	0.1	0.999
0.006	116.94	26.335	−72.02	−144.1912	1	0.0118	0.09	1.7	5	0.111	2	0.1	0.1	0.962
0.004	−76.8	−20.36429	55.01429	238.0022	1	0.099	0.09	1.7	5	0.111	2	0.1	0.1	0.968
0.002	72.075	57.91875	−99.25	−2076.323	10	0.09	0.09	1	2.9	0.111	2	0.1	0.1	0.998
0.25% aliphatic amines	3.164631	22.00367	−45.11757	297.5605										0.905

Table 6.
Comparison of z values calculated from Equations (2) and (20) and approximation Equations (21), (22), (23), (24)

Inhibitor	concentration									
(1) = Eq. (2), (20); (2) = Eq. (21), (22), (23), (24)	m/dm^3									
	0.01		0.008		0.006		0.004		0.002	
	1	2	1	2	1	2	1	2	1	2
2A	93.6	93.9	92.0	92.2	88.6	86.5	83.0	82.8	74.5	71.5
3A	95.9	96.0	93.0	93.0	86.7	87.5	74.4	72.7	50.8	46.7
4A	89.5	89.4	86.2	87.1	81.8	86.0	76.0	76.9	68.3	69.7
5A	90.8	92.3	88.4	91.2	85.1	86.4	81.0	79.2	75.7	72.7
6A	97.9	97.8	96.6	96.5	93.2	94.6	86.3	87.2	72.2	70.9
8A	90.3	89.0	89.5	86.7	87.9	83.4	84.5	80.9	71.5	68.3
7A	91.0	89.0	89.5	86.7	86.7	83.4	80.6	80.9	63.4	68.3
1A	87.4	89.2	85.1	87.0	81.5	83.7	75.0	81.2	60.7	69.2

z is a function of the three parameters linear equation [16]:

$$z = \beta'_1 X_1 + \beta'_2 X_2 + \beta'_3 X_3 + y'_0 \tag{21}$$

where X_1 is electron affinity [eV], X_2 is HOMO energy [eV] (the highest occupied molecular orbital energy), X_3 is electron density on N atom.

Table 5 presents values β'_1, β'_2, β'_3, y'_0 for aliphatic amines [16].

Parameters X_1, X_2, and X_3 can be approximated with indices of molecular connectivity:

$$X_1 = a_1 {}^1\chi + a_2({}^1\chi)^2 + a_3({}^1\chi)^3 \tag{22}$$

$$X_2 = a_4 {}^1\chi^v + a_5({}^1\chi^v)^2 + a_6({}^1\chi^v)^3 \tag{23}$$

$$X_3 = a_7 {}^1\chi {}^1\chi^v + a_8({}^1\chi)^2 {}^1\chi^v + a_9 {}^1\chi({}^1\chi^v)^2 \tag{24}$$

Table 5 presents coefficients a_i (i= 1 to 9) and correlation coefficients r_{y123} for alkylarylamines. It is possible to approximate values of z with good correlation coefficients r_{y123}. *Table 6* presents values of z calculated from Equations (2) and

(20) compared with those calculated from Equations (21), (22), (23), (24) for different concentrations. For each 8 inhibitors values z calculated by two different ways are close. It is possible to predict or anticipate with Equations (21), (22), (23) and (24) values of z of alkylarylamines, which structures and concentrations are known *(Fig. 3)*.

The contour map *(Fig. 3)* $z({}^1\chi, {}^1\chi^v)$ strongly depends on the concentration of inhibitors. In concentration 0.004 mol/dm^3 an inversion of parameters was observed. The highest values of z for highest values of ${}^1\chi$ and ${}^1\chi^v$ were obtained.

SYMBOLS

γ	coefficient of corrosion inhibition
i_{ok}	corrosion rate without inhibitor
i_k	corrosion rate with inhibitor
z	degree of protection
θ	degree of coverage
α	transition coefficient
$\Delta\Psi_1$	slope of the linear dependence adsorption potential on degree of coverage
Ψ_2	adsorption potential without inhibitor
Ψ_1	adsorption potential with inhibitor
ΔG	change of free activation enthalpy of the electrochemical corrosion process when the degree of surface coverage increases from 0 to 1
A	adhesion potential
γ_S	thermodynamic potential of the pure solid surface
γ_{SL}	thermodynamic interphase potential between the solid and the liquid
γ_{SV}	thermodynamic potential of the gas – solid interphase
α_1	wetting angle
K'	constant
π	difference between the thermodynamic potential of the pure solid surface and thermodynamic potential of the gas – solid interphase
γ_{LV_0}	surface tension of the liquid being in equilibrium with its vapour
γ_0	surface tension of pure solvent
B_1	constant
c_1	concentration of uncomplexed inhibitor
c_{Fe}	concentration of Fe^{2+} ions
c_2	concentration of the complexed inhibitor molecules
c	concentration of inhibitor
Γ	surface excess of the inhibitor of concentration c
Γ_{00}	surface excess of the inhibitor of saturation concentration c_{00}
a	constant for a given inhibitor
K	stability constant of the complexes of the metal ions with inhibitor
c_{00}	saturation concentration of inhibitor for degree of coverage equal 1
Δm_0	mass loss of StO steel during corrosion in acidic solution without inhibitor (g)
Δm	mass loss of StO steel during corrosion in acidic solution with inhibitor (g)
F	surface of the sheet of steel (m^2)
τ	time (hour)
β	constant
β_1, β_2, y_0	parameters of correlation 2
r_{y12}	correlation coefficient of two parameters correlation 2
$\beta'_1, \beta'_2, \beta'_3, y'_0$	parameters of correlation 21
r_{y123}	correlation coefficient of three parameters correlation 21

d_c calculated from Equation 17 side length of a cube occupied by the molecule of inhibitor concentration c_{oo}
d_g calculated from geometric dimensions of molecule length of inhibitor molecule
a_i ($i = 1$ to 9) approximate constants
$^1\chi$ indice of molecular connectivity contains information on the chain length, ring size and branching
$^1\chi^v$ indice of molecular connectivity related to polarizability
N Avogadro number
X_1 electron affinity (ev)
X_2 HOMO energy (the Highest Occupied Molecular Orbital energy)
X_3 electron density on N atom

REFERENCES

1. Praca zbiorowa pod redakcją Z. GALUSA "Elektroanalityczne metody wyznaczania stałych fizykochemicznych", PWN, Warsaw 1979.
2. ANTROPOV, L. I.: Zashch. Met., *1977,* 13 (3), 336.
3. STUDNICKI, M.: Ochr. Koroz., *1988,* 31 (11), 273.
4. DAMBORENEA, J.: Rev. Metal. Madrid, *1987,* 23 (5), 347.
5. STUDNICKI, M.: Ind. Eng. Chem. Prod. Res. Dev., *1983,* 22 (3), 482.
6. STUDNICKI, M.: Ind. Eng. Chem. Prod. Res. Dev., *1986,* 25 (1), 96.
7. STUDNICKI, M.: Hung. J. Ind. Chem., *1984,* 12 (3), 187.
8. STUDNICKI, M.: Hung. J. Ind. Chem., *1985,* 13 (2), 149.
9. STUDNICKI, M.: Hung. J. Ind. Chem., *1985,* 13 (3), 347.
10. HACKERMAN, N. and ROEBUCK, A. H.: Ind. Eng. Chem. *1954,* 46, 1481.
11. METSEN, F. A., MAKRIDES, A. C. and HACKERMAN, N.: J. Chem. Phys. *1954,* 22, 1800.
12. SMITH, H. A. and ALLEN, K. A.: J. Phys. Chem., *1954,* 58, 449.
13. BIELAŃSKI, A.: "Podstawy chemii nieorganicznej", Vol. 2, PWN, Warsaw, 1987.
14. ADAMSON, A. W.: "Chemia fizyczna powierzchni", PWN, Warsaw, 1963.
15. EKIERT, L., BOJARSKI J., MOKROSZ J. L.: Wiad. Chem., *1986,* 40 (1–2), 65.
16. FOUDA, A. S., MADKOUR, L. H. et SOLIMAN, M. S.: Bull. Soc. Chim. Fr., *1986,* 3, 358.
17. OPFERMANN J.: "Programpaket Nichtlineare Ausgleichrechnung", FSU Jena, *1984,* No 42.

HUNGARIAN JOURNAL
OF INDUSTRIAL CHEMISTRY
VESZPRÉM
Vol. 17. pp. 383–396 (1989)

ANALYSIS OF NONISOTHERMAL NONADIABATIC TUBULAR REACTORS IN THE PRESENCE OF EXTERNAL DISTURBANCES

Y. S. SRINIVAS, V. K. JAYARAMAN and B. D. KULKARNI

(Division of Chemical Engineering National Chemical Laboratory Pune-411 008 INDIA)
Received: January 18, 1989

A nonisothermal nonadiabatic tubular reactor was analyzed in the presence of external disturbances. The study, while not revealing any noise induced transitions, clearly shows the preference of evolving states in the presence of noise.

Introduction

Multiple steady states are known to exist in nonisothermal nonadiabatic systems for a certain range of parameter values [1, 2]. It has been elucidated that in a certain region of Damkohler numbers five steady states classified as kinetic, diffusion and intermediate regimes are possible. The results of the effects of the external fluctuations on the system behaviour are reported here.

Attention is restricted to a simple reaction $A \rightarrow B$ accompanied by the evolution of heat. If a chemical reaction is accompained by heat effects, then the transient behaviour of the system is described by a set of parabolic partial differential equations. The assumptions underlying the developments are [3]: no radial velocity and concentration gradients in the reactor, the temperature gradient may be described by the use of a proper value of the effective radial conductivity, absence of temperature and concentration gradients within and outside of a catalyst particle, the properties of a reaction mixture may be characterized by average values, and the mechanism of axial mixing can be described by means of a single parameter in the Fick's or Fourier's law respectively. The heat and mass balances can then be written in the dimensionless form [3]:

$$\frac{\partial y}{\partial t} = \frac{1}{Pe_y}\frac{\partial^2 y}{\partial z^2} - \frac{\partial y}{\partial z} + \mathrm{Da}(1-y)\exp\left(\frac{\theta}{1+\theta/\gamma}\right) \tag{1}$$

$$\frac{\partial \theta}{\partial t} = \frac{1}{Pe_\theta}\frac{\partial^2 \theta}{\partial z^2} - \frac{\partial \theta}{\partial z} + \mathrm{B}\,\mathrm{Da}(1-y)\exp\left(\frac{\theta}{1+\theta/\gamma}\right) - \beta(\theta-\theta_c) \tag{2}$$

where y is dimensionless conversion, $y \in [0, 1]$; θ is the dimensionless temperature, γ is dimensionless activation energy, Pe_y is the Peclet number for axial mass transport, Pe_θ is the Peclet number for axial heat transport, B is the dimensionless parameter of heat evolution, θ_c is the dimensionless cooling temperature and β is the heat transfer parameter. All parameters are positive, but θ_c can also be negative.

The corresponding boundary conditions chosen here are:

$$z=0: \quad Pe_y y = \frac{\partial y}{\partial z}; \quad Pe_\theta \theta = \frac{\partial \theta}{\partial z} \tag{3}$$

$$z=1: \quad \frac{\partial y}{\partial z} = \frac{\partial \theta}{\partial z} = 0 \tag{4}$$

The variables and the parameters used in the dimensionless formulation are:

$$Pe_\theta = \frac{\varrho v c_p l}{k_e} \quad Pe_y = \frac{vl}{D_e} \quad B = \frac{(-\Delta H) C_0}{\varrho c_p T_0} \frac{E}{RT_0}$$

$$\gamma = E/RT_0 \quad \beta = \frac{4H}{\varrho v c_p} \frac{l}{D_e} \quad \theta = \frac{E}{RT_0^2}(T - T_0)$$

$$\theta_c = \frac{E}{RT_0^2}(T_c - T_0) \quad z = \frac{x}{l} \quad t = \frac{t'v}{l}$$

The external noise can be incorporated into the above model by the following Ornstein-Uhlenbeck equation:

$$\frac{d\xi}{dt} = -\frac{1}{\tau}\xi + \frac{\sigma}{\sqrt{\tau}}\left(\frac{dW}{dt}\right) \tag{5}$$

where ξ is the noise term, σ is the strength of the noise and τ the correlation time. The distribution chosen here for the random generation is of the Gaussian type.

Damkohler number, D_a, is taken as the parameter to be fluctuating and the noise term ξ is incorporated into this parameter. The resulting stochastic equations of the axial mass and heat transports by the incorporation of noise are given by:

$$\frac{\partial y}{\partial r} = \frac{1}{Pe_y}\frac{\partial^2 y}{\partial z^2} - \frac{\partial y}{\partial z} + (\mathrm{Da} + \xi/\varepsilon)(1-y)\exp\left(\frac{\theta}{1+\theta/\gamma}\right) \tag{6}$$

$$\frac{\partial \theta}{\partial t} = \frac{1}{Pe_\theta}\frac{\partial^2 \theta}{\partial z^2} - \frac{\partial \theta}{\partial z} + \mathrm{B}(\mathrm{Da} + \xi/\varepsilon)(1-y)\exp\left(\frac{\theta}{1+\theta/\gamma}\right) - \beta(\theta - \theta_c) \tag{7}$$

Numerical Methods of Solution of Transport Equations

Equations (5), (6) and (7) have to be simultaneously solved along with the boundary conditions given by Equations (3) and (4). To generate the solution or dependence diagram a mapping technique [4] was used and solved numerically. The calculation of steady state profiles from Equations (1–4) represents a

difficult problem. For this purpose, a shooting procedure [5] was used with a backward integration from $z=1$ to $z=0$. The partial differential equations [Equations (6) and (7)], were solved by the method of finite differences [6] with the noise term ξ incorporated. This was achieved by a random noise generator of the Gaussian distribution and Equation (5), solving them by fourth order Runge-Kutta method.

Results and Discussion

Figure 1 gives the dependence of exit temperature and exit concentration on the value of Damkohler number (Da). This figure shows a loop like dependence of $\theta(l)$ on $f(Da)$. For a certain small range of Da as shown in *Figure 1*, the system admits the existence of the five steady states. The different steady states are marked as 1, 2, 3, 4 and 5 for the value of $Da=0.07$. For the steady state 1, the exit temperature and conversion is low. This steady state is referred to as the "kinetic profile". The steady state 5 corresponds to the "diffusion profile"

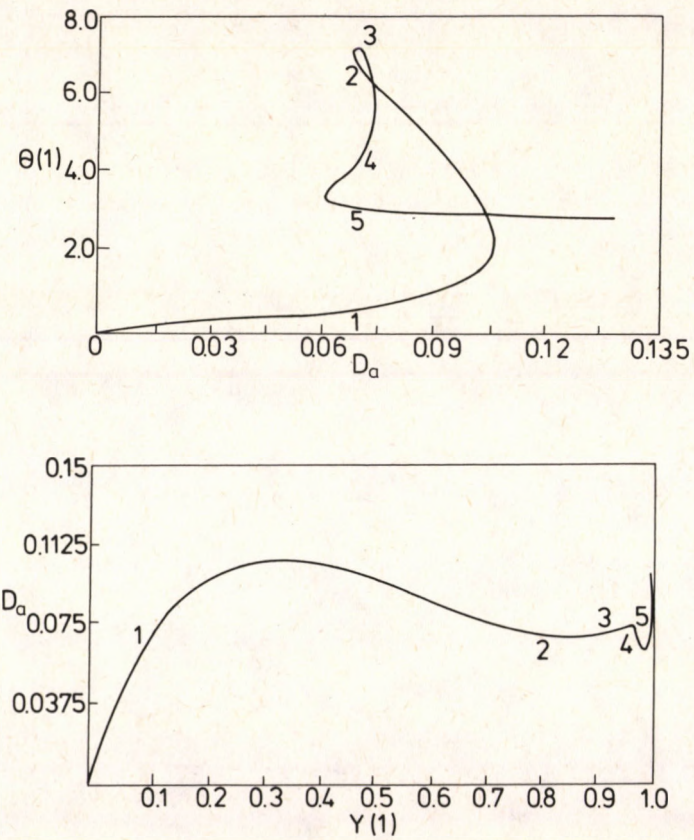

Figure 1.

observed for adiabatic reactors. Here the axial mass and heat dispersion are the rate determining steps. The steady state 3 occurs over a narrow range of *Da* values and exists only for nonadiabatic systems and is termed as the "intermediate regime". It was reported earlier that for high values of both B and β the "intermediate regime" vanishes [1].

Figure 1 reveals that the hysteresis loop is of the type

kinetic regime → diffusion regime → kinetic regime

i.e. an increase of the value of *Da* gives rise to a jump towards the "diffusion regime". The extinction process is a jump from the diffusion branch to the kinetic branch.

The deterministic analysis reveals that the steady state 1, representing the "kinetic profile", and steady state 5, representing the "diffusion profile" are stable. The stochastic analysis was performed on both the stable and unstable profiles, and the corresponding results show a marked change in the stability properties from that of the deterministic analysis, which was shown in the subsequent figures. These results are classified under the "effect of τ (correlation time)" and the "effect of σ (strength of noise)".

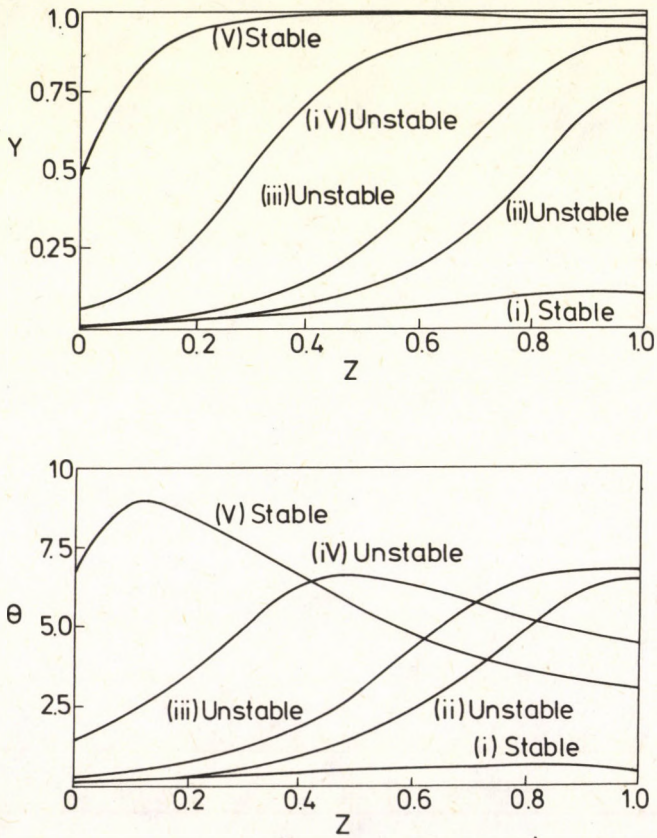

Figure 2.

Figure 2 reveals the steady state profiles (i, ii, iii, iv and v) of the five steady state region solutions [1, 2, 3, 4 and 5 respectively of *Figure 1*] of both the mass and temperature variables. The profiles indicate how the steady states 1, 2, 3, 4 and 5 (see *Figure 3.1*) look in the space dimension for the dimensionless concentration and dimensionless temperature. The Newton-Fox shoot method [5] was employed to evolve these spatial profiles. The point '1' on *Figure 1* indicates the exit values (i.e. at $z = 1$) of the dimensionless concentration (y) and dimensionless temperature (θ). For these exit values, a guess is made for the corresponding inlet values of y and θ. A backward shooting technique was used, where a guess is made at one boundary ($z = 0$), and the integration was iterated until the boundary condition at the other end ($z = 1$) was matched. These profiles evolved by the shoot algorithm are given in this Figure, and represent the steady state values of y and θ in the space dimension; the same were taken as initial profiles for the subsequent deterministic and stochastic analyses.

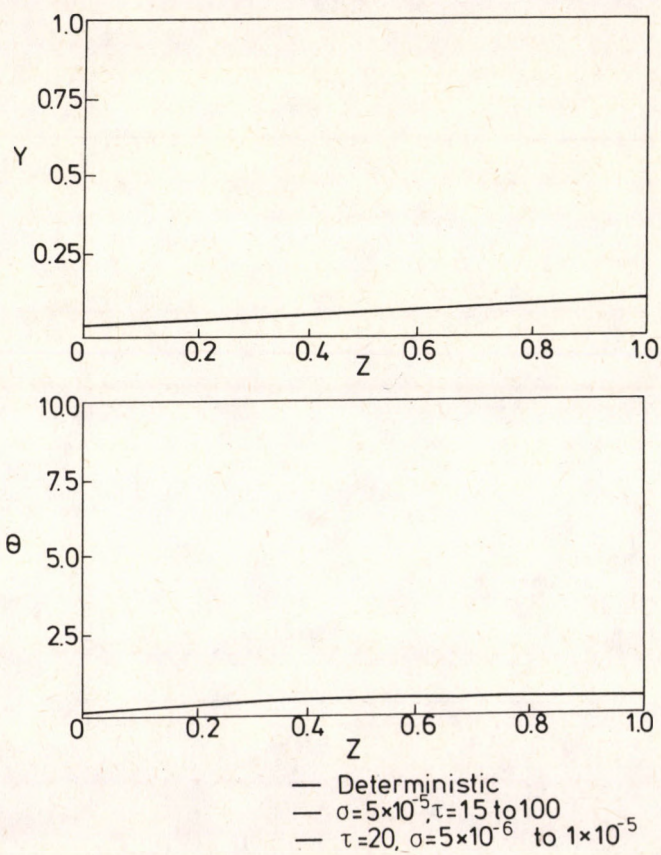

Figure 3.

Figures 3 and *4* reveal the results of deterministic and stochastic analyses performed on the "kinetic profile (i)" of *Figure 2*. *Figure 3* depicts the spatial profiles of the dimensionless concentration and dimensionless temperature for different values of the noise intensity and the noise correlation time. The parabolic partial differential equation representing axial mass and heat dispersion was simultaneously solved for both the deterministic and stochastic evolution. The concentration profile (i) (see *Figure 2*), was taken as the initial condition for the finite difference approach. The single profile, marked as deterministic (in the absence of noise) in *Figure 3*, is the solution profile that eventually reached a steady state, after a certain magnitude of time ($t = 15$). In other words, it means that the initial profile (i) we started with, evolves in a time dimension and stabilises as shown in *Figure 3*. The same initial profile (i) was subjected to external fluctuations for varying noise strengths ($\sigma = 5 \times 10^{-6}$ to

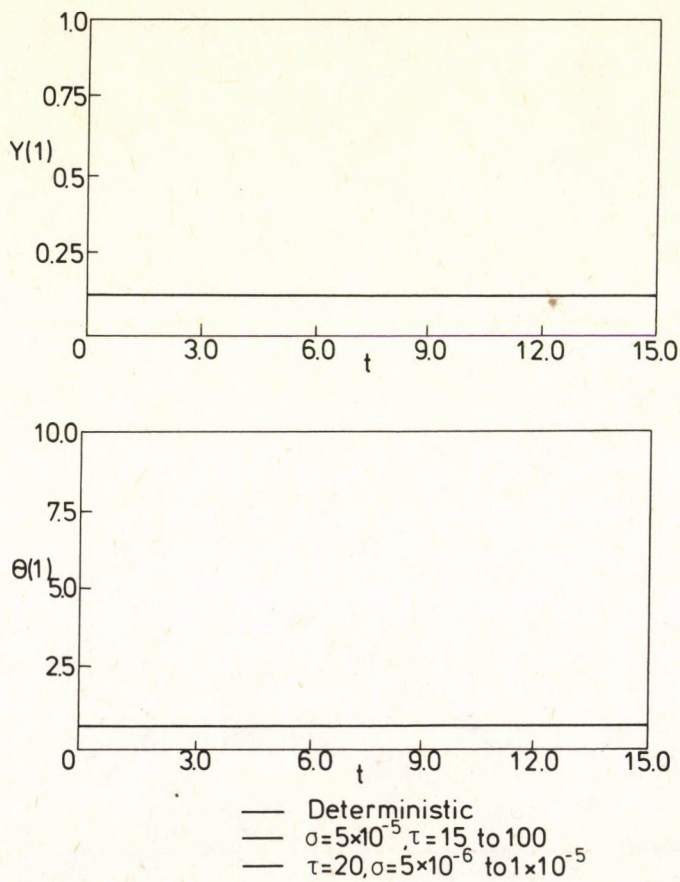

Figure 4.

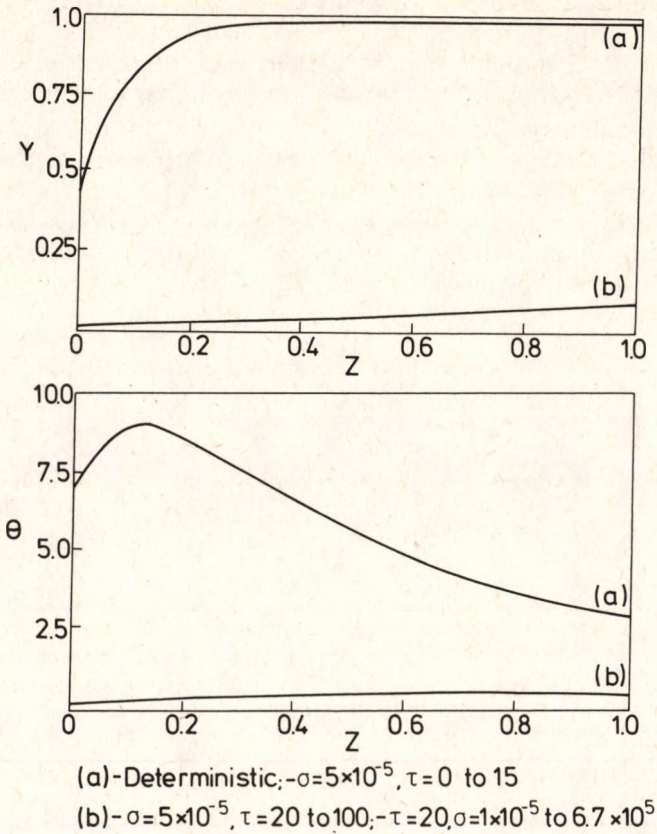

Figure 5.

1×10^{-5}) at a fixed noise correlation time ($\tau = 20$) and varying noise correlation times ($\tau = 15$ to 100) at a fixed noise intensity ($\sigma = 5 \times 10^{-5}$). In this particular case, the effect of these external fluctuations had no effect whatsoever, and hence the stochastically evolved profile conforms to that of the deterministically evolved. Hence one can conclude that the system operating in the "kinetic regime" is a remarkably stable state.

Over the subsequent stochastic analysis of the other steady states 2, 3, 4 and 5 (see Figure 1), it was observed that the magnitude of the macroscopic time variable ($t = 15$), is sufficient for any of these states to reach a steady value. In the Figures to follow, the spatial profiles of y and θ are those profiles at $t = 15$. The temporal profiles, depicted in the Figures to follow, show how these variables (y and θ) evolve in the time dimension to reach a steady state. These are drawn with the variable values at $z = 1$ i.e. $y(1)$ and $\theta(1)$ and hence depict the exit concentrations and temperatures at various times.

Figures 5 and *6* give the results of both deterministic and stochastic analyses of initial profile (ii) (see *Figure 2*). The deterministic analysis reveals that the system operating in the steady state region corresponding to point '2' of *Figure 1* stabilizes in the "diffusion regime", i.e. profile (v) (see *Figure 2*). The corresponding stochastic profile showing the effect of τ is also depicted in the Figures. It is observed from the above plots that a slight change of τ, above $\tau = 15$, brings the system to the "kinetic regime", i.e. profile (i), which otherwise (deterministically) would have led to a "diffusion regime" (i.e. profile (v) of *Figure 2*). The system which originally was diffusion controlled, with the fluctuation of the dependence parameter *Da*, would now be kinetically controlled. The temporal evolution of the dimensionless concentration y and dimensionless temperature θ is given in *Figure 6*. The effect of σ was realized and it was observed that for

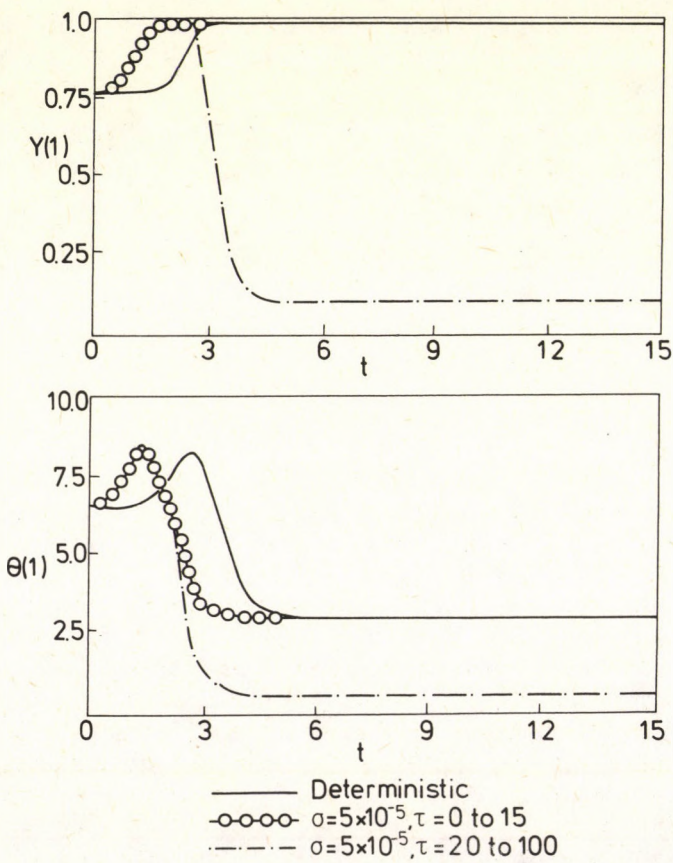

Figure 6.

a particular value of $\tau = 20$, even a marked increase in σ always brings the system to the kinetic profile (i). This is marked as profile (b) in *Figure 5*.

One can notice that the "intermediate regime", profile (iii) (see *Figure 2*), which stabilizes at the kinetic profile (i), reverses its trend by going to the diffusion profile (v) upon the incorporation of fluctuations *(Figures 7* and *8)*. An interesting feature one can observe is that even a slight fluctuation (of the order of 0.49% to 0.82%) would make the system shift from the "kinetic regime" to the "diffusion regime". This stability shift is only between limits of $\tau = 0.6$ and 1.7, and $\sigma = 5 \times 10^{-8}$, below and above which the noise does not have any effect *(Figure 7)*. The surprising feature that was observed is the consistency of the effect of σ. For a fixed value of $\tau = 20$ and varied values of $\sigma = 5 \times 10^{-8}$ to 1×10^{-5}, whatever the intensity of noise, there is no marked change in the temporal as well as the spatial profiles of the concentration and temperature variables.

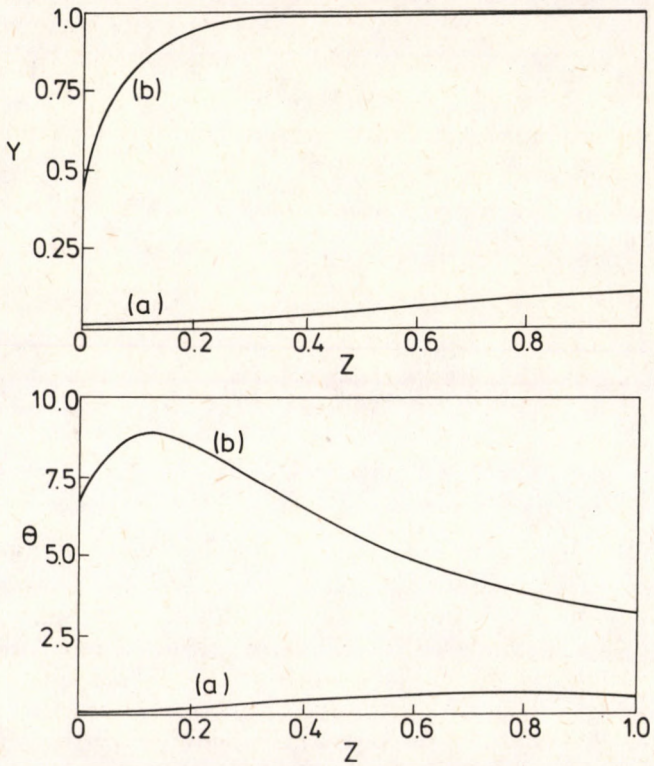

(a)- Deterministic; $\sigma = 5 \times 10^{-8}$, $\tau < 0.5$, $\tau > 1.8$
(b)- $\sigma = 5\ 10^{-8}$, $\tau = 0.6$ to 1.7

Figure 7.

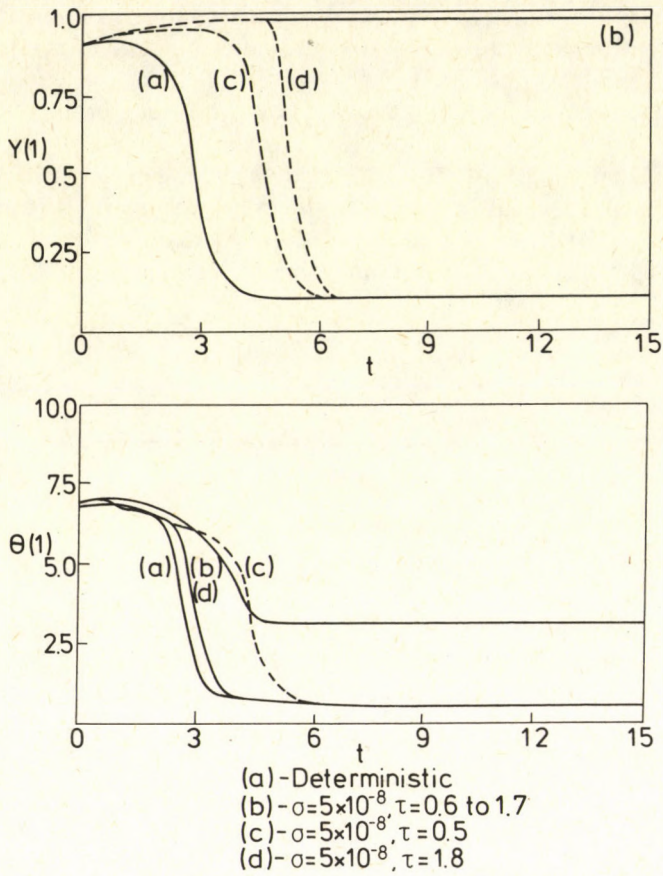

Figure 8.

The deterministic and stochastic analyses results of profile (iv) are depicted in *Figures 9* and *10*. The effect of τ and σ can be qualitatively seen to be the same as that for the "intermediate regime", i.e. profile (iii). The percentage noise used for this analysis is higher compared to the previous profile. Though the temporal evolution varies initially slightly, there is not much of a marked difference in the qualitative features from that of profile (iii) *(Figures 9* and *10)*. It is also observed that the effect of σ, for $\tau = 50$, is to bring the system to profile (v) (the "diffusion regime") for whatsoever the noise intensity may be.

The diffusion profile (v) which was stable in the deterministic analysis was found to stabilize in the kinetic regime, upon the incorporation of noise, thus revealing that the diffusion controlled solution profile would no longer exist.

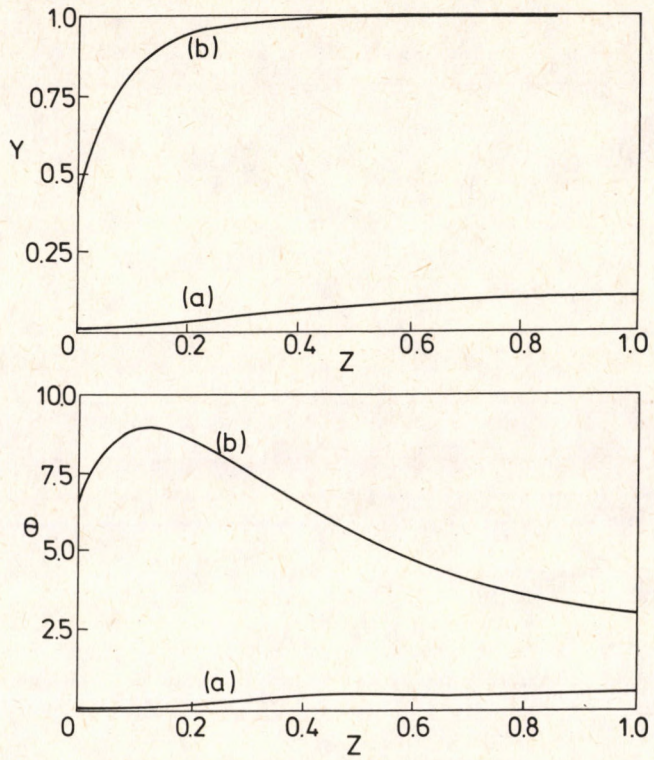

Figure 9.

Conclusions

The overall conclusions from the above qualitative study of the five steady state regimes is that the kinetic profile (i) is deterministically and stochastically stable. The diffusion profile (v) stabilises to the kinetic profile regime.

The system initially at an unstable steady state, which would have evolved to a steady state in a kinetic regime, now under the influence of noise, evolves to the other steady state in a diffusion regime, thus showing a total reversal.

SYMBOLS

B dimensionless adiabatic temperature
C concentration
C_0 initial concentration

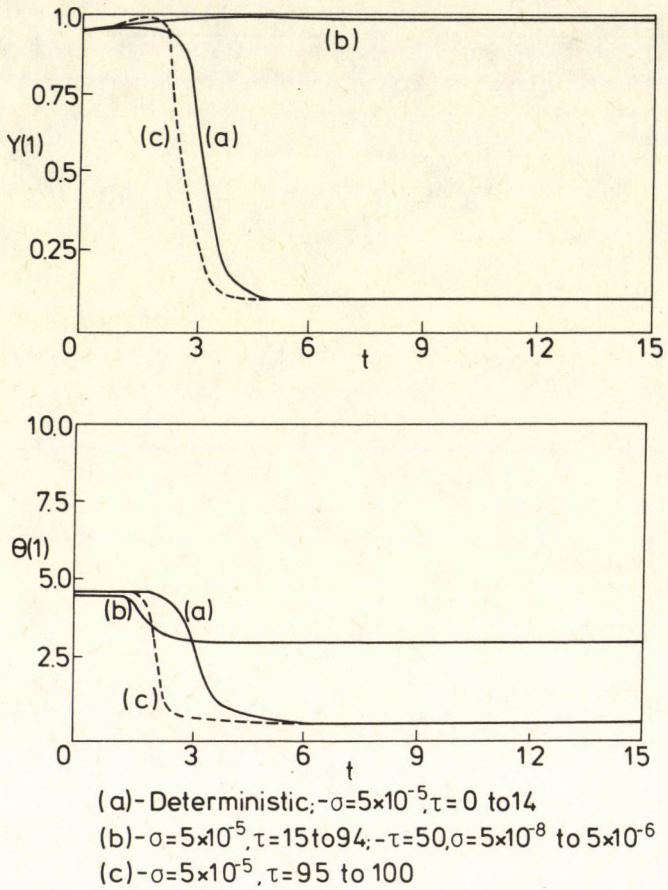

Figure 10.

c_p	specific heat at constant pressure
D_a	Damkohler number
D_e	effective conductivity in axial direction
E	activation energy
H	heat transfer coefficient
k_e	effective conductivity in axial direction
k_0	initial rate constant
l	length of reactor
Pe_y	Peclet number for axial mass transport
Pe_θ	Peclet number for axial heat transport
R	gas constant
t	dimensionless time
t'	time
T	temperature
T_0	initial temperature

v	linear velocity
W	Wiener process variable
x	axial coordinate
y	conversion
z	dimensionless axial coordinate
β	dimensionless heat transfer parameter
θ	dimensionless temperature
θ_c	dimensionless cooling temperature
γ	dimensionless activation energy
ϱ	density
$(-\Delta H)$	heat of reaction
τ	correlation time of noise
σ	intensity of the noise
ε	$\frac{1}{\tau}$

LITERATURE

1. KUBICEK, M. and MAREK, M.: Chem. Eng. Sci. *1979,* 34, 593.
2. HLAVACEK, V. and HOFMANN, H.: Chem. Eng. Sci. *1970,* 25, 1517.
3. HLAVACEK, V. and HOFMANN, H.: Chem. Eng. Sci. *1970,* 25, 173.
4. HLAVACEK, V. and KUBICEK, M.: "Numerical Solution of Nonlinear Boundary Value Problems with Applications", Prentice-Hall, 1983.
5. KUBICEK, M. and MAREK, M.: "Computational Methods in Bifurcation Theory and Dissipative Structures", Springer-verlag, 1983.
6. ALKIS CONSTANTINIDES: "Applied Numerical Methods with Personal Computers", McGraw-Hill, New York (1987).

HUNGARIAN JOURNAL
OF INDUSTRIAL CHEMISTRY
VESZPRÉM
Vol. 17. pp. 397–402 (1989)

THE EFFECTS OF RAW PHOSPHATE PARTICLE SIZE AND THE INTENSITY OF MIXING ON THE EFFICIENCY OF DIGESTION

M. NAJJAR and F. SZÜCS

(Institute of Inorganic Chemical Technology Veszprém University of Chemical Engineering, P.O. Box 158, H-8201 Veszprém, Hungary)

Received: January 26, 1989

The digestion of raw phosphate of various particle sizes in sulphuric acid-phosphoric acid mixtures has shown that the digestion rate significantly increased with the decrease of the particle size. As a consequence, the duration of digestion required for $a > 95\%$ extraction is about 20 minutes for fine particles (less than 50 μm) and about 320 minutes for coarser ones (under 500 μm). The increase of mixing intensity also shows a favourable effect. Some 12% increase in efficiency was observed with increased mixing intensity after a digestion time of 320 minutes.

Introduction

As it is well-known for heterogeneous systems, the contact surface area plays an important role in the sulphuric acid digestion of raw phosphate. The rates of digestion and simultaneous crystallization are determined – among others – by the magnitude of the contacting surface area. Therefore, the conclusion of SLACK [1] – i.e. the digestion time is linearly proportional to the particle size of raw phosphate – seems to be quite reasonable.

As to the wet procedure utilized by industrial plant, raw phosphate with 60% (m/m) under 74 μm is used for making phosphoric acid, while that with 80% under 149 μm is utilized for superphosphate production [1].

Apart from the particle size, the reactivity of the raw material and the digestion technology used are also of high importance. It happens that raw phosphate under 471 μm, or even under 833 μm, can be processed [2]. Some 40% of the raw phosphate processed in the USSR is over 180 μm [3]. E.g. various fractions of phosphorite from Karatau [under 63, 63–100, 100–160, 160–200 and 200–300 μm] were processed by the dihydrate method, and it was found that up to 160 μm the digestion efficiency changed between 93–98% and above this particle size a slight decrease could be observed [4]. At higher particles sizes the

efficiency is around 90%. At the same time, the filterability of the solid residue (phosphogypsum) obtained after digestion goes through a maximum curve in the function of the particle size. The 100–160 μm fraction was found to be optimal.

Under given experimental conditions, the digestion efficiency of Kagarban raw phosphate increased from 82.1% to 98.8% when the particle size gradually decreased (80–100% of the particles were under 177, 149, 105 and 75 μm) [5].

After a digestion time of 15 minutes, the digestion efficiency of Florida raw phosphate fractions of 149–177, 68–88, and 44–53 μm was 68.0%, 99.9%, and 99.9%, respectively [6].

The rate of transport phenomena taking place between the solid and liquid phases is also influenced by the speed difference between the particles and the solution. There should be a correlation between the speed difference and the rotation speed of the mixer. In commercial digesters the homogenization and transfer of the slurry is made by propeller or turbine type mixers with rotation speeds of 400–600/min [7].

The influence of mixer rotation speed and the particle size on the digestion efficiency was investigated in connection with extraction phosphoric acid production using Syrian raw phosphate.

Raw Material

The composition of the raw phosphate used is shown in *Table 1*. The density is 2.95 g/cm^3, while the specific surface area is 24.9 m^2/g. The original raw material (having a particle size range of 0–500 μm) was separated into five fractions of different particle sizes. The amounts and particle size ranges of the original material and the fractions are shown in *Table 2* together with the specific surface areas and the phosphorus pentoxide and calcium oxide concentrations.

Table 1.

Composition of the phosphate rock

Component	Content, m/m%
P_2O_5	34.06
CaO	51.21
Fe_2O_3	0.25
Al_2O_3	0.35
MgO	0.40
SiO_2	2.12
SO_3	1.80
F	3.81
Cl	0.075
Moisture	1.30
Loss on ignition	6.70

Table 2.
Characteristic features of the individual fractions

Specific surface area (BET), m^2/g	Particle size μm	Amount of the fraction, m/m%	P_2O_5 m/m%	CaO m/m%
34.00	0–56	18.90	33.57	50.07
27.60	56–125	22.90	34.22	51.32
23.90	125–200	16.90	33.89	51.98
17.40	200–315	34.20	34.30	52.07
20.13	315–500	7.10	34.12	51.95
24.80	0–500	100.00	34.03	51.21

Experimental Method

The experiments were made under laboratory conditions in a flask having a reflux condenser and a mixer. The digestion temperature was controlled to 75 ± 1 °C by means of an ultra-thermostat. The raw phosphate was digested with an acid mixture containing phosphoric acid (20% P_2O_5) and sulphuric acid (its amount was calculated from the CaO content). Analytical grade reagents were used. A liquid-solid ratio of 5 : 1 was used during the digestion process. The rotation speed of the mixer was 500/min for the fractions, while rotation speeds of 500/min, 375/min, and 250/min were used for the digestion of the original raw phosphate.

Samples taken during the reaction at various time intervals were filtered and the solid residues washed with acetone and dried. The filtrate and solid residue were analyzed. The analyses were carried out by titrimetric, photometric, gravimetric, and atomic absorption methods, taking into consideration – where it was possible – the specifications of the (HUNG. Stand. 1426–78). The digestion efficiency was calculated from the analytical results, using the equation proposed by POZIN [3].

Experimental Results

The digestion efficiency obtained for the starting material of given particle size as a function of the digestion time is shown in *Table 3.*

Table 3.
Digestion efficiency of the raw phosphate rock with different particle size, m/m%

Particle size μm	Specific surface area m^2/g	Time, min.						
		5	10	20	40	80	160	320
0–56	34.00	78.87	86.76	95.59	–	–	–	–
56–125	27.60	33.85	41.80	51.54	66.97	79.60	88.56	97.10
125–200	23.90	14.55	21.12	29.94	40.97	55.78	77.34	94.83
200–315	17.40	8.79	12.73	20.39	26.23	36.08	51.65	76.67
315–500	20.13	10.24	15.85	23.18	32.61	45.54	64.15	89.43
0–500	24.90	31.25	38.56	46.94	55.95	72.22	86.36	94.63

Table 4.

Digestion efficiency, m/m%

Number of revolutions of the stirrer, l/min.	Time, min.						
	5	10	20	40	80	160	320
250	30.19	35.66	39.92	47.65	58.58	70.15	82.77
375	30.50	36.45	43.65	52.64	63.50	78.00	88.31
500	31.25	38.65	46.94	55.95	72.22	86.36	94.63

The effect of the change of the stirrer rotation speed is shown in *Table 4*. The particle size of the starting material was between 0–500 μm.

Results and Discussion

Of the fractions obtained from the raw phosphate (< 500 μm) by sieving, the 200–315 μm (relatively coarse) fraction is of the highest quantity (see *Table 2*). Although the specific surface area decreases with the increase of the particle size, the 200–315 μm fraction has the lowest value. A higher specific surface area belongs to the largest particles (315–500 μm). It can be assumed that these particles contain more pores than the smaller ones.

Particles of different sizes have practically the same phosphorus pentoxide and calcium oxide contents. This can be explained by the fact that fractionation was made after grinding the raw phosphate instead of sieving the original raw material of natural particle size distribution.

The change of the digestion efficiency in the function of time obtained for starting materials of different specific surface areas is shown in *Fig. 1*.

Under the experimental conditions used a high digestion rate and an efficiency of over 95% could be obtained after 20 minutes for the < 56 μm fraction

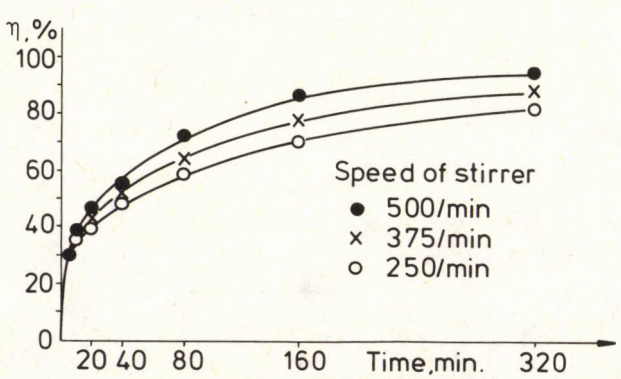

Fig. 1.
The change of digestion efficiency for raw phosphate of different specific surface area (Temp.: 75 °C; L/S = 5 : 1).

(the specific surface area is 34.0 m^2/g). The digestion rate decreases with the decrease of the specific surface area (with the increase of the particle size). As to the 200–315 μm fraction, which has the lowest specific surface area, the digestion efficiency is only 76% even after 320 min. The digestion curve of the original raw phosphate – in accordance with its specific surface area – is located between the curves obtained for the 56–125 and the 125–200 μm fractions. The higher specific surface area can reduce the thickness of the solid reaction product layer, while the lower particle size can shorten the diffusion path length of the reagent in the pores.

The presence of calcium-sulphate hemihydrate and anhydrite in the digestion residue is confirmed by X-ray diffraction. The crystallization of the hemihydrate is characteristic of the early stage of the digestion process (up to about 40 minutes). After a reaction time of 320 min. the recrystallization of the hemihydrate to anhydrite is practically complete. As to the 0–56 μm fraction, anhydrite already begins to form during the fast digestion stage, and after 20 min. the residue contains anhydrite only. In the case of the 56–125 μm fraction, the complete conversion of the hemihydrate takes place after 160 min. The difference in the recrystallization rate is probably due to the different acid concentration of the solution.

The change of the digestion efficiency in the function of time at different stirring speeds is shown in *Fig. 2*. It seems that the increase of the mixing speed

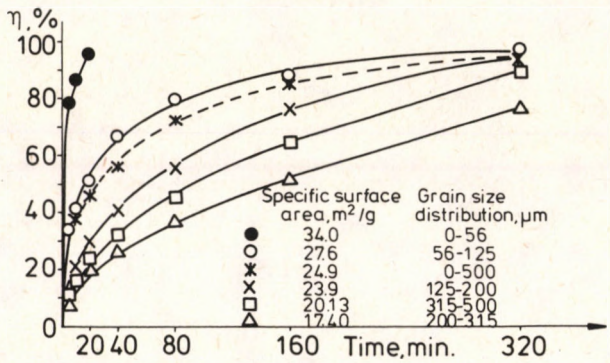

Fig. 2.
The change of digestion efficiency with time at different mixer speeds (particle size: 0–500 μm).

can increase the rate of the transport processes – i.e. the transport of hydrogen ions to the surface of the raw phosphate particles and that of the calcium ions to the bulk of the solution. As a result, the rate of surface crystallization, or the thickness of the calcium sulphate layer is decreased (or the porosity of the layer increased).

Summary

The digestion of Syrian raw phosphate of different particle sizes (< 56, 56–125, 125–200, 200–315, and 315–500 μm) was investigated in a sulphuric acid – phosphoric acid mixture with a P_2O_5 concentration of 20% m/m at 75 °C. No significant differences were found among the main characteristics (e.g. the CaO and P_2O_5 contents) of the raw phosphate fractions.

The digestion rate and, accordingly, the digestion efficiency vs. time increased with the decrease of the particle size. A close correlation can be found between the digestion rate and the specific surface area of the raw material. The phosphorus content of the lowest particle size fraction – having the highest specific surface area – could be digested after 20–40 minutes under the experimental conditions used.

The lowest digestion rate was observed for the 200–315 μm fraction (having a specific surface area of 17.4 m^2/g). The digestion efficiency after 320 minutes was 76–77%.

The digestion rate could also be increased by increasing the intensity of mixing. The rate difference obtained by improved mixing is especially remarkable after prolonged digestion times (more than 40 min). Doubling the rotation speed of the mixer increased the efficiency of the digestion from 82–83% to 94–95% after a time of 320 minutes.

REFERENCES

1. SLACK, A. V.: Phosphoric Acid. Vol. 1. Marcell Dekker Inc. New York, 1968. p. 123. Production of Wet-Process Phosphoric Acid.
2. HIGNETT, T. P.: 2nd International Congress on Phosphorus Compounds Proceedings. Boston USA 1980. p. 401–429.
3. POZIN, M. E.: Fertilizer Manufacture. MIR. Publ., Moscow, 1986. p. 120.
4. BUHMAN, P. A., YAKUBOV, R. YA. i KAMALOV, K. M.: Usb. Khim. Zhurn. *1984,* 5, 67–70.
5. ISHAGUE M. and AHMED, I.: Fertilizer News (New Delhi) *1980,* 25. (8) 33–39.
6. GILBERT, R. L. and MORENO, E. C.: Ind. Eng. Chem. Proc. Design and Dev. *1965,* (4) 368–371.
7. KOPILEV, B. A.: Tekhnologiya ekstrakcionnoy fosfornoy kisloti. Khimiya, Leningrad 1981. p. 74.

HUNGARIAN JOURNAL
OF INDUSTRIAL CHEMISTRY
VESZPRÉM
Vol. 17. pp. 403–414 (1989)

CUBIC EQUATIONS OF STATE IN PROCESS SIMULATION CONTEXTS

R. P. STATEVA, CHR. BOYADJIEV and S. G. TSVETKOV

(Institute of Chemical Engineering, Bulgarian Academy of Sciences,
Sofia 1040, BULGARIA)

Received: February 2, 1989

A new method for organizing the equation of state (EoS) model in a process simulator is presented. It physically implements reasonable criteria for identifying a root of the EoS as corresponding to a liquid or a vapour phase volume and uses an unified approach to estimate the volume and derived properties at infeasible, for a given phase, and pressure specifications.

Introduction

A strategy, widely used for organizing process simulators, proved to be most satisfactory for implementing an equation of state (EoS) technique for calculating thermophysical properties. The two levels of the process simulator – the higher with the simulation algorithms and the lower with EoS model – typically interact through changing, with each iteration, the values of the temperature and composition of the specified phase (liquid and/or vapour) and through a specified pressure. Quite often, because of iterative excursions, the pressure specifications can become infeasible according to the equation of state being used and suitable decisions have to be taken. They can become a responsibility either of the higher level algorithms, as discussed in HURON et al. [6], ASSELINEAU et al. [1], MILLS et al. [10] or of the EoS model – POLLING et al. [11] and MATHIAS et al. [7]. As pointed out by MATHIAS et al. [7] the second approach is more suitable and effective. Thus the EoS model has to be organized in such a way as to allow: supplying at all conditions values for the volume and the derived properties, corresponding unequivocally to the phase specified; recognizing and handling infeasible specifications. There are several excellent methods for determining a solution of the EoS with specifications (T, P, x) such as that of GUNDERSEN [5] for a cubic EoS, MILLS et al. [10] for the BWRS EoS, and MATHIAS et al. [7] for any type of EoS, etc. The problems of unequivocally identifying a root of the EoS as corresponding to a liquid or a vapour phase

and providing estimates of the solution to the higher level algorithms when the pressure specifications lie outside the feasible region, though much more challenging, have still received limited attention in literature (ASSELINEAU et al., [1], GOSSET et al., [3], POLLING et al, [11], VEERANNA and RIHANI, [18], SANDLER and DODD, [13]). A new method for organizing the EoS model in a process simulator, providing solutions to the above problems, is presented here. The development of the ideas will be realized based on the example of the cubic EoS (CEoS). For convenience, we assume that the pressure is the specified parameter. Solving a CEoS for a liquid or a vapour mixture volume leads to two separate problems – the liquid and the vapour phase problem, of which the first will be discussed in detail.

The Liquid Phase Problem

Three subproblems exist here, depending on the current value of the temperature. The first treats cases when it is below the pseudocritical temperature of the mixture. The isothermal $(P-v)$ correlations are of the van der Waals type and iterative second order Newton methods prove to be quite satisfactory for finding a solution of the CEoS. A root of the CEoS, corresponding unequivocally to a volume of the liquid phase, satisfies the inequality $b_m < v_1 < v_{pc}$ (ASSELINEAU et al., [1]). Part of this interval includes volume values for wich the mechanical stability criterion (ROWLINSON, [12]) is not satisfied. Additional narrowing of the region of feasible solutions is suggested, requiring:

$$b_m < v_1 < v_{lim} \tag{1},$$

where v_{lim} is the maximum feasible value of a liquid molar volume satisfying the mechanical stability criterion. An initial guess for the iterative procedure is determined from $v_0 = (v_{pc} + b_m)/2$ and compulsory $\left(\frac{\partial P}{\partial v_0}\right)_{T,\,x} < 0$ is checked. If it is violated, a new guess is found from $v_0 = (b_m + v_0)/2$. The iterative procedure converges either quickly to a feasible solution, usually in two-three iterations, or to the stationary point of the isotherm, for which the conditions:

$$\left(\frac{\partial P}{\partial v}\right)_{T,\,x} = 0 \quad \text{and} \quad \left(\frac{\partial^2 P}{\partial v^2}\right)_{T,\,x} > 0 \tag{2}$$

hold. Thus it identifies the minimum value of the pressure $P = P_{lim}$ for which a solution of the CEoS, corresponding to a liquid molar volume, can still be found. Consequently, an infeasible pressure specification is recognized if it satisfies the inequality:

$$O < P_{spec} < P_{lim} \tag{3}$$

The second subproblem includes cases when the temperature is above the pseudocritical, but below the true critical temperature of the liquid phase. The isothermal $(P-v)$ correlations are degenerated and the region of feasible CEoS solutions can no longer be characterize through condition (1). Taking into consideration the monotonous character of the isotherms and that for a given

mixture along its equilibrium dome the liquid volume is always smaller than that at the critical point, while the true critical volume is smaller than the pseudocritical, a solution of the CEoS, corresponding unequivocally to a liquid molar volume satisfies the condition:

$$b_m < v_1 < v_{TC} \tag{4}$$

A CEoS solution, predicted in this temperature region, corresponds to (or is consistent with) the volume of a liquid mixture – either subcooled or equilibrium. Even in cases when it lies inside the diffusional stability dome, it reflects the expected volumetric behaviour of a liquid mixture and will not destabilize the performance of a higher level algorithm. Finally, such solutions are continuous in the thermodynamic phase space. A modified SECANT method is used and it converges to the desired solution in 4–6 iterations, provided the pressure specifications are in the feasible region. An infeasible pressure specification satisfies the inequality $0 < P_{spec} < P_{lim}$, where P_{lim} can be calculated directly from the CEoS (for example, that of Soave–Redlich–Kwong; (SOAVE, [16]):

$$P_{lim} = \frac{RT}{v_{TC} - b_m} - \frac{a(T)}{v_{TC}(v_{TC} + b_m)} \tag{5}$$

The third subproblem treats situations occurring when a higher level algorithm requires from the EoS model a liquid molar volume at a temperature higher than the liquid phase true critical temperature or when a solution to a vapour-liquid equilibrium problem has converged to a supercritical, for the equilibrium liquid phase, temperature. Such situations require reliable means of determining in the first case, whether at the specified pressure a root of the CEoS, corresponding to the volume of a liquid phase, can be found and of recognizing whether the corverged solution is an unfortunate result of the EoS predictions, in the second. There is a physical reasoning behind such investigations, as some strongly asymmetric mixtures can have bubble points at temperatures and pressures higher than their true critical temperature and pressure, which, according to Kuenen's classification speaks of retrograde behaviour of the second type. As shown by STATEVA et al. [17] a vapour-liquid equilibrium at a temperature higher than the liquid phase true critical temperature is possible only if the equilibrium liquid phase exhibits type II retrograde behaviour. This, though, is only a necessary, but not a sufficient condition. The whole complex of reasons, providing such phenomenon, and its nature (kinetic or thermodynamic) are not known or very poorly understood at this point. Here we are concerned only with some qualitative aspects of the problem.

In the first case, a solution of the CEoS can be accepted as corresponding to a liquid molar volume if it is in the interval $b_m < v_1 < v_{TC}$ provided the pressure specification is in the feasible region, i.e. $P_{spec} > P_{lim}$, where P_{lim} is determined from (4). In this temperature region almost any method performs well (the isotherms are near linear) and the CEoS solutions determined define the volume of a liquid phase or of a fluid with a liquid like volume. The latter will not diverge a higher level algorithm from its progress to the solution.

In a case of a vapour-liquid equilibrium problem, converged to a temperature, higher than the liquid phase true critical temperature, the solution can be accepted only if: i) the liquid phase cricondentherm temperature Tct is a bubble point temperature (characterizing type II retrograde behaviour) and ii) the equilibrium temperature and pressure satisfy the conditions $T_{TC} < T_{eq} < T_{ct}$ and $P_{lim} < P_{eq} < P_{cb}$, respectively, as the liquid-vapour equilibrium is bounded on pressure by the cricondenbar pressure – P_{cb} and on temperature – by the cricondentherm temperature. A helpful observation is that mixtures of almost equimolar composition and mixtures of close boiling components or symmetric mixtures usually have their critical points located between the cricondenbar and cricondentherm points and in such cases the solutions can be discarded as false. However, without at least calculating the true critical point of the mixture it is difficult to provide sufficient grounds for accepting a solution or not.

To topologically demonstrate this, the P–T–x diagram of a two component asymmetric mixture (components A and B) will be considered *(Fig. 1)*. It is believed that a continuous vapour-liquid critical locus exists for such mixtures, connecting the critical points of the pure components and that the (T_c, x) correlation is convex and in many cases sigmoid (ROWLINSON, [12]). The true critical points of mixtures I, II and III with composition, respectively x_I, x_{II}, x_{III}, are denoted by $(CP)_I$, $(CP)_{II}$, $(CP)_{III}$. A liquid phase (mixture I) with composition β on the x_I co-ordinate, demonstrates type II retrograde behaviour and is in equilibrium, at $P = P_{spec}$, with a vapour phase (mixture II), determined by point D on the x_{II} co-ordinate (following WICHTERLE, [19]). The equilibrium point is

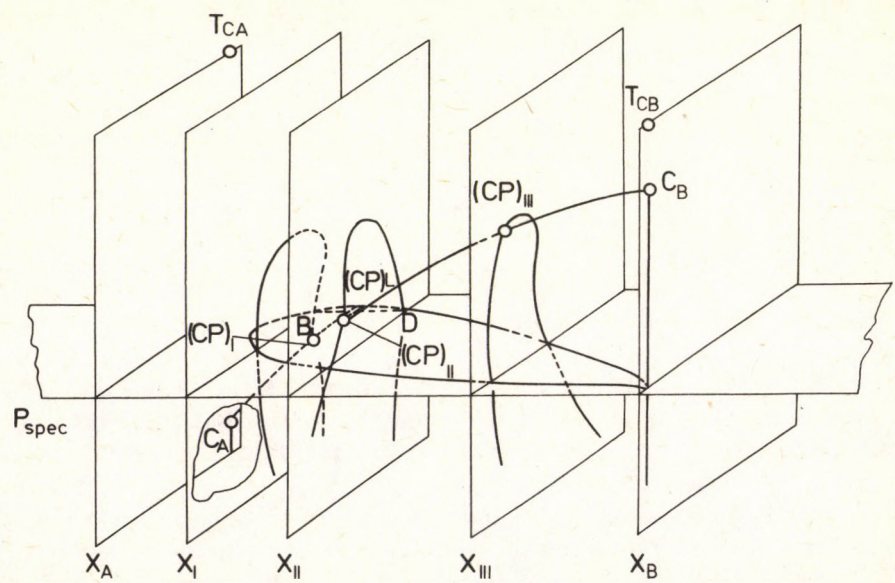

Fig. 1.
The P–T–x diagram of a strongly asymmetric mixture

characterized by a Teq and a Peq, for which $T_{eq} > (T_{TC})x_I$, $P_{eq} = P_{spec} > (P_{TC})x_I$ hold. The intersection of the critical locus and the x–y–T diagram corresponds to the critical point CP_L. The (Tc, x) correlation is sigmoid and can be written $(T_{TC})x_I < T_{eq} < (T_{CP})_L < Tc_A$.

The Vapour Phase Problem

Two subproblems are identified here – the first deals with cases when the current temperature is below the pseudocritical of the vapour mixture and the second – when it is above it. Solutions of the CEoS corresponding unequivocally to the volume of a vapour mixture lie in the interval $v_{lim} < v_v$, where v_{lim} is determined from:

$$\left(\frac{\partial P}{\partial v}\right)_{T,\,y} = 0 \quad \text{and} \quad \left(\frac{\partial^2 P}{\partial v^2}\right)_{T,\,y} < 0 \tag{6}$$

in the first case and v_{lim} equals the true critical volume in the second. Infeasible pressure specifications are recognized if:

$$P_{spec} > P_{lim} \tag{6a}$$

where P_{lim} satisfies (6) in the case of a temperature below the pseudocritical of the vapour phase or is otherwise determined from (5).

Handling Infeasible Specifications

Once an infeasible pressure specification is recognized, the behaviour of the liquid phase in the thermodynamic (P–T–x) phase space is simulated on the EoS level through a pseudocomponent for which the (P–T–x) relationship is given: with the original equation of state in the interval $(b_m - v_0)$, a quadratic spline of the form $a_0 + a_1 v + a_2 v^2$ in the interval $(v_0 - v^*)$, a cubic spline of the form $Ao + A_1 v + A_2 v^2 + A_3 v^3$ in the interval $(v^* - v'')$ and with the original equation of state in the interval $(v'' - \infty)$, where v_0 is an arbitrary chosen value in the interval of feasible for the CEoS solutions, v^* is the volume of the pseudocomponent at $P = P_{spec}$ and v'' is the pseudocritical volume at $T < Tpc$ or the true critical volume at $T > Tpc$. The new model yields an accurate prediction of the volumetric properties as well as accurate derivatives of pressure to mole fractions and can supply values for the volume and the derived properties to the higher level algorithms. The equation $P_{spec} = a_0 + a_1 v + a_2 v^2$ is solved for a v^*, satisfying (1) or (4). The coefficients a_0, a_1, a_2 are determined by matching P and $\frac{\partial P}{\partial v}$ at p. (v_0, P_{calc}) and by requiring that $P = 0$ at $v = v_{lim}$, where v_{lim} satisfies (2) at $T < Tpc$ *(Fig. 2)* or $v_{lim} = v_{TC}$, at $T > Tpc$ *(Fig. 3)*.

Fugacity coefficients are very important thermodynamic properties as almost

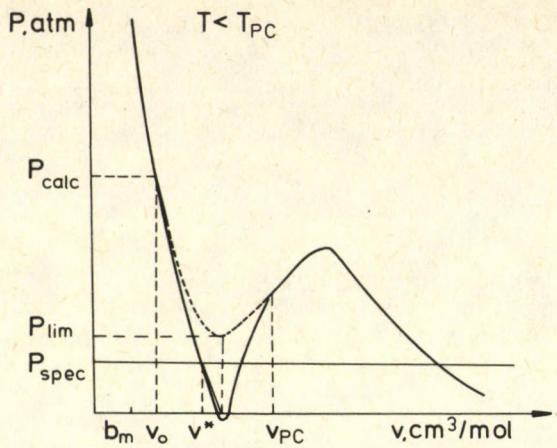

Fig. 2.
The P–v correlation of a pseudocomponent at $T < Tpc$ a simulated by the liquid model (full line). The dashed line represents a portion of the original P–v isotherm

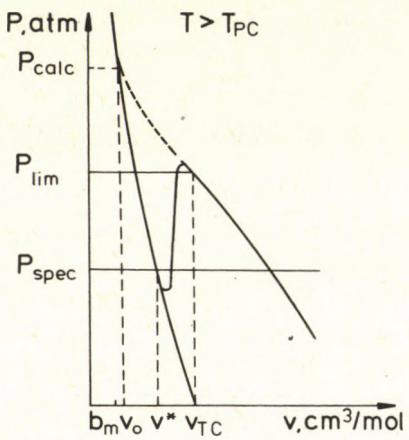

Fig. 3.
The P–v correlation of a pseudocomponent at $T > TTC$ simulated by the liquid model (full line)

all derived properties can be quite easily determined from them. That is why it is imperative to have a reliable and efficient technique estimating them at infeasible specifications of the pressure. The new model of the liquid phase transfers the earlier infeasible pressure specifications into feasible, at the same time retaining the restrictions of the original EoS and thus allows the standard thermodynamic relationship to be used for calculating the fugacity coefficients (written for one mole. MICHELSEN, [9]):

$$\ln \varphi i^*_{v*} = \frac{\partial}{\partial x_i}\int_{v*}^{\infty}\left(\frac{P}{RT}-\frac{1}{v}\right)dv - \ln Z^* = \frac{\partial}{\partial x_i}\left\{\int_{v*}^{v''}\left[\frac{A_0+A_1+A_2v^2+A_3v^3}{RT}-\right.\right.$$
$$\left.\left.-\frac{1}{v}\right]dv+\int_{v''}^{\infty}\left(\frac{P}{RT}-\frac{1}{v}\right)dv\right\}-\ln Z^* \qquad (7)$$

where:

$$\frac{\partial}{\partial x_i}\left[\int_{v''}^{\infty}\left(\frac{P}{RT}-\frac{1}{v}\right)dv\right] = \ln \varphi i_l(v'')+\ln Z(v'') \qquad (7a)$$

and can be calculated directly. The coefficients A_0, A_1, A_2, A_3 are determined by matching P and $\dfrac{\partial P}{\partial v}$ at p.p. (v^*, P_{spec}), (v_{pc}, P_{pc}) at $T < Tpc$ and at the p.p. (v^*, P_{spec}), (v_{lim}, P_{lim}) at $T > Tpc$. The differentiation of the first integral is carried out numerically, because of the rather complicated dependence of the Ai coefficients on composition. As our model is a valid representation of the behaviour of a liquid phase, the derived property $\ln \varphi^*_{i_l}$ should also be accurate.

The idea outlined in the previous section could successfully be used to simulate the behaviour of a vapour phase in the thermodynamic (P–T–y) phase space. However, taking into consideration that a solution of the CEoS, corresponding unequivocally to a volume of a vapour phase satisfies (6), the model can be simplified. Thus, when an infeasible pressure specification is recognized on an EoS level, the behaviour of a pseudocomponent with composition y and at temperature T is simulated through the relationship:

$$P = F/(v-v_{lim})+c_0+c_1v \qquad (8)$$

in the interval ($v_{lim}-v_0$) and through the original CEoS in the interval ($v_0-\infty$) *(Fig. 4)*. The coefficients c_0, c_1 determined by matching P and $\dfrac{\partial P}{\partial v}$ at the p. (v_0, P_{calc}), where v_0 is an arbitrary chosen value among the feasible, for the CEoS, solutions. The coefficient F, from empirical investigation, is accepted as 1000. This model yields an accurate prediction of the volumetric properties of a vapour phase in the whole region of changing pressures from zero to infinity and hence the derived propertly $\ln \varphi i^*_v$, calculated using the standard thermodynamic relationship, should also be accurate:

$$\ln \varphi i^*_v = \frac{\partial}{\partial y_i}\int_{v*}^{\infty}\left(\frac{P}{RT}-\frac{1}{v}\right)dv - \ln Z^* = \frac{\partial}{\partial y_i}\left\{\int_{v*}^{v0}\left[\frac{F/(v-v_{lim})+c_0+c_1v}{RT}-\right.\right.$$
$$\left.\left.-\frac{1}{v}\right]dv+\int_{v0}^{\infty}\left(\frac{P}{RT}-\frac{1}{v}\right)dv\right\}-\ln Z^* \qquad (9),$$

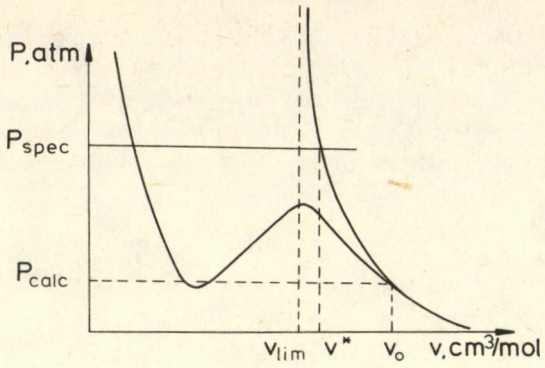

Fig. 4.
The P–v correlation of a pseudocomponent simulated by the vapour model

where:

$$\frac{\partial}{\partial y_i}\left[\int_{v^0}^{\infty}\left(\frac{P}{RT}-\frac{1}{v}\right)dv\right] = \ln \varphi i_v(v_0) + \ln Z(v_0) \tag{9a}$$

and can be calculated directly, while the differentiation of the first integral is carried out numerically.

The functional relationships for $\ln \varphi i_l^*$ and $\ln \varphi i_v^*$ can be further differentiated numerically with respect to temperature, pressure and compositon.

Results and Discussion

The method presented here is embodied in the EQUILIBRIA process simulator (BANCHEVA et al., [9]), where it is constantly addressed by all higher level algorithms available. The method was extensively tested and proved to be reliable, robust and efficient. It is not claimed that it is a panacea in all possible cases, occurring in a process simulation, but usually it greatly helps and promotes convergence of higher level algorithms.

The discussed method concerns only organizing the EoS model in a process simulator, not the higher level algorithms, and it will be wortwhile to compare its efficiency with the efficiency of existing analogues. However, such data, as memory requirements and computational time, are either not published or the data reported concern a higher level algorithm. We shall, however, use the example discussed in MATHIAS et al. [7] to demonstrate and compare the ability of the method to provide trustworthy derived properties (fugactiy coefficients) at infeasible pressure specifications. The fugacity coefficients of the components in an equimolar ethane-n-heptane mixture in the liquid and vapour phase at a temperature below the pseudocritical and above the true critical of the mixture are shown in *Fig. 5* and *6*. In both cases, the pseudofugacity coefficients calculated at infeasible pressure specifications are continuous with the true values and promote the convergence of the higher level algorithms. For both

components in the liquid and for the n-heptane in the vapour phase they follow the trend, as the pressure changes, of the true values. However, the pseudofugacity coefficient of ethane in the vapour phase at $T=420$ K does not quite correspond to the truly observed, the deviations being more pronounced at pressures far removed from the maximum feasible value of the specified ($P_{lim}=26.34$ atm). However, this does not influence the orderly progress towards a solution of the higher level algorithms.

A second example, demonstrating the workability of the method in a phase equilibrium calculation, is shown in *Fig. 7*. The P–T diagram of a nitrogen-pentane binary (17.1 mol percent nitrogen) is predicted with the Soave–Redlich–Kwong EoS (the binary coefficient $k_{ij}=0.0793$). The quite unusual phase behaviour generated fairly well fits the experimental data of SCHINDLER et al. [15] and GROUSLO et al. [4] with the exception of the low temperature region, where the deviations are considerable. However, it is felt that the predicted behaviour is reasonable, because i) of some previous experience with nitrogen – hydrocarbon

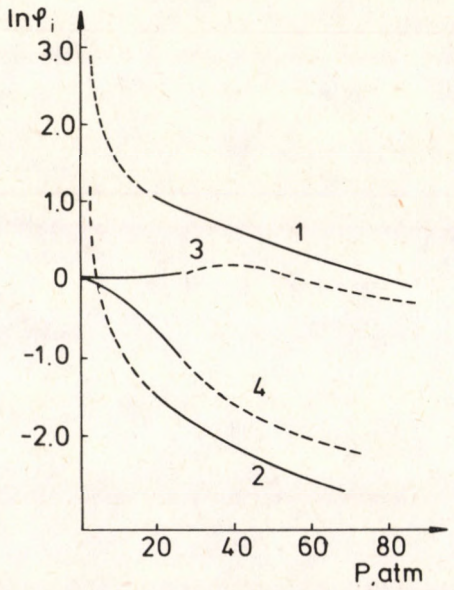

Fig. 5.

Fugacity coefficients of an equimolar ethane-n-heptane mixture at 420 K. The full lines show the true values. 1 – fugacity coefficient of ethane in the liquid phase; 2 – fugacity coefficient of n-heptane in the liquid phase; 3 – fugacity coefficient of ethane in the vapour phase; 4 – fugacity coefficient of n-heptane in the vapour phase

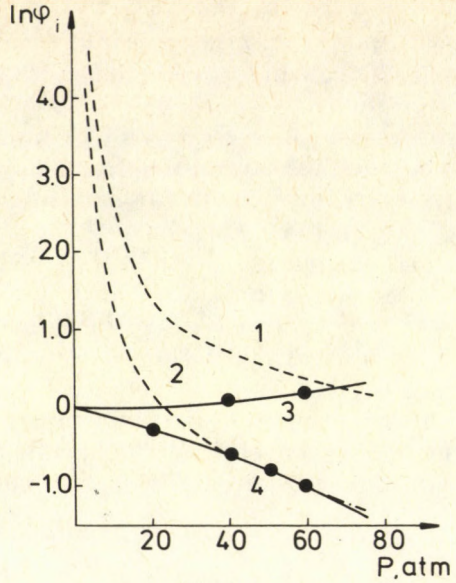

Fig. 6.
Fugacity coefficients of equimolar ethane-n-heptane mixture at 500 K. Full lines show those in the vapour phase, dashed – pseudofugacity coefficients in the liquid phase

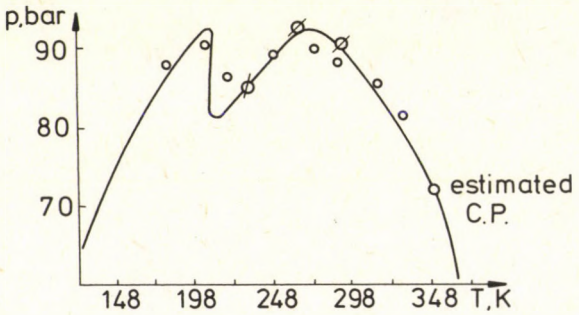

Fig. 7.
P–T diagram of nitrogen-propane mixture (17.1 mol% nitrogen), predicted by the Redlich–Kwong–Soave EoS
Ø – experimental data by GRAUSLO et al., [4]
○ – experimental data by SCHINDLER et al., [15]

mixtures, demonstrating multiple bubble points and ii). our estimated true critical point (using the rigorous method, proposed by MICHELSEN and HEIDEMANN, [9], for calculating the true critical temperature and volume, and by SCHICK and PRAUSNITZ, [14], for estimating the true critical pressure) falls in line with the phase envelope.

The method described here physically implements reasonable criteria for identifying a root of the CEoS as corresponding to the volume of a liquid or vapour phase. It uses a unified approach to estimate the volume and derived properties infeasible pressure specifications for a given phase and does not need any additional correlations to keep up with the tendency of the true values. The method does not require expensive calculations, because the functional relationships simulating the behaviour of the pseudocomponents are of the lowest possible order and their integration and numerical differentiation are quite simple.

Acknowledgement

This work was completed with the financial assistance of the Ministry of Culture and Science, under grant No. 162.

SYMBOLS

bm	van der Waals volume
k_{ij}	binary interaction parameter
P	pressure
R	universal gas constant
T	temperature
v	molar volume
x, y	component mole fractions in the liquid, vapour phase
Z	compressibility factor

Greek symbols

φ_i	fugacity coefficient, component i

Subscripts

calc	calculated from the CEoS
cb	cricondenbar
ct	cricondentherm
eq	equilibrium
l	liquid
lim	limiting value
pc	pseudocritical
spec	specified value
TC	true critical
v	vapour
*	value of a parameter at the point of the solution

REFERENCES

1. ASSELINEAU, L., BOGDANIC, G. and VIDAL J., Fluid Phase Equilibria, *1979* 3, 273–290.
2. BANCHEVA, IV. and STATEVA, R. P.: Organizing thermophysical properties calculation in a process simulator, Proc. IV Mediterranean Congress on chemical engineering, *1987*. v. II: 540–542.
3. GOSSET, R., HEYEN, G. and KALITVENTZEFF, B.: Fluid Phase Equilibria, *1986* 25 (1), 51–61.
4. GRAUSLO, L., FREDENSLUND, A. and MOLLERUP, J.: Fluid Phase Equilibria *1977* 1, 13–26.
5. GUNDERSEN T.: Computers and Chem. Engineering *1982* 6, 246–255.
6. HURON, M. J., DUFOUR, G. N. and VIDAL, J.: Fluid Phase Equilibria, *1978* 1, 247–265.
7. MATHIAS, P. M., BOSTON, J. F. and WATANASIRI, S.: AIChE J. *1984* 30 (2), 182–186.
8. MICHELSEN, M. L., "Partial Derivaties of Thermodynamic Properties from EoS", SEP 8109. *1981*.
9. MICHELSEN, M. L. and HEIDEMANN, R. A.: AIChE J. *1981* 27 (3), 521–523.
10. MILLS, M. B., WILLS, M. J. and BHIRUD, V. L.: AIChE J. *1980* 26, 902–910.
11. POLLING, B. E., GRENS, E. A. and PRAUSNITZ, J. M.: Thermodynamic properties from a cubic equation of state: Avoid trivial roots and and spurious derivatives. Ind. Eng. Chem. Process Des. Dev., *1981*, 20, 127–130.
12. ROWLINSON, J. S.: "Liquids and Liquid Mixtures", 2 ed., Plenum Press, New York, 1969.
13. SANDLER, ST. I. and DODD, L. R.: *1986*, 36, 313–316.
14. SCHICK, L. M., and PRAUSNITZ, J. M.: AIChE J. *1968* 14, 673.
15. SCHINDLER, D. L., SWIFT, G. W., and KURATA, F.: Hydrocarbon Process *1986* 11, 205.
16. SOAVE, G.: Chem. Eng. Sci. *1972* 27, 1197–1203.
17. STATEVA, R. P., BANCHEVA, IV. and BOYADJIEV, CHR.: Efficient algorithm for calculating vapour-liquid equilibrium. Hung. J. Ind. Chem. *1985*, 13, 301–310.
18. VEERANA, D. and RIHANI, D. N.: Fluid Phase Equilibria *1984* 16, 41–55.
19. WICHTERLE, I.: Fluid Phase Equilibiria, *1977*, 1, 161–172.

Guide for authors

The "Hungarian Journal of Industrial Chemistry" is a joint publication of the Veszprém scientific institutions of the chemical industry that deals with the results of applied and fundamental research in the field of chemical processes, unit operations and chemical engineering in the form of original articles written in English.

In addition to the scientific workers of the institutions at Veszprém, the Editorial Board of this publication also welcomes articles for inclusion in this periodical, which are written by authors who are engaged in the above mentioned fields.

1. Manuscripts should be sent – in duplicate – to the Editor-in-Chief:

Dr. Endre Bodor
Veszprém University of Chemical Engineering (VVE), P.O.B. 158
H-8201, Veszprém, Hungary

2. *In a brief letter attached to the manuscripts, authors should declare that:*
   a) their work is *original* and *has not previously been published elsewhere in its present format,* and
   b) for the purposes of correspondence, they can be contacted at the address and telephone number which they give.
3. Manuscripts should be typed on paper of A/4 size.

The first page should give the title, the author's name, place of work and a brief summary of the article (maximum of 15 lines).

If possible the article should be presented with an introduction, experiments carried out, conclusions and discussion. Tables and Figures must be presented on separate sheets and their position in the text should be noted on the margin. A summary of the symbols used, and captions of the Figures should be attached separately to the manuscripts.

It is regretted that photographs cannot be included in the periodical.

The Tables and Figures should not exceed an A/4 size. If diagrams are presented, only the explanation and dimensions of the ordinate and abscissa, and marking numbers are required, while further explanatory texts can be given in the captions of the Figures. The equations used should be numbered, and Tables and Figures should be numbered and noted on the margin.

With regard to units, it is essential that an SI (Système International d'Unités) should be used.

4. References should be prepared in the following manner:
   a) Publications which have appeared in periodicals; e.g.

WAKAO, N. and SCHWARTZ, J. M.: Chem. Eng. Sci. *1962,* 17 (3), 825–827.

   b) Books; e.g.

SATTERFIELD, C. N.: Mass Transfer in Heterogeneous Catalysis. MTI Press, Cambridge, Mass., 1951. pp. 26–32.

   c) Patents; e.g.

U.S. Pat. 3,425,442 Brit. Pat. 997,665 Hung. Pat. 553,243

   d) Published lectures; e.g.

HIH, S., HHU, C. and LEECH, W. J.: A Discrete Method to Heat Conduction Problems. 5th International Heat Transfer Conference, Tokyo, 1975. Co. 2.4.

5. Authors receive 50 complimentary copies of their paper.

Editorial Board
Hungarian Journal of Industrial Chemistry

Ára: 300,— Ft

CONTENTS

Egyetemi Nyomda – 89.7454 Budapest, 1989. Felelős vezető: Sümeghi Zoltán igazgató

HUNGARIAN

Journal of

INDUSTRIAL CHEMISTRY

Edited by

the Hungarian Oil & Gas Research Institute (MÁFKI),
the Research Institute for Heavy Chemical Industries (NEVIKI),
the Research Institute for Technical Chemistry of the
Hungarian Academy of Sciences (MÜKKI),
the Veszprém University of Chemical Engineering (VVE).
Veszprém (Hungary)

Volume 17. **1989** **Number 4.**

HU ISSN: 0133–0276
CODEN: HJICAI

The "Hungarian Journal of Industrial Chemistry" is a joint publication of the Veszprém scientific institutions of the chemical industry that deals with the results of applied and fundamental research in the field of chemical processes, unit operations and chemical engineering. The papers are published in four numbers at irregular intervals in one annual volume, in English.

Editorial Office:
Veszprémi Vegyipari Egyetem
"Hungarian Journal of Industrial Chemistry"
H-8201 Veszprém, P.O. Box: 158.
Hungary

Distributor:
KULTURA Foreign Trading Co. H-1389, BUDAPEST, P.O. Box 149. Hungary.

FELELŐS SZERKESZTŐ: DR. BODOR ENDRE H-8201 Veszprém. P.O. Box: 158
KIADJA AZ IDEGENNYELVŰ FOLYÓIRAT KIADÓ LEÁNYVÁLLALAT 1052 BUDAPEST, ALPÁRI GYULA U. 2.
TELEFON: 1189-895
A KIADÁSÉRT FELELŐS: ROÓZ FERENC IGAZGATÓ

HUNGARIAN

Journal of
INDUSTRIAL CHEMISTRY

Edited by

the Hungarian Oil & Gas Research Institute (MÁFKI),
the Research Institute for Heavy Chemical Industries (NEVIKI),
the Research Institute for Technical Chemistry of the
Hungarian Academy of Sciences (MÜKKI),
the Veszprém University of Chemical Engineering (VVE).
Veszprém (Hungary)

Volume 17. **1989** **Number 4.**

HU ISSN: 0133–0276
CODEN: HJICAI

The "Hungarian Journal of Industrial Chemistry" is a joint publication of the Veszprém scientific institutions of the chemical industry that deals with the results of applied and fundamental research in the field of chemical processes, unit operations and chemical engineering. The papers are published in four numbers at irregular intervals in one annual volume, in English.

Editorial Office:
Veszprémi Vegyipari Egyetem
"Hungarian Journal of Industrial Chemistry"
H-8201 Veszprém, P.O. Box: 158.
Hungary

Distributor:
KULTURA Foreign Trading Co. H-1389, BUDAPEST, P.O. Box 149. Hungary.

FELELŐS SZERKESZTŐ: DR. BODOR ENDRE H-8201 Veszprém. P.O. Box: 158
KIADJA AZ IDEGENNYELVŰ FOLYÓIRAT KIADÓ LEÁNYVÁLLALAT 1052 BUDAPEST, ALPÁRI GYULA U. 2.
TELEFON: 1189-895
A KIADÁSÉRT FELELŐS: ROÓZ FERENC IGAZGATÓ

INDEX

Guide for authors

The "Hungarian Journal of Industrial Chemistry" is a joint publication of the Veszprém scientific institutions of the chemical industry that deals with the results of applied and fundamental research in the field of chemical processes, unit operations and chemical engineering in the form of original articles written in English.

In addition to the scientific workers of the institutions at Veszprém, the Editorial Board of this publication also welcomes articles for inclusion in this periodical, which are written by authors who are engaged in the above mentioned fields.

1. Manuscripts should be sent–in duplicate–to the Editor-in-Chief:

Dr. Endre Bodor
Veszprém University of Chemical Engineering (VVE), P.O.B. 158
H–8201, Veszprém, Hungary

2. In a brief letter attached to the manuscripts, authors should declare that:
   a) their work is original and has not previously been publisched elsewhere in its present format, and
   b) for the purposes of correspondence, they can be contacted at the address and telephone number which they give.
3. Manuscripts should be typed on paper of A/4 size.

The first page should give the title, the author's name, place of work and a brief summary of the article (maximum of 15 lines).

If possible the article should be presented with an introduction, experiments carried out, conclusions and discussion. Tables and Figures must be presented on separate sheets and their position in the text should be noted on the margin. A summary of the symbols used, and captions of the Figures should be attached separately to the manuscripts.

It is regretted that photographs cannot be included in the periodical.

The Tables and Figures should not exceed an A/4. size. If diagrams are presented, only the explanation and dimensions of the ordinate and abscissa, and marking numbers are required, while further explanatory texts can be given in the captions of the Figures. The equations used should be numbered, and Tables and Figures should be numbered and noted on the margin.

With regard to units, it is essential that an SI (Système International d'Unités) should be used.

4.References should be prepared in the following manner:

a) Publications which have appeared in periodicals; e.g.

WAKAO, N. and SCHWARTZ, J. M.: Chem. Eng. Sci. *1962,* 17 (3), 825–827.

b) Books; e.g.

SATTERFIELD, C. N.: Mass Transfer in Heterogeneous Catalysis. MTI Press, Cambridge, Mass., 1951, pp. 26–32.

c) Patents; e.g.

U. S. Pat. 3,425,442, Brit. Pat. 997,665 Hung. pat. 553, 243

d) Published lectures; e.g.

HIH, S., HHU, C. and LEECH, W. J.: A Discrete Method to Heat Conduction Problems. 5th International Heat Transfer Conference, Tokyo, 1975. Co. 2.4.5. Authors receive 50 complimentary copies of their paper.

Editorial Board
Hungarian Journal of Industrial Chemistry

Egyetemi Nyomda – 89.7590 Budapest, 1990. Felelős vezető: Sümeghi Zoltán igazgató

HUNGARIAN JOURNAL
OF INDUSTRIAL CHEMISTRY
VESZPRÉM
Vol. 17. pp. 417–436 (1989)

AUTOMATIC pH-CONTROL OF ACIDIC WASTE WATER. EFFECTS OF THE pH-ELECTRODE AND DAMPING TANKS

M. C. PALANCAR, J. M. ARAGON and P. LARDIEZ

(Dept. of Chemical Engineering, Universidad Complutense de Madrid, 28040-MADRID, SPAIN)

Received: July 12, 1988

The automatic neutralization of acidic waste water was studied. The waste-water stream was simulated by aqueous solutions of acetic and propionic acids. The neutralization was made in a continuous stirred tank by means of aqueous solutions of ammonia and sodium hydroxides. The pH was measured by a glass electrode at the output of the tank.
The dynamic response of both the pH-electrode and neutralization tank was measured. Three control algorithms (PID, nonlinear PID and adaptive PID) were used in a computer simulation of the automatic pH-control. It also simulated the damping effects of additional tanks in series. The experimental results showed that the dynamic response of the pH-electrode was strongly nonlinear and can affect the relative stability of the closed loop system. When nonlinear PID action was imposed, the feedback response was away from the usual specifications. The adaptive PID action considerably improves this response. The linear PID action gives acceptable responses, but not as good as the adaptive one. The damping tanks in series (one or two extra tanks) led to responses within control specifications, but the improvements on the relative stability were less important than that given by the adaptive action.

Introduction

According to environment protection normatives, effluent waste water from industrial activities must have a pH within a narrow range of values close to neutrality point. The neutralization plants required for treating acidic waste water are difficult to design, due to the particular characteristics of acid-base processes. In fact, these processes involve instantaneous reactions and have a high gain; moreover, the gain is dependent on the pH itself, being thus a control parameter that is strongly non-linear and time variant.

The design of automatic pH control systems needs a proper model for describing the neutralization process, elements and the subsystems, which constitute the whole system.

In relation to the modellization of the neutralization processes, three main characteristics should be considered:

- There is non-linearity between the pH value and the amount of base added to a given amount of acid (titration curve).
- Different titration curves are obtained for different composition of waste water and the neutralizing alkaline solution.
- Several instantaneous chemical reactions are involved with complex ionic-equilibrium mechanisms.

Some authors [1] assume that the neutralization process is simply a gain element, which is variant with time. From this, the pH is related to the alkali/acid ratio, WR, by the expression:

$$\text{pH} = K \cdot WR$$

where K is a gain, which is depending on the pH. This dependence can easily be simplified by supposing three averaged values of the gain: one for the acidic part of the titration curve (acidic operation gain), an other for the neutralization part of the curve (process gain) and the third for the alkaline part of the titration curve (alkaline operation gain). This model provides a way for treating the system dynamics as a case of linear dynamics. Evidently, it is necessary to know the actual titration curves or the chemical equilibrium equations for calculating the gains of a given process.

For modelling the neutralization plant, two main subsystems should be considered: the reactor and the pH-measuring element. The reactor is commonly one stirred tank followed by one or more tanks, which act as damping elements (to avoid eventual pH oscillations in the final effluent). The geometrical and structural design details of such tanks are well described in literature [2]. They are mainly directed to achieve the ideal behaviour of the reactor (perfect mixing, absence of short-circuiting, and temperature uniformity, etc.).

The pH-measuring element is commonly a pH-electrode. The dynamics of pH-electrodes were studied in profusion [3, 4, 5], but the models proposed are very dissimilar and have a wide degree of complexity. In the most simple ones, the pH-meter is treated as a linear element (first of second order lag). The results of these and other more complex models are usually unsatisfactory, due mainly to the non-linear and asymmetric responses that they generate.

Recently, some dynamic models and algorithms to treat and simulate the behaviour of automatic control of pH were proposed [6–9]. In this work, the neutralization of acidic wastewater streams was studied for obtaining a better knowledge of the influences that the dynamics of pH-electrodes have on the response of a neutralization closed-loop. The neutralization process and the electrode and reactor dynamics were determined experimentally and the closed-loop behaviour was studied by computer simulation (three different control actions were assumed and perturbations on the pH during start-up and steady-state were imposed).

Models

Neutralization Process Model

The system studied in this work involves the following reactions of dissociation:

Acetic acid:	$AcH \rightleftharpoons Ac^- + H^+$
Propionic acid:	$PrH \rightleftharpoons Pr^- + H^+$
Ammonium hydroxide:	$NH_4OH \rightleftharpoons NH_4^+ + OH^-$
Sodium hydroxide:	$NaOH \rightleftharpoons Na^+ + OH^-$
Water:	$H_2O \rightleftharpoons H^+ + OH^-$

The concentrations of ions are:

$$(Na^+) = C_c$$
$$(Ac^-) = C_a/(1+(H^+)/k_a)$$
$$(Pr^-) = C_d/(1+(H^+)/k_d)$$
$$(NH_4^+) = C_b/(1+(OH^-)/k_b)$$

for water: $(H^+)\cdot(OH^-) = 10^{-14}$
where:

$$C_a = \frac{WTA \cdot R_a \cdot D \cdot 500}{M_a \cdot WT}$$

$$C_b = \frac{WTB \cdot R_b \cdot D \cdot 500}{M_b \cdot WT}$$

$$C_c = \frac{WTB \cdot R_c \cdot D \cdot 500}{M_c \cdot WT}$$

$$C_d = \frac{WTA \cdot R_d \cdot D \cdot 500}{M_d \cdot WT}$$

The principle of conservation of charge leads to:

$$\frac{C_a}{1+\frac{10^{-pH}}{k_a}} + \frac{C_d}{1+\frac{10^{-pH}}{k_d}} + 10^{(pH-14)} = \frac{C_b}{1+\frac{10^{(pH-14)}}{k_b}} + C_c + 10^{-pH} \qquad (1)$$

For a given set of operating conditions (WTA, WTB, WT, R_a, R_b, R_c, R_d) the value of pH in equilibrium can be calculated by Eq. (1). Due to the form of this expression, it should be used with some numerical method. We used the method of the dichotomy (interval halving), which leads to a calculated value of pH in no more than 11 iterations, with an error less than 0.01 pH-units.

The pH of aqueous solutions of several acid-base compositions is shown in *Fig. (1)*. The nine titration curves were calculated by Eq. (1). Each alkaline solution was assumed to be initially formed by equal amounts of sodium and

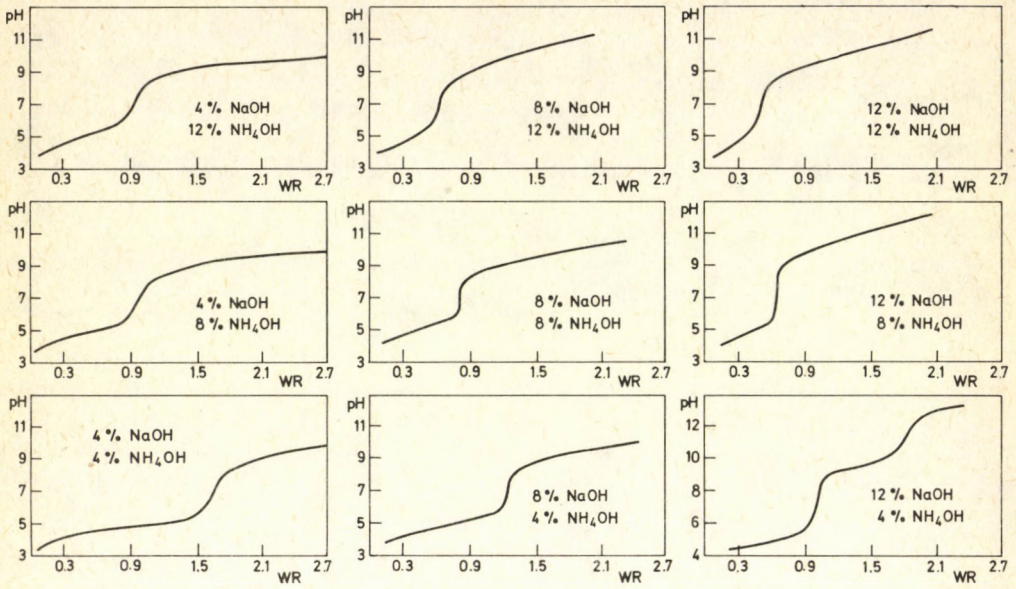

Figure. 1.
Theoretical titration curves

ammonium hydroxides of the weight contents indicated in *Fig. 1* (these percentages refer to the base solutions before being mixed). The titration curves were calculated as pH at equilibrium for a given ratio WR, mass of alkaline solution/mass of acidic solution. The acidic solution was always a mixture of two equal amounts of propionic acid (17%) and acetic acid (20%). The acidic solution then contained 8.5% of propionic acid and 10% of acetic acid (weight percentages). It can be observed from these curves that the neutralization point is affected by the base contents. The values of WR corresponding to the neutralization point ranged between 0.5 (for 12% NaOH-12% NH_4OH) and 1.6 (for 4% NaOH-4% NH_4OH); in the case of 12% NaOH-4% NH_4OH two neutralization points were encountered, one at pH = 7 and the other at pH = 11.

The gains of the system were calculated from these titration curves. Three gains were defined:

· Acidic operation gain: $$K_1 = \frac{7 - \mathrm{pH}}{\mathrm{WRN} - \mathrm{WR}} \tag{2}$$

· Process gain: $$K_2 = \frac{^{\mathrm{pH}}(\mathrm{WRN} + \Delta\mathrm{WR}) - ^{\mathrm{pH}}(\mathrm{WRN} - \Delta\mathrm{WR})}{2\Delta\mathrm{WR}} \tag{3}$$

where ΔWR is a small increment of WR

· Alkaline operation gain: $$K_3 = \frac{\mathrm{pH} - 7}{\mathrm{WR} - \mathrm{WRN}}$$

The calculated values of K_1, K_2 and K_3 for the curves depicted in *Fig. 1* are shown in *Tables 1–3*.

Table 1.

Acidic operation gain, K_1

% NaOH / % NH_4OH	4	8	12
4	1.39	1.74	2.21
8	2.23	2.78	3.26
12	2.89	0.17	3.82

Table 2.

Process gain, K_2

% NaOH / % NH_4OH	4	8	12
4	20.25	34.84	44.70
8	25.50	51.00	59.30
12	41.00	50.00	57.72

Table 3.

Alkaline operation gain, K_3

% NaOH / % NH_4OH	4	8	12
4	0.90	2.00	2.82
8	1.06	1.26	1.93
12	0.96	0.46	2.13

Reactor Modell

The continuous strirred tank reactor, with a behaviour close to the ideal one (perfect mixing, isothermal, constant volume and flow rate), can be described by a first order lag model:

$$C + T_1 \frac{dc}{dt} = K \cdot m \tag{5}$$

where m and C are the input and output variables respectively. In the present case, the input variable m is either the acid or base concentration at the inlet of the reactor, and C is one of these concentrations at the outlet (for perfect

mixing the concentration at the outlet is equal to the concentration inside the tank). For the species involved in this work we have:

Acetic acid: $$C_{al} = C_{ao} - T_1 \frac{dc_{al}}{dt} \quad (6)$$

Ammonium hydroxide: $$C_{bl} = c_{bo} - T_1 \frac{dC_{b1}}{dt} \quad (7)$$

Sodium hydroxide: $$C_{cl} = C_{co} - T_1 \frac{dC_{cl}}{dt} \quad (8)$$

Propionic acid: $$C_{dl} = C_{do} - T_1 \frac{dC_{dl}}{dt} \quad (9)$$

When the system has two or more tanks in series, the concentration of any compound at the inlet of a tank is equal to the concentration at the outlet of the preceding one:

$$C_{i,n} = C_{i,n-1} + T_n \frac{dC_{i,n}}{dt} \quad (10)$$

where i = a, b, c, d
n = 2, 3, ...

The values of concentrations of species are obtained by solving Eq. 6–10 by numerical methods (we used Euler's algorithm). These values were finally used in Eq. (1) to calculate the pH in the tank.

pH-Electrode Model

The dynamics of a pH-electrode are described in literature by several models, none of them is clearly advantageous compared any other. For this reason, we assumed in this work two types of models: one considers that the response of the electrode is instantaneous (electrode dynamics defined simply as a gain element), the second assumes dynamics similar to the dynamics of a first order lag, but with a value of the time constant, which is dependent on the indication of the perturbation (this assumption was confirmed experimentally,as will be seen later). The equation which expresses this dynamics is:

$$pH_1 = pH_T + T' \frac{dpH_1}{dt} \quad (11)$$

where pH_T is the actual pH of the tank content and pH_1 the value of pH given by the pH-meter at the same time. The value of T' is evaluated experimentally from the open loop responses of the system to perturbations on pH.

Controller Model

The automatic control by closed-loop (feedback) involves three main subsystems:

- error detector
- control action
- final actuator

The error detector compares at each instant the measured value of pH with a set point, usually pH = 7. The error is then defined by:

$$E = 7 - \mathrm{pH}_1 \tag{12}$$

The action of a PID controller is:

$$\Delta WR = WR + K_c\left(\mathrm{E} + \frac{1}{T_I} E_I + T_D E_D\right) \tag{13}$$

where E_I and E_D are, respectively, the integral and derivative errors, defined by:

$$E_I = \int_0^t E\, dt \tag{14}$$

$$E_D = \frac{dE}{dt} \tag{15}$$

For a linear PID action, the response signal is only dependent on the error. The controller parameters, K_c, T_I and T_D can easily be estimated, for example, by the Ziegler-Nichols' tuning method [10].

For a non-linear PID action, the proportional gain, K_c, is related with the value of pH. We assumed the following relationships:

Value of pH_1	Value asigned to K_c
2 to 6	K_1
6·1 to 8	K_2
8·1 to 14	K_3

the values of K_1, K_2, and K_3 are given in *Tables 1, 2, 3*.

For an adaptive PID action, the parameters of the controller are the function of both the error and the system parameters. We used Dahlin's method [11] for obtaining such relationships, which are expressed by:

$$T_I = T_1 = \frac{V \cdot D}{WT} \tag{16}$$

$$T_D = T' \tag{17}$$

$$K_c = \frac{WRN - WR}{E} \tag{18}$$

The final actuator element was assumed to be a gain element (gain equal to unity), fitted with two limiting conditions: the actuation signal should be zero if $\Delta WR < 0$, and the integral error, Eq. (14), is made zero when it becomes greater than 1.8 pH untis.

Experimental

The parameters and dynamic constants required for the computer simulation of closed-loop behaviour were obtained experimentally. The study was concerned with the dynamics of the neutralization reactor and pH electrode and with the neutralization process (titration curves).

Neutralization Process

The theoretical curves, *Fig 1,* were confirmed experimentally. The experiments also served to obtain some evidence of collateral phenomena, such as thermal effects, due to the exothermic neutralization reactions, and precipitation of solids under some operating conditions.

The apparatus used in this study is shown in *Fig. 2.* A mixture of 300 g of aqueous propionic acid (17% of acid) and 300 g of aqueous acetic acid (20% of acid) were loaded in the reactor. The resulting mixture contained 8.5% of

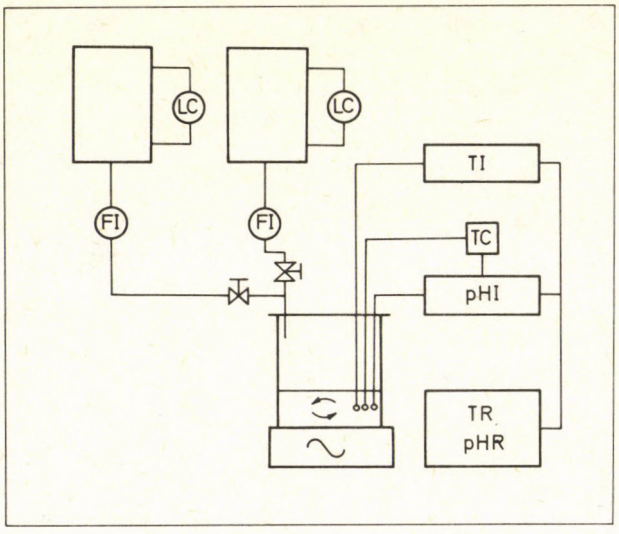

Figure. 2.
Apparatus for the study of the neutralization process. FI: flow rate indicators for acidic and alkaline solutions, TI: temperature indicator, PHI: pH meter with temperature adjustment (TC); TR, PHR: graphic register. The tank is stirred by a magnetic plate.

propionic acid and 10% acetic acid. The temperature and pH were measured continuously during neutralization, which was performed by means of alkaline solutions of sodium and ammonium hydroxides that were slowly fed into the reactor. The flow rates and concentrations of the alkaline solution in the three experimental runs are shown in *Table 4* (the concentrations refer to the solutions in the storage tanks, that is, before its mixing at the reactor inlet). These values

Table 4.
Concentrations and flow-rates of alkaline solutions in the experiments of neutralization.

Exp.	1	2	3
% NaOH	4	4	4
% NH_4OH	4	8	12
Flow Rate (cm^3/min)			
NaOH	23	14	15
NH_4OH	23	14	15

of concentration were selected under the basis of stability criteria, mainly taking into account the process gain values, K_2 calculated from the titration curves of *Fig. 1.*

The good agreement between the theoretical and experimental values of pH can be evaluated from the data shown in *Fig. 3.* The slight deviations for high pH values can be attributed to thermal effects. These deviations were considerably reduced by recalculation of the theoretical pH values at the actual temperatures [the main effects of temperature are on dissociation constants, Eq. (1)].

The values of the experimental process gain, K_2 and of the ratio K_2/K_1 are shown in *Table 5.* As can be seen, by comparing the values of *Tables 1* and *2,* the average difference between the theoretical and experimental values was about 16%.

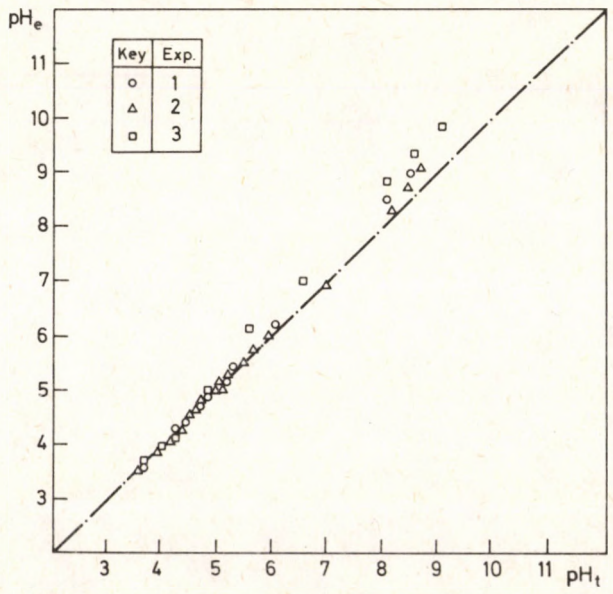

Figure. 3.
Regression between experimental and theoretical titration curves.

Table 5.
Experimental values of K_2 and K_2/K_1

Exp.	1	2	3
K_2	19.12	26.50	39.00
K_2/K_1	10.50	10.43	11.60

Dynamics of the Continuous Neutralization Reactor

The experiments of neutralization were made with the system shown in *Fig 4*. The continuous stirred tank had a volume of 2,000 cm^3 It was fitted with internal baffles and funneled inlets and outlets to avoid short-circuiting of the reactants. The pH electrode was located at the outlet of the tank; it was arranged in a tubular device of small volume to avoid as far as possible the existence of delay times in the measure of pH.

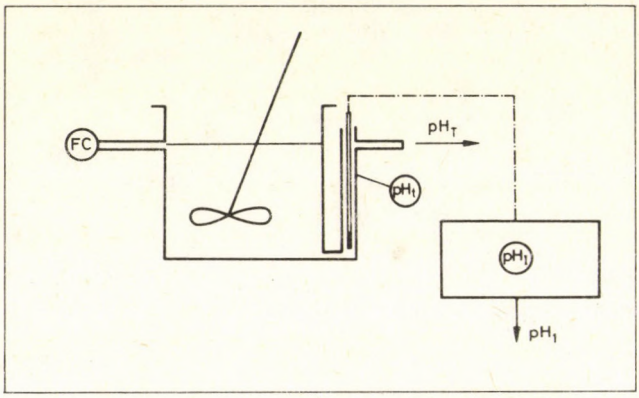

Figure. 4.
Apparatus for the study of continuous neutralization FC: feed rate control, pH_t: electrode, pH_T: actual pH, pH_I: indicator, pH_1: measured pH.

The experiments on dynamics were performed following the usual stimulus-response techniques (in this case the input signals are steps of pH, obtained by quickly changing the acid concentration at the inlet of the reactor). From the results obtained, the reactor can be represented as a perfect mixing tank of 1,760 cm^3 (a dead volume of 240 cm^3) with a delay time less than 1% of the time constant.

Dynamics of the pH Electrode

The pH electrode was a commercial glass electrode with internal reference based in the pair Ag-AgCl saturated with KCl (4 mol/1).

The dynamic characteristics of the electrode were measured by stimulus-response techniques in the system shown in *Fig. 4*. The input signal was a step of pH, made by the addition of a given amount of either an acid or a base (the additions were quasi-instantaneous). The response curve was obtained form a continuous recording of the pH-meter output.

Two representative response-curves of the electrode are shown in *Fig. 5*. As it can be seen, the response is asymmetric, it is faster for negative perturbations of pH (acidic perturbation) than for positive ones.

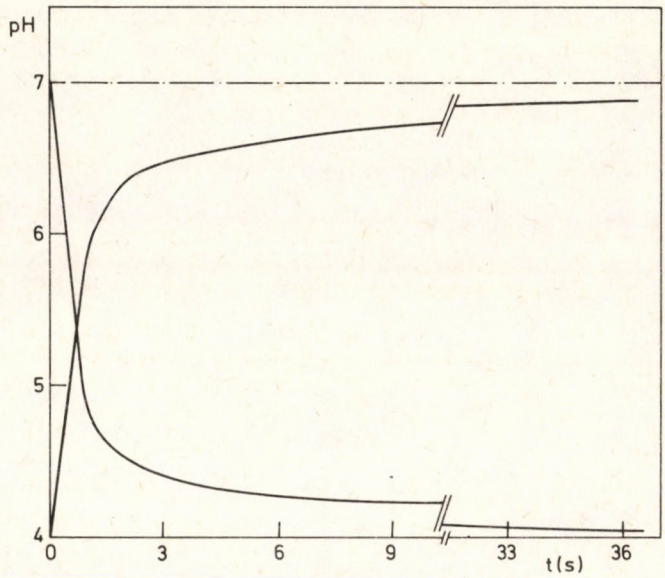

Figure. 5.
Non-symmetrical response of the electrode

The value of the time constant of the electrode [assuming a first order lag dynamics, Eq. (11)] is dependent on the sign of the perturbation. The values established in this study are:

$$T = 4\,(\mathrm{s}) \quad \text{if} \quad \mathrm{pH}_1 > \mathrm{pH}_T$$
$$T = 20\,(\mathrm{s}) \quad \text{if} \quad \mathrm{pH}_1 < \mathrm{pH}_T$$

Simulation

The behaviour of a closed-loop neutralization system was simulated by computer aid. The reactor was assumed to be similar to the experimental vessel, *Fig. 4*. with the following conditions:

- Volume: 1760 cm^3
- Flow pattern: perfect mixing (no dead volume neither delay times).

· Feed flow rates: 300 g/min. of acidic stream
300 g/min of alkaline neutralizing solution.
Acidic stream composition: 10% acetic acid
8.5% propionic acid
81.5% water
Alkaline stream composition: 2% sodium hydroxide
2% ammonium hydroxide
96% water

The dynamic state which were simulated are:

· Start-up
· Perturbations of steady states by changes in the acidic stream composition.

The following factors were also considered in the simulation:

· Control action: · Linear PID
· Non-linear PID
· Adaptive PID
· Dynamics of the pH electrode: · Gain
· First order lag
· Damping tanks after the main reactor: · none
· one
· two

The calculations were carried out for small steps of time following three main sets of operations:

· Read the initial operating conditions data (composition and flow rates of streams, volume of reactors, and action control algorithms, etc.)
· Calculate the pH of the reactor content, Eq. (1), control parameters, Eq. (13), and errors, Eq. (12), (14), (15).
· Calculate the control action, Eq. (13), and the new values of concentrations, Eq. (6)–(10).

These operations are successively made until the required final time is reached. The results are shown in *Fig. 6–11,* in which the continuous curves of pH vs time were obtained by fitting the discrete points obtained in the digital simulation (about 50 points per curve). The points were not drawn for easier visualization of the Figures.

Simulation of Start-Up

This operation was simulated under the following assumptions:

· At time zero the pH is 7 (reactor filled with pure water).
· No damping tanks are connected
· The electrode is a gain element, gain = 1, in cases a-1, a-2 and a-3, and a first order lag in the case a-4.

The start-up was made by feeding a mixture of acidic and alkaline solutions (flow rates and compositions given at the beginning of the above paragraph).

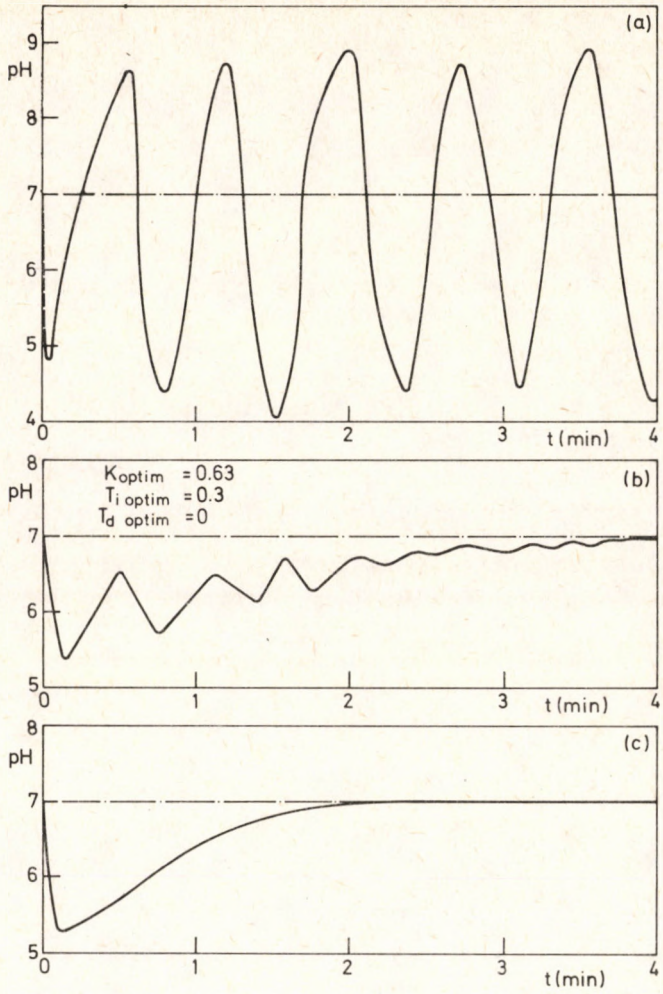

Figure. 6.
Start-up. a). non-linear PID, b). linear PID, c). adaptive PID.

The response of the system (pH at the outlet of the reactor) is shown in *Fig. 6*. Three cases were simulated:

Case a-1. – Non-linear PID
The response is shown in *Fig. 6-a*. The instability is evident, with strong pH oscillations ranging between 4 and 9.

Case a-2. – Linear PID
The behaviour of the system during start-up with a linear PID action is shown in *Fig. 6-b*. In this case, the values of the parameters K_c, T_I and T_D [Eq. (13)] were obtained by the method of Ziegler-Nichols.

The simulation was made assuming different values of K_c; the ultimate value of K_c (constant oscillation of response) is 1.26, and the period of the oscillating response $0 \cdot 6$ min. From these values, the tuning gives the following parameters:

$$K_c = 0.63$$
$$T_I = 0.3 \text{ min}$$
$$T_D = 0.075 \text{ min} \approx 0$$

With these control parameters the pH of the reactor reaches the set point (pH = 7) in about 4 minutes since the beginning of the start-up operation.

Case a-3. – Adaptive PID
By using the adaptive control action, Eq. (16)–(18), the response was very good, *Fig 6-c*. There were no over-shoots and the time to reach the 99% of the set point was about 2 minutes.

Case a-4. – pH-electrode with first order lag dynamics
In the preceding 3 cases the electrode was assumed to have an instantaneous response (gain element). When a first order lag dynamics was assumed, the response of the closed-loop was very close to instability; with linear PID with a $K_c = 0 \cdot 075$ the pH oscillated between 6 and 8 after 3-5 minutes from the beginning of the start-up. The adaptive PID improves this type of response, but it did not achieve the complete elimination of oscillations.

Simulation of Responses to Perturbations on the Inlet Acid Concentration

The control actions simulated in this case were only the linear PID and adaptive PID (the non-linear PID was neglected since its effects in start-up were clearly undesirable).
The additional following assumptions were made:

- The neutralization system was a main tank ractor that can be followed by either one or two extra tanks, which serve as damping elements. These tanks were assumed to be well stirred.
- The control variable, pH, was always the value of pH at the outlet of the main tank. The action control (alkaline addition) was always at the inlet of the main tank.
- The frequency of perturbations was twice the corner frequency of the system. That meant an acidic perturbation every 1.7 min., value close to half the time constant of the tank reactor.
- The intensity of perturbations (absolute value of perturbations) was not higher than the 98% of the actual acid concentration at the inlet of the main tank.

Four cases were simulated:

Case b-1
This case was made under the following particular conditions:

· Control action: linear PID
· pH-electrode dynamics: simple gain (equal to unity)
· Damping tanks: none

The behaviour of the system is shown in *Fig. 7.* The start-up takes about 3-4 min. The response after perturbations of the steady state was oscillatory, but the pH aproached the set point in 3-4 min.

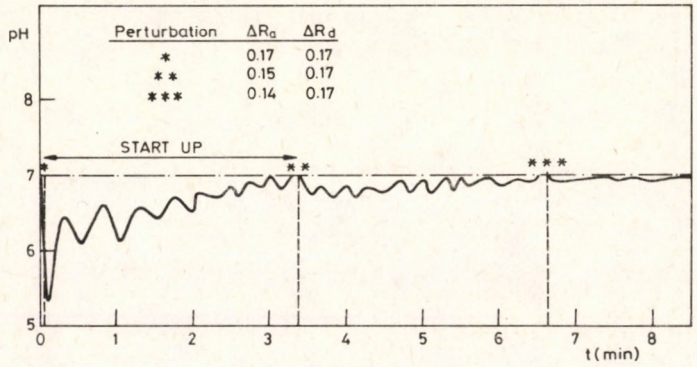

Figure. 7.
Case b-2. Linear PID

Case b-2
In this case the particular conditions were:

· Control action: Adaptive PID
· pH electrode dynamics: simple gain (equal to unity)
· Damping tanks: none

The output signal was very good, *Fig. 8.* the adaptive action clearly reduced the effects of perturbations (the over-shoot produced after the third perturbations can be attributed to the fact that the system was not yet at a new steady state after the second perturbation)

Case b-3
The particular conditions were:

· Control action: linear PID
· pH electrode dynamics: first order lag
· Damping tanks: none

The output signal was clearly affected by the dynamics of the electrode, *Fig. 9.* This influence can clearly be evaluated by comparing the response curve with the *Fig. 7.* (Case b-1).

Case b-4
In this case, the effects of damping tanks was simulated. The particular conditions assumed were:

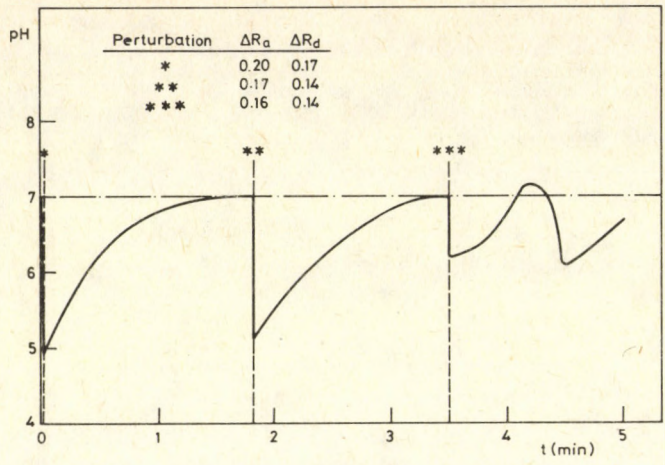

Figure. 8.
Case b-2. Adaptive PID

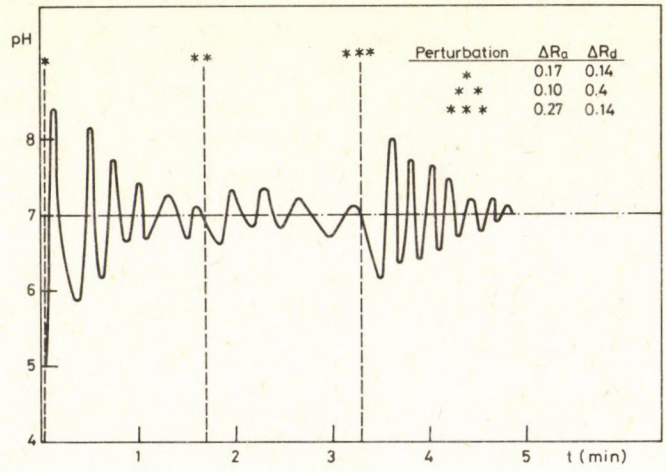

Figure. 9.
Case b-3. Linear PID, electrode: first order lag

- Control action: linear PID, adaptive PID
- pH electrode dynamics: simple gain (equal to unity)
- Damping tanks: 2; 3

When two or three damping tanks are connected with the main reactor, both control actions gave a better behaviour of the system (compared to cases b-1 and b-2, in which no damping tanks were disposed). Although the amplitude of the output signal was not significantly improved, the frequency of such response was reduced with respect to the system without damping tanks.

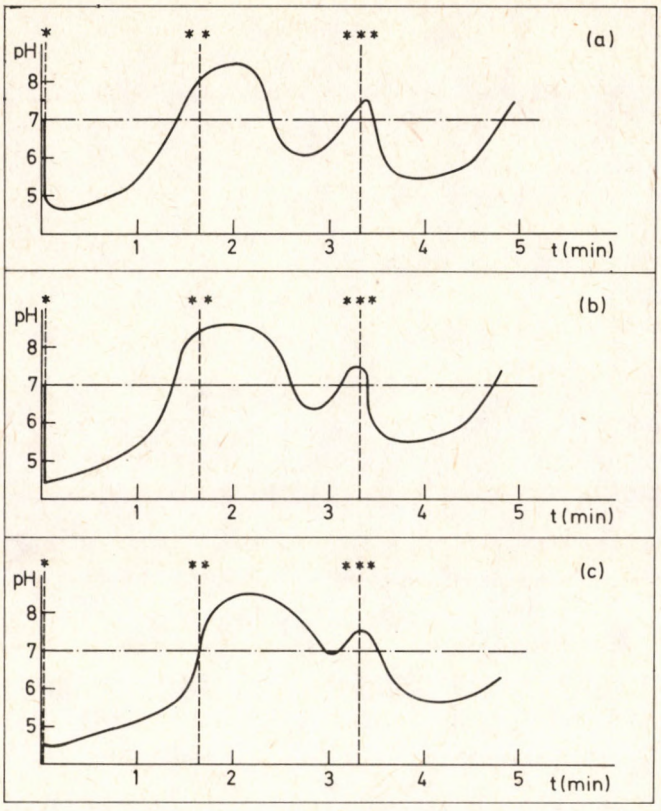

Figure. 10.
Case b-4. Linear PID. *a)*. main reactor, *b)*. one damping tank, *c)*. two damping tanks. Perturbations in acids are: $*\Delta R_a = 0.17$; $\Delta R_d = 0.14$; **: 0.16–0.14; ***: 0.27–0.15.

Some examples of this simulation are shown in *Fig. 10*. The curve in *Fig. 10-a* is for a linear PID actions (gain $K_c = 0{,}025$) and no damping tanks. The output pH for the system with one extra tank is shown in *Fig 10-b* (the pH now corrsponds to the output of the damping tank). The response for two extra tanks is shown in *Fig. 10-c*. By comparing these three curves it can be observed that the frequency and amplitude of the output pH were reduced.

When adaptive PID action was used, the output response, *Fig. 11,* only slightly improved by the use of damping tanks, but as better than in the system with linear PID action, *Fig. 10*.

Conclusions

Simulation models can be used for predicting the behaviour of pH control systems under a great number of operating conditions and design factors. It also provides a good understanding of the phenomena involved in such systems and

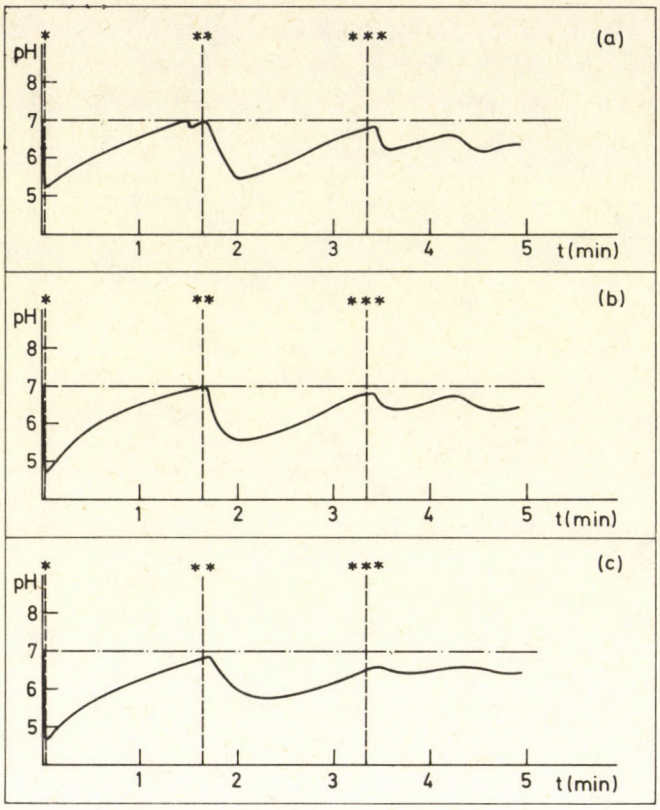

Figure. 11.
Case b-4. Adaptive PID: a). main reactor; b). one damping tank c). two damping tanks. (Perturbations equal that in *Fig. 10)*.

can be a good way to save costs and time in the design and performance of industrial processes.

Models should take three main subjects into account: the neutralization process, the dynamics of the neutralization reactor and the pH electrode.

Although the neutralization process (acid-base reacting systems) and the dynamics of the reactors (well stirred tanks) can be relatively well known by approximate theoretical calculation, the dynamics of the electrode should be determined as close to reality as possible, since the main cause of instability (or at least, of decreasing the relative stability) is closely related to the nonsymmetrical dynamics of the pH electrode.

The addition of damping tanks is not an important factor if strict control criteria are taken into account, but, in any case, this should be considered to prevent or reduce the effects of eventual failures or unexpected perturbations.

The type of control action should be selected in conjunction with other factors. Thus, for example, the non-linear PID action cannot be used if the only precise information available is about titration curves, since the dynamics of the reactor and electrode could strongly affect the behaviour of the closed loop system.

The linear PID action can be sufficient when using one or more damping tanks. Finally, the adaptive PID control action needs a deeper knowledge of the actual system, but it is a safe and advisable control action; the design of the plant with adaptive control can be very flexible and successful (with adaptive control, the effects of the electrode dynamics are reduced, one or more damping tanks can be used without affecting the stability of the loop and wide ranges of frequency and amplitude of perturbations are allowed).

Symbols

C	concentration, $mol \cdot dm^{-3}$
D	average density of the final solution, $g \cdot cm^{-3}$
E	error, pH units
D	gain of the controller, pH units
k	dissociation constant, $mol \cdot dm^{-3}$
M	molecular weight, $g \cdot mol^{-1}$
R	fractional mass content, dimensionless
T	time constant, min
t	time, min
V	volume, cm^3
WR	flow rate ratio, alkaline/acid, dimensionless
WRN	id. at the neutralization point, dimensionless
WT	total flow rate, $g \cdot min^{-1}$
WTA	acidic solution flow rate, $g \cdot min^{-1}$
WTB	alkaline solution flow rate, $g \cdot min^{-1}$

Subscripts

a	acetic acid
b	ammonium hydroxide
c	sodium hydroxide
d	propionic acid
D	derivative
I	integral

REFERENCES

1. SHINSKEY, F. G.: „pH and pION Control in Process and Waste Streams", John Willey and Sons, N. Y. 1973.
2. HOYLE, D. L.: Chem. Eng., *1976,* 8 (Nov.), 121-126.
3. GUSTI, A. L. (Jr) and HOUGEN, J. O.: Control Eng., *1964,* 8 (4), 136-141.
4. JOHANSON, G. and NORBERG, K.: Journal of Electroanalytical Chem. *1968,* 18 (3) 239-245.
5. HOUGEN, J. O.: Chem. Eng. Prog. Monograph Series, *1964,* 60 (4), 49-53.
6. MOHILLA, R. and FERENCZ, B.: Hung. J. Ind. Chem. *1983,* 11, 425-434
7. GUSTAFSSON, T. K. and WALLER, K.: Chem. Eng. Sci. *1983,* 38 (3) 389-398.
8. JUTILLA, P. and JAAKOLA, P.: Rep. 65 (June 86) Control Eng. Lab., Helsinki Univ. of Technol.

9. JUTILLA, P. et al., „Computer Control of pH Reactor", Proc. of 1985 American Control Conf., Vol 2, 1165-1171.
10. ZIEGLER, J. G.; and NICHOLS, N. B.: ASME Trans., *1942,* 64 (11), 759-768.
11. DAHLIN, E. B.; et al: Inst. Cont. Syst. *1968,* 41 (jun.) 87-91.

HUNGARIAN JOURNAL
OF INDUSTRIAL CHEMISTRY
VESZPRÉM
Vol 17. pp. 437–448 (1989)

HEAT TRANSFER IN A SPOUTED BED GRANULATOR

J. KUCHARSKI

(Institute of Chemical Engineering an Heating Equipment, Technical University of Wrocław, Poland)

Received: March 1, 1989

The results of a fluid–to–particle heat transfer study in air spouted bed of coated and simultaneous dried tablets, using a 30 cm I.D. column with a 33° conical base, are reported. The effect of gas velocity, inert particle size, bed depth on the heat transfer coefficient are discussed. An equation correlating heat transfer coefficient was established.

Introduction

The fluid and particle mechanics of a spouted bed, and their applications, were reviewed by many authors [1–4]. Relatively little has been published, however, on heat and mass transfer between particle and fluid [5–8].

Application of a spouted bed in a coating and simultaneous drying of coated inert particles [9–12] is justified by such advantages as limited contact of the wet material with the supporting grid. The gas–solid heat transfer in this technology, apart from both the hydrodynamics of gas flow and solid movement in a spouted bed, is also a very important factor from the point of view of the above–mentioned process as well as of the homogeneity of the product.

The present study deals with fluid–to–particle heat transfer during coating of tablets in a spouted bed. In this paper a complementary description of earlier papers [13–16] is given, related to the discussion of experimental investigations on the heat transfer in a spouted bed.

Description Method

Measurement of the drying rate of coated inert particles confirmed the existence of a constant–rate drying period for this material. The average fluid–to–particle heat transfer coefficient h_s could therefore be evaluated from the data in this

regime. Methodology of calculation of the above–mentioned heat transfer coefficient was based on the static bed model [17] and on an overall effective temperature driving force:

$$\Delta t_m = \frac{(t_{g,1} - t_{g,2})}{\ln\left[\frac{t_{g,1} - t_{gn,2}}{t_{g,2} - t_{gn,2}}\right]} \tag{1}$$

The particle surface area, instead of not being correspondingly limited to the spout region alone, was based on the total particle surface area in the bed. Taking into account these assumptions, the average heat transfer coefficient h_s was defined by the following equation:

$$Q = h_s a V \Delta t_m \tag{2}$$

where:

$$a = \frac{6(1-\varepsilon_0)\emptyset}{d_q} \tag{3}$$

The heat flux Q was calculated from the mass vapour flux, described by the formula:

$$Q = m_g(x_2 - x_1) \tag{4}$$

In order to find the air humidity, the partial pressure of water vapour was calculated from the psychrometric measurements using the formula recomended by LUIKOV [18]:

$$p_v = p_{vn} - A(t_{g,2} - t_{gn,2}) \tag{5}$$

where A parameter is a function of gas velocity in the measurement section:

$$A = 10^{-5}\left[65 + \frac{6.75}{u_{g,2}}\right] \tag{6}$$

Based on the assumption that the bed depth H_0 was less than the conical part height of apparatus, the bed depth H_0 was calculated from the bulk volume of material, defined as follows:

$$H_0 = \left[\frac{3\left[V_0 + \frac{\pi d_0^3}{24\,\mathrm{tg}\,(\gamma/2)}\right]}{\pi\,\mathrm{tg}^2\,(\gamma/2)}\right]^{\frac{1}{3}} - \frac{d_0}{2\,\mathrm{tg}\,(\gamma/2)} \tag{7}$$

The conformity with the above–mentioned rules, related to the description of the average heat transfer coefficient, was corroborated by other authors who discussed the heat transfer problem [19,20]

Material Used and Experimental Procedure

The investigations were conducted in an experimental column. *Fig. 1,* consisting of a cylindrical part, 0.3 m in diameter, and of a conical bottom, 0.082 m in inlet diameter and $\gamma = 0.5892$ rad in angle of conical base, with a nozzle placed on the axis at the bottom. The experimental facilities and procedure of measurement were described in earlier papers [21–23].

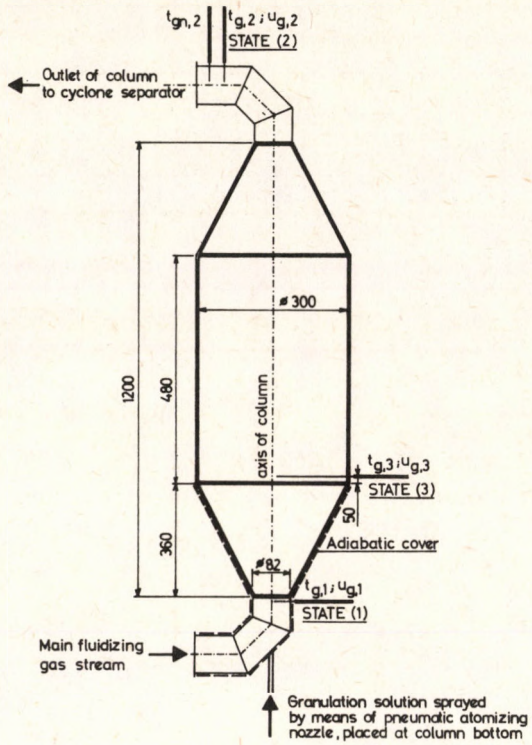

Fig. 1
Cross sectional view of experimental column

Tablets of "Placebo" and "Raphacholin" were investigated. The geometry and characteristic dimensions of the tablets are shown in *Fig. 2.*

Results

Because of the mean gas velocity $u_{g,3}$ in the cylindrical part of experimental column satisfied the applicability condition of the Luikov method for the description of the partial pressure of water vapour aspect, this is why the Luikov

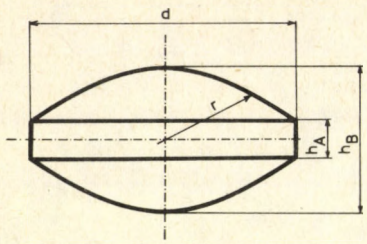

h_A – height of cylindrical part of tablet,
h_B – overall height of tablet,
d – diameter of cylindrical part of tablet,
r – radius of tablet.

Tablet	d	h_A	h_B	r	Description ; c_s(kg/kg)=:		
	m	m	m	m	0.5	0.6	0.6965
"Placebo"	0.007	0.0015	0.0040	0.005525	♦	-	◊
	0.008	0.0015	0.0043	0.0064143	●	-	○
	0.009	0.0015	0.0043	0.008021	■	-	□
	0.012	0.0035	0.0075	0.0101014	▲	-	△
"Raphacholin"	0.010	0.0020	0.0020	0.009083	-	▲	-

Fig. 2
Geometry and dimensions of tablet.

method was utilized for the calculation of the wet bulk temperature above dynamic bed height (state (3)). Iterational method of the wet bulk temperature approximate was adopted. This was done as soon as the difference between the partial pressure of water vapour in gas obtained by the psychrometic method for both the outlet of column and cylindrical part of this one (states (2) and (3) respectively) was equal zero:

$$p_{v,i} = p_{v,3,i} - p_{v,2} = 0 \tag{8}$$

where:

$$p_{v,3,i} = f(p_{vn,3,i}, u_{g,3}, t_{g,3}, t_{gn,2} + 0.05i) \tag{9}$$

on the assumption that for $i = 1$, $t_{gn,3} = t_{gn,2}$ and $p_{vn,3} = p_{vn,2}$.

The saturated water vapour for the gas temperature $t_{gn,3}$ was found from the Antoine equation [24]:

$$p_{vn,3} = \exp\left(23.1964 - \frac{3816.44}{t_{gn,3}}\right) \tag{10}$$

It is interesting to analyse the dependence of the relative error, defined from the following equation:

$$\delta_{\Delta t_m} = \frac{1}{n_{exp}} \sum_{i=1}^{i=n_{exp}} \left[\frac{\Delta t_m\,(\text{state}(3)) - \Delta t_m\,(\text{state}(2))}{\Delta t_m\,(\text{state}(2))}\right]_i 100\% \tag{11}$$

on the overall effective temperture driving force, described by Eq. (1). Comparison of these parameters [13] confirms an insignificant influence of the overall technological conditions, related to the cylindrical part of the column, on

determining the temperature driving force (mean relative error – 1.45%, maximum relative error – 2.94%). Thus, the value of the overall effective temperature driving force, described on the basis of the thermal conditions related to the outlet of column, was taken as an experimental one.

Furthermore, the comparison of experimental values of Nu_s dimensionless number was based on the double description of mass vapour flux:

$$Nu_s = \frac{h_s d_p}{k_g} \tag{12}$$

and

$$Nu_s^* = \frac{h_s m^S (1 - c_s) d_p}{m_g (x_2 - x_1) k_g} \tag{13}$$

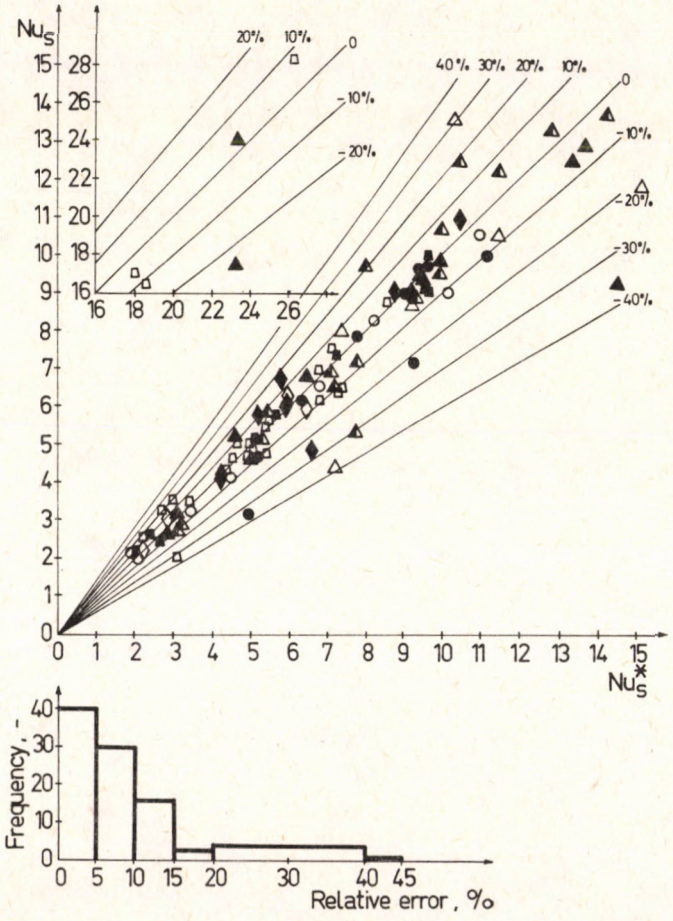

Fig. 3
Comparison of Eq. (12) and Eq. (13) for describing the Nu_s number. Description as for *Fig. 2*

where c_s is the mass fraction of the granulated component in the sprayed solution is presented in *Fig. 3*. The relative error histogram shows that 70% of the values of the analyzed data of Nu_s number do not exceed the ± 10% limit of relative error for the Nu_s number, described with regard to the amount of water, included in the sprayed solution (Eq. 13)

Experimental data on the behaviour of the average heat transfer coefficient or Nu_s number is illustrated in *Fig. 4, 5*. *Figure 4* shows the heat transfer

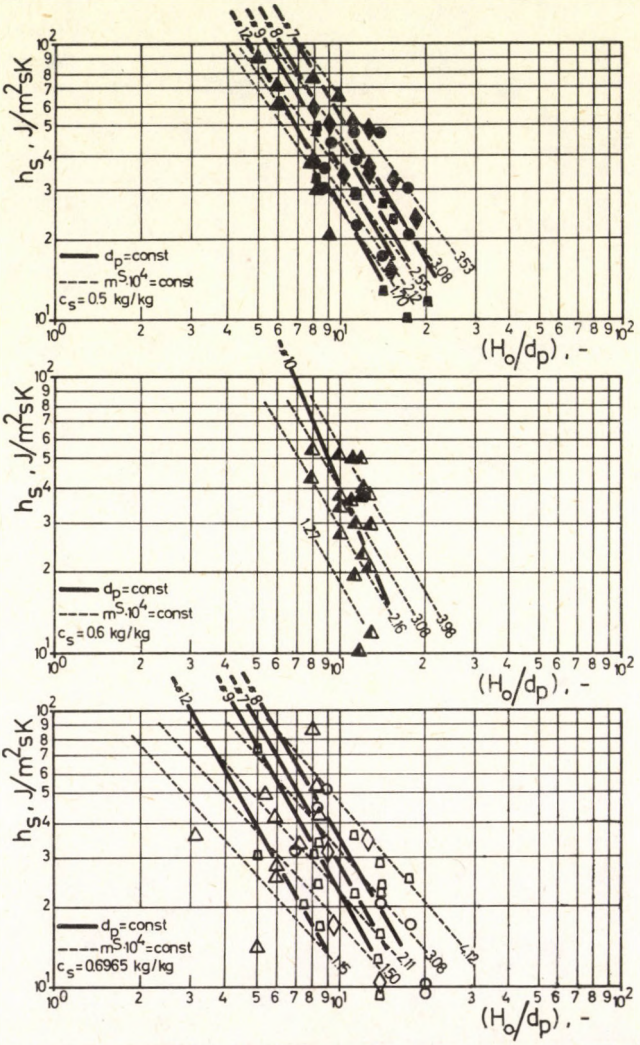

Fig. 4
Air–to–particle heat transfer coefficient dependence on the (H_0/d_p) dimensionless moduli. Description as for *Fig. 2*

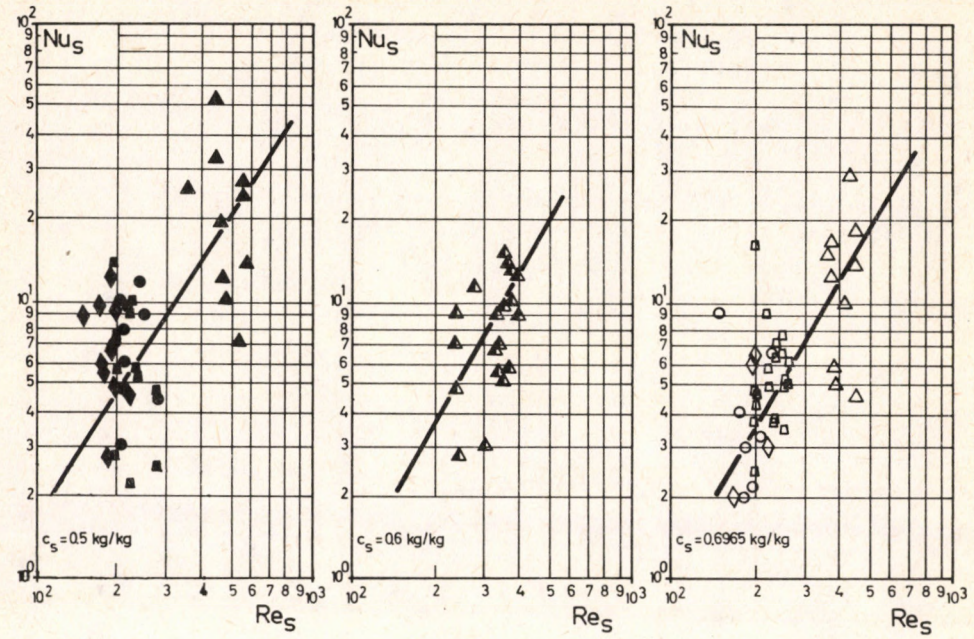

Fig. 5
Nu_s number dependence on Re_s number. Description as for *Fig. 2*

coefficient plotted against the dimensionless moduli (H_0/d_p). An increase in static bed depth for constant mean diameter of inert particle causes the decrease in the heat transfer coefficient directly proportionally in relation to the each kind of tablet. An increase in the mean diameter of inert particle for constant (H_0/d_q) value makes the gas–solid heat exchange worse, particulary for a simultaneous increase in the mass fractions of the granulated component in the sprayed solution. Furthermore, taking into account both the optimum coating and heat conditions (high values of heat transfer as well as granulation coefficients), the constant value curves of mass sprayed solution flux suggests the employment of a less mean diameter of the inert particle or small values of (H_0/d_p) dimensionless moduli respectively for the increase in the feed sprayed solution.

The dependence of the Nu_s number on the Re_s number is shown in *Fig. 5*. The slope of the experimental curves is independent on the mass fraction of the granulated component in the sprayed solution. Simultaneously, the increase in the above-mentioned mass fraction causes the decrease in the experimental Nu_s number values for a constant value of the mean diameter of the inert particle. In other words, the higher the mass fraction of the granulated component in the sprayed solution, the less utilization of the heat energy, included in the gas flux.

Applying a dimensionless analysis, the following relationship was developed:

$$Nu_s = C\, Re_s^m\, Pr^n\, Ar^p \left[\frac{H_0}{d_p}\right]^r \left[\frac{m^S}{m_g}\right]^s (1-c_s)^t 0^w \tag{14}$$

This form is somewhat similar to that of the REGER et al [5] as well as KMIEĆ [8] equations. By least–square fitting the following corelation was obtained:

$$\frac{Nu_s}{Pr^{0.333}} = 9.4723\, Re_s^{0.6128} Ar^{0.2302} \left[\frac{H_0}{d_p}\right]^{-1.031} \left[\frac{m^s}{m_g}\right]^{0.8135} \cdot (1-c_s)^{0.7954}\, \varnothing^{0.8326} \qquad (15)$$

where $n = 0.333$ is an assumption. The fluid properties were evaluated at a mean temperature, calculated as the arithmetical mean of the gas inlet and outlet temperatures. The mean absolute deviation between the experimental and calculated values is 18.68%, and maximum deviation does not exceed 30%.

Comparison of the experimental and calculated values of the Nu_s number values is shown in *Fig. 6*. The divergence between these values may result from the statistical treatment of the experimental data as well as from an inaccurate description of the fluid properties, included in Eq. (15). Nevertheless, the proposed equation performs the average–making function, related to the change of mass fraction of the granulation compent in the sprayed solution.

It is interesting to compare both the proposed equation and the other correla-

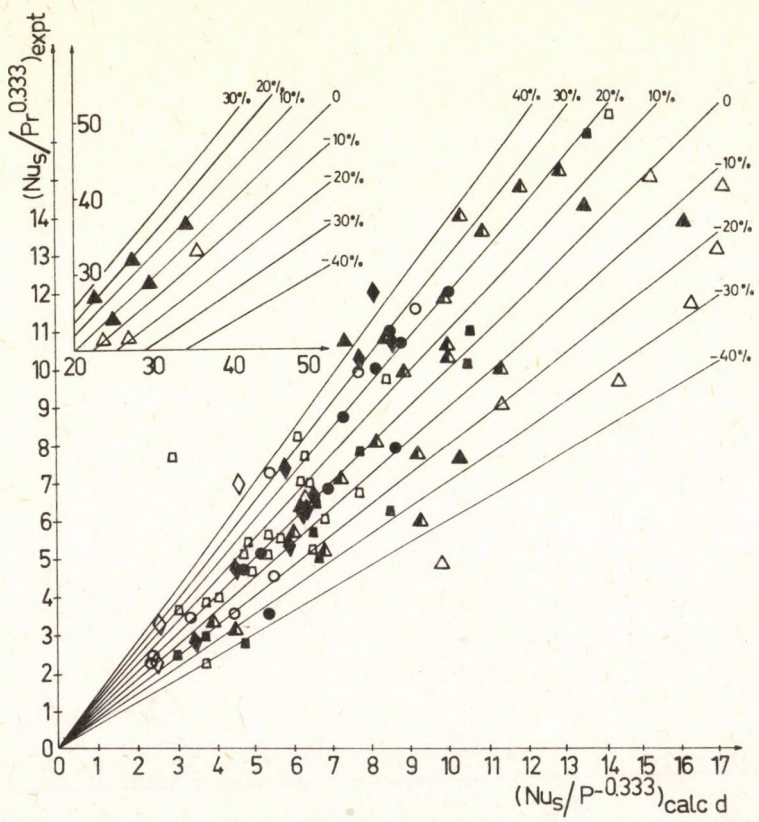

Fig. 6
Comparison of experimental and calculated values of the Nu_s number. Description as for *Fig. 2*

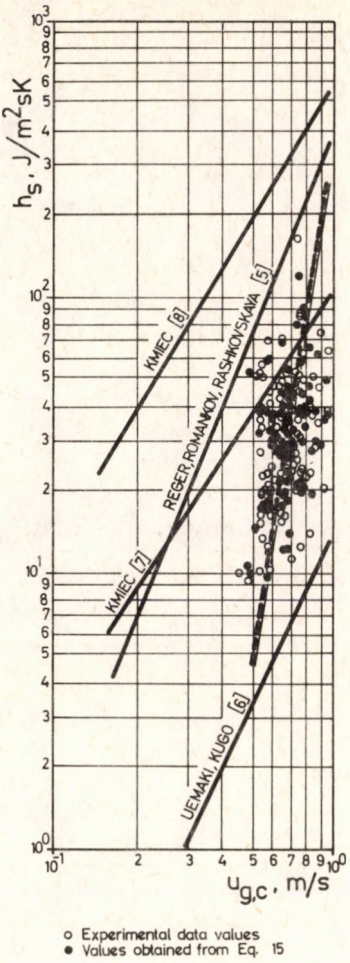

Fig. 7
Comparison of calculated air–to–particles heat transfer comparison.

tions, describing the average heat transfer coefficient in a spouting system. As *Fig. 7* shows, the values of the heat transfer coefficient, obtained from Eq. (15) are in a good agreement with the correlation of REGER et al. [5]. It results from the similarities of both the REGER et al. and above discussed technological conditions. Differences between the heat transfer coefficients at a low value of gas velocity result in the first place from the small efficiency of the granulation process, obtained by REGER et al. Simultaneously, based on the total particle surface area in the bed (the real surface of evaporation, including the surface developed by drops of sprayed liquid was much higher than the surface of the bed), it conclusively gives the higher values of the heat transfer coefficient,

obtained from the REGER et al equation. The similar conditions of the sprayed solution utilization were performed only for the higher gas velocities, related to the increase of both the mean diameter of the inert particle and the static bed depth.

It is interesting to note that for the average values of the heat transfer coefficients, obtained from the proposed equation, the differences between this one and calculated from the KMIEĆ equation [7] (the investigations were conducted in a conic-cylindrical apparatus by means of a cylindrical part, 0.09 m in diameter, related to the inlet diameter of my own column, 0.082 m in diameter) values are negligible. This fact seems to be due to the considerable utilization of the central zone of a spouting system in the gas–solid heat transfer aspect.

Conclusions

1. Rates of heat transfer between the gas and particles in a spouted beds can be described by the following equation:

$$\frac{Nu_s}{Pr^{0.333}} = 9.4723\ Re_s^{0.6128}\ Ar^{0.2302}\left[\frac{H_0}{d_p}\right]^{-1.031}\left[\frac{m^s}{m_g}\right]^{0.8135}\cdot(1-c_s)^{0.7954}\,\varnothing^{0.8326}$$

2. The dependence of mean process parameters (H_0, d_p, c_s) on the heat transfer coefficient h_s was illustrated. The higher the mass fraction of the granulated component in the sprayed solution, the less utilization of the heat energy, included in gas, was shown among other things.

3. An insignificant influence of the overall technological conditions on determining the temperature driving force, was shown. Furthermore, an argeement between the double description of mass vapour flux, included in the Nu_s dimensionless number, was presented.

SYMBOLS

a specific surface area of particles, m^2/m^3
A equation constant (Eq. 6)
c_s mass fraction of granulated component in sprayed solution, kg/kg
c_{pg} heat capacity of gas, J/kg deg
d diameter, m
g acceleration of gravity, m/s^2
H_0 bed depth, m
h_s average heat transfer coefficient between gas and particle, J/m^2s deg
k_g thermal conductivity of gas, J/m s deg
m_g mass gas velocity kg/s
m^s mass granulation solution velocity, kg/s
p partial pressure, kg/m s^2
t temperature, deg
tg tangent of angle of conical base, –
u superficial gas velocity, m/s
x gas humidity, kg/kg
V volume, m^3

Greek Symbols

μ_g gas viscosity, kg/m s
ϱ density, kg/m^3
γ an angle of conical base, rad
ε bed voidage, m^3/m^3
$\emptyset$ shape factor, –
$\triangle$ difference, –
δ relative error, %

Subscripts

c column
g gas
gn wet bulb thermometer
m average
o initial
p particle
s solid
v vapour
vn vapour saturated at the surface of particle
1 inlet
2 outlet of column
3 outlet of bed

Dimensionless Numbers

$$\mathrm{Ar} = \frac{g\, d_p^3(\varrho_p - \varrho_g)\, \varrho_g}{\mu_g^2}$$

$$\mathrm{Pr} = \frac{\mu_g\, c_{pg}}{k_g}$$

$$\mathrm{Nu}_s = \frac{h_s\, d_p}{k_g}$$

$$\mathrm{Re}_s = \frac{u_{g,c} d_p \varrho_g}{\mu_g}$$

REFERENCES

1. MATHUR, K. B. and GISHLER, P. E.: A.I.Ch.E.J. *1955*, 1, 175.
2. SUCIU, G. C. and PATRASCU, M.: Powder Technology *1978*, 19, 1, 109.
3. MATHUR, K. B. and EPSTEIN, N.: Spouted Beds. Academic Press, New York, 1974.
4. DAVIDSON J. F., CLIFT R. and HARRISON, D.: Fluidization. Academic Press, New York, 1985, p.201.
5. ROMANKOW P. G. and RASHKOVSAYA, N. B.: Drying in a Suspended State. Khimiya, Leningrad, 1968, p. 273, (in Russian)
6. UEMAKI, O. and KUGO, M.: Kagaku Kogaku *1967*, 31, (4) 348.
7. KMIEC, A.: Inż. Ap. Chem. *1972*, 6, 6, (in Polish)
8. KMIEC, A.: Bed Expansion and Heat and Mass Transfer in Fluidized Bed. Scientific Papers of the Inst. Chem. Engng of Wrocław Techn. University, No 36/19, Wrocław, 1980, p. 74, (in Polish)

9. ROBINSON, T. and WALDIE, B.: Trans. I. Chem. Eng. *1979*, 57, 121.
10. UEMAKI, O. and MATHUR, K. B.: Ind. Eng. Chem. Process Des. Dev. *1976*, 15, 504.
11. STOCKBURGER, D.: Chem. Ing. Tech. *1976*, 48, 199.
12. DOLIDOVICH, A. F. and EFREMTSEV, V. S.: Can J. Chem. Eng. *1983*, 61, 454.
13. KUCHARSKI, J.: Heat Transfer and Kinetics of Granulation Process During Coating of Tablets in a Spouted Bed. Ph. D. Thesis, Technical University of Wrocław, Poland, 1988, (in Polish)
14. KUCHARSKI, J. and KMIEC, A.: Can. J. Chem. Eng. *1983*, 61, 435.
15. KUCHARSKI, J. and KMIEC, A.: Inż. Chem. Proc. *1982*, 3, 573.
16. MIELCZARSKI, S. and KUCHARSKI, J.: Investigations of Coat Forming Process on the Inert Particle Surface in a Spouted Bed. Proc. 5th All = Polish Drying Symposium, Wrocław, 1984, p. 165, (in Polish)
17. MKIEC, A.: Can. J. Chem. Eng. *1975*, 53, 18.
18. LUIKOV, A. V.: Heat and Mass Exchange in Drying Process. Khimiya, Moscow, 1956, in Russian.
19. PETROVIC, L. J. and THODOS, G.: Can. J. Chem. Eng. *1968*, 46, 114.
20. CIBOROWSKI, J. and MŁODZINSKI, B.: Przem. Chem. *1961*, 40, 596, (in Polish).
21. KUCHARSKI, J. and KMIEC, A.: Chem. Eng. Sci. (submitted 1988, in press).
22. KUCHARSKI, J. and KMIEC, A.: Analysis of Simultaneous Drying and Coating of Tablets in a Spouted Bed. Proc. 5th International Drying Symposium, Cambridge, Massachussetts, 1986, Paper No II/17P, p. 204.
23. KUCHARSKI, J. and KMIEC, A.: The Effect of Process Parameters on Mass Distributions and the Efficiency of Tablet Coating in a Spouted Bed. Proc. 6th International Drying Symposium, Versailles, 1988, Paper No II, p. PA27.
24. STRUMIŁŁO, C.: Principles of Theory and Technique of Drying. WNT, Warsaw, 1975, p. 198.

HUNGARIAN JOURNAL
OF INDUSTRIAL CHEMISTRY
VESZPRÉM
Vol. 17. pp. 449–456 (1989)

MULTIOBJECTIVE LARGE SCALE SYSTEMS OPTIMISATION BY DECOMPOSITION : ALGORITHMS AND APPLICATIONS

AWONO ONANA

(Laboratoire Mathematiques Appliquees et Informatique, Ecole Nationale Superieure Polytechnique Universite de Yaounde, Cameroun)

Received: March 23, 1989

The paper deals with a method for feasible decomposition and its application to multilevel, multicriteria optimal design of systems consisting of N interconnected subsystems each of which has its own objective. The fact that subsystem variables are classified into local design and coupling, and the introduction of an additive utility function justify the application of classical decomposition schemes. Practical examples are given.

Introduction

Tremendous progress was accomplished in multiobjective optimisation. Many methods were developed, including those proposed by some authors [1–5], but the idea of coupling decomposition methods, which were classically developed for single objective optimisation problems [6–10] with methods of multiobjective optimisation was poorly presented so far. This paper deals with the application of a decomposition approach.

A multiobjective optimisation problem is stated as follows:

$$\min_{x \in \Omega} F(x) \tag{1}$$

where:

F: $\Omega \rightarrow R^n$ is the multiobjective function defined by:

$$F(x) = [f_1(x), f_2(x), \ldots, f_N(x)] \tag{2}$$

ΩxN is the feasible set:

$$\Omega = [x \in R^n / G(x) < 0] \tag{3}$$

The attainable set is the image of the feasible set and is defined by:

$$\Phi = [Z \in R^n / Z = F(x), x \in \Omega] \tag{4}$$

Usually no point exists, which would give an optimum for all N objective simultaneously.

Definition: a vector $x^* \in \Omega$ is said to be Pareto optimal for problem (1) if and only if no $x \in \Omega$ exists so that:

$$F(x) \leqq F(x^*)$$

with $f_j(x) < f_j(x^*)$ for at least one j.

Let us suppose the existence and uniqueness of a Pareto optima and that the attainable set is not empty.

Solution of the Problem

Suppose the system consists of N subsystems and let x_i be the design variable vector of the i-th subsystem and z the coupling variable vector. Then equations (1)–(2) become:

$$\min(f_1(x_1, z)\, f_z(x_z, z) \ldots, f_N(x_N, z)) \tag{5}$$

$$\begin{aligned} g_i(x_1, z) &\leqq 0 \\ i &= 1, \ldots, N \end{aligned} \tag{6}$$

Where g_i is the constraint vector associated to subsystem i.

Algorithm 1

The decomposition method, pictorially illustrated in *Fig. 1,* consists of the following steps:

STEP 1: initialisation of variables $x_i (i = 1, 2, \ldots, N)$ by setting $x_1 = x_1^*$, $(i = 1, 2, \ldots, N)$.

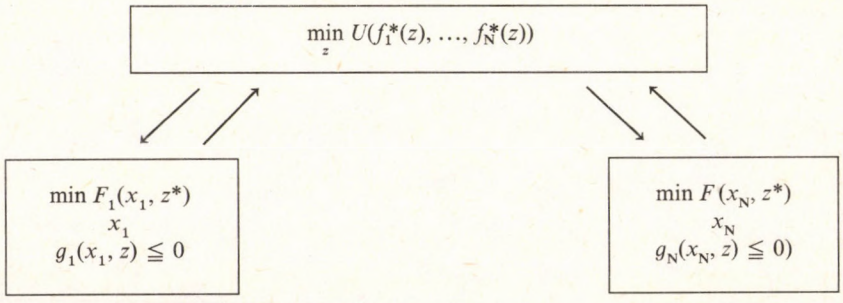

Fig. 1 Data transfer in a multilevel, multiobjective optimisation scheme

STEP 2: The upper level solves the co-ordination task:

$$\min (f_1^*(z), f_2^*(z), \ldots, f_N^*(z)) \tag{7}$$

Where:

$$f_i^*(z) = f_i(x_i^*, z) \tag{8}$$

Following [2], this problem is reformulated as a single optimisation problem by the introduction of a decision maker utility function defined as:

$$U = U(f_1(z), f_2(z), f_3(z), \ldots, f_N(z)) \tag{9}$$

STEP 3: with fixed value of $z = z^*$, problem (3)–(4) decomposes at the lower level into N independant subproblems:

$$\min f_i(x_i, z^*) \tag{10}$$

with respect to:

$$g_i(x_i, z^*) \leqq 0 \quad i = 1, 2, \ldots, N \tag{11}$$

STEP 4: $$\text{if} \quad |z^{k+1} - z^k| + \sum_{i=1}^{N} |x_i^{k+1} - x_i^k| \tag{12}$$

Then end or go to step 1.

Algorithm 2

Let us now define the regret function as:

$$R(x, z) = \sum_{i=1}^{N} (f_i(x_i, z) - f_i^*)^2 \tag{13}$$

where f_i^* solves the problem

$$\min f_i(x_i, z) \tag{14}$$

$$g_i(x_i, z) \leqq 0 \quad i = 1, 2, \ldots, N \tag{15}$$

The point $(f_1^*, f_2^*, \ldots, f_N^*)$ in the N-dimensional metric space is the ideal point of the problem.

So following [2] instead of (1)–(2) or (3)-(4) we consider the single optimisation problem:

$$\min_{(x_1, x_2, \ldots, x_N, z)} R(x_1, x_2, \ldots, x_N, z) = \sum_{i=1}^{N} (f_i(x_i, z) - f_i^*)z \tag{16}$$

with respect to:

$$g_i(x_i, z) \leqq 0 \quad i = 1, 2, \ldots, N \tag{17}$$

The solution of this problem includes the steps:
STEP 1: initialisation of x_i by setting:
$x_i = x_i^*, i = 1, 2, ..., N$
STEP 2: The upper level solves the problem

$$\min R\, x_1^*, x_z^*, ..., z) \tag{18}$$

STEP 3: with fixed values of coupling variables, the problem (14)–(15) at the lower level reduces to N independant subproblems

$$\min (f_i (x_1^*, z^*) - f^*)^z \tag{19}$$

with respect to

$$g_i(x_i, z^*) \leqq 0 \quad i = 1, ..., N \tag{20}$$

The Case of Complex Chemical Plants

Consider the following multiobjective complex chemical plant optimisation problem:

$$\max (f_1, f_z, ..., f_N) \tag{21}$$

with respect to:

$$z_i = T_i(x_i, u_i) \tag{22}$$

$$x_i = \sum_{i=1}^{N} B_{ij} z_j \tag{23}$$

$$g_i (x_i, u_i) \leqq 0 \quad i = 1, 2, ..., N \tag{24}$$

Where x_i, u_i, z_i are respectively the input, control and output variables vector of the subsystem i and $f_i = f_i(x_i, u_i)$

Application of Algorithm 1

In this case, the subsystem's design variables are x_i; u_i whilst the coupling variables vector is $z = (z_i, z_z, ..., zN)$. So following algorithm 1 at the first step design variables are initialised by setting $x_i = x_i^*$ $u_i = u_i^*$ at the second step the co-ordinator solves the problem.

$$\max (f_i, f_z, ..., f_N) \quad i = 1, ..., N \tag{25}$$

At the third step, the problem (20)–(23) decomposed into N subproblems following the model co-ordination principle of [8]:

$$\max f_i (x_i, u_i, z_i^*) \tag{26}$$

with respect to:

$$z_i^* = T_i(x_i, u_i) \tag{27}$$

where:

$$x_i^* = \sum_{i=1}^{N} B_{ij} z_j \qquad i = 1, 2, \ldots, N \tag{28}$$

The problem is solved when:

$$\sum_{i=1}^{N} (|z_i^{k+1} - z_i^k| + |x_i^{k+1} - x_i^k| + |u_i^{k+1} - u_i^k|) < \mu \tag{29}$$

Application of Algorithm 2

The regret function is:

$$R(x, u, z) = \sum_{i=1}^{N} |f_i(x_i, u_i, z_i) - f_i^*|^2 \tag{30}$$

where:

$$f_i^* = \max(f_i(x_i, u_i, z_i)$$

with respect to:

$$\begin{aligned} z_i &= t_i(x_i, u_i) \\ x_i &= \sum_{i=1}^{N} B_{ij} z_j \\ g_i(x_i, u_i) &\leqq 0 \\ i &= 1, 2, \ldots, N \end{aligned} \tag{31}$$

At the upper level, the co-ordinator improves the values of z by a gradient-like method [6]:

$$z^{k+1} = z^k - c^{k*} \in R/\sigma z | z = z^k \tag{32}$$

At the lower level with fixed values of coupling, the problem falls into N subproblems according to the decomposition scheme of MESAROVIC [8].

$$\max |f_i(x_i^*, u_i, z_i^*) - f_i^*| \tag{33}$$

$$z_i^* = t_i(x_i, u_i) \tag{34}$$

$$g_i(x_i, u_i) \leqq 0 \tag{35}$$

$$i = 1, 2, \ldots, N$$

where:

$$x_i^* = \sum_{j=1}^{N} b_{ij} z_j^*$$

Numerical Examples

The following examples illustrate the applications of the proposed algorithms. First of all with the same set of constraints single objective optimisation problems are solved and then we proceed to the solution of a three-objective optimisation problem respectively by linear weighting method [2] and algorithms 1 and 2. Consider the following example:

$$y_1 = 2x^2 + u_1 x_1 + u_1^z \tag{36}$$

$$x_1 = \frac{x_0 + y_3}{10} \tag{37}$$

$$y_2 = x^2 + u_z^z + x_z u_z \tag{38}$$

$$x_2 = \frac{4}{5^* y_1} \tag{39}$$

$$y_3 = x_3\, u^3 + u_3^2 + x_3^3 \tag{40}$$

$$y_4 = \frac{9}{10 y_3} \tag{41}$$

$$x_3 = \frac{y_z + y_1}{5} \tag{42}$$

The constraints of the inclusion type are the following:

$$0 < x_i < 1000 \quad i = 0, 1, 2, 3 \tag{43}$$

Problem 1:

$$\max y_i \quad \text{with respect to (36)–(42)} \tag{44}$$

Problem 2:

$$\max y_2 \quad \text{with respect to (36)–(42)} \tag{45}$$

Problem 3:

$$\max y_3 \quad \text{with respect to (36)–(42)} \tag{46}$$

Problem 4:

$$\max \{y_1, y_2, y_3\} \quad \text{with respect to (36)–(42)} \tag{47}$$

Problems (44)–(47) were solved on a AT–PC–286 computer by a penalty method. Problem (47) was solved first by the linear weighting (LW) method and then by algorithms 1 (ALGI) and 2. (ALG2) the results of the computations are given in *Table 1.*

Table 1.

Numerical comparison of the proposed methods

	Problem 1	Problem 2	Problem 3
x1	10.08	8.01	16.2
u1	4.33	0.82	3.01
y1	259.7	136.25	876.65
x2	207.9	108.91	700
u2	1.17	147.8	2.36
y2	43467	47799.48	491657
x3	259.3	136.25	151.02
u3	6.36	19.2	12.33
y3	1196.6	2529354	3740229
y4	1076.4	2276419	3366206

Table 2.

Solution of problem 4

	ALG1	ALG2	LW
x1	6.17	6.137	6.025
u1	4.33	4.36	4.085
y1	121.08	111.89	122.09
x2	97.01	98.26	97.096
u2	6.021	5.587	6.125
y2	10029.01	10198.002	10098.84
x3	121.068	121.16	119.65
u1	8.61	8.52	9.065
y3	1746119	1896512	1586942
y4	1326947	2111691	2089741

Conclusion

The paper is devoted to the multiobjective optimisation of systems consisting of N interconnected subsystems each of which has its own objective. In these conditions, coupling multilevel systems theory with multiobjective optimisation methods allows the decomposition of the problem into n independent subproblems at the first level, and a co-ordination through coupling variables at the upper level. The hierarchical nature of these methods makes the application of a high speed multiprocessor easy and their efficiency is demonstrated by practical examples.

REFERENCES

1. AMELJANCZYK, A.: Multicriteria Optimisation Elements (in Polish, wat, Warsaw, Poland), 1978.
2. BOYCHUK, I. M. and OVCHINNIKOV, V. O.: Soviet automatic control, *1973,* 3, 1–4.
3. FISHBURN, P. C.: Management Science, *1974,* 11, 1442–1471
4. JENDO, S., MARKS W. and THIERAUF G.: Large Scale Systems, *1985,* 9, 141–150
5. COHON, J. L. and MARKS D. H.: Water Resources Res., *1975,* 11, (2), 208–220.
6. AWONO ONANA: Large scale systems optimisation by decomposition, Ph. D. thesis, MIT, 1984.
7. WISMER (ed.). Optimisation methods for large scale systems with applications. McGraw-hill Book Company, 1971.
8. MESAROVIC, M. D., MACKO, D. and TAKAHARA, Y.: Theory of multilevel systems, Academic Press, 1970.
9. SCHWEPPE, F. C. and MITTER, S. K.: Hierarchical system theory and electrical power systems. Amsterdam, Elsevier, 1970.
10. RAY, W. H. and SZÉKELY, J.: Process optimisation with applications in metallurgy and chemical engineering. John Wiley & Sons, New York, 1973.

HUNGARIAN JOURNAL
OF INDUSTRIAL CHEMISTRY
VESZPRÉM
Vol. 17. pp. 457–463 (1989)

ASYMPTOTIC THEORY OF NONLINEAR TRANSPORT PHENOMENA IN BOUNDARY LAYERS I.

MASS TRANSFER

CHR. BOYADJIEV and E. TOSCHEV*

(Institute of Chemical Engineering, Bulgarian Academy of Sciences, Sofia 1040, Bulgaria.
* Institute of Mechanics and Biomechanics, Bulgarian Academy of Sciences, Sofia 1040, Bulgaria.)

Received: March 29, 1989.

An asymptotic theory of nonlinear mass transfer in the boundary layer along a semi-infinite plate is presented. It is shown that the direction of the intensive mass exchange with the rigid surface influences the rate of mass transfer.

Introduction

The linear theory of the diffusive boundary layer shows [1, 2], that the rate of mass transfer does not depend on the direction of the interphase mass exchange.

The theoretical analysis of systems with intensive mass transfer [3, 4] proved that large mass fluxes can initiate secondary flows of direction colinear to the direction of the mass transfer. This leads to nonlinearity in the equation of convective diffusion. This effect is connected with the change in velocity distribution in the boundary layer. As a result it has been shown that the direction of the intensive mass exchange influences the rate of the nonlinear mass transfer [6], the heat transfer [6] and the multicomponent mass transfer [7]. The numerical theory described in [5–7] shows that the rate of the transport processes considerably depends on the Schmidt and Lewis numbers. As a result in each case it is necessary to solve a system of nonlinear equations with boundary conditions for both sides of the boundary layer. This led to developing an asymptotic theory, which will be described in a series of three papers. The first deals with the asymptotic theory of nonlinear mass transfer in the diffusive boundary layer.

* This project was completed with the financial support of the Ministry of Culture, Science and Education, under contract No. 154.

Mathematical Model

The rate and concentration distribution will be demonstrated for the case of a diffusive boundary layer along a semi-infinite plate [5]. The mathematical model for this case takes the form:

$$u\frac{\partial u}{\partial x}+v\frac{\partial u}{\partial y}=\nu\frac{\partial^2 u}{\partial y^2} \tag{1}$$

$$\frac{\partial u}{\partial x}+\frac{\partial v}{\partial y}=0$$

$$u\frac{\partial c}{\partial x}+v\frac{\partial c}{\partial y}=D\frac{\partial^2 c}{\partial y^2}$$

$$x=0, \quad u=u_0, \quad c=c_0$$

$$y=0, \quad u=0, \quad v=-\frac{\mathscr{M}D}{p_0}\frac{\partial c}{\partial y}, \quad c=c^*$$

$$y\to\infty, \quad u=u_0, \quad c=c_0$$

The similarity variables can be introduced in (1):

$$u=0.5u_0\varepsilon\Phi' \tag{2}$$

$$v=0.5\left(\frac{u_0\nu}{x}\right)^{0.5}(\eta\Phi-\Phi)$$

$$c=c_0+(c^*-c_0)\Psi$$

$$\eta=y\left(\frac{u_0}{4Dx}\right)^{0.5}, \quad \Phi=\Phi(\eta), \quad \Psi=\Psi(\eta)$$

As a result we obtain:

$$\Phi'''+\varepsilon^{-1}\Phi\Phi''=0, \quad \Psi''+\varepsilon\Phi\Psi'=0 \tag{3}$$

$$\Phi(0)=\theta\Psi'(0), \quad \Phi'(0)=0, \quad \Psi(0)=1$$

$$\Phi'(\infty)=2\varepsilon^{-1}, \quad \Psi(\infty)=0$$

where:

$$\varepsilon=Sc^{0.5}, \quad Sc=\frac{\nu}{D}, \quad \theta=\frac{\mathscr{M}(c^*-c_0)}{\varepsilon p_0}. \tag{4}$$

The solution of (3) can be found from:

$$\Phi=\Phi_0+\theta\Phi_1+\theta^2\Phi_2+\ldots$$

$$\Psi=\Psi_0+\theta\Psi_1+\theta^2\Psi_2+\ldots \tag{5}$$

as θ is a small parameter.

Substitution of Eq. (5) into (3) leads to systems of equations from which the different approximations can be obtained.

In the zeroth order approximation holds:

$$\Phi_0''' + \varepsilon^{-1}\Phi_0 F_0'' = 0, \quad \Psi_0'' + \varepsilon\Phi_0\Psi_0' = 0 \tag{6}$$

$$\Phi_0(0) = 0, \quad \Phi_0'(0) = 0, \quad \Phi_0'(\infty) = \frac{2}{\varepsilon}$$

$$\Psi_0(0) = 1, \quad \Psi_0(\infty) = 0$$

The solution of (6) can be obtained directly [1, 2]:

$$\Phi_0(\eta) = f(z)$$

$$\Psi_0(\eta) = 1 - \frac{1}{\varphi_0}\int_0^z E(\varepsilon, p)\, dp, \quad z = \frac{2}{\varepsilon}\eta, \tag{7}$$

where:

$$\varphi_0 = \int_0^\infty E(\varepsilon, p)\, dp \approx \begin{cases} 3.01 Sc^{-0.35} - \text{for gases [8]} \\ 3.12 Sc^{-0.34} - \text{for liquids } \textit{(Table 1)} \end{cases} \tag{8}$$

$$E(\varepsilon, p) = \exp\left[-\frac{\varepsilon^2}{2}\int_0^p f(s)\, ds\right]$$

and $f(z)$ is a solution of the problem:

$$2f''' + ff'' = 0 \tag{9}$$

$$f(0) = f'(0) = 0, \quad f'(\infty) = 1.$$

Table 1.

Sc	φ_0	$3.12\ Sc^{-0.34}$	φ_3	$5.08\ Sc^{-0.67}$
100	0.656	0.652	0.233	0.232
225	0.494	0.495	0.135	0.135
400	0.406	0.407	0.0916	0.0917
625	0.349	0.350	0.0679	0.0681
900	0.308	0.309	0.0532	0.0533
1225	0.278	0.278	0.0433	0.0433
1600	0.254	0.254	0.0362	0.0362
2025	0.234	0.234	0.0308	0.0309
2500	0.218	0.218	0.0267	0.0269

The first order approximation of the solution of Eq. (3) is:

$$\Phi_1''' + \varepsilon^{-1}(\Phi_0\Phi_1'' + \Phi_1\Phi_0'') = 0 \tag{10}$$

$$\Psi_1'' + \varepsilon(\Phi_0\Psi_1' + \Phi_1\Psi_0') = 0$$

$$\Phi_1(0) = \Psi_0'(0), \quad \Phi_1'(0) = 0, \quad \Phi_1'(\infty) = 0$$

$$\Psi_1(0) = 0, \quad \Psi_1(\infty) = 0$$

The solution of (10), using (7) is:

$$\Phi_1(\eta) = -\frac{2}{\varepsilon\varphi_0}\varphi(z)$$

$$\Psi_1(\eta) = \frac{\varepsilon\varphi_3}{\varphi_0^3}\int_0^z E(\varepsilon, p)\,dp - \frac{\varepsilon}{\varphi_0^2}\int_0^z\left[\int_0^p \varphi(s)\,ds\right]E(\varepsilon, p)\,dp, \tag{11}$$

where:

$$\varphi_3 = \int_0^\infty\left[\int_0^p \varphi(s)\,ds\right]E(\varepsilon, p)\,dp \approx \begin{cases} 6.56Sc^{-0.8} - \text{for gases [8]} \\ 5.08Sc^{-0.67} - \text{for liquids } \textit{(Table 1)} \end{cases} \tag{12}$$

while $\varphi(z)$ is a solution of the problem:

$$2\varphi''' + f\varphi'' + f''\varphi = 0 \tag{13}$$

$$\varphi(0) = 1, \quad \varphi'(0) = 0, \quad \varphi'(\infty) = 0$$

The second-order approximation of the solution of Eq. (3) is

$$\Phi_2''' + \varepsilon^{-1}(\Phi_0\Phi_2'' + \Phi_2\Phi_0'' + \Phi_1\Phi_1'') = 0 \tag{14}$$

$$\Psi_2'' + \varepsilon(\Phi_0\Psi_2' + \Phi_2\Psi_0' + \Phi_1\Psi_1') = 0$$

$$\Phi_2(0) = \Psi_1'(0), \quad \Phi_2'(0) = 0, \quad \Phi_2'(\infty) = 0$$

$$\Psi_2(0) = 0, \quad \Psi_2(\infty) = 0$$

Table 2.

Sc	φ_{33}	$12.2\,Sc^{-1}$	φ_{33}	$-0.035\,Sc^{-1.1}$
100	0.127	0.122	−0.000192	−0.000221
225	0.0552	0.0542	−0.0000946	−0.0000905
400	0.0307	0.0305	−0.0000518	−0.0000481
625	0.0196	0.0195	−0.0000315	−0.0000294
900	0.0135	0.0135	−0.0000206	−0.0000197
1225	0.00994	0.00996	−0.0000143	−0.0000140
1600	0.00760	0.00762	−0.0000104	−0.0000105
2025	0.00598	0.00602	−0.00000780	−0.00000807
2500	0.00480	0.00488	−0.00000595	−0.00000640

Eq. (14) can be solved using Eq. (7) and (11):

$$\Phi_2(\eta) = \frac{2\varphi_3}{\varphi_0^3}\varphi(z) - \frac{4}{\varepsilon^2\varphi_0^2}\bar{\varphi}(z) \tag{15}$$

$$\Psi_2(\eta) = \left(-\frac{2\varepsilon^2\varphi_3^2}{\varphi_0^5} + \frac{\varepsilon^2\varphi_{33}}{2\varphi_0^4} + \frac{2\bar{\varphi}_{33}}{\varphi_0^4}\right)\int_0^z E(\varepsilon, p)\,dp + \frac{2\varepsilon^2\varphi_3}{\varphi_0^4}\int_0^z\left[\int_0^p \varphi(s)\,ds\right]E(\varepsilon, p)\,dp -$$

$$-\frac{\varepsilon^2}{2\varphi_0^3}\int_0^z\left[\int_0^p \varphi(s)\,ds\right]^2 E(\varepsilon, p)\,dp - \frac{2}{\varphi_0^3}\int_0^z\left[\int_0^p \bar{\varphi}(s)\,ds\right]E(\varepsilon, p)\,dp,$$

where:

$$\varphi_{33} = \int_0^\infty\left[\int_0^p \varphi(s)\,ds\right]^2 E(\varepsilon, p)\,dp \approx \begin{cases} 24Sc^{-1.3} - \text{for gases [8]} \\ 12.2Sc^{-1} - \text{for liquids } \textit{(Table 2)} \end{cases} \tag{16}$$

$$\bar{\varphi}_{33} = \int_0^\infty\left[\int_0^p \bar{\varphi}(s)\,ds\right]E(\varepsilon, p)\,dp \approx \begin{cases} 0.326Sc^{-1.63} - \text{for gases} \\ -0.035Sc^{-1.1} - \text{for liquids } \textit{(Table 2)} \end{cases}$$

while $\bar{\varphi}(z)$ is a solution of the problem:

$$2\bar{\varphi}''' + f\bar{\varphi}'' + f''\bar{\varphi} = \varphi\varphi'' \tag{17}$$

$$\bar{\varphi}(0) = 0, \quad \bar{\varphi}'(0) = 0, \quad \bar{\varphi}'(\infty) = 0$$

The Mass Transfer Kinetic

The nonlinear mass transfer average rate for a plate of a length "L" can be determined from the average mass flux [1, 2]:

$$J = \mathcal{M}k(c^* - c_0) = \frac{1}{L}\int_0^L I\,dx. \tag{18}$$

This flux has a diffusive and a convective component, as a result of the initiated flow on the interphase [3, 4], and can be determined from:

$$I = -\frac{\mathcal{M}D\varrho^*}{\varrho_0}\left(\frac{\partial c}{\partial y}\right)_{y=0}, \quad \varrho^* = \varrho_0 + \mathcal{M}c^*, \tag{19}$$

where ϱ_0 is the density of the gas (liquid) flowing along the rigid plate. The Sherwood number can directly be obtained from Eq. (2), (18), (19):

$$Sh = \frac{kL}{D} = -\frac{\varrho^*}{\varrho_0(c^* - c_0)}\int_0^L\left(\frac{\partial c}{\partial y}\right)_{y=0} dx = -\frac{\varrho^*}{\varrho_0}Pe^{0.5}\Psi'(0), \tag{20}$$

Table 3.

Θ	$\varepsilon=1$		$\varepsilon=2$		$\varepsilon=10$		$\varepsilon=20$	
	$-\Psi'_N(0)$	$-\Psi'(0)$	$-\Psi'_N(0)$	$-\Psi'(0)$	$-\Psi'_N(0)$	$-\Psi'(0)$	$-\Psi'_N(0)$	$-\Psi'(0)$
0	0.664	0.664	0.535	0.535	0.314	0.305	0.250	0.246
+0.03	0.650	0.650	0.515	0.516	0.270	0.265	0.190	0.199
−0.03	0.679	0.679	0.553	0.555	0.384	0.365	0.406	0.363
+0.05	0.641	0.641	0.503	0.504	0.248	0.250	0.166	0.205
−0.05	0.689	0.689	0.572	0.570	0.459	0.415		0.479
+0.10	0.620	0.620	0.475	0.478	0.207	0.250		0.355
−0.10	0.716	0.716	0.616	0.611		0.581		0.903
+0.20	0.581	0.584	0.429	0.442	0.160	0.418		1.229
−0.20	0.779	0.776	0.736	0.707		1.080		2.325
+0.30	0.548	0.555	0.393	0.425		0.808		2.868
−0.30	0.855	0.843	0.936	0.822		1.800		4.512

where:

$$Pe = \frac{u_0 L}{D}, \tag{21}$$

while $\Psi'(0)$ can be determined from Eq. (5), (7), (11) and (15):

$$\Psi'(0) = -\frac{2}{\varepsilon\varphi_0} + \theta\frac{2\varphi_3}{\varphi_0^3} + \theta^2\left(-\frac{4\varepsilon\varphi_3^2}{\varphi_0^5} + \frac{\varepsilon\varphi_{33}}{\varphi_0^4} + \frac{4\bar{\varphi}_{33}}{\varepsilon\varphi_0^4}\right). \tag{22}$$

Comparison of the results obtained from the asymptotic theory (22) for a dimensionless diffusive flow, with data from the numerical theory $\Psi'_N(0)$, discussed in [5], is shown in *Table 3*.

The accuracy of the asymptotic solution (22) depends on the values of θ and can be accepted as satisfactory if its smallest correction is not bigger that one tenth of the value of zeroth-order approximation:

$$\left|\theta^2\left(-\frac{4\varepsilon\varphi_3^2}{\varphi_0^5} + \frac{\varepsilon\varphi_{33}}{\varphi_0^4} + \frac{4\bar{\varphi}_{33}}{\varepsilon\varphi_0^4}\right)\right| \leqq 0.1\left|-\frac{2}{\varepsilon\varphi_0}\right| \tag{23}$$

The boundory values of θ, for which the asymptotic solution has an acceptable accuracy, can be directly determined from Eq. 23. These values obviously depend on the Schmidt number and for the cases in *Table* 3 one obtains:

$\varepsilon = 1 \quad \theta \leqq 0.41$
$\varepsilon = 2 \quad \theta \leqq 0.23$
$\varepsilon = 10 \quad \theta \leqq 0.056$
$\varepsilon = 20 \quad \theta \leqq 0.025$

These results are very well confirmed by those obtained with the numerical theory *(Table 3)*. In some, a numerical solution cannot provide solutions due to an increasing singular perturbation (or stiffness) of the solution of the boundary value problem.

Conclusion

The results obtained demonstrate that intensive mass transfer from the volume to the solid surface ($\theta > 0$) leads to increasing the rate of the mass transfer in comparison to the linear theory predictions ($\theta = 0$). When mass transfer is from the solid surface to the volume ($\theta > 0$), its rate decreases. The relationship for a mass transfer rate, accurate to the second order approximation for θ, obtained, provides the necessary accuracy for solving different problems in chemical engineering.

REFERENCES

1. BOYADJIEV, CHR. and BESCHKOV, V.: Mass Transfer in Liquid Film Flows. Publ. House Bulg. Acad. Sci., 1984, pp. 102–107.
2. BOYADJIEV, CHR. and MITEV, PL.: Chem. Eng. J. *1977*, 14, 225–228.
3. BOYADJIEV, CHR.: Int. J. Heat Mass Transfer *1982*, 25 (4), 535–540.
4. BOYADJIEV, CHR.: Int. J. Heat Mass Transfer *1984*, 27 (8), 1277–1280.
5. BOYADJIEV, CHR. and VULCHANOV, N.: C. r. Acad. Bulg. Sci. *1987*, 40 (11), 35–38.
6. BOYADJIEV, CHR. and VULCHANOV, N.: C. r. Acad. Bulg. Sci. *1988*, 41 (10), 49–52.
7. BOYADJIEV, CHR. and VULCHANOV, N.: Chem. Eng. Sci. (in press).
8. BOYADJIEV, CHR. and TOSCHEV, E.: J. Eng. Phys. (USSR) – in press.
9. BOYADJIEV, CHR. and VULCHANOV, N.: Int. J. Heat Mass Transfer (in press).

HUNGARIAN JOURNAL
OF INDUSTRIAL CHEMISTRY
VESZPRÉM
Vol. 17. pp. 465–475 (1989)

DECREASE OF IRON CONTENT OF BAUXITE THROUGH HIGH TEMPERATURE CHLORINATION

I. SZABÓ, A. ÚJHIDY, R. JELINKÓ, AND I. VASSÁNYI*

(Research Institute for Technical Chemistry of the Hungarian Academy of Sciences, Veszprém, Hungary; *University of Chemical Engineering, Veszprém, Hungary)

Received: May 12, 1989

Selective iron extraction from Hungarian bauxite of low grade was studied in the temperature range of 600–850 °C, in a chlorine flow, using a batch chlorination device and a fluidized bed of laboratory scale. A reduction of Fe_2O_3 content from 16.8% to 3-3.5% was achieved. The results of structure analytical methods (DTG, X-ray diffractometry, Moessbauer spectroscopy, and EDAX, etc.) proved that acidic extraction and the chlorination studied are suitable only for extracting that part of the iron content, which is in hematite or in goethite form, while the iron content built into the mineral structure, having an oxidation degree of three and co-ordination number six, cannot be removed by these methods. The previous reduction or sulphidation of the samples before iron reducing chlorination also only affected the hematite phase. This means that the method tested is suitable only for iron content reduction and not for total iron extraction.

Introduction

When anhydrous aluminum chloride is produced from minerals by high temperature reductive chlorination, the iron content always causes difficulties, because it is chlorinated together with the aluminum content and forms an impurity that cannot be easily removed from the product. An iron chloride content in anhydrous aluminum chloride is especially disturbing if metallic aluminium is to be made by chloride electrolysis, in which case the $FeCl_3$ content permitted is only a few ppm. The product composite obtained by the chlorination of bauxite can be relatively easily separated from $SiCl_4$ and $TiCl_4$ since the volatility of these compounds is higher than that of aluminum chloride. The separation of $AlCl_3$ and $FeCl_3$ by rectification is, however, diffucult because $FeAlCl_6$ is formed in the vapour phase. Consequently it is reasonable to extract the iron content or at least to lessen it before removal of the aluminum by chlorination.

The most commonly applied and oldest method of iron removal is solvent extraction which is performed with mineral acids, usually with hydrochloric acid [1–3]. This process is, however, very slow and during the long period of solvent extraction not only the iron content, but also a part of the less reactive aluminum content is dissolved. Iron removal with ammonium chloride can be regarded as a solvent extraction in which iron is attacked during the heating of the bauxite – NH_4Cl mixture in the solid phase and this procedure is followed by aqueous leaching [4, 5]. Another possibility to remove iron is high temperature chlorination without using any reductive agent during chlorination [6–8]. Much effort was devoted to transform the iron content into a more active form before chlorination and thus increase the efficiency of chlorination. For example, under intensive reductive conditions the iron content can be reduced to elementary iron. Using solid carbon a satisfactory reduction rate can be achieved at about 1000 °C, the iron content can be decreased after that by chlorination even below 1% [9]. Performing the reduction with hydrogen and dissolving the FeO formed in this way in hydrochloric acid, a very low iron content can be obtained, but the reaction rate is so slow that this method is unsuitable for practical application [2]. Transforming the iron content into sulphide may lead to considerable losses in aluminum content [10]. Performing the sulphidation and then the reduction at high temperature (1340 °C), the iron content can be nearly perfectly removed by chlorination, but the reaction conditions and the use of sulphur do not permit practical use [11].

In order to find a method of selective Fe_2O_3 or Al_2O_3 extraction, the thermodynamical probabilities of 450 possible gas-solid chemical reactions were studied by MILNE and HOLLIDAY [12] for bauxite components and reagents that can be used in practice. They pointed out that a direct transformation of the iron content by chlorination into $FeCl_2$ or $FeCl_3$ without any reaction of Al_2O_3 is a possible, but very slow process. An indirect removal of iron content by chlorination is possible at relatively low temperature after forming FeS, FeS_2, Fe_2N, Fe and $FeCO_3$ with cheap reagents in the first step. For this latter purpose, the mixture of SO_2 and CO seems to be especially advantageous. In the reported experiments, the iron content of bauxite was decreased to 0.1–0.3% from the original 7–8% by sulphidation and chlorination, having an aluminum loss of about 2% [13].

One of our tasks was to determine the limit of Fe_2O_3 extraction in the direct chlorination of bauxites with relatively high iron content and to find out why this purity limit cannot be exceeded. On the other hand, a reduction of this limit or if possible, a perfect iron removal was intended to be achieved.

Experimental

The oxide and phase composition *(Table 1)* and the morphology of the Gánt bauxite used as model material is a good representative of the Hungarian low grade bauxites excavated by open-cast mining. The processing of these bauxites

Table 1.
Phase composition, oxide composition, calculated from phase composition and oxide composition analyzed in bauxite, %

Phase	Quantity of phase	TiO_2	Al_2O_3	FeO_3	SiO_2	H_2O
Moisture content and chemisorbed water	2.00	–	–	–	–	2.00
Gibbsite	5.79	–	3.78	–	–	2.01
Boehmite	30.60	–	26.00	–	–	4.60
Kaolinite	34.70	–	13.70	–	16.20	4.80
Chlorites	8.30	–	4.50	0.1-0.2	2.50	1.14
Alumo-goethit	10.70	–	0.98	8.58	–	1.14
Hematit (+ others)	8.00	–	(?)	8.00	–	–
Rutile and anatase	2.10	2.10	–	–	–	–
Total	102.2	2.10	48.98	16.80	18.70	15.69
Chemical analysis:	99.8	2.10	47.70	16.80	18.70	14.50*

*Heating loss (referring to sample dried at 105 °C)

with bad modulus value might prove to be more economic in the future by halogen metallurgy than by the conventional Bayer-Hall method. It derives from the paleogene age, is relatively soft, and can be easily powdered. Before treating it with chlorine gas, the raw material had to be dehydrated, since its water content disturbs chlorination (formation of hydrochloric acid, and hydrolysis). The optimum temperature of dehydration is determined by the requirement that the material to be chlorinated has to lose its water content perfectly, but formation of alpha-aluminum oxide, which cannot be easily chlorinated, should not start. From this point of view, a treatment at 750 °C for 45 minutes proved to be suitable.

The samples of 1–2 g were treated in a *boat-type, heated tube device*. The given gas or gas mixture was streamed with a flow rate of 8–12 l (STP)/h in a heated quartz tube (20 mm I. D.) over the sample filled into a quartz boat. The product of reaction was absorbed in diluted hydrochloric acid. After a properly chosen experimental time, the mass reduction, composition of the samples and the quantities of the components trapped in the absorbent were measured.

The *fluidization type chlorination device* consisted of a vertical quartz tube with an inner diameter of 50 mm and length of 900 mm, its external surface was electrically heated. The fluidized bed formed by bauxite grains with diameters of 0.3–0.8 mm filled the lower third part of the tube, over a porous quartz plate. The space under the fluid bed was used for preheating the gas introduced at the lower end. The powder content of the gas, leaving through an outlet at the upper part of the tube, was separated in a heated cyclone, then the reaction products were condensed and absorbed in cooled vessels.

Results and Discussion

The results of the experiments carried out in the boat type, heated tube device proved *(Table 2)* that a selective extraction of most of the iron content is possible. It was found that after a period of 30 minutes, the process slowed down

Table 2.

Deironing experiments in the boat-type, heated tube device

Test No.	Pretreatment				Deironing			F, %	X, %		
	t, °C	CO, l/h	SO_2 l/h	τ, min	t, °C	Cl_2, l/h	τ, min		Al_2O_3	SiO_2	Fe_2O_3
B1	–	–	–	–	850	8	60	3.6	0.0	2.5	84.1
B2	–	–	–	–	850	8	30	4.6	0.0	2.1	80.0
B3	850	12	–	30	850	8	60	3.4	0.3	2.7	85.8
B4	700	12	–	30	700	8	30	3.8	0.2	3.6	83.1
B5	850	12	–	15	850	8	30	3.6	0.4	4.1	84.7
B6	850	12	–	15	850	8	30	4.2	0.4	2.5	82.0
B7	850	10	5	30	850	8	60	3.2	0.3	3.4	87.9
B8	700	10	5	30	700	8	30	3.5	0.3	3.1	85.3
B9	850	10	10	30	850	8	60	3.3	0.4	2.9	86.1

Particle size of bauxite: 0.3-0.8 mm

and after achieving a Fe_2O_3 content of 3–4% it practically stopped (Tests B1 and B2). The lowest iron content was obtained by pretreatment with a $SO_2 + CO$ gas mixture, but even this minimum value meant 3.2% Fe_2O_3. Permitting a few percent of SiO_2 conversion in the experiments, the Al_2O_3 loss increased to a few tenths of a percent, i. e. the selectivity was acceptable.

In the fluidized bed experiments, the iron extracting chlorination was performed with different Cl_2/N_2 gas mixtures to keep the bed in a fluidized state and decrease the chlorine excess *(Table 3)*. In this case, a removal of only cca. 50% of the iron content was achieved (V1, V2). A nitrogen content of about 25 v/v% in the chlorinating gas resulted in a considerable decrease in efficiency (V3), while the presence of CO in 10 v/v% facilitated the removal of iron, but at the same time it caused significant Al_2O_3 losses (V4). A further decrease in the CO content did not lead to satisfactory selectivity either (V5) and with a shorter time of treatment the efficiency was also low (V6). A simultaneous increase in selectivity and purity could also not be provided by Cl_2/CO treatment at much

Table 3.

Deironing experiments in fluidized bed

No. of runs	t, °C	τ, min	v, l(STP)/h			F, %	X*, %		
			Cl_2	CO	N_2		Al_2O_3	SiO_2	Fe_2O_3
V1	850	30	150	–	225	8.6	0.0	0.2	60.3
V2	850	30	200	–	200	8.4	0.0	0.2	60.7
V3	850	60	300	–	100	5.5	0.0	0.3	75.4
V4	850	60	300	30	–	1.8	10.7	16.0	93.3
V5	850	40	300	5	–	6.6	0.3	0.9	70.3
V6	850	60	300	5	–	3.8	0.4	3.4	83.9
V7	650	60	150	200	–	4.2	44.3	51.5	90.2
V8	450	60	180	270	–	11.5	2.8	8.2	48.0
V9	850	60	300	–	–	3.5	0.1	3.2	85.6

*Referring to the original bauxite sample

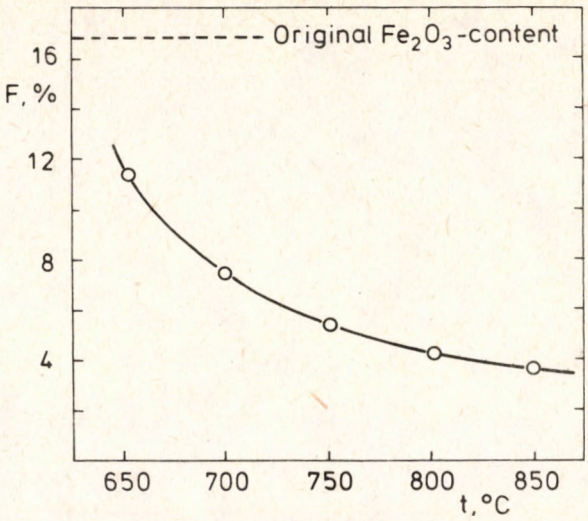

Figure 1.
Effect of temperature on the effectiveness of deironing treatments with chlorine gas. Sample: 150 g bauxite calcined. Conditions of the deironing experiments: 60 min; 300 l (STP)/h Cl_2 gas; fluidized bed.

higher temperatures (V7, V8). Evidently a satisfactory iron removal can be achieved only with a pure chlorine gas stream providing a fluidized state and with a period of treatment not less than 60 minutes. The role of the temperature was studied in the range 650-850 °C under such conditions *(Fig. 1)*. Increasing the temperature, the lowest value of Fe_2O_3 content again proved to be 3–3.5%.

Dehydration (calcination) of the raw material before treatment with chlorine gas proved to be necessary in all cases, so it seemed to be reasonable to perform it together with the previous reduction. In *Fig. 2,* the iron contents of samples calcined in a fluidized bed, in neutral gas (N_2) and in reducing gas (CO) streams are plotted against time, keeping the parameters at constant levels (850 °C, 300 l (STP)/h Cl_2) during the iron-extracting chlorination. The lowest value of the iron content was 3.0–3.5%, this purity could not be exceeded even with reductive pretreatment, though the limit was more rapidly achieved in this way. It is also clear from this figure that most of the iron content leaves in the first 30 minutes (using a reductive pretreatment in the first 10 minutes), then the process rapidly slows down.

From the results of these experiments, it can be concluded that the given type of bauxite cannot be perfectly freed of iron in the process studied, an amount of 3.0–3.5% Fe_2O_3 remains in the samples in all cases, even after the pretreatments mentioned earlier. The presence of iron modifications built into the structure of minerals from where they cannot be removed by chlorination is confirmed by the fact that an amount of 0.2–1.0% Fe_2O_3 remains in the samples even after chlorination in a reductive atmosphere ($Cl_2 + CO$), carried out to produce $AlCl_3$. It was therefore presumed that two kinds of iron content

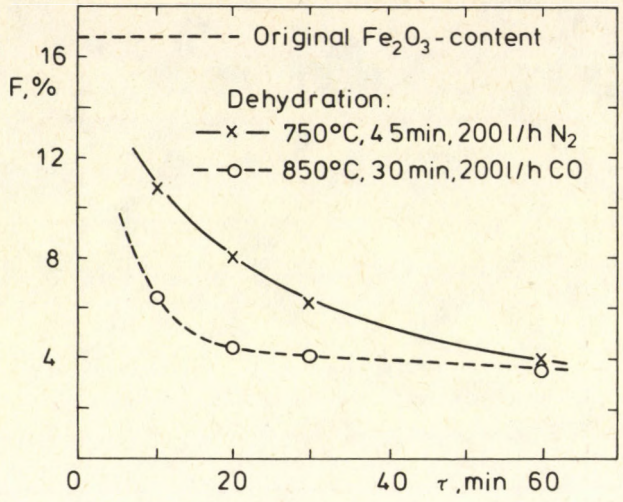

Figure 2.
Effect of reductive pretreatment on the rate of deironing with chlorine gas. Sample: 175 g bauxite with Fe_2O_3 content of 16.8%; 850 °C; 60 min; 300 l (STP)/h Cl_2 gas; fluidized bed.

co-exist (or are formed during the treatment) in the bauxite; one of them can be more easily chlorinated, while the other less easily. In order to follow their quantitative and qualitative variations, the following experiments were performed.

The iron oxide acitivity indicating the reactivity of iron containing minerals was expressed as the ratio of Fe_2O_3 soluble in oxalate buffer and in hydrochloric acid. The successive hydrochloric acid leaching tests were carried out with a first treatment of the original bauxite in hydrochloric acid solution of 8% for 1 hour at a temperature of 80-90 °C, then the residue was put again into hydrochloric acid solution of 8% for 3 hours, finally the residue of the second treatment was treated in a hydrochloric acid solution of 20% for 3 hours. Another part of the original sample was used to determine the quantity of Fe_2O_3 soluble in oxalate by treating it with oxalate buffer at 60 °C for 6 hours. The following results were obtained

	1. solving	2. solving	3. solving	Total
Weight loss, %	14.5	10.8	8.1	33.4
Fe_2O_3 dissolved in hydrochloric acid, %	9.5	3.7	0.6	13.8
Fe_2O_3 dissolved in oxalate buffer, %	–	–	–	3.1

Iron oxide activity =

$$= \frac{Fe_2O_3 \text{ soluble in oxalate buffer}}{Fe_2O_3 \text{ soluble in hydrochloric acid}} = \frac{3.1}{13.8} = 0.22$$

Such a value of activity is characteristic for iron containing minerals of relatively low reactivity. It is nevertheless remarkable that the total amount of Fe_2O_3 dissolved by hydrochloric treatment was only 82% of the total Fe_2O_3 content of the sample analyzed chemically (16.8%). An even more aggressive treatment did not result in a perfect dissolution of iron oxide content either.

According to the results of *X*-ray diffractometry, the treatment with hydrochloric acid mainly affected the mineral phases containing iron: hematite and most of the geothite was also removed. The difference-IR spectra and derivatograms showed that the gibbsite, kaolinite and chlorite contents were also slightly affected by acid treatment. The difference between mass loss and dissolved Fe_2O_3 presumably derived from this fact. In *Fig. 3,* Moessbauer spectra of the

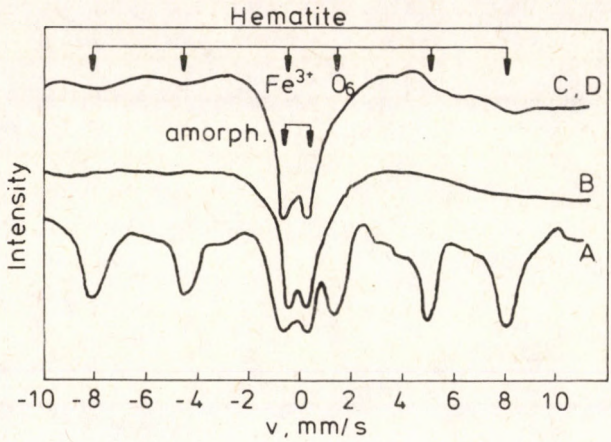

Figure 3.
Moessbauer spectra of bauxite samples after calcination and deironing treatments
A bauxite calcined (750 °C, 45 min)
B bauxite calcined and treated with HCl (18% conc., 95 °C and 60 min)
C bauxite calcined and treated with Cl_2 gas (in fluidized bed, 850 °C and 60 min)
D bauxite calcined and treated with $COCl_2$ gas (in fluidized bed, 750 °C and 20 min)

original bauxite and that of the sample after hydrochloric treatment are shown. The spectrum of the original bauxite has the typical hematite lines. The peaks of iron with a valency of 3, co-oridnation value of 6 can also be seen, indicating amorphous type, and peaks referring to iron with a valency of 2 are also there. The hematite lines were eliminated by hydrochloric treatment of 1 hour, while the iron peaks belonging to iron with oxidation degrees of two and three were still present. The intensity of the peak representing iron with an oxidation degree

of three and a co-ordination value of six did not decrease during the further hydrochloric treatment of several hours, i. e. this type of iron content could not be removed.

The original bauxite sample, the calcined samples and the residues of the iron removal tests were investigated with the same methods. According to the *X*-ray diffractometric phase analysis, the kaolinite content of the bauxite decomposed in the process of calcination performed at 750 °C for 45 minutes before the iron removal tests with chlorine gas: the reflection observed around 0.44 μm indicates that some parts of the destroyed kaolin lattice survived the treatment. The decay of boehmite, chlorite, gibbsite, goethite, and calcite was perfect, anatase and rutile did not change. The quantity of hematite increased as a result of the goethite decay. Treating this calcined sample during the more and more aggressive steps of the series V1 → V5 a gradual decrease in hematite content was observed. In the residue of the test V1 hematite is a dominant phase, together with gamma-aluminum oxide, while in the residue of test V5 no hematite was found. The reflections referring to anatase and rutile gradually decreased in the series V1-V5 as well; they disappeared in the tests V4 and V5, respectively. A small amount of ferrocorundum was observed in the residues of each test. The small quantity of this material and the frequent peak overlappings made the identification of ferrocorundum peaks uncertain. This fact is reflected by the data of *Table 4*. reffering to the d-values of reflections caused by phases regarded as ferrocorundum in the residues of test V1-V5. A typical shift of these values toward *d*-values of pure ferrocorundum can be observed. The observed decrease in iron content might have been caused by the chlorine

Table 4.
The *d*-values of some reflexions of ferrocorundum phase on the *X*-ray pattern in the bauxite samples treated with chlorine gas in fluidized bed, nm.

Sample	(012)	(104)	Miller index (110)	(113)	(116)
V1	–	–	0.2449	0.2132	0.1645
V2	–	0.2622	0.2436	0.2138	0.1643
V3	–	0.2607	0.2436	0.2132	0.1637
V9	0.3541	0.2603	0.2429	0.2126	0.1633
V4	0.3520	0.2602	0.2420	0.2118	0.1629
Corundum in literature	0.3479	0.2552	0.2379	0.2085	0.1601

treatments of increasing aggressivity, nevertheless this process seems to be much less intense than the chlorination of hematite. Some iron content may have remained in the amorphous phase and in the gamma aluminum oxide, but the iron content of these parts are not known. It can be seen that the further the chlorination process advanced, the closer the d values got to that referring to pure corundum.

The Moessbauer spectrum of the residue obtained in test V4 is shown in *Fig.*

3.). As a result of chlorination performed at 850 °C for 60 minutes, the hematite content of the sample almost totally disappeared, the intensity of iron with a valency of two drastically decreased, the iron content remaining in the sample had a valency of three and a co-ordination number of six, just as in the case of hydrochloric acid treatment. This is the form of iron in bauxite, which cannot be easily chlorinated. This conclusion is confirmed by the fact that the Moessbauer spectrum of the residue obtained in a clorination test carried out for 20 minutes in a reductive ($COCl_2$) atmosphere at 750 °C (during which a mass loss of 34% was observed and 81% of the iron content left the sample) practically did not differ from the spectrum of the sample the iron content of which was reduced by chlorine *(Fig. 3.)*. These results are in good accordance with data obtained by magnetic susceptibility measurements; at the beginning of chlorination, the samples were definitely paramagnetic, and in the process of chlorination their magnetic property became diamagnetic.

Since the previous reduction or sulphidation increased only the rate of iron removal by chlorination and did not influence the limit of iron content, it seemed to be probable that these pretreatments convert only the hematite content into a form that can be more easily chlorinated, while the other iron components are not altered.

In order to study the behaviour of hematite during a reduction process with carbon monoxide and in the treatment with chlorine gas following the reduction, some investigations were carried out earlier [14.] From these examinations it became clear that the rate of chlorination reaction is proportional to the length of the reductive pretreating period of hematite before chlorination. It has been shown by *X*-ray diffraction measurements that in the reduction Fe_3O_4, FeO and alpha–Fe are formed from hematite. In the chlorination following the reduction the reduced formations were chlorinated out of the system more rapidly than hematite. This can explain why no reduced formations were found in the hematite after a chlorination with Cl_2/CO gas mixture. Another important observation was that the hematite phase occurred again in those samples in which only traces of hematite were present before chlorination, due to the reduction. As no oxygen could get into the system, the only possible explanation is that during the chlorination of iron oxides, the oxygen atoms remained in the crystal lattice and a disproportionation developed, as also presumed by other authors [15, 16].

The same investigations were carried out with bauxite samples (supported by *X*-ray diffractometric and Moessbauer spectrometric studies of the samples pretreated in a reductive atmosphere) treated in a chlorine gas stream for different periods and finally chlorinated with a gas mixture of Cl_2/CO *(Fig. 4.)*. Both tests proved that a reduction was restricted to the hematite phase and resulted in the formation of considerable amounts of Fe_3O_4, FeO and alpha-Fe. According to the Moessbauer spectra, hematite almost perfectly disappeared during the reduction, but the iron content with an oxidation degree of three and a co-ordination number of six was not affected. The level of this iron content was not significantly altered by the treatment with chlorine gas either, while the reduced forms were perfectly removed and in this process the quantity of

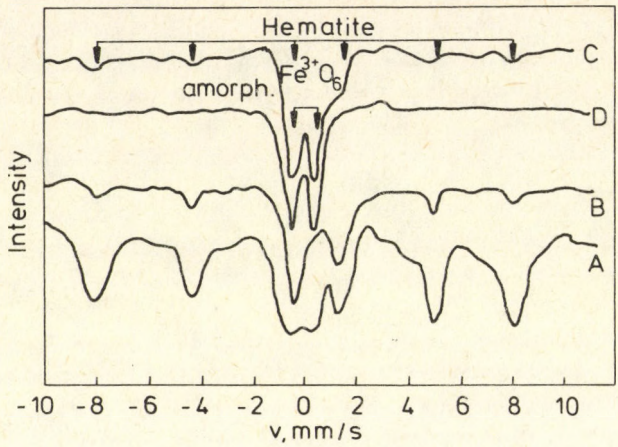

Figure 4.
Changes in Moessbauer spectra of bauxite samples during the reductive pretreatment and deironing treatment with chlorine gas
A bauxite calcined (750 °C, 45 min)
B bauxite calcined and pretreated with CO gas (in fluidized bed, 850 °C and 15 min)
C sample *B* after deironing treatment with Cl_2 gas (in fluidized bed, 850 °C and 30 min)
D sample *C* after treatment with Cl_2/CO gas mixture (in fluidized bed, 850 °C and 60 min)

hematite temporarily increased due to the „inner oxidation" mentioned earlier. This hematite sample reacted – with a rate lower than that of the reduced forms – only during the last phase of chlorination *(Fig. 4.)*. The chlorination with a gas mixture of Cl_2/CO carried out thereafter did not remove the phase presumed to be ferrocorundum perfectly, but the chlorination of this part resulted in a $FeCl_3$ content of 2.4% in the anhydrous aluminum chloride product, so that a further purification is necessary before electrolysis to produce metallic aluminum.

Conslusions

While aluminum oxide can be chlorinated only in a reductive atmosphere ($Cl_2 + CO$, $COCl_2$, $Cl_2 + C$) iron oxides react with chlorine gas even without reducing components, and at high temperatures (above 300 °C) they can be removed in the volatile form of $FeCl_3$. This fact in principle makes it possible to remove the iron content selectively from bauxite or other minerals containing aluminum without considerable losses in aluminum content. Our investigations proved, however, that this method of high temperature iron removal with chlorine gas is suitable only for the elimination of hematite. In the bauxite samples tested other iron components were also present, which are incorporated

more strongly into the mineral structure and neither the method mentioned above nor leaching with hydrochloric acid solution are suitable for perfectly removing these components. Pretreatments carried out to accelerate iron extraction (sulphidation, and reduction) affect practically only the hematite content by transforming it into a form that can be more easily chlorinated, but have no effect on the iron content built into the mineral structure. These pretreatments therefore increase only the rate of iron extraction, but do not influence the efficiency, i. e. the degree of iron removal.

The iron content which cannot be easily removed from bauxite has a degree of oxidation of three and co-ordination number of six and can be found after high temperature treatments (calcination, reductive pretreatment, iron removal with chlorine gas, and reductive chlorination) in the form of ferrocorundum. This phase does not leave the sample perfectly even during chlorination carried out in a reductive atmosphere to recover the aluminum content. It reacted partly, however, during this chlorination in a reductive atmosphere and formed an $FeCl_3$ impurity of 1-2% in the anhydrous aluminum chloride product.

The iron extracting methods investigated are therefore suitable only for reducing the iron content and not for perfect deironization. Nevertheless, they can still be advantageous in practical production.

SYMBOLS

F Fe_2O_3 content in the treated bauxite sample, %
t temperature, °C
v sample velocity of the Moessbauer spectrometer, mm/s
X conversion of metal oxides in the bauxite sample, %
τ reaction time, min

REFERENCES

1. Spitzin, V.: Z. Anorg. Chem., *1930,* 189, 350.
2. Khundkar, M. and Ahmad, N.: J. Indian Chem. Soc., *1955,* 18, 109.
3. Buntin, A.: Tr. Tomsk. Gos. Univ.: Serv. Khim., *1962,* 154, 52.
4. Hung. Pat. 150 471
5. Molnár, L.: Kohászati Lapok *1964,* 97, 360.
6. US Pat. 4 288 414
7. Hung. pat. 181 723
8. Szabó, I., Ujhidy, A., Jelinkó, R. and Szabó, L. S.: Proc. of the 4th Conf. Appl. Chem. Unit Op. and Proc., Veszprém, 1983. Vol. 1. pp. 110.
9. Foley, E. and Tittle, K.: Proc. Aust. Inst. Min. Metall., *1971,* 239. 59.
10. Finke, C. and de Marchi, V.: Trans. Electrochem. Soc., *1938,* 74, 469.
11. French Pat. 1 495 002
12. Milne, D. J. and Holliday, R. D.: Ind. Eng. Chem. Proc. Des. Dev., *1975,* 14, 442.
13. Holliday, R. D. and Milne, D. J.: Ind. Eng. Chem. Proc. Des. Dev., *1975,* 14, 447.
14. Szabó, L. S., Vassányi, I. and Szabó, S.: Sprechsaal, *1981,* 114, 437.
15. Szabó, P., Ms. Dissertation, Veszprém, 1981.
16. Neuschütz, D., Mann, E. and. Knacke, O.: Erzmetall, *1977,* 30, 464.

HUNGARIAN JOURNAL
OF INDUSTRIAL CHEMISTRY
VESZPRÉM
Vol. 17. pp. 477–490 (1989)

CHEMICAL PROCESSING OF BIOMASS II.

PRODUCTION OF LEVULINIC ACID BY ACIDIC HYDROLYSIS OF PLANT MATERIALS

L. SZOKONYA, M. KOVÁCS, GY. MARTON and J. HAVAS-DENCS

(Department of Chemical Process Engineering, Veszprém University of Chemical Engineering, Veszprém, Hungary)

Received: June 12, 1989.

The cellulose parts of plants hydrolyse to various products in the presence of acidic catalysts. The desired main product of acid hydrolysis can be varied by the appropriate selection of the operation parameters. In the case of industrial-scale cellulose hydrolysis, the diffusion rates of the products formed should be taken into consideration. A mathematical model was developed in order to describe cellulose hydrolysis accompanied by diffusion. The parameters of the solution functions of the mathematical model were identified by the Nelder-Mead optimization method by using experimental kinetic curves.

Introduction

Acid-catalyzed hydrolysis of cellulosics in one of the renewed processes to producing glucose, hydroxy-methyl-furfural, levulinic acid, formic acid and humic as the main products. The nature of the main product has changed in accordance with the demands of a given stage of the technical-economical development. Levulinic acid has been known since 1840 to result from the reaction of carbohydrates with mineral acid. It has great potential for producing diphenolic acid, pharmaceuticals, pesticides and plasticizers. A number of interesting uses are developing in the cosmetics, textile, polymer and food additive fields [1].

Kinetics of Acid Hydrolysis of Cellulose

The cellulose part of plant material can be hydrolyzed with concentrated or diluted mineral acids. The kinetics of dilute acid hydrolysis are dealt with here. The cellulose chain of a highly complicated structure consists of d-glucose units linked by β-glucosid bonds.

In an acidic medium the chain is decomposed to monomers, which are further decomposed in dehydration reactions [2]:

$$\text{cellulose} \xrightarrow{k_1} \text{glucose} \xrightarrow{k_2} \text{dehydration products} \qquad (1)$$

Considering the components identified during the decomposition of glucose and taking into account the fact that plant cellulose for certain plants consists of fast and slowly hydrolyzable parts, the mechanism of cellulose hydrolysis in a slightly acidic medium can be given according to the following scheme [3–6]:

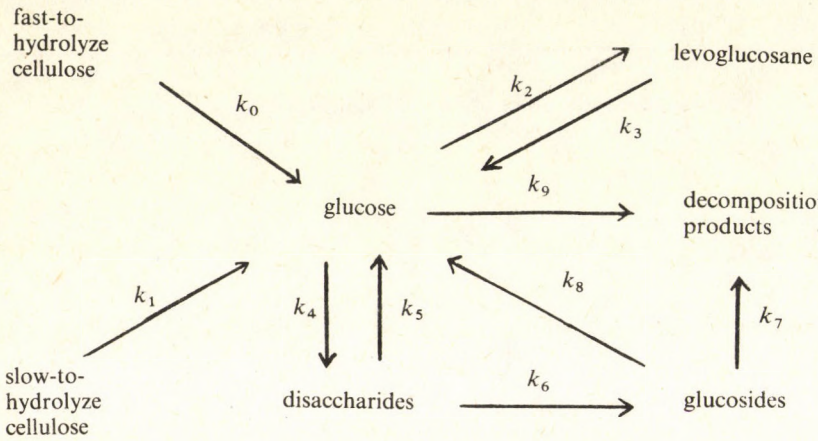

(2)

Levulinic acid yields of cellulose hydrolysis in the function of time for various plant materials are shown in *Fig. 1* and *2*. The hydrolysis of the cellulose content of the prehydrolysis residue was carried out using different concentrations of phosphoric acid. The results obtained are shown in *Fig. 3* and *4*.

Since Al^{3+}, K^+ and Na^+ ions can promote the catalytic effect of mineral acids used for cellulose hydrolysis, the effect of $Al_2(SO_4)_3$ alongside phosphoric acid was studied. The change of levulinic acid yield in the function of time obtained during cellulose hydrolysis carried out with dilute $Al_2(SO_4)_3$—H_3PO_4 solutions under various reaction conditions are shown in *Fig. 5* and *6*.

The liquid chromatogram of reed hydrolysate obtained with a solution of 2% (w/w) H_3PO_4 and 2% (w/w) $Al_2(SO_4)_3$ at a temperature of 170 °C, a hydromodulus of 7, and a contact time of 40 min is shown in *Fig. 7*.

Based on liquid chromatographic analysis, the following reaction mechanism

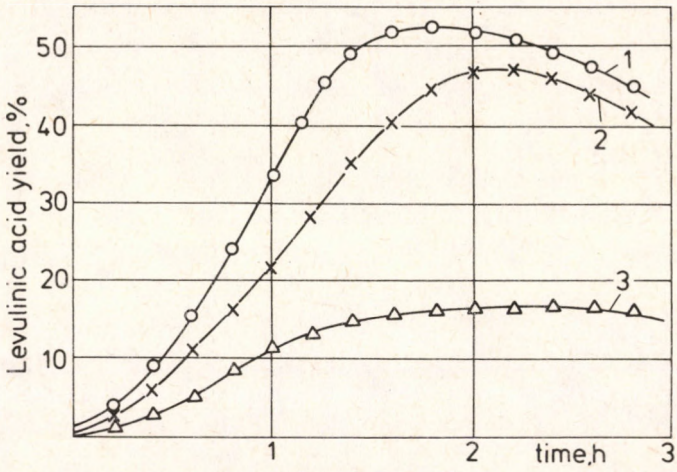

Figure 1
Levulinic acid yield
Raw material: reed; Temperature: 200 °C; Liquid-to-solid ratio = 15 : 1
1 – hydrochloric acid concentration: 2% (w/w); *2* – sulphuric acid concentration: 2% (w/w); *3* – phosphoric acid concentration: 2% (w/w).

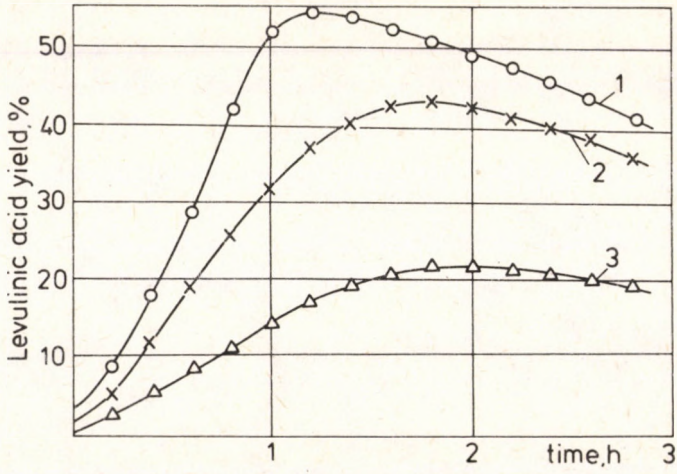

Figure 2
Levulinic acid yield
Raw material: wheat straw; Temperature: 200 °C; Liquid-to-solid ratio = 15 : 1
1 – hydrochloric acid concentration: 2% (w/w); *2* – sulphuric acid concentration: 2% (w/w); *3* – phosphoric acid concentration: 2% (w/w).

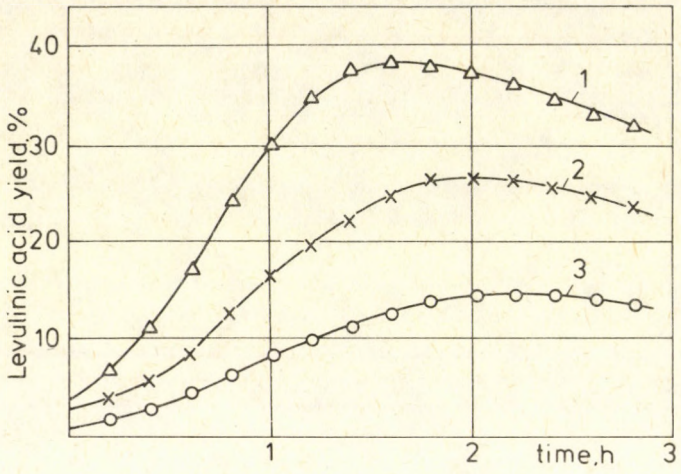

Figure 3
Levulinic acid yield
Raw material: prehydrolyzed reed residue; Temperature: 200 °C; Liquid-to-solid ratio = 9 : 1
1 – phosphoric acid concentration: 12% (w/w); *2* – phosphoric acid concentration: 6% (w/w); *3* – phosphoric acid concentration: 3% (w/w).

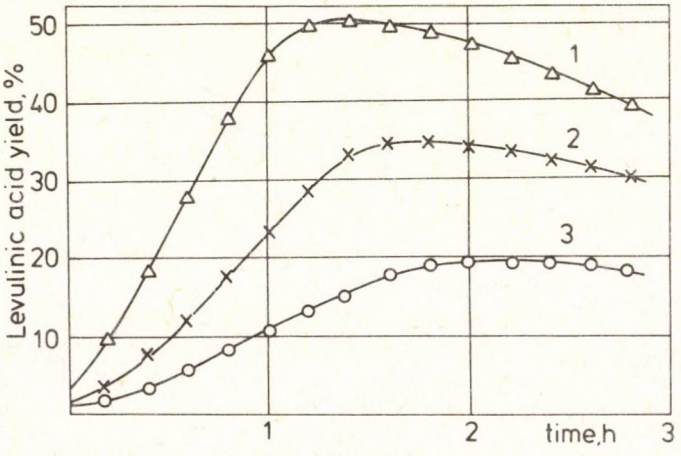

Figure 4
Levulinic acid yield
Raw material: prehydrolyzed wheat straw residue; Temperature: 200 °C; Liquid-to-solid ratio = 9 : 1
1 – phosphoric acid concentration: 12% (w/w); *2* – phosphoric acid concentration: 6% (w/w); *3* – phosphoric acid concentration: 3% (w/w).

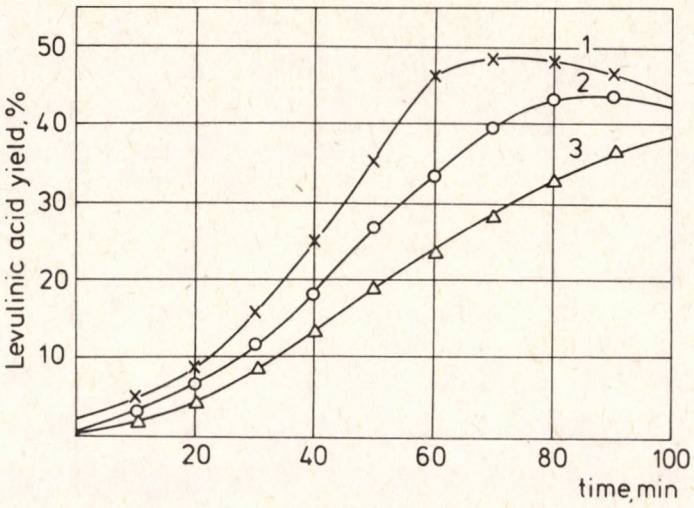

Figure 5
Levulinic acid yield
Raw material: reed; Liquid-to-solid ratio = 7 : 1; Catalysts: 2% (w/w) H_3PO_4 and 2% (w/w) $Al_2(SO_4)_3$;
1 – Temperature: 220 °C; *2* – Temperature: 200 °C; *3* – Temperature: 180 °C.

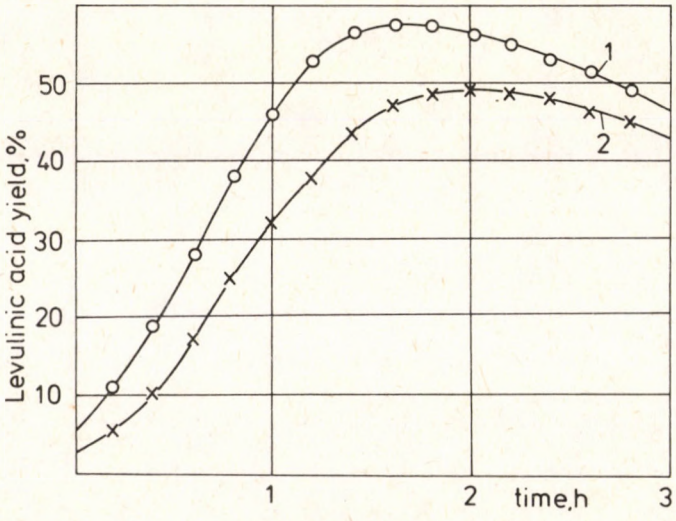

Figure 6
Levulinic acid yield
Raw materials:
1 – prehydrolyzed wheat straw residue; *2* – prehydrolyzed reed residue
Catalysts: 4% (w/w) H_3PO_4 and 4% (w/w) $Al_2(SO_4)_3$; Temperature: 200 °C; Liquid-to-solid ratio = 7 : 1

Method: \GILSON\LEVULIN.USR\LEVUL.MTH
Data: \GILSON\LEVULIN.USR\LEVUL.069\DATA008.DAT
Report: \GILSON\LEVULIN.USR\LEVUL.069\LEVUL.008
Inject time: Tue Mar 07 1989 12 : 15 : 47
Reanalysis on: Tue Mar 07 1989 16 : 19 : 54

Collection Method: LEVUL.069 Analysis Method: LEVUL
Cycle: 1 Sample: 8 Loop: (8/30)
Analysis Channel: B

Operator: Jutka
Detector: Gilson 131 RID
Column: BST HH-08
Flow: 0.7 ml/min
Mobile Phase: 0.006N H2SO4
Inject volume: 20 ul
Temperature: 40C

Integration time 19.90 min
Peak width 0.40 min
Peak sensitivity 2.0%
Minimum height 20
Sample amount 1.000
Factor 0.010

Internal standard report
Standard: succin

RT	Height	Amount	% Conc	Label
7.22	329			
8.26	1214	1.704e−001	1.704e+001	glukoz
8.81	142	2.638e−002	2.638e+000	xiloz
9.68	24	2.794e−003	2.794e−001	arabinoz
11.08	414	1.000e−001	1.000e+001	succin
12.05	59	2.295e−002	2.295e+000	hangya
13.34	104	3.797e−002	3.797e+000	ecet
15.09	149	4.176e−002	4.176e+000	levulin

10. Peaks integrated
* Reference * Internal Std

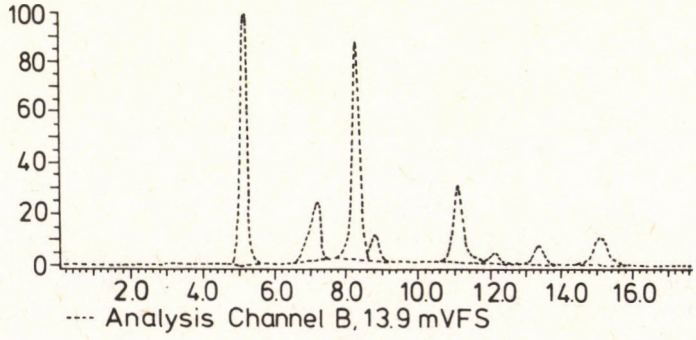

Figure 7
Liquid chromatogram of reed hydrolysate
Temperature: 170 °C; Liquid-to-solid ratio = 7 : 1;
Catalysts: 2% (w/w) H_3PO_4 and 2% (w/w) $Al_2(SO_4)_3$;
Time: 40 min.

can be proposed for the description of cellulose hydrolysis with $Al_2(SO_4)_3$—H_3PO_4 solutions:

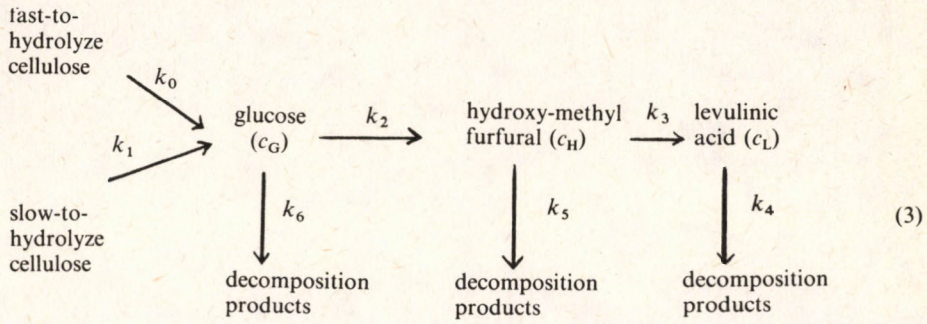

(3)

Since the hydrolysis of plant cellulose was aimed at producing levulinic acid, the results obtained concerning levulinic acid are given.

Parallel with cellulose hydrolysis, the hydrolysis of the hemicellulose part also takes place. As to the hydrolysis of reed cellulose, the concentration of the components formed in the function of time are shown in *Fig. 8*.

In the case of industrial-scale cellulose hydrolysis the diffusion rates of the products formed should also be taken into consideration.

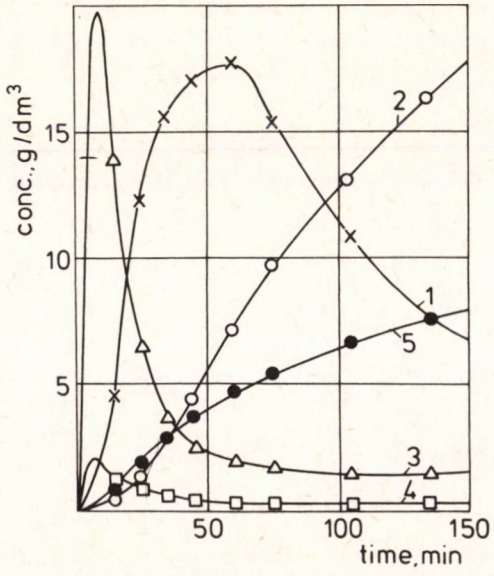

Figure 8
Kinetic curves of the main components of reed hydrolysate
Temperature: 170 °C; Liquid-to-solid ratio = 7 : 1;
Catalysts: 2% (w/w) H_3PO_4 and 2% (w/w) $Al_2(SO_4)_3$;
1 – glucose, *2* – levulinic acid, *3* – *d*-xylose, *4* – arabinose, *5* – formic acid.

Modelling of cellulose hydrolysis accompanied by diffusion

Hydrolysis products of cellulose were formed in the pore liquid of solid matter in a batch-type, two-phase, isotherm tank reactor. The transport of the components formed from the pores to the liquid phase was carried out by diffusion.

The mathemathical model was based on the kinetics of cellulose hydrolysis described in the previous scheme (3) and those conditions which were summarized earlier [7].

The component balance of the fast-to-hydrolyze cellulose in the solid phase is:

$$\frac{dc_{cf}^{S}}{dt} = -k_0 c_{cf}^{S} \tag{4}$$

and for the slow-to-hydrolyze cellulose in the solid phase:

$$\frac{dc_{cs}^{S}}{dt} = -k_1 c_{cs}^{S} \tag{5}$$

The initial conditions:

$$c_{cf}^{S}(0) = c_{cf}^{S0}; \quad c_{cs}^{S}(0) = c_{cs}^{S0} \tag{6}$$

The component balance of the glucose in the solid phase is:

$$\frac{\partial c_G^S}{\partial t} = k_0 c_{cf}^{S} + k_1 c_{cs}^{S} - (k_2 + k_6) c_G^S + D_G \frac{\partial^2 c_G^S}{\partial y^2} \tag{7}$$

The boundary conditions:

$$\frac{\partial c_G^S(t, 0)}{\partial y} = 0; \quad \text{if} \quad y = 0, \tag{8}$$

$$c_G^S\left(t, \frac{H}{2}\right) = \theta c_G^L; \quad \text{if} \quad y = \frac{H}{2}, \tag{9}$$

where H is the thickness of phases of plant material. The initial condition:

$$c_G^S(0, y) = 0 \tag{10}$$

In the liquid phase:

$$\frac{dc_G^L}{dt} = -\left| (k_2' + k_6') c_G^L + \frac{\omega}{\varepsilon} \left(-D_G \frac{\partial c_G^S}{\partial y} \right|_{y = \frac{H}{2}} \right) \tag{11}$$

The initial condition:

$$c_G^L(0) = 0 \tag{12}$$

The component balance of the hydroxy-methyl-furfural in the solid phase is:

$$\frac{\partial c_H^S}{\partial t} = k_2 c_G^S - (k_3 + k_5) c_H^S + D_H \frac{\partial^2 c_H^S}{\partial y^2}, \tag{13}$$

while in the liquid phase:

$$\frac{dc_H^L}{dt} = k'_2 c_G^L - (k'_3 + k'_5) c_H^L + \frac{\omega}{\varepsilon} \left(- D_H \frac{\partial c_H^S}{\partial y} \bigg|_{y = \frac{H}{2}} \right) \tag{14}$$

The initial conditions:

$$c_H^S(0, y) = 0, \tag{15}$$

$$c_H^L(0) = 0 \tag{16}$$

The boundary conditions:

$$c_H^S \left(t, \frac{H}{2} \right) = \theta c_H^L; \quad \text{if} \quad y = \frac{H}{2}, \tag{17}$$

$$\frac{\partial c_H^S(t, 0)}{\partial y} = 0; \quad \text{if} \quad y = 0 \tag{18}$$

The component balance of the levulinic acid in the solid phase is:

$$\frac{\partial c_L^S}{\partial t} = k_3 c_H^S - k_4 c_L^S + D_L \frac{\partial^2 c_L^S}{\partial y^2}, \tag{19}$$

while in the liquid phase:

$$\frac{dc_L^L}{dt} = k'_3 c_H^L - k'_4 c_L^L + \frac{\omega}{\varepsilon} \left(- D_L \frac{\partial c_L^S}{\partial y} \bigg|_{y = \frac{H}{2}} \right). \tag{20}$$

The initial conditions:

$$c_L^S(0, y) = 0, \tag{21}$$

$$c_L^L(0) = 0. \tag{22}$$

The boundary conditions:

$$\frac{\partial c_L^S(t, 0)}{\partial y} = 0 \quad \text{if} \quad y = 0, \tag{23}$$

$$c_L^S \left(t, \frac{H}{2} \right) = \theta c_L^L \quad \text{if} \quad y = \frac{H}{2}. \tag{24}$$

The method of the solution of the differential equation system was described earlier [7].

The solution functions in the liquid phase are:

$$c_G^L(t) = N_1 e^{-k_0 t} + N_2 e^{-k_1 t} + N_3 e^{\alpha_1 t} + N_4 e^{\alpha_2 t} \quad (25)$$

$$c_H^L(t) = N_6 e^{-k_1 t} + N_7 e^{\alpha_1 t} + N_8 e^{\alpha_2 t} + N_9 e^{\beta_1 t} + N_{10} e^{\beta_2 t} \quad (26)$$

$$c_L^L(t) = N_{11} e^{-k_0 t} + N_{12} e^{-k_1 t} + N_{13} e^{\alpha_1 t} + N_{14} e^{\alpha_2 t} + N_{15} e^{\beta_1 t} + N_{16} e^{\beta_2 t} + N_{17} e^{y_1 t} + N_{18} e^{y_2 t} \quad (27)$$

The values of $N_1 \ldots N_{18}$ coefficients are shown in the Appendix.

The solution of the equation system contains – as parameters – the k_0, k_1, k_2, k_3, k_4, k_5, k_6 rate constants and the D_G, D_H, D_L diffusion coefficients of glucose, hydroxy-methyl-furfural and levulinic acid.

Based on the experimentally obtained kinetic curves of glucose and levulinic acid, the rate constants and diffusion coefficients were determined.

The experimental conditions and the parameters obtained are summarized in *Table 1.* The measured and calculated kinetic curves at 170 °C are shown in *Fig. 9.*

Table 1. Experimental and identified parameters

Experimental parameters:

Volume of reed, $V_s = 1.54$ dm^3;
Volume of liquid, $V_L = 5.93$ dm^3;
Contentration of liquid: 2% (w/w) H_3PO_4, 2% (w/w) $Al_2(SO_4)_3$;
Apparent densitya of reed, $\varrho_r = 0.59$ kg m^{-3};
Void fraction of solid phase, $\varepsilon = 0.794 \frac{\text{dm}^3 \text{ liquid volume}}{\text{dm}^3 \text{ total volume}}$;
Porosity of solid phase, $\theta = 0.69 \frac{\text{dm}^3 \text{ pore volume}}{\text{dm}^3 \text{ solid volume}}$;
Specific surface, $\omega = 5650 \frac{\text{m}^2 \text{ transfer surface}}{\text{m}^3 \text{ total volume}}$;
Potential levulinic acid content: 28,5% (w/w);
20% (w/ws) of the potential levulinic acid is fast hydrolysable
Moisture of reed: 9.2% (w/w);
Hydrolysis temperature, T = 170 and 180 °C;
Avarage thickness of reed, $H = 8.5.10^4$ m.

Identified parameteres:

Reaction rate constans, s^{-1}		Temperature	
		170 °C	180 °C
	k_0	$2.818\ 10^{-3}$	$8.955\ 10^{-3}$
	k_1	$2.652\ 10^{-4}$	$8.141\ 10^{-4}$
	k_2	$4.072\ 10^{-4}$	$5.199\ 10^{-4}$
	k_3	$5.330\ 10^{-4}$	$1.313\ 10^{-3}$
	k_4	$2.003\ 10^{-10}$	$1.032\ 10^{-7}$
	k_5	$9.848\ 10^{-4}$	$2.539\ 10^{-3}$
	k_6	$1.945\ 10^{-4}$	$2.493\ 10^{-4}$
Diffusion coefficients, $m^2 s^{-1}$			
glucose	D_G	$4.383\ 10^{-12}$	$6.942\ 10^{-12}$
hydroxy-methyl-fufural	D_H	$3.981\ 10^{-11}$	$5.516\ 10^{-11}$
levulinic acid	D_L	$7.738\ 10^{-12}$	$3.857\ 10^{-11}$

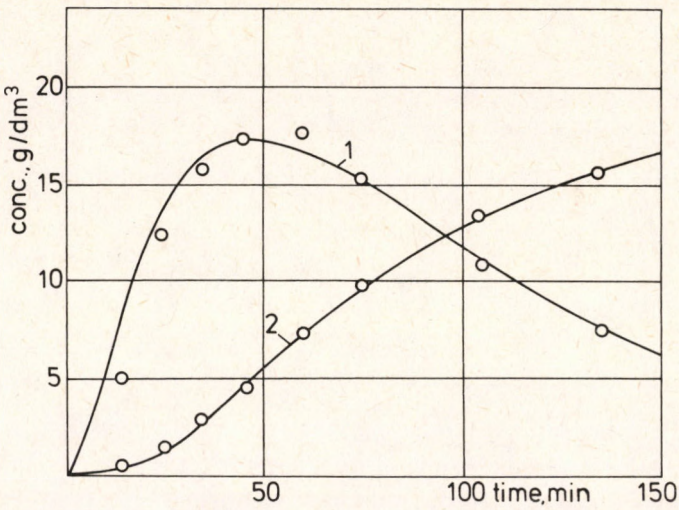

Figure 9
Comparison of calculated glucose and levulinic acid concentrations (solid lines) to those obtained experimentally (open symbols)
1 – glucose, *2* – levulinic acid.

Appendix

The values of the coefficients of solution functions:

$$N_1 = \frac{a_{21}k_0}{k_0^2+(a_{11}+a_{22})k_0+(a_{11}a_{22}-a_{12}a_{21})}\,c_{cf}^{s0},$$

$$N_2 = \frac{a_{21}k_1}{k_1^2+(a_{11}+a_{22})k_1+(a_{11}a_{22}-a_{12}a_{21})}\,c_{cs}^{s0},$$

$$N_3 = \left(-\frac{\alpha_1+k_0}{\alpha_2-\alpha_1}-1\right)N_1+\left(-\frac{\alpha_1+k_1}{\alpha_2-\alpha_1}\right)N_2,$$

$$N_4 = \frac{\alpha_1+k_0}{\alpha_2-\alpha_1}N_1+\frac{\alpha_1+k_1}{\alpha_2-\alpha_1}N_2,$$

$$N_5 = -\frac{(k_0+b_{11})+\dfrac{b_{21}}{a_{21}}(k_0+a_{22})\theta}{k_0^2-(b_{11}+b_{22})k_0+(b_{11}b_{22}-b_{12}b_{21})}k_2N_1,$$

$$N_6 = -\frac{(k_1+b_{11})+\dfrac{b_{21}}{a_{21}}(k_1+a_{22})\theta}{k_1^2-(b_{11}+b_{22})k_1+(b_{11}b_{22}-b_{12}b_{21})}k_2N_2,$$

$$N_7 = \frac{\alpha_1 - b_{11} + \frac{b_{21}}{a_{21}}(\alpha_1 - a_{22})\theta}{\alpha_1^2 - (b_{11}+b_{22})\alpha_1 + (b_{11}b_{22} - b_{12}b_{21})} k_2 N_3,$$

$$N_8 = \frac{\alpha_2 - b_{11} + \frac{b_{21}}{a_{21}}(\alpha_2 - a_{22})\theta}{\alpha_2^2 - (b_{11}+b_{22})\alpha_2 + (b_{11}b_{22} - b_{12}b_{21})} k_2 N_4,$$

$$N_9 = \left(- \frac{\beta_1 - b_{22}}{\beta_2 - \beta_1} - 1 \right)(N_5 + N_6 + N_7 + N_8) + \frac{b_{21}}{\beta_2 - \beta_1}(V_1 + V_2 + V_3 + V_4),$$

$$N_{10} = \frac{\beta_1 - b_{22}}{\beta_2 - \beta_1}(N_5 + N_6 + N_7 + N_8) - \frac{b_{21}}{\beta_2 - \beta_1}(V_1 + V_2 + V_3 + V_4),$$

$$N_{11} = \left(- \frac{\gamma_1 - c_{22}}{\gamma_2 - \gamma_1} - 1 \right)(V_5 + V_6 + V_7 + V_8 + V_9 + V_{10}) +$$

$$+ \frac{c_{21}}{\gamma_2 - \gamma_1}(N_{13} + N_{14} + N_{15} + N_{16} + N_{17} + N_{18}),$$

$$N_{12} = \frac{\gamma_1 - c_{22}}{\gamma_2 - \gamma_1}(V_5 + V_6 + V_7 + V_8 + V_9 + V_{10}) -$$

$$- \frac{c_{21}}{\gamma_2 - \gamma_1}(N_{13} + N_{14} + N_{15} + N_{16} + N_{17} + N_{18}),$$

$$N_{13} = \frac{(\beta_1 - c_{22})V_5 - k_3 N_9}{c_{21}}; \quad N_{16} = \frac{(\alpha_2 - c_{22})V_8 - k_3 N_8}{c_{21}},$$

$$N_{14} = \frac{(\beta_2 - c_{22})V_6 - k_3 N_{10}}{c_{21}}; \quad N_{17} = - \frac{(k_0 + c_{22})V_9 + k_3 N_5}{c_{21}},$$

$$N_{15} = \frac{(\alpha_1 - c_{22})V_7 - k_3 N_7}{c_{21}}; \quad N_{18} = - \frac{(k_1 + c_{22})V_{10} + k_3 N_6}{c_{21}},$$

$$V_1 = \frac{(\alpha_1 - b_{22})N_7 - k_2 N_3}{b_{21}}; \quad V_2 = \frac{(\alpha_2 - b_{22})N_8 - k_2 N_4}{b_{21}},$$

$$V_3 = - \frac{(k_0 + b_{22})N_5 + k_2 N_1}{b_{21}}; \quad V_4 = - \frac{(k_1 + b_{22})N_6 + k_2 N_2}{b_{21}},$$

$$V_5 = \frac{\beta_1 - c_{11} + \frac{c_{21}}{b_{21}}(\beta_1 - b_{22})\theta}{\beta_1^2 - (c_{11}+c_{22})\beta_1 + (c_{11}c_{22} - c_{12}c_{21})} k_3 N_9,$$

$$V_6 = \frac{\beta_2 - c_{11} + \frac{c_{21}}{b_{21}}(\beta_2 - b_{22})\theta}{\beta_2^2 - (c_{11}+c_{22})\beta_2 + (c_{11}c_{22} - c_{12}c_{21})} k_3 N_{10},$$

$$V_7 = \frac{(\alpha_1 - c_{11})N_7 + c_{21}\theta V_1}{\alpha_1^2 - (c_{11}+c_{22})\alpha_1 + (c_{11}c_{22} - c_{12}c_{21})} k_3,$$

$$V_8 = \frac{(\alpha_2 - c_{11})N_8 + c_{21}N_2}{\alpha_2^2 - (c_{11}+c_{22})\alpha_2 + (c_{11}c_{22} - c_{12}c_{21})} k_3,$$

$$V_9 = \frac{-(k_0+c_{11})N_5+c_{21}V_3}{k_0^2-(c_{11}+c_{22})k_0+(c_{11}c_{22}-c_{12}c_{21})}k_3,$$

$$V_{10} = \frac{-(k_1+c_{11})N_6+c_{21}V_4}{k_1^2-(c_{11}+c_{22})k_1+(c_{11}c_{22}-c_{12}c_{21})}k_3,$$

$$\alpha_1 = \frac{a_{11}+a_{22}+(a_{11}-a_{22})^2+4a_{12}a_{21}}{2},$$

$$\alpha_2 = \frac{a_{11}+a_{22}-(a_{11}-a_{22})^2+4a_{12}a_{21}}{2},$$

$$\beta_1 = \frac{b_{11}+b_{22}+(b_{11}-b_{22})^2+4b_{12}b_{21}}{2},$$

$$\beta_2 = \frac{b_{11}+b_{22}-(b_{11}-b_{22})^2+4b_{12}b_{21}}{2},$$

$$\gamma_1 = \frac{c_{11}+c_{22}+(c_{11}-c_{22})^2+4c_{12}c_{21}}{2},$$

$$\gamma_2 = \frac{c_{11}+c_{22}-(c_{11}-c_{22})^2+4c_{12}c_{21}}{2},$$

$$a_{11} = -(k_2+k_6)-6\frac{D_G\omega}{H(1-\varepsilon)} \qquad b_{11} = -(k_3+k_5)-6\frac{D_H\omega}{H(1-\varepsilon)} \qquad c_{11} = -k_4-k_6\frac{D_L\omega}{H(1-\varepsilon)}$$

$$a_{12} = 6\frac{D_G\omega}{H(1-\varepsilon)} \qquad b_{12} = 6\frac{D_H\omega}{H(1-\varepsilon)} \qquad c_{12} = 6\frac{D_L\omega}{H(1-\varepsilon)}$$

$$a_{21} = 6\frac{D_G\omega}{H\varepsilon} \qquad b_{21} = 6\frac{D_H\omega}{H\varepsilon} \qquad c_{21} = 6\frac{D_L\omega}{H\varepsilon}$$

$$a_{22} = -(k'_2+k'_6)-6\frac{D_G\omega}{H\varepsilon} \qquad b_{22} = -(k'_3+k'_5)-6\frac{D_H\omega}{H\varepsilon} \qquad c_{22} = -k'_4-k_6\frac{D_L\omega}{H\varepsilon}$$

$$k_n = \theta k'_n \quad \text{if} \quad n = 2, 3, 4, 5, 6.$$

SYMBOLS:

c_{b1}, c_{b2}, c_{b3} concentration of decomposition products, $g \cdot dm^{-3}$
c_{cf}^{S} concentration of fast hydrolyzable celluloze, $g \cdot dm^{-3}$ solid phase
c_{cf}^{S0} initial concentration of fast hydrolyzable cellulose, $g \cdot dm^{-3}$
c_{cs}^{S} concentration of slow hydrolyzable cellulose, $g \cdot dm^{-3}$
c_{cs}^{S0} initial concentration of slow hydrolyzable cellulose, $g \cdot dm^{-3}$
c_G^S solid phase glucose concentration, $g \cdot dm^{-3}$
c_G^L liquid phase glucose concentration, $g \cdot dm^{-3}$
c_H^S solid phase hydroxy-methyl-furfural concentration, $g \cdot dm^{-3}$
c_H^L liquid phase hydroxy-methyl-furfural concentration, $g \cdot dm^{-3}$
c_L^S solid phase levulinic acid concentration, $g \cdot dm^{-3}$
c_L^L liquid phase levulinic acid concentration, $g \cdot dm^{-3}$
D_G diffusion coefficient of glucose, $m^2 s^{-1}$
D_H diffusion coefficient of hydroxy-methyl-furfural, $m^2 s^{-1}$

D_L diffusion coefficient of levulinic acid, m^2s^{-1}
H average thickness of reed in the direction of co-ordinate y, m
$k_0, k_1, \ldots, k_6$ reaction rate constants, s^{-1}
y space co-ordinate, m
t reaction time, sec
ε void fraction, m^3 liquid volume/m^3 total volume
ϱ density of solid phase, $kg \cdot dm^{-3}$
θ porosity, m^3 pore liquid/m^3 solid phase
ω specific surface, m^2 transfer surface/m^3 total volume

REFERENCES

1. MASAO KITANO, FUMIO TANIMATO and MASAYUKI OBAYASHI: Chem. Econ. Eng. Rev. *1975,* 7 (7), 25–29.
2. SAEMAN, J. F.: Ind. Eng. Chem. *1945,* 37 (7).
3. MEKIBBINS, S. W., HARRIS, J. F. and SAEMAN, J. F.: Forest Products Journ., *1962,* 12 (7).
4. VAN DAM, H. E. et al.: Stark/Staerke, *1986,* 38 (95).
5. GARVES, K.: J. Wood Chem. Techn. *1981,* 1, 223.
6. CONNER, A. H., WOOD, B. F., HILL. C. G. and HARRIS, J. F.: Cellulose. Structure, modification and hydrolysis. Wiley-Intersci. Pub., New York, 1986, 281.
7. SZOKONYA, L., MARTON, G., DENCS, J. and KOVÁCS, M.: Hung. J. Ind. Chem. *1988,* 16, 511.

HUNGRIAN JOURNAL
OF INDUSTRIAL CHEMISTRY
VESZPRÉM
Vol. 17. pp. 491–498 (1989)

CASE STUDIES OF SOME FIRE ACCIDENTS IN YUGOSLAVIA'S OIL REFINERIES

M. PERUNIČIĆ and M. SKOTOVIČ*

(Faculty of Technology, 21000 Novi Sad, Yugoslavia; *Institute of Judical Expertise, 21000 Novi Sad, Yugoslavia)

Received: June 22, 1989.

A report on the descriptions and causes of four fire accidents in Yugoslavia's oil refineries. In each of these cases, the point of origin was the bad running of the equipment and units or evident failure caused by operators. Preventive action for avoiding such events in similar circumstances in the future is outlined.

Introduction

Most fire accidents in the hydrocarbon-chemical industries, accordingly to the activities of the Marsh & McLennan Protection Consultants Company [1] in many states over the world, occur in oil refineries. The criterion for including such cases to this analysis, was a minimum of $ 10,000,000 loss, and the period from 1956 to 1986 was considered. It is characteristic that there was an increase in such cases over the years, indicating the need for more preventive activity.

Here are some technical details and causes of following fire accidents, in Yugoslavia's oil refineries:

- 1st case: explosion in an open room and a fire in the floating roof tank for gasoline produced from refinery gaseous sources;
- 2nd case: fire in a bitumen tank after mechanical damage of the tank roof caused by pressure increasing in the vapour space;
- 3rd case: fire in the open room of an atmospheric distillation unit, caused by the flooding of the kerosene stripping column and kerosene spilling through the safety valve on the top of the column;
- 4th case: fire in open room of a fluidized catalytic cracking unit, caused by the discharge of fuel gas through the drainage valve at the bottom of the fuel gas vessel.

The amounts of the loss caused by these fire accidents, are not presented here, but each of them involved a substance loss and damage to the unit parts affected by fire. However, in the first two cases, the amounts of the loss were certainly bigger than in the other cases, resulting from material damage to the tanks.

1st Case

This fire accident started on July 7, 1982 at 23 : 40 with an explosion in one of the Yugoslavia's oil refineries, located in the eastern part of the country. The explosion occurred in an open room around the floating roof tank for gasoline produced from refinery gaseous sources [2]. Soon after the explosion, the tank caught fire. The steps taken after the accident were aimed at localizing and extinguishing the fire. Before the explosion, the tank had been filled with the total volume of 871,707 m^3 gasoline during 68 h and 10 min. From the available data on July 7, 1982 the average values of the gasoline characteristics were: 1.64 bar Reid vapour pressure (RVP) and 0.65 relative density 60/60. However, a consideration of the actual data shown in *Fig. 1,* indicates that a volatility of gasoline increased with time on July 7, 1982. At the same time, it indicated an increased vapour flow from the tank in to the environment.

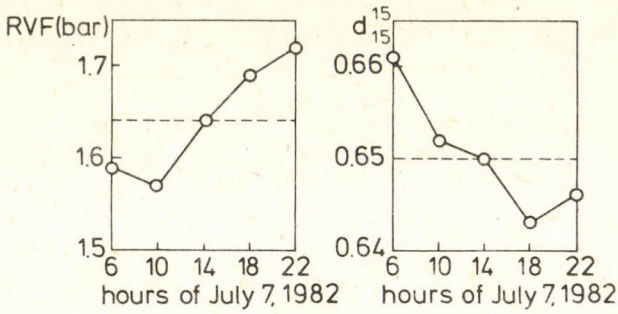

Figure 1.
The characteristics of gasoline on July 7, 1982.

Seven days after the fire, a gasoline sample from the tank bottom was taken. Gas chromatographic determination of the gasoline composition in the laboratory of refinery, gave the results shown in *Table I.*

Table 1.

Composition of gasoline seven days after the fire

Component	Composition weight %	M kg/kmole	Composition mole %	Normal Boiling Point °C
propane	0.03	44.09	0.0475	−42.07
i-butane	0.60	58.12	0.7216	−11.73
n-butane	17.60	58.12	21.1556	−0.50
i-pentane	49.33	72.15	47.4754	27.85
n-pentane	25.62	72.15	24.8072	36.07
hexane	6.59	86.17	5.3423	68.74
heptane	0.23	100.19	0.1604	98.43

Using a value RVP = 1.64 bar it is easy to find the value of true vapour pressure at the temperature of 37,78° C, which is 1.79 bar [3]. However, using the data from Table I, one can get the mole average boiling temperature of 25.87 °C, and after that, the value of true vapour presure at the temperature 37,78 °C is 1.51 bar [4]. Naturally, such a decrease of vapour pressure was followed by the vaporisation of gasoline during seven days after fire.

The reliability of the storage of such gasoline, characterized with the above mentioned data, in the floating roof tank, will be considered accordingly with the graphical presentation [5] given in *Fig. 2.*

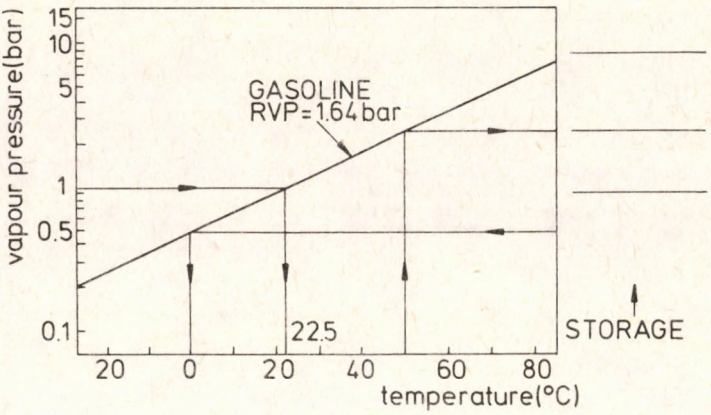

Figure 2.
Types of storage tank for RVP = 1.64 bar gasoline

As seen in *Fig. 2,* the maximum temperature of liquid in the tank is 50 °C according to the meteorological data and project documents, and a floating roof tank is not recommended for this gasoline. Similarly, using this tank, the internal tank temperature should be about 0 °C, which is unrealistic here, except in the winter. Moreover, in *Fig. 2* we can also recognize a limiting temperature of liquid in the tank, at the boiling start of gasoline. This temperature is approximatively 22.5 °C.

In *Fig. 3* the boiling point distribution from *Table I* and equilibrium flash vaporization line for gasoline calculated on the basis of Soave-Redlich-Kwong equation of state [6], for the atmospheric pressure, are shown.

One can see a typical agreement between the two characteristic lines for gasoline in *Fig. 3.* This fact means that the calculated EFV line is quite exact. The start of equilibrium boiling is at a temperature of 22.9 °C, which is confirmation of very good agreement with the preliminary obtained value of 22.5° C in *Fig. 2.* Moreover, a temperature difference of 0.4 °C was also be explained by decreasing of the gasoline volatility during seven days from the fire (RVP = 1.64 bar) to the determination of the gasoline composition, which was a basis for the EFV line calculation. With regard to the fact that each atmospheric tank

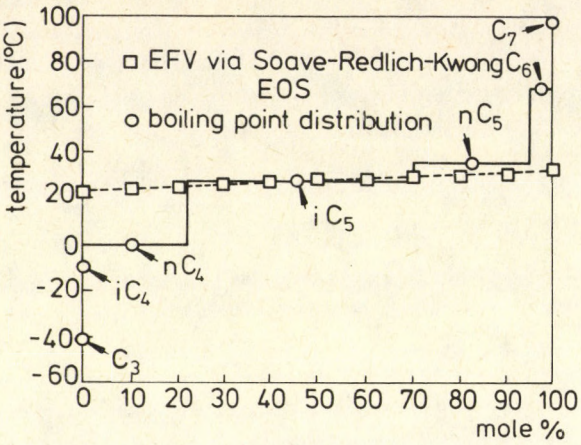

Figure 3.
Boiling point distribution and equilibrium flash vaporization line for gasoline

represents an equilibrium flash separator, previously determined data in common with the actual temperature in the tank on the fire day, can be used for the approximative calculation of the gasoline vapour amount, which flowed out from the tank in the surrounding space. So, the mean average temperature of gasoline in the tank on July 7, 1982 was 25.4 °C, which is more than the start point of EFV line: 22.5 °C. At the temperature of 25.4 °C about 21.1. mole % of gasoline was in a vapour phase, so by using a modified equation of state the volume of gasoline vapour was about 39,350 m^3. This volume of gasoline vapour could not be kept back in the tank, and the hydrocarbon cloud was formed in the surrounding space. This cloud was carried by with the wind to the burner of the process heater. After that, an explosion in the open room and a tank fire occurred. In this case, the burner construction operated in the usual manner, drawing combustion air from the surrounding space with the natural draught. This air made a contact between the hydrocarbon cloud and the flame in the heater, and was the cause of the explosion and fire.

Thus, the general cause of this fire was the unsuitable storage of very volatile gasoline, produced from the refinery gaseous sources, in the atmospheric floating roof tank. In order to avoid such a fire in the future, it is necessary to make an accordance between the hydrocarbon mixture (i.e. oil product) characteristics and the tank type, using the sketch given in *Fig. 2.* A suitable gasoline storage could then prevent a hydrocarbon cloud forming in the refinery open room.

2nd Case

This fire accident started on May 20, 1983 at 18 : 20 in one of the Yugoslavia's oil refineries, located in the eastern part of the country. The accident involved material damage to the bitumen tank roof followed by a fire [7]. It was establish-

ed that the accident was caused by a continuous throwing of stripping liquid (i.e. heavy fuel oil) used for heater stripping, in the bitumen tank, instead in the slop system. From a handling purpose, the bitumen temperature in the tank was about 200 °C, and the stripping liquid included a certain amount of water. The result was a vaporisation of water in the tank. About ten minutes later there was mechanical damage to the tank roof, caused by increase in pressure in the vapour space. This was followed by the breaking of the tank roof, and the scattering of bitumen and bitumen foam in the open room. It seems that the fire was caused by a preignition of the bitumen – stripping oil mixture in some local position in the tank.

In order to avoid such a fire accident in the future, an exact prediction of possible undesirable events during the material streams handling and blending in a refinery, is necessary.

3rd Case

This fire accident started on July 11, 1986 at 8 : 20 a.m. in one of the Yugoslavia's oil refineries, located in the western part of the country. The place of the fire was in the open room at the atmospheric crude distillation unit, shown on *Fig. 4.*

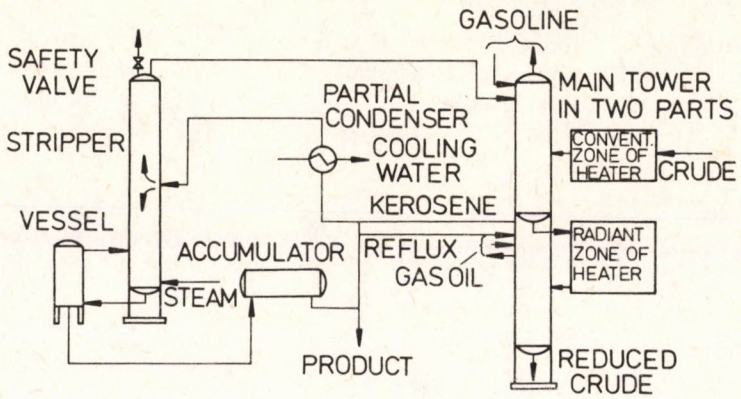

Figure 4.
Sketch of the part of atmospheric distillation unit

The unit had been running for thirty days before the fire occurred. The conditions under which the fire started, were the following: the column, for kerosene stripping with steam, was in a flooding regime and the whole column inside was filled with kerosene liquid. This liquid crushed the safety valve on the top of the column and kerosene expansion in the open room around the column began. Contact occurred between kerosene in liquid and also in vapour phase, and the hot metal unisolated surface, at the feed entry in the main column. Since the temperature of this surface was about 300 °C, which is more

than the preignition temperature of kerosene, a small explosion and fire occurred.

Naturally, the cause of the column flooding simultaneously represented the cause of the fire. At first, the court of original jurisdiction was of the view that the operators caused the column flooding with a reduction of the throughput of cooling water in the partial condenser (see *Fig. 4*). However, we ignored this assumption, as a higher temperature of the feed entry into the column is followed by the excess of vapour, but no liquid in it. On the other hand, in this case the flooding meant an excess of liquid into the column. At the same time, the fact that a column was in flooding regime, while the vessel near the column was liquid free, indicated that local drag for the kerosene flow to the bottom was too high. This new assumption was confirmed by the following facts:

- before running the unit, the personnel made an alteration to the kerosene stripper column by building in an additional layer of a Raschig rings package;
- on the metal wire net at the top of the Raschig rings layer an additional layer of mud and rust was observed. The thickness of this layer was about 10 cm.

Both layers produced a certain local drag for the kerosene flow to the bottom of the column. During a thirty day running of the unit, this local drag increased and finally caused the flooding of the column. After flooding and kerosene spilling out from the column, the fire occurred.

Thus, the cause of the fire was the incorrect alteration of the kerosene stripping column. In this case, it was obvious that very careful consideration of the equipment alteration must be made, from the viewpoint of the regular flow of the fluids to avoid the flooding regime.

4th Case

This fire accident started on April 27, 1987 at 21 : 30 in one of the Yugoslavia's oil refineries, located in the eastern part of the country. The place of fire was in the open room of the fluid catalytic cracking unit (FCCU). The unit was in preparation condition before running. An accumulation vessel into the unit was filled with fuel gas, used for the heating of the feed in the pipe heater. This fuel gas originated from the other gas finishing unit, as the similar unit, included in the FCCU, was not yet in stationary working condition. A third possibility to supply the vessel with fuel gas was preheating of liquid petroleum gas (LPG). After observing a bad quality of the flame in the heater, the two operators concluded that the fuel gas vessel contained too much liquid. However, they made no careful opening of the valve, so, after a small amount of liquid, through the valve a vapour flow started, at a too large rate. A terminal position of the pipe with the valve, was on the top of the sewerage system for the waste liquid drainage. Immediately after the fuel gas outlet a large hydrocarbon cloud was formed in the open room. It also filled the pipes of the sewerage system, and after ten seconds the fire occurred, exactly on the burner under the process heater. The way the fire began was exactly the same as in the first case, except

that there was no explosion, because the hydrocarbon content in the cloud was higher than the upper limit of the explosivity.

Thus, the cause of this fire was obvious: no careful opening of the drainage valve on the bottom of the fuel gas vessel. To avoid similar accidents, the careful opening of the drainage valve or the building of an automatic system for the liquid discharge from the fuel gas vessel with the level control, is necesary.

Discussion

On the basis of these fire accident descriptions and causes in Yugoslavia's oil refineries, one can remark on the fact that the preventive measures for avoiding such events in the future must include a careful prediction of the fire occurring possibilities. For the first case, this is valid because of the project of the gasoline storage. Actually, in this case the hydrocarbon cloud in an open room, would have been eliminated only with stopping the unit, that was done after the fire occurred. However, the second case showed that a preventive measure to avoid the fire involved a previously careful analysis of possible unwanted effects by different material streams blending. If the pressure increased in the vapour space of the bitumen tank, which was not predicted in advance, then the tank damage and fire would have not been stopped. Similar to the first case, the third case indicated the need for a preventive measure, but for the alteration of the internal structure in the separation column. So, after a regular prediction of possible consequences by the Rasching rings layer building in the column, the column flooding and, of course, the fire could have been prevented. The fourth case represented a typical error caused by the operators and there is no doubt about this. A possible building of a system of automatic discharge of liquid from the fuel gas vessel, could help avoid such events. Nevertheless, this case also indicated the problematic usage of preheated LPG for the process heater, instead of fuel gas. Indeed, in the case of using LPG, there are the following problems connected with some possible troubles: the partial condensation of preheated LPG and the burners effect from the principle of the fuel gas replacement point of view.

With regard to the fact that the hydrocarbon cloud in the open room of a oil refinery represents a typical explosion and fire precursor [1], it is always justified to build in a system for detection and alarm, which reacts in the presence of hydrocarbons.

Conclusion

With regard to the analysis of the cause of four fire accidents in Yugoslavia's oil refineries it is possible to conclude that the preventive measures, to avoid damage and fire events, are very complex. This indicates a need for regular design and alteration of refinery units and equipment, regular material streams blending and careful work by operators.

REFERENCES

1. GARRISON, W. G.: Hydrocarbon Processing *1988,* 67 (9), 115–120.
2. PERUNIČIĆ, M. and SKOTOVIČ, M.: Nafta (Zagreb) 1988, 39 (10), 583–588.
3. NELSON, V. F.: Petroleum Refinery Engineering. McGraw-Hill, New York, 1958, p. 138.
4. ibid.: p. 208.
5. ibid.: p. 272.
6. SOAVE, G.: Chem. Eng. Sci. *1972,* 27, 1197–1203.
7. PERUNIČIĆ, M. i SKOTOVIČ, M.: Hemijska industrija *1988,* 42 (3), 114–117.

HUNGARIAN JOURNAL
OF INDUSTRIAL CHEMISTRY
VESZPRÉM
Vol. 17. pp. 499–507 (1980)

A STUDY ON CATALYTIC ACTIVITY AND AGEING OF METAL-LOADED MORDENITE FOR *m*-XYLENE ISOMERIZATION

F. I. KENAWI and A. K. EL-MORSI

(Egyptian Petroleum Research Institute, Nasr City – Cairo-Egypt)

Received: July 3, 1989

H-Mordenite of silica-alimina ratio of 10, H-M10 catalyst was loaded with some metals such as Pt, Pd and Ni to produce metal loaded H-mordenite catalysts: Pt-HM10, Pd-HM10 and Ni-HM10. These catalysts were used in the hydroisomerization of *m*-xylene. The catalyst activity versus ageing was studied and the experimental data indicate that Ni-HM10 catalyst exhibits the highest activity, selectivity and stability towards the isomerization reaction, as compared to the other two catalysts prepared.

Introduction:

The development of polyfunctional catalysts seems to be one of the most important and promising applications of zeolites in catalysis. Catalysts of this type can simultaneously accelerate a number of reactions integrated in a single process and they are now widely used in petroleum refining and the petroleum chemistry [1, 2].

Most of the polyfunctional catalysts available are discomponent systems, such as metal/acidic oxide, metal/amorphous aluminosilicate or metal/zeolite [1, 2, 3].

In a previous work [4] by the same authors of this investigation, the effect of ageing and dealumination of *H*-mordenite catalyst on the activity and selectivity for *m*-xylene isomerization were studied.

The use of some metals loaded on *H*-mordenite, such as Pt, Pd, and Ni, in the isomerization of *m*-xylene, aimed at improving the catalysts selectivity, and stability towards production of *o*- and *p*-xylenes, are the main objective of this work.

Experimental

Equipment and Procedure

The equipment used for this investigation consisted of a fixed bed down-flow reactor operated under isothermal condition at atmospheric pressure. The reactor tube was of a silica glass. The catalyst (20 ml) was diluted with quartz particles (5 ml) and placed in the middle zone of the reactor tube. The charge stock (*m*-xylene) was introduced down flow via injection of H_2 gas. The product effluent was condensed and collected in a receiver.

The experimental conditions used were 430 °C reaction temperature, and 1.5 sec. contact time. The activity vs. time-on-stream data on fresh activated catalysts were obtained by analyzing "Spot" product samples drawn at various intervals.

The liquid products were analyzed using the gas-liquid partition chromatography method. The apparatus was a Perkin Elmer type, model Sigma 3B, using the flame ionization detector in the analysis. The partition column was a copper tube (7 feed long, 1/8″ I. D.), packed with chromosorb P (80–100 mesh) support, which carries 5% by wt. Bentone-34 and 5% by wt. diisodecylphthalate as stationary phase.

Catalyst Preparation and Characterization:

H-Mordenite of a silica-alumina ratio of 10, obtained from the Norton Co., as Zeolon 900, in the form of aggregates (1–2 mm).

Preparation of Pt-HM10 Catalyst:

The parent HM10 catalyst was impregnated with the requisite quantity of an aqueous solution of chloroplatinic acid, H_2PtCl_6 of 0.4 gm Pt/gm ($H_2PtCl_6 \cdot 6\,H_2O$), so that the final catalyst contained 0.35 wt.% Pt. Solid citric acid equal to 3 wt.% of the mordenite weight was added to the impregnating solution. The catalyst was then filtered, dried at 110 °C overnight, and calcined at 510 °C for three hours.

Preparation of Pd-HM10 Catalyst:

The same procedure was done, but the impregnating solution was $PdCl_2$.

Preparation of Ni-HM10 Catalyst:

The preparation of a catalyst containing 2.5 wt.% Ni, was done via a dry impregnation method for HM10 catalyst using Ni-acetate solution, followed by drying at 110° C overnight, then calcination at 510° C for three hours.

Catalyst Activation:

The former prepared catalyst were activated by using a H_2 gas stream, and the previously mentioned apparatus, at 530 °C, for 7 hours. Then the activated catalysts were ready to be used in the ivnestigation.

Properties of the Metal-Loaded Mordenites. Characterization

Catalyst	Pt-HM10	Pd-HM10	Ni-HM10
Silica-alumina ratio	10	10	10
Metal content, wt.%	0.35	0.35	2.5
Total acidity mequiv/gm	0.36	0.39	0.44

The total acidity of the catalysts was measured by the Benesi technique, using dimethyl yellow (pka = +3.3) as indicator.

The coke deposits were determined by the catalyst regeneration by roasting coke of the catalyst in O_2 atmosphere at 500 °C for four hours [5]. The difference in weight before and after regeneration gave the wt.% of the coke deposits on the catalyst.

Results and Discussion

H-Mordenite is one of the most active acid-catalyzed reactions like isomerization, disproportionation and dealkylation reactions of alkylaromatics [6]. As a result, when *m*-xylene is subjected for the isomerization over metal loaded *H*-mordenite catalysts, it produces a liquid product having xylene isomers in addition to the side reaction products of the disproportionation and the dealkylation reactions. These reactions can be summarized and illustrated in the following chemical equations:

i – *Isomerization Reaction (main reaction):*

$$\underset{\text{o-xylene}}{C_8H_{10}} \rightleftharpoons \underset{\text{m-xylene}}{C_8H_{10}} \rightleftharpoons \underset{\text{p-xylene}}{C_8H_{10}}$$

ii – *Disproportionation Reaction (side reaction):*

$$\underset{\text{m-xylene}}{2\,C_8H_{10}} \rightarrow \underset{\text{Toluene}}{C_7H_8} + \underset{\text{Trimethylbenzenes}}{C_9H_{12}}$$

iii – *Dealkylation Reaction (side reaction):*

$$\underset{\text{m-xylene}}{2\,C_8H_{10}} \xrightarrow{+3\,H_2} \underset{\text{Toluene}}{C_7H_8} + \underset{\text{Benezene}}{C_6H_6} + \underset{\text{methane}}{3\,CH_4}$$

However, *H*-mordenites are deactivated very fast in a few hours. WALSH and ROLLMAN [7] showed that coke formation during reactions of alkylaromatics

over zeolites is spatially demanding and mainly depends on the pore dimensions of the zeolites, less woke being formed over zeolites possessing 10 ring pores (like ZSM-5) than those with 12 ring pores (like mordenite and *Y*-zeolite). The addition of some metals such as Ni, Pt and Pd, which have a hydrogenation activity on the *H*-mordenite zeolite, may improve the catalyst stability throughout decreasing the amount of coke formed on the catalyst during the isomerization of m-xylene process, as they can hydrogenate the olefinic products that are produced, which are the precursors of the coke on the catalyst.

Catalyst Activities and Ageing in m-Xylene Isomerization

The three prepared metal loaded mordenites, namely, Ni-HM10, Pt-HM10 and Pd-HM10 catalysts were used in the isomerization of *m*-xylene, which mainly produce, o- and *p*-xylenes. Moreover, the liquid reaction products contain benzene, toluene and trimethylbenzenes as competitive side reaction products, that are produced via dealkylation and disproportionation reactions. The conversion in mole percentage of charge to give o-, and *p*-xylene are illustrated in *Figure 1*.

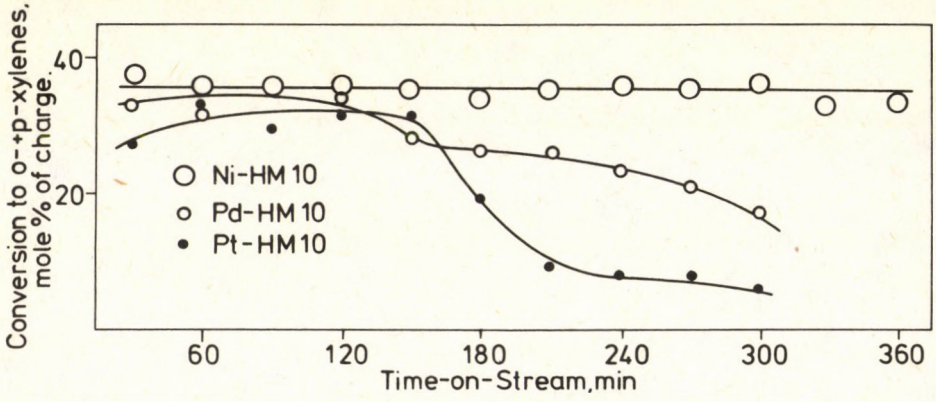

Figure 1.

From this given graph, it is clear that the catalyst stability for the isomerization reaction is relatively high in the case of the Ni-HM10 catalyst, compared to the other two catalysts (Pt-HM10 and Pd-HM10), during time on stream. In the case of the Ni-HM10 catalyst at the beginning of streaming the conversion % of *m*-xylene to give o- + *p*-xylene isomers is 35.5, which continues more or less constant on increasing time, even after 360 minutes. On the other hand, the conversions that were obtained in the case of Pt-HM10 and Pd-HM10 catalysts, were found to be 27.1% and 33.3% respectively and on the parallel they drop

to 6.4% and 18.1% after 300 minutes time on stream. As a result, the catalysts can be arranged according to their activities and stabilities towards isomerization reaction in the following order:

Ni-HM10 > Pd-HM10 > Pt-HM10

The superiorty of Ni-HM10 catalysts towards isomerization over the other two catalysts may be due to the distinguished bifunctional action of Ni over Pt and Pd metals. As in the presence of hydrogen, the activity of metallic Ni would assist hydrogenation and the elimination of some unsaturated hydrocarbons, more than Pt and Pd metals. These unsaturated compounds, unless they are removed, would block the active sites and cause catalyst deactivation [8, 9].

The previously given explanation is confirmed by the experimental results obtained as shown in *Table 1*. The amount of coke deposits on the catalysts in mgm coke/gm catalyst, were found to be 3, 6 and 8 for Ni-HM10, Pd-HM10 and Pt-HM10 respectively i.e. the lowest amount of coke deposits was found in the case of the Ni-HM10 catalyst.

Table 1
Coke Deposits Formed on the Catalyst, After 300 minutes time on stream

Catalysts	Time of stream, min.	Coke deposits in mgm/gm catalyst
Ni-HM10	300	3
Pd-HM10	300	6
pt-HM10	300	8

Catalyst Activities and Ageing for m-Xylene Disproportionation

Data, illustrated in *Fig. 2,* show the conversion of *m*-xylene, via disproportionation reaction, which can be considered as a competitive reaction for the isomerization.

Generally, data reveal that the disproportionation activities of the three investigated catalysts are comparatively low compared to their isomerization activities, specially with the Ni-HM10 catalyst.

The activities of the three investigated catalysts for *m*-xylene conversion to disproportionation products decrease by time. This drop in catalyst activities was found to be parallel with the further accumulation of coke that occurs on the catalyst by increasing time. The possible explanation for this decrease may be attributed to the partial blocking of the channels of the catalysts due to the deposited coke [7]. Consequently, the extent of production of trimethylbenzenes via disproportionation, which have larger molecular size compared to xylene molecules that are produced via isomerization are greatly affected for steric reasons, may arise from the accumulation of coke on the catalysts [8].

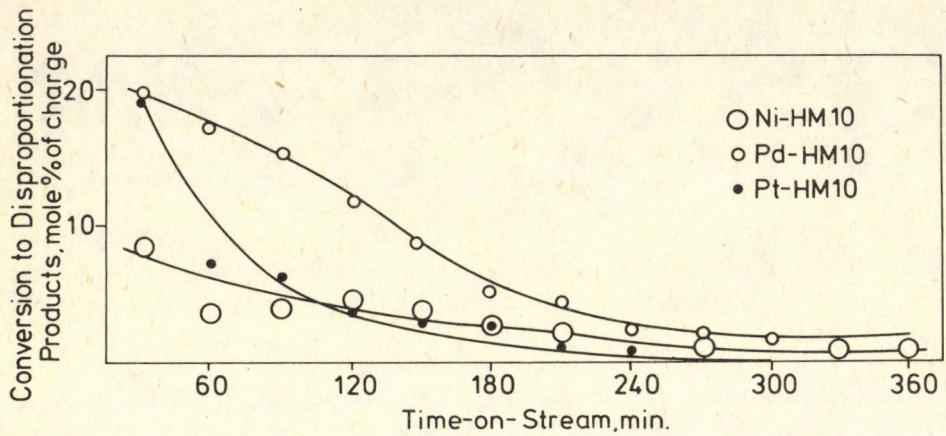

Figure 2.

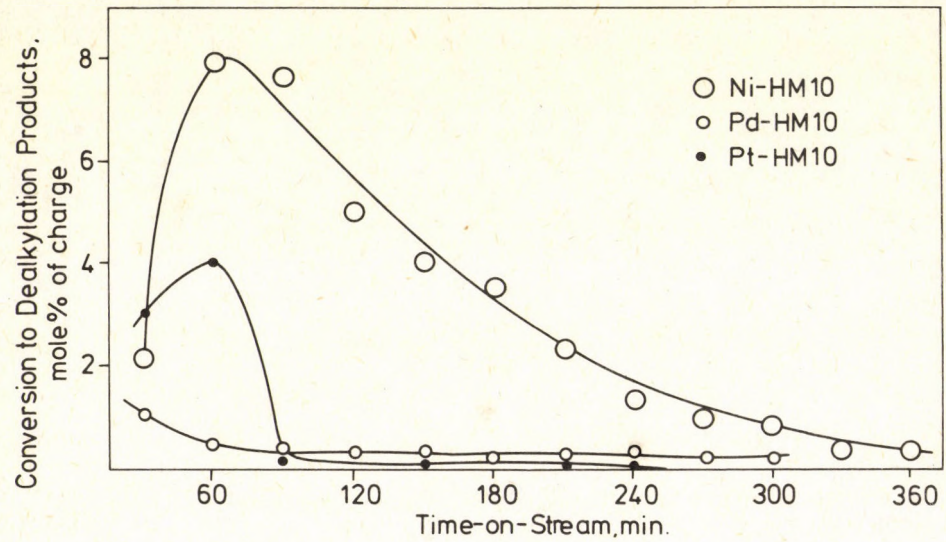

Figure 3.

Catalyst Activities and Ageing for m-Xylene Dealkylation:

Figure 3, represents *m*-xylene conversion to dealkylation products versus time on stream for Ni-HM10, Pt-HM10 and Pd-HM10 catalysts. These data reveal that in all cases the dealkylation activities of the catalysts used is very low compared to their isomerization activities. Ni-HM10, shows the highest activity for the dealkylation reaction with respect to the other two catalysts, specially at 60 minutes time on stream.

The highest dealkylation activity of the Ni-HM10 catalyst over Pt-HM10 and Pd-HM10 catalysts was found to be parallel with the highest hydrogenolysis activity of Ni metal over Pt and Pd, as reported in literature [10]. On the other hand, the decrease in the catalytic activity for the dealkylation by time, which was observed for the three catalysts, may be as a result of the deactivation by coke deposits, with which Pt and Pd are greatly affected, more than Ni metal.

Catalyst Selectivities towards Isomerization Products:

The selectivity of the catalysts towards the isomerization of *m*-xylene, versus time on stream is shown in *Fig. 4*.

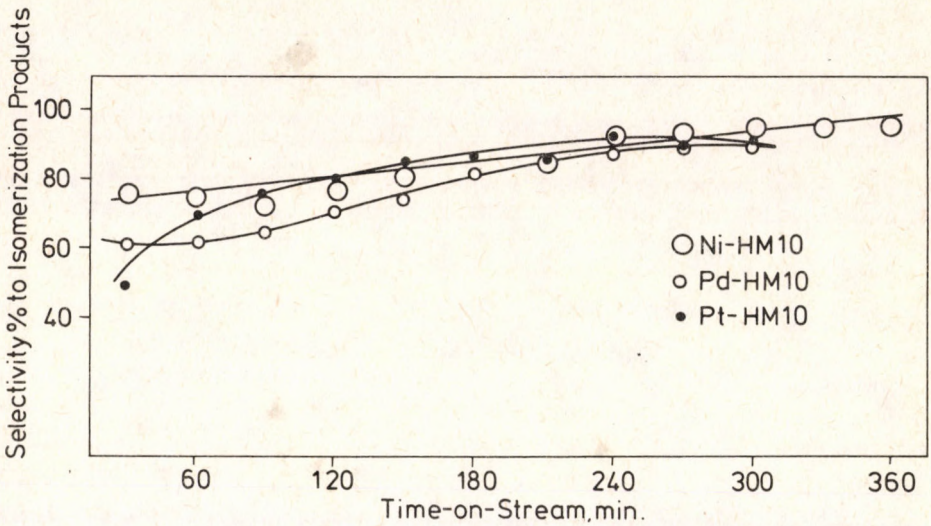

Figure 4.

Generally, the selectivity for isomerization increases by time for all the catalysts used in this investigation. The Ni-HM10 catalyst has the highest selectivity for isomerization, compared to that obtained in the case of the Pt-HM10 and Pd-HM10 catalysts. The Ni-HM10 catalyst gives selectivity percentages for the isomerization in the range of 76%–95%.

Catalyst Selectivities towards the Side Reaction Products (Disproportionation and Dealkylation Reactions)

The catalyst selectivities for disproportionation and dealkylation side reactions are low as shown in *Fig. 5* and *6*. This reflects on the high selectivity for the isomerization reaction, specially on increasing the time on stream. As a result, the Ni-HM10 catalyst appears to be a very promising isomerization

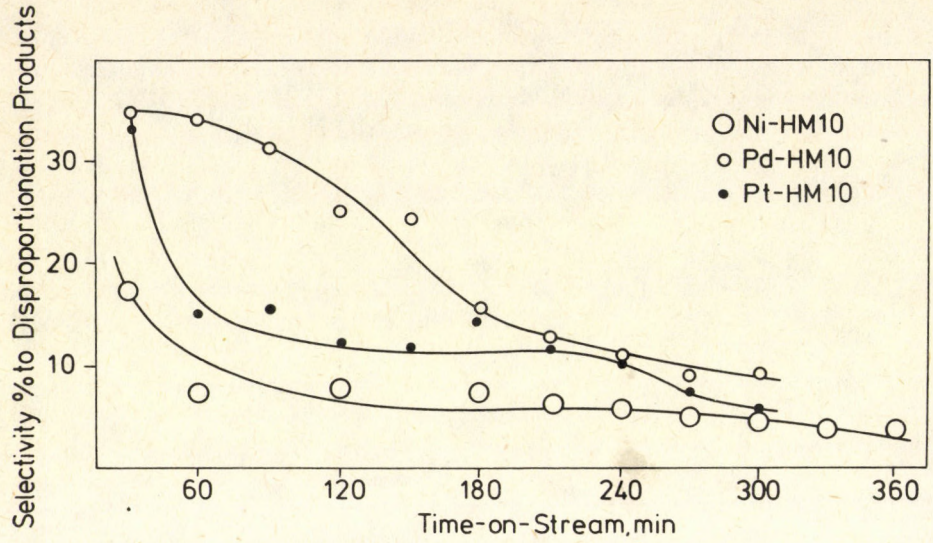

Figure 5.

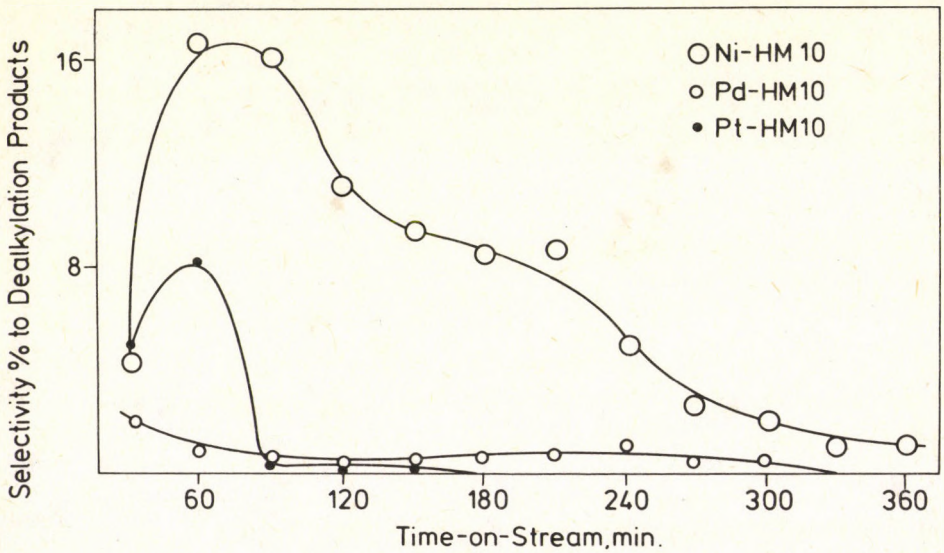

Figure 6.

catalyst for production of *o*- and *p*-xylene in a high purity and quantity, as the other two catalysts give a relative higher selectivity for side reactions and at the same time they show low isomerization activity.

Conclusions:

The following major conclusions are drawn from the present work.

The parent H-mordenite H-M10 catalyst [4], and Ni-HM10, have higher isomerization activity and stability compared to the Pt-HM10 nad Pd-HM10 catalysts.

The Ni-HM10 catalyst is characterized by a relative lower activity for the total side reactions, (Dealkylation and disproportionation reactions), than the HM-10 catalyst.

The Ni-HM10 shows the highest selectivity for the isomerization of *m*-xylene, than all the catalysts used, (HM10, Pt-HM10 and Pd-HM10).

The highest selectivity and activity for *m*-xylene isomerization (>95% selectivity, and 34.4% conversion) to give *o*- and *p*-xylenes were obtained using the Ni-HM10 catalyst, after 360 minutes time on stream.

REFERENCES

1. Thomss, C. L.: "Catalytic Processes and Proven Catalysts", Academic Press, New York and London, 1970.
2. Sukhanov, V. P.: "Catalytic Processes in Petroleum Refining", Khimiya, Moscow, 1973.
3. Minachev, Kh. M. and Isakov, Ya. I.: "Zeolite Chemistry and Catalysis", Ed. Rabo, J. A., Washington, D. C., p 552. 1976.
4. A paper presented to "ERDOL-ERDGAS-KOHLE JOURNAL" for Publication in July 1986, entitled "A Study on the Catalytic Activity and Aging for *m*-Xylene Isomerization over Aluminum Deficient-*H*-Mordenites" by F. I. Kenawi and A. K. El-Morsi.
5. Mukhlyonov, I. P., Dobkina, E. I., Deryuzhkina, V. I. and Soroko, V. E.: "Catalyst Technology" Mir, Publishers, Moscow, p 77. 1976.
6. Savita, V. and Paul, R.: Journal of Catalysis, 1981, 72, 111.
7. Walsh, D. E. and Rollman, L. D.: Journal of Catalysis, 1979, 56, 195.
8. Shashidnar, S. B. and Suresh, R. P.: Ind. Eng. Chem. Prod. Res. Dev. 1981, 20. 102.
9. Imelik, B., Naccache, C., Ben Taarit, Y., Verdine, J. C., Coudurier, G. and Pralioud, H.: Catalysis by Zeolite. Elsevier Scientific Publishing Co., p 241, 1980.
10. Germain, J. E.: Catalytic Conversion of Hydrocarbons. Academic press, London and New York, pp. 54–118, 1969.

HUNGARIAN JOURNAL
OF INDUSTRIAL CHEMISTRY
VESZPRÉM
Vol. 17. pp. 509–521 (1989)

RESIDENCE TIME AND DISPLACEMENT DISTRIBUTIONS IN THE CASE OF CONTINUOUS-FLOW COMBINED WITH AN IMBEDDED MARKOV PROCESS IN THE FIXED BED*

Á. PETHÖ

(Institut für Technische Chemie, Universität Hannover, D-3000 Hannover, West Germany)

Dedicated to Professor L. T. FAN, Kansas State University, on the occasion of his 60th birthday

Received: July 6, 1989

The distribution of the residence times and displacements of the solute particles is considered in a continuous-flow column of infinite length, where convection, dispersion and "sorption" of the solute take place simultaneously. The sorption, however, will be described by a continuous-time MARKOV process with a transition matrix of general type.

The Reaction Mixture of WEI and PRATER [1]

Consider n fixed (stationary) *phases,* henceforth also called *states,* interconnected with each other and well-mixed. Consider a *tracer,* which can be solved (or sorbed) in these phases in such a way that *interfacial reactions:*

$$A_i = A_j \qquad (i, j = 1, 2, \ldots, n;\ i \neq j) \tag{1.1}$$

take place between the single *tracer components* in the respective phases A_1; $i = 1, 2, \ldots, n$. Define r_{ij} $(i \neq j)$ as the *rate of formation* of A_i in the "reaction" (1.1) and let there be:

$$r_{ij} = k_{ij}x_j - k_{ji}x_i, \qquad k_{ij} \geqq 0 \tag{1.2}$$

where:

x_i: concentration of A_i, kg
k_{ij}: rate constant, 1/s

* Presented at the North American/German Workshop on Chemical Engineering Mathematics and Computation, Göttinger, West Germany; July 18–23. 1989.

In the absence of any inputs or outputs we have the dynamical (kinetic) equations:

$$\frac{dx_i}{dt} = \sum_{j \neq i} r_{ij}; \quad i = 1, 2, \ldots, n \tag{1.3}$$

(where t: time, sec) with the initial conditions, say:

$$\text{for } t=0: \quad x_i = \delta_{1i} = \begin{cases} 1, & i=1 \\ 0 & \text{otherwise} \end{cases} \tag{1.4}$$

(1.3), taking into account (1.2), can be written as:

$$\frac{dx_i}{dt} = \sum_{j \neq i} (k_{ij}x_j - k_{ji}x_i) = \sum_{j=1}^{n} k_{ij}x_i \tag{1.5}$$

with:

$$k_{ii} = -\sum_{j \neq i} k_{ji} \tag{1.6}$$

The *System (or Transition) Matrix:*

$$\mathbf{K} = [k_{ij}]; \quad i, j = 1, 2, \ldots, n \tag{1.7}$$

is such that in each column the sum of the elements amounts to zero. This type of matrix is fundamental in the theory of MARKOV processes. (However, we are not so much interested in this theory, because our concern will be focused on continuous-flow systems, where one of the phases is no longer stationary.)

The Moving-Phase system [4, 5]

Let us consider a tube (or column), which should be of infinite length in the positive direction. This column should contain a mobile phase and a fixed bed (consisting of several stationary phases). Consider now a solute in the mobile phase, which is capable of being solved (or sorbed) in the fixed bed. The solute in question should be uniformly distributed in each cross section of the moving phase (i.e. no diffusion is supposed to take place in the lateral direction). Under such conditions the process, namely diffusion and convection (in the mobile phase) as well as sorption (in the fixed bed) of the solute, can be described by two independent variables: by the *position* (axial coordinate) z ($0 \leqq z \leqq \infty$) and by the time t ($0 \leqq t \leqq \infty$).

Let us now define a MARKOV process (1.1) in this model. Suppose that A_1 is the mobile phase, the rest $\{A_2, A_3, \ldots, A_n\}$ constituting the fixed bed. Between the phases so described "reactions" of type (1.2) should take place, irrespective of the other transport process mentioned above. Let us further define the concentration of the solute x_1 (z, t) in state A_i as its amount related to the unit length of column. Presuming that the flow of phase A_1 may be characterized by the constant linear velocity U, further that the diffusion of the solute therein is governed by Fick's law and can be described by the constant diffusivity D,

the *fluxes* in the single phases become:

$$y_1 = UX_1 D \frac{\partial x_1}{\partial z}; \quad y_2 = y_3 = \ldots = y_n = 0 \tag{2.1}$$

The continuity equations will be, instead of (1.3):

$$\frac{\partial x_i}{\partial t} + \frac{\partial y_i}{\partial z} = \sum_{j \neq i} r_{ij}; \quad i = 1, 2, \ldots, n \tag{2.2}$$

or shorter:

$$\sum_{j=1}^{n} k_{ij} x_j = 0; \quad i = 1, 2, \ldots, n \tag{2.3}$$

with:

$$k_{ii} = \begin{cases} D \frac{\partial^2}{\partial z^2} - U \frac{\partial}{\partial z} - \frac{\partial}{\partial t} - \sum_{j \neq i} k_{j1}, & \text{for } i = 1 \\ - \sum_{j \neq i} k_{ji} & \text{for } i \neq 1 \end{cases} \tag{2.4}$$

Finally, the initial and boundary conditions become:

$$\text{for } t = 0: \quad x_i = 0 \text{ for each } i \tag{2.5}$$
$$\text{for } z = 0: \quad y_1 = \delta(t) \tag{2.6}$$
$$\text{for } z \to \infty: \quad x_i < \infty \text{ for each } i \tag{2.7}$$

$\delta(t)$ being the DIRAC-δ-function.
The *problem* now is to solve the system (2.3)–(2.4) along with (2.5)–(2.6)–(2.7).

The Laplace-Transformed Equations

Define the *bivariate* LAPLACE transforms (in z as well as in t) of x_i, for the sake of simplicity, as $x_i(v, s)$, v and s being the transform variables:

$$x_i \xrightarrow{L_z L_t} x_i(v, s) \tag{3.1}$$

The notations $x_i(z, s)$ and $x_i(v, t)$ will also be used for the univariable transforms. Further, define $\xi(s)$ as:

$$\text{for } z = 0: \quad x_1 \xrightarrow{L_t} \xi(s) \tag{3.2}$$

We thereby obtain the following system of linear algebraic equations from (2.3)–(2.4):

$$\sum_{j=1}^{n} k_{ij}(v, s) x_j(v, s) = \begin{cases} Dv\xi(s) - 1, & i = 1 \\ 0, & i = 2, 3, \ldots, n \end{cases} \tag{3.3}$$

where the matrix elements $k_{ij}(v, s)$ are as follows:

$$k_{ij}(v, s) = \begin{cases} k_{ij}, & i \neq j \\ k_{ii}(v, s) & i = j \end{cases} \tag{3.4}$$

with:

$$k_{ii}(v, s) = \begin{cases} Dv^2 - Uv - s \sum\limits_{j \neq i} k_{j1}, & i = 1 \\ -s - \sum\limits_{j \neq i} k_{ji}, & i \neq 1 \end{cases} \tag{3.5}$$

The auxiliary parameter $\xi(s($ in (3.3) can be determined by the boundedness condition (2.7). In what follows we shall use the notation:

$$\det [k_{ij}(v, s)] = \Delta(v, s) \tag{3.6}$$

An Example: the Case of $n = 1$

We now have for (3.3):

$$(Dv^2 - Uv - s)x(v, s) = Dv\xi(s) - 1 \tag{3.7}$$

i.e.:

$$x(v, s) = \frac{Dv\xi(s) - 1}{\Delta(v, s)} = \frac{a_1}{v - v_1} + \frac{a_2}{v - v_2}$$

where v_1 and v_2 are the *roots* of the equation:

$$\Delta(v, s) = Dv^2 - Uv - s = 0 \tag{3.8}$$

a_1 and a_2 being the coefficients of the above partial fraction expansion:

$$a_1 = \frac{v_1\xi - 1/D}{v_1 - v_2} \qquad a_2 = \frac{v_2\xi - 1/D}{v_2 - v_1} \tag{3.9}$$

For the *inverse transform* of $x(v, s)$ with respect to v we obtain:

$$x(z, s) = a_1 e^{v_1 z} + a_2 e^{v_2 z} \tag{3.10}$$

with:

$$v_1 = U/D(\tfrac{1}{2} - r), \qquad v_2 = U/D(\tfrac{1}{2} + r) \tag{3.11}$$

$$r = \sqrt{\tfrac{1}{4} + \frac{Ds}{U^2}} \tag{3.12}$$

Equation (3.10) has to comply with the boundedness condition (2.7) for $z \to \infty$, i.e. since $v_2 > 0$ (for $s = 0$) we have:

$$a_2 = 0 \quad \text{or} \quad \xi(s) = \frac{1}{Dv_2}$$

whereby:

$$a_1 = \frac{1}{Dv_2}$$

and:

$$x(z, s) = \frac{1}{Dv_2} e^{v_1 z} \tag{3.13}$$

We immediately get for the respective *flux:*

$$y(z, s) = Ux(z, s) - D\frac{dx(z, s)}{dz} = \frac{1}{Dv_2}(U - Dv_1)e^{v_1 z} = e^{v_1 z} \tag{3.14}$$

The equations (3.13) and (3.14) will be the starting point of what follows.

The General Case [2, 3]

Let us now consider the general n-phase system. In the Appendix it will be proved that the transformed concentration and flux, $x_1(z, s)$ and $y_1(z, s)$, are determined by (3.11–(3.13)–(3.14) with the substitution:

$$r = \sqrt{1/4 - \frac{D}{U_2}\frac{\Delta(0, s)}{d(s)}} \tag{4.1}$$

where $\Delta(0, s)$ is given by (3.6) inserting $v = 0$, and $d(s)$ is the minor obtained when erasing the 1st row and 1st column in $\Delta(v, s)$. To be explicit, we thus can write:

$$x_1(z, s) = \frac{1}{Dv_2} e^{v_1 z} \tag{4.2}$$

and:

$$y_1(z, s) = e^{v_1 z} \tag{4.3}$$

where v_1 and v_2 are those in (3.11) with (4.1). Let us simplify our notation by defining the *total (overall) flux* in the system, see also (2.1), as:

$$y = y_1 + \ldots + y_n = y_1 \tag{4.4}$$

regardless of whether we use Laplace transforms or not, and similarly let us write for the *total (overall) concentration* of the solute:

$$x = x_1 + \ldots + x_n \tag{4.5}$$

In the Appendix it will be proved that:

$$\frac{x(z, s)}{x_1(z, s)} = -\frac{\Delta(0, s)}{s\, d(s)} \tag{4.6}$$

further that:

$$x(z, s) = -\frac{v_1}{s} e^{v_1 z} \tag{4.7}$$

The relationship (4.6) means, surprisingly enough, that the left-hand side is independent of the position z as well as fo U and D; it depends on the sorption process only. (4.6) can be rewritten as:

$$\frac{x(z, s)}{x_1(z, s)} = -\frac{\Delta(0, s)}{s\, d(s)} = Cf(s) + 1 \tag{4.8}$$

where the transformed *transient function* $f(s)$ has been introduced; it is such that

$$\text{for } s=0: \quad f(s)=1 \tag{4.9}$$

Namely, in the equilibrium case ($t=\infty$) we have:

$$\lim_{t=\infty} \frac{x(z,t)}{x_1(z,t)} = \lim_{s=0} \frac{x(z,s)}{x_1(z,s)} = C+1 \tag{4.10}$$

where the *equilibrium constant:*

$$C = \lim_{t=\infty} \frac{x_2(z,t)+\ldots+x_n(z,t)}{x_1(z,t)} = \lim_{s=0} \frac{x(z,s)+\ldots+x_n(z,s)}{x_1(z,s)} \tag{4.11}$$

has been defined (under assumption that equilibrium can be established).

Remark

It will be shown in a subsequent paper that the transient function $f(t)$ is the density of a residence time distribution ("desorption time" distribution) defined for the original MARKOV process (Section 1) when describing diffusion in the fixed bed.

Two examples

Firstly let us investigate the two-phase system ($n=2$). From (3.4–(3.5)–(3.6) we have:

$$\Delta(0,s) = \begin{vmatrix} -(s+k_{12}) & k_{12} \\ k_{21} & -(s+k_{12}) \end{vmatrix} = (s+k_{21})(s+k_{12}) - k_{12}k_{21} \tag{5.1}$$

and:

$$d(s) = -(s+k_{12}) \tag{5.2}$$

i.e. according to (4.8)–(4.9):

$$Cf(s)+1 = \frac{(s+k_{21})(s+k_{12})-k_{12}k_{21}}{s(s+k_{12})} = \frac{s+k_{12}+k_{21}}{s+k_{12}} \tag{5.3}$$

and:

$$C+1 = \frac{k_{12}+k_{21}}{k_{12}}$$

or: (5.4)

$$C = \frac{k_{21}}{k_{12}}$$

and the transformed transient function $f(s)$ becomes:

$$f(s) = \frac{k_{12}}{s+k_{12}} \tag{5.5}$$

Secondly, let us investigate the three-phase system ($n=3$). From (3.4)–(3.5)–(3.6) we have:

$$\Delta(0,s)=\begin{vmatrix} -(s+k_{21}+k_{31}) & k_{12} & k_{13} \\ k_{21} & -(s+k_{12}+k_{32}) & k_{23} \\ k_{31} & k_{32} & -(s+k_{13}+k_{23}) \end{vmatrix}$$

and: (5.6)

$$\mathrm{d}(s)=\begin{vmatrix} -(s+k_{12}+k_{32}) & k_{23} \\ k_{32} & -(s+k_{13}+k_{23}) \end{vmatrix}$$

In order to develop a straightforward algorithm we need the general form of the *characteristic determinant* of nth order, $\mathbf{I}$ being the respective identity matrix:

$$|s\mathbf{I}-\mathbf{K}| = (-1)^n\Delta(0,s) = s^n - \sum_i k_{ii}s^{n-1} + \sum_{i,j}\sum \begin{vmatrix} k_{ii}k_{ij} \\ k_{ji}k_{jj} \end{vmatrix} s^{n-2} + \ldots + (-1)^n|\mathbf{K}| \tag{5.7}$$

where the 1st summation concerns the *principal minors* of the 1st order of $\mathbf{K}$, the 2nd summation concerns those of the 2nd order, and so on. In our case, see (1.6), $|\mathbf{K}|$ becomes zero, whereby (5.7) will be simpler; e.g. if $n=3$, see (5.6):

$$|s\mathbf{I}-\mathbf{K}| = -\Delta(0,s) = s^3 - \sum_i k_{ii}s^2 + \sum_i K_{ii}s \tag{5.8}$$

having used the notation:

$$K_{ii}; \quad i = 1, 2, \ldots, n \tag{5.9}$$

for the principal minors of the $(n-1)$th order of the system matrix $\mathbf{K}$. Similarly, $d(s)$ in (4.8) can be written, introducing the *submatrix* $\mathbf{K}^1$ obtained when deleting the 1st row and 1st column in $\mathbf{K}$, as:

$$|s\mathbf{I}^1-\mathbf{K}^1| = (-1)^{n-1}\,d(s) = s^{n-1} - \sum_{i\neq 1} k_{ii}s^{n-2} + \ldots + (-1)^{n-1}K_{11} \tag{5.10}$$

and, if $n=3$, see (5.6), we obtain:

$$d(s) = s^2 - \sum_{i\neq 1} k_{ii}s + K_{11} \tag{5.11}$$

In view of (4.8) we eventually have:

$$Cf(s)+1 = \frac{|s\mathbf{I}-\mathbf{K}|}{s|s\mathbf{I}^1-\mathbf{K}^1|} = -\frac{\Delta(0,s)}{s\,d(s)} = \frac{s^{n-1} - \sum_i k_{ii}s^{n-2} + \ldots + (-1)^{n-1}\sum_i K_{ii}}{s^{n-1} - \sum_{i\neq 1} k_{ii}s^{n-2} + \ldots + (-1)^{n-1}K_{11}} \tag{5.12}$$

wherefrom, by inserting $s=0$, C becomes:

$$C = \frac{\sum_i K_{ii}}{K_{11}} - 1 = \frac{\sum_{i=1} K_{ii}}{K_{11}} \tag{5.13}$$

Finally, we write down the respective formulae for $n=3$, see (5.6)–(5.8)–(5.11):

$$Cf(s) = \frac{(a+g)s + (ah+ad+gd) + (ac+gb+gc)}{s^2 + (b+c+h+d)s + (bh+bd+ch)} \tag{5.14}$$

wherefrom, by inserting $s=0$, C can be obtained; for the sake of simplicity, we have introduced the following notations:

$$\mathbf{K} = [k_{ij}] = \begin{bmatrix} -(a+g) & b & h \\ a & -(b+c) & d \\ g & c & -(h+d) \end{bmatrix} \tag{5.15}$$

Remark

If we *a priori* know that the left-hand side of (4.6): $x(z, s)/x_1(z, s)$ is independent of whether or not the "mobile" phase A_1 is moving along the fixed one, the relationship (5.12) can immediately be obtained. I.e., consider the reaction mixture of WEI and PRATER (Section 1) and take the Laplace transforms of (1.4)–(1.5); we thus get for the Laplace transforms of $x_i(t)$, say $x_i(s)$, $i = 1, 2, \ldots, n$, the following system of linear algebraic equations:

$$(s-k_{ii})x_i(s) - \sum_{j\neq i} k_{ij}x_j(s) = \delta_{1i} \tag{5.16}$$

whose system matrix is obviously $s\mathbf{I}-\mathbf{K}$. Applying CRAMERS's rule we have:

$$x_1(s) = \frac{|s\mathbf{I}^1-\mathbf{K}^1|}{|s\mathbf{I}-\mathbf{K}|} \tag{5.17}$$

where the submatrix $\mathbf{K}^1$ is obtained by deleting the 1st row and 1st column in $\mathbf{K}$ (and similary $\mathbf{I}^1$ too). Let us now determine the relationship $x(s)/x_1(s)$, $x(s)$ being the Laplace transform of the total mass (1 kg); in view of (5.17) we have:

$$\frac{x(s)}{x_1(s)} = \frac{|s\mathbf{I}-\mathbf{K}|}{s|s\mathbf{I}^1-\mathbf{K}^1|} = Cf(s)+1$$

The distribution of Residence Times and Displacements, respectively

Let us consider a particle of the solute and the time ψ_z when this particle has left the column section $[0, z]$. This time is the *residence time* of the particle at the place z. The quantity ψ_z may be considered as a random variable, and its probability *density function* is obviously the *total flux*: y, for which we have, see (4.3)–(4.4)

$$y(z, t) \xrightarrow{L_t} y(z, s) = e^{v_1 z} \tag{6.1}$$

with, see (3.11)–(4.1)–(4.8):

$$v_1 = \frac{U}{D}(\tfrac{1}{2}-r) \tag{6.2}$$

$$r = \sqrt{\tfrac{1}{4} + \frac{Ds}{U^2 q}\,[pf(s) + q]} \tag{6.3}$$

after having introduced the new notations:

$$p = \frac{C}{1+C}, \quad q = \frac{1}{1+C}. \tag{6.4}$$

Let us now turn our attention to the *displacement* (position) η_t of a particle of the solute at time t. The quantity η_t may be considered as a random variable, and its probability *density function* will obviously be the *total concentration: x*, for which we have, see (4.5)–(4.7):

$$x(z, t) \xrightarrow{L_t} x(z, s) = -\frac{v_1}{s} e^{v_1 z} \tag{6.5}$$

and:

$$x(z, s) \xrightarrow{L_t} x(v, s) = -\frac{1}{s}\,\frac{v_1}{v - v_1} \tag{6.6}$$

with v_1 as above.
Moments of both random variables (residence times and displacements) can be easily obtained. Let us first consider the transformed density (6.1); it is a wellknown fact that:

$$E(\psi_z) = -\left.\frac{dy(z, s)}{ds}\right|_{s=0} \tag{6.7}$$

and:

$$D^2(\psi_z) + E^2(\psi_z) = \left.\frac{d^2 y(z, s)}{ds^2}\right|_{s=0} \tag{6.8}$$

where by:

$$E(\psi_z) \quad \text{and} \quad D^2(\psi_z)$$

the *mean* and *variance* of the residence times have been denoted. The calculations can be even simplified by observing that:

$$\ln y = v_1 z$$

consequently:

$$E(\psi_z) = \left(-\left.\frac{dv_1}{ds}\right|_{s=0}\right) z \tag{6.9}$$

and:

$$D^2(\psi_z) = \left(\left.\frac{d^2 v_1}{ds^2}\right|_{s=0}\right) z \tag{6.10}$$

It is an easy matter to show, see (6.2)–(6.3)–(6.4), that:

$$E(\psi_z) = \frac{1}{Uq} z \tag{6.11}$$

and:

$$D^2(\psi_z) = \frac{2D_{\text{eff}}}{U^3 q^2} z \tag{6.12}$$

with:

$$D_{\text{eff}} = D - U^2 pq \left.\frac{df}{ds}\right|_{s=0} \tag{6.13}$$

Let us now consider the time transformed density (6.5) of the displacement distribution; in order to determine the mean and variance, the bivariate transformed density (6.6) is needed along with the following relationships:

$$E(\eta_t) \xrightarrow{L_t} - \left.\frac{dx(v, s)}{dv}\right|_{v=0} \tag{6.14}$$

and:

$$D^2(\eta_t) + E^2(\eta_t) \xrightarrow{L_t} - \left.\frac{d^2x(v, s)}{dv^2}\right|_{v=0} \tag{6.15}$$

where:

$$E(\eta_t) \quad \text{and} \quad D^2(\eta_t)$$

stand for the mean and variance in question. Regarding (6.2)–(6.6) one obtains:

$$- \left.\frac{dx(v, s)}{dv}\right|_{v=0} = \frac{D}{U} \frac{1}{s(r-\frac{1}{2})} \tag{6.16}$$

and:

$$\left.\frac{d^2x(v, s)}{dv^2}\right|_{v=0} = 2\left(\frac{D}{U}\right)^2 \frac{1}{s(r-\frac{1}{2})^2} \tag{6.17}$$

Now, instead of giving the exact inverse transforms of these equations, we rather determine asymptotic relationships for large values of t. This may be done by expansions into asymptotic series of the right-hand sides. Taking into account (6.3) as well as the derivatives, see also (6.13):

$$\left.\frac{dr}{ds}\right|_{s=0} = \frac{D}{U^2 q}, \quad \left.\frac{d^2r}{ds^2}\right|_{s=0} = - \frac{2DD_{\text{eff}}}{(U^2 q)^2} \tag{6.18}$$

we immediately have:

$$r - \tfrac{1}{2} = \frac{Ds}{U^2 q}\left(1 - \frac{D_{\text{eff}}}{U^2 q} s + \ldots\right) \tag{6.19}$$

i.e.:

$$\frac{1}{r-\frac{1}{2}} = \frac{U^2 q}{Ds}\left(1 + \frac{D_{\text{eff}}}{U^2 q} s + \ldots\right) \tag{6.20}$$

and so, see (6.16.):

$$- \left.\frac{dx(v, s)}{dv}\right|_{v=0} = \frac{Uq}{s^2}\left(1 + \frac{D_{\text{eff}}}{U^2 q} s + \ldots\right) \tag{6.21}$$

Inverse transformation yields the asymptotic relationship:

$$E(\eta_t) = Uqt + \frac{D_{eff}}{U} \quad \text{for large } t \tag{6.22}$$

Further, comparison of (6.17 and (6.20) results in:

$$\left.\frac{d^2x(v,s)}{dv^2}\right|_{v=0} = \frac{2(Uq)^2}{s^3}\left(1 + \frac{2D_{eff}}{U^2q}s + \ldots\right) \tag{6.23}$$

whose inverse transform, due to (6.15)–(6.22), gives the asymptotic relationship:

$$D^2(\eta_t) = 2D_{eff}qt \quad \text{for large } t \tag{6.24}$$

Finally, we might compare the variance/mean values of the residence time and displacement distributions, see (6.11)–(6.12) and (6.22)–(6.24), obtaining the simple equation:

$$\frac{D^2(\psi_z)}{E(\psi_z)} = \frac{1}{Uq}\frac{D^2(\eta_t)}{E(\eta_t)} \quad \text{for large } t \tag{6.25}$$

Acknowledgement

The author gratefully acknowledges the research support of the Max-Buchner-Forschungsstiftung, FRG.

Symbols

C	equilibrium constant, see Eq. (4.11)
D	diffusivity, m^2/sec
$d(s)$	see Eq. (A3)
$f(s)$	see Eq. (4.8)–(4.9)
i	index (= 1, 2, ..., n)
j	index (= 1, 2, ..., n)
k_{ij}	rate constant, 1/s
K_{ii}	minor of **K** obtained when deleting its ith row and ith column
p	see Eq. (6.4)
q	see Eq. (6.4)
r	see Eq. (6.3)
s	Laplace transform variable, 1/s
t	time, s
U	flow rate, m/s
v	Laplace transform variable, 1/m
$v_1(s)$	that root of Eq. (A10) for which $v_1(0) = 0$
x	see Eq. (4.5), kg/m
x_i	concentration, kg/m
y	see Eq. (4.4), kg/s
y_i	flux, kg/s
z	length co-ordinate, m
$\Delta(v, s)$	see Eq. (A2)
ψ_z	residence time, s
η_t	displacement (position), m
I	identity matrix
$\mathbf{K} = [k_{ij}]$	system (transition) matrix

References
1. WEI J. and PRATER, C. D.: Adv. Catal. *1962*, 13, 203.
2. PETHŐ Á. and SCHAY, G.: Chromatographia *1969*, 2, 158.
3. PETHŐ Á.: Chem. Eng. Sci. *1970*, 25, 769.
4. PETHŐ Á. and SCHÜGERL, K.: Can. J. Chem. Eng. *1974*, 52, 685.
5. PETHŐ Á. and KÜHNE, J.: Computers and Chem. Eng. *1980*, 4, 63.

Appendix

In order to prove (4.1)–(4.2)–(4.3) let us write down (3.4)–(3.5)–(3.6) in detail. For the sake of shortness, let us introduce:

$$S_i = -\left(s + \sum_{j \neq i} k_{ji}\right); \quad i = 1, 2, \ldots, n \tag{A1}$$

whereby we obtain:

$$\Delta(v, s) = \begin{vmatrix} Dv^2 - Uv + S_1 & k_{12} & \ldots & k_{1n} \\ k_{21} & S_2 & \ldots & k_{2n} \\ & \vdots & & \\ k_{n1} & k_{n2} & \ldots & S_n \end{vmatrix} \tag{A2}$$

On developing this determinant according to the (let us say) 1st column we have:

$$\Delta(v, s) = (Dv^2 - Uv)\, d(s) + \Delta(0, s) \tag{A3}$$

where $d(s)$ is the minor if erasing the 1st row and 1st column in $\Delta(v, s)$. Let us now apply CRAMER'S rule in order to get $x_1(v, s)$ from (3.3):

$$x_1(cv, s) = \frac{1}{\Delta(v, s)} \begin{vmatrix} Dv\xi(s) - 1 & k_{12} & \ldots & k_{1n} \\ 0 & S_2 & \ldots & k_{2n} \\ & \vdots & & \\ 0 & k_{n2} & \ldots & S_n \end{vmatrix} = \frac{Dv\xi(s) - 1}{\Delta(v, s)}\, d(s) \tag{A4}$$

i.e.:

$$\left[Dv^2 - Uv + \frac{\Delta(0, s)}{d(s)}\right] x_1(v, s) = Dv\xi(s) - 1 \tag{A5}$$

which will be the same as (3.7) if substituting:

$$-\frac{\Delta(0, s)}{d(s)} \quad \text{for } s$$

I.e., (3.13)–(3.14) are still valid if in (3.12) the above substitution is made. In order to prove (4.6) let us add the n equation in (3.3) obtaining:

$$\sum_{i=1}^{n} \sum_{j=1}^{n} k_{ij}(v, s) x_j(v, s) = Dv\xi(s) - 1 \tag{A6}$$

where the left-hand side can be simplified in view of (3.4)–(3.5):

$$(Dv^2 - Uv) x_1(v, s) - s \sum_{i=1}^{n} x_i(v, s) = Dv\xi(s) - 1 \tag{A7}$$

i.e.:

$$\frac{s\sum_{i=1}^{n} x_i(v, s)}{x_1(v, s)} = Dv^2 - Uv - \frac{Dv\xi(s) - 1}{x_1(v, s)} \tag{A8}$$

Because of (A4) the last term here is $\Delta(v, s)/d(s)$ whereby we immediately obtain, in view of (A3), the following relationship in the bivariate LAPLACE domain:

$$\sum_{i=1}^{n} x_i(v, s) = -\frac{\Delta(0, s)}{s\, d(s)} x_1(v, s) \tag{A9}$$

Taking the inverse transforms on both sides with respect to v we get (4.6) indeed. In order to prove (4.7) let us observe that v_1 and v_2 (see (3.11)) are the roots of the bracket-expression in (A5):

$$Dv^2 - Uv + \frac{\Delta(0, s)}{d(s)} = D(v - v_1)(v - v_2) \tag{A10}$$

from which we also have the relationship:

$$Dv_1v_2 = \frac{\Delta(0, s)}{d(s)} \tag{A11}$$

Comparing (4.2)–(4.6)–(A11) we get (4.7) indeed.

HUNGARIAN JOURNAL
OF INDUSTRIAL CHEMISTRY
VESZPRÉM
Vol. 17. pp. 523–543 (1989)

OPTIMAL CONTROL BY DYNAMIC PROGRAMMING USING ACCESSIBLE GRID POINTS AND REGION REDUCTION*

R. LUUS

(Department of Chemical Engineering University of Toronto
Toronto, Ontario M5S 1A4, Canada)

Received: July 26, 1989.

To reduce computational effort and avoid the curse of dimensionality in using dynamic programming, it is proposed to use for the x-grid only accessible states. Then a relatively small number of grid points suffice, even if the dimension of **x** is large. The effect of the reduction factor for region contraction is investigated with the use of two systems that have been difficult to optimize by other methods. For both systems, results are obtained that are better than have been presented in literature. The use of accessible states and region reduction provides an attractive means for using dynamic programming to obtain an optimal control policy of highly nonlinear systems.

Dedication

This paper is dedicated to Professor RUTHERFORD ARIS for his 60th birthday. Professor ARIS has provided mathematical inspiration and guidance to chemical engineers for over 30 years and has had a profound influence on this author for at least 25 years. It is hoped that this paper will rekindle the interest in dynamic programming taht Professor ARIS aroused with his book entitled "Discrete Dynamic programming", 25 years ago.

Introduction

To investigate the design possibilities of some engineering system, we frequently encounter the problem of determining the maximum or minimum value of some performance criterion when the system is described by a set of ordinary differen-

* Presented at the North American/German Workshop on Chemical Engineering Mathematics and Computation, Göttingen, West Germany; July 18–23. 1989.

tial equations. If the equations are linear, the problem is not difficult in general. However, if the equations are nonlinear, then this optimal control problem can be quite difficult. What is most annoying is when a mathematical procedure, that works well for many systems, gives a wrong answer or converges to a value that is not the global optimum for the particular system for which the optimal solution is not known. To avoid such a problem, one would like to cross-check the optimization by a completely different procedure, rather than simply taking different starting points. For systems of low order, dynamic programming with region contraction as presented by LUUS [3] gives an excellent means of obtaining the optimal control. The goal of this paper is to extend the procedure to high-order systems through the use of accessible states only for the **x**-grid, as suggested by DETREMBLAY and LUUS [1] in the study of oscillating systems. But there the optimum was sought in a single pass. Here we would like to take advantage of both approaches to provide a useful procedure for the determination of optimal control of nonlinear systems.

When BELLMAN first introduced dynamic programming, there was much interest in applying the approach to solve many engineering problems as illustrated in the books written by BELLMAN and DREYFUS [12] and ARIS [11]. However, to apply the dynamic programming computational procedure to optimal control problems presents several difficulties. The greatest difficulty is the problem of setting up the grid values for the state and the control. To have meaningful results, the state grid must be sufficiently fine. For optimization then, at each time step, for each grid point in the state, the state equations must be integrated for each allowable value for control. Therefore, a large number of integrations must be performed at each time step. A greater problem, however, arises when the trajectory calculated for a particular grid point does not meet a grid point at the next time step. Interpolation as outlined by LAPIDUS and LUUS [2] may be used, but the resulting approximation may be unreliable. The need for a very large number of grid points and the interpolation problem tended to discourage the use of dynamic programming for optimal control problems. WALLER et al. [9] introduced the proportional operator dynamic programming for optimal control. The method yielded rapid convergence to the vicinity of the global optimum, but could not reach sufficiently close to the optimum.

To overcome the problem of interpolation, LUUS [3] showed that simply taking the optimal control policy obtained for the nearest state vector grid point as used by DETREMBLAY and LUUS [1] works very well. The use of a coarse grid with region contraction to provide an accurate answer worked very well with three test problems (LUUS [3]). But even here the curse of dimensionality comes to the forefront. If we visualize an **x**-grid having only 5 values for each state variable, we see that for $n=3$ there are 125 points to consider, which is still manageable; but with $n=5$ the number of grid points would increase to 3,125, which is a very large number. We also observe that most of such grid points are inaccessible form the initial state specified and therefore the computations are not very efficient.

This problem of a very large number of grid points is overcome by using only the points that can be reached from the given initial state by applying control. Therefore, instead of choosing the **x**-grid points independently, a procedure where these are generated by applying different control action as used by DeTremblay and Luus [1] appears to be very attractive. Then all the grid points are at least accessible through the control applied to the initial state.

The purpose of this paper is to test this approach on optimal control problems. Also we wish to investigate the choice of the number of grid points to use, number of allowable levels for control, and the effect of the reduction factor used after each iteration.

Problem Formulation

Let us consider the system described by the differential equation:

$$\frac{d\mathbf{x}}{dt} = \mathbf{f}(\mathbf{x}, u) \tag{1}$$

with $\mathbf{x}(0)$ given, where $\mathbf{x}$ is an $(n \times 1)$ state vector and u is a scalar control, bounded by:

$$\alpha \leqq u \leqq \beta \tag{2}$$

The performance index to be maximized is a scalar function of the state at the final time t_f given by:

$$I[\mathbf{x}(0), t_f] = \Phi(\mathbf{x}(t_f)) \tag{3}$$

where the final time t_f is given. This is a very general type of performance index, since we can always define additional state variables to cast an optimal control problem into this form. The optimal control problem is to find the control $u(t)$ in the time interval $0 \leqq t < t_f$ so that the performance index in Eq. (3) is maximized. There is no loss in generality in maximizing, since to minimize an expression, we can simply change the sign of the performance index.

To apply dynamic programming, we approximate the optimal control problem by seeking a piecewise constant control policy, rather than a continuously varying control policy, over P time stages, each of length L, so that:

$$L = \frac{t_f}{P} \tag{4}$$

so that in the time interval $t_{k-1} \leqq t < t_k$ we have the constant control:

$$u(t) = u(k-1) \tag{5}$$

The problem then is to find $u(0)$, $u(1)$, ..., $u(P-1)$ that maximized the performance index in Eq. (3).

Construction of Grid for x

Instead of using the procedure of constructing a uniform grid by assigning values to each state variable as was done in the earlier paper (LUUS [3]), we shall use the scheme used by DETREMBLAY and LUUS [1], where we assign some values to the control variable and integrate Eq. (1) to generate values of **x** at different time stages. This ensures that only accessible states will be included in the grid, and for a high-dimensional system we can still have a reasonably small number of grid points, and the computational effort will not become excessive. We shall therefore assign N values to the control value to generate a grid of N state variables at each time stage. The centre point of the grid corresponds to the state obtained by using the best control policy from the previous iteration.

Allowable Values for the Control for Optimization

We assign M values to the control at each time stage so that the centre point is the best value from the previous iteration. To have a uniform distribution M is chosen to be odd. If the assigned value is outside the bounds specified by Eq. (2), clipping technique is used to substitute either α or β for that value. The allowable values for the control are taken over a region r, so that the extreme values are:

$$u = u^0 \pm r \tag{6}$$

and the rest of them are distributed inside the region. After each iteration, the region r is contracted by a small amount ε, so that the range over which we are seeking the optimum u becomes smaller as the iterations proceed. This technique of region contraction was used by LUUS and JAAKOLA [4] for steady-state optimization.

Use of Dynamic Programming with Region Contraction

To set up the grids and start the iteration, we first examine Eq. (1) and the constraints specified by Eq. (2). For the first run, the number of time stages P can be chosen to be a small number such as 10. The number of **x**-grid points N can be chosen to be between 20 and 50. The centre value for the control can be chosen as $(\beta+\alpha)/2$ and the initial region size r to be $(\beta-\alpha)/2$. The N values for the **x**-grid are generated by taking N values of control inside the region r. A reasonable choice for M is 3 or 5. Since iteration is used, very little is gained by having too many values of control for each grid point.

First Pass Optimization

Let us start at stage P corresponding to the time interval $t_f - L \leqq t < t_f$. For each of the N grid points, integrate Eq. (1) with M values of control and evaluate the performance index:

$$I[\mathbf{x}(t_f - L), t_f] = \Phi(\mathbf{x}(t_f)) \tag{7}$$

Compare the M values of the performance index and keep the control that gives the largest value. Continue this for all the N grid points for the state at time $t_f - L$. We now know the best control policy (from the M allowed values) to use at the last stage for each grid point.

Now we are ready to proceed to stage $P-1$ corresponding to the time interval $t_f - 2L \leqq t < t_f - L$. As before, for each grid point we consider M allowable values of control. Suppose we take one of these values and integrate Eq. (1) from $t_f - 2L$ to $t_f - L$. It is unlikely that the state $\mathbf{x}(t_f - L)$ will be exactly one of the grid points at stage P for which we already know the optimal control policy. Therefore to decide what control to use in the time interval $t_f - L \leqq t < t_f$ we simply take the optimal control policy corresponding to the grid point that is *closest* to the state $\mathbf{x}(t_f - L)$ as suggested by DeTremblay and Luus [1]. This is much better than using interpolation. This problem of not hitting the grid point directly is illustrated by Luus [3]. At t_f we then compare the performance indices and choose the control that gives the maximum value.

Now we are ready to proceed to stage $P-2$ corresponding to the time interal $t_f - 3L \leqq t < t_f - 2L$. We proceed as before. We take a grid point and integrate Eq. (1) with an allowable value of control from $t_f - 3L$ to $t_f - 2L$ to bring the state to $\mathbf{x}(t_f - 2L)$. To integrate from $t_f - 2L$ to $t_f - L$ we choose the best control policy corresponding to the grid point at stage $P-1$ that is closest to $\mathbf{x}(t_f - 2L)$. Integration over one time stage gives us $\mathbf{x}(t_f - L)$. To integrate up to final time we choose again as before the control policy that corresponds to the grid point that is closest to $\mathbf{x}(t_f - L)$. Integration over the last time stage gives us $\mathbf{x}(t_f)$ and allows the performance index to be evaluated. By continuing with the remaining $M-1$ controls, we now have M values of the performance index to compare. The control policy that gives the maximum value to the performance index becomes the optimal control for that grid point at stage $P-2$.

The pattern of calculations is now established and we proceed in this manner backwards until stage 1 is reached. Stage 1 corresponds to the time interval $0 \leqq t < L$ and there is only a single point in the **x**-grid. Now keeping the trajectory and the corresponding optimal control, we have finished the first pass. Even if a large number of grid points is chosen, the optimal policy obtained in this pass is quite far from the global optimal solution. Therefore we proceed to the main part of the proposed procedure, which involves iteration to improve the optimal solution obtained in the first pass.

Iteration with Systematic Reduction in Region Size

The optimal trajectory and the corresponding optimal control from the first pass provides the centre point for the grids for the first iteration. The region r is contracted by a small amount ε, to provide a finer resolution, and the procedure outlined for the first pass is carried out again. At the end of this pass, therefore, an improved solution results.

When this procedure is carried out for a sufficiently large number of such iterations it is clear that the grid will become sufficiently fine to provide an accurate solution. Whether or not the resulting solution is the actual global optimum remains to be determined. As was shown by LUUS [3], one may get a local optimum. We can now summarize the proposed procedure into the following algorithm:

Algorithm:

1. Divide the time interval t_f into P time stages, each of length L.
2. Choose the number of **x**-grid points N and the number of allowable values M for the control u.
3. Choose the region r for the control values.
4. By choosing N values of control inside the allowable region, integrate Eq. (1) N times to generate the **x**-grid at each time stage.
5. Starting at the last time stage P, corresponding to time $t_f - L$, for each **x**-grid point integrate Eq. (1) form $t_f - L$ to t_f for all the M allowable values of control. Choose the control that maximizes the performance index and store the value of control for use in step 6.
6. Step back to stage $P-1$, corresponding to time $t_f - 2L$, and integrate Eq. (1) from $t_f - 2L$ to $t_f - L$ for each **x**-grid point with the M allowable values of control. To continue integration from $t_f - L$ to t_f choose the control from step 5 that corresponds to the grid point closest to the resulting **x** at $t_f - L$. Compare the **M** values of the performance index and store the value of control that gives the maximum value.
7. Continue the procedure until stage 1, corresponding to the initial time $t = 0$ is reached. Store the control policy that maximizes the performance index and store the corresponding **x**-trajectory.
8. Reduce the **x**-grid region and the region for allowable control values by a factor ε; i.e.:

$$r^{(j+1)} = (1-\varepsilon)r^{(j)} \tag{8}$$

where j is the iteration index. Use the optimal **x**-trajectory from step 7 as the mid-point for the **x**-grid at each time stage, and use the optimal control policy from step 7 as the midpoint for the allowable values for the control u.

9. Increment the iteration index j by 1 and go to step 4. Continue the iteration for a specified number of iterations such as 20 and examine the results.

Numerical Examples

Computations were done on a Cray X-MP/24 digital computer in single precision corresponding to 48 binary digits or 14 decimal places. For integration the standard fourth-order Runge-Kutta method was used.

Example 1

We consider first the problem used by YEO [10] to illustrate the use of quasilinearization to solve nonlinear singular control problems. The system is described by:

$$\frac{dx_1}{dt} = x_2 \tag{9}$$

$$\frac{dx_2}{dt} = -x_3 u + 16x_5 - 8 \tag{10}$$

$$\frac{dx_3}{dt} = u \tag{11}$$

$$\frac{dx_4}{dt} = x_1^2 + x_2^2 + 0.0005(x_2 + 16x_5 - 8 - 0.1x_3 u^2)^2 \tag{12}$$

$$\frac{dx_5}{dt} = 1 \tag{13}$$

with the initial condition:

$$\mathbf{x}(0) = \begin{bmatrix} 0 \\ -1 \\ -\sqrt{5} \\ 0 \\ 0 \end{bmatrix} \tag{14}$$

The control is bounded by:

$$-4 \leqq u \leqq 10 \tag{15}$$

It is required to find the control in the time interval $0 \leqq t \leqq 1$ so that the performance index:

$$I = x_4(1) \tag{16}$$

is minimized. By choosing 10 time stages and using a $5 \times 5 \times 5$ grid for x_1, x_2 and x_3 and allowing 7 values for control, LUUS [3] obtained a minimum for I of 0.12012 in 7 minutes of computation time. Here we shall show that we can do much better with the use of a grid having accessible states only as proposed in this paper. For the computations to get reliable results the integration step-size was 0.01 or smaller and clipping technique was used to satisfy Eq. (15).

By choosing $P = 25$, $N = 21$, $M = 3$ and $\varepsilon = 0.1$, we were able to obtain convergence to $I = 0.11937$ in less than 1 minute of computation time. The initial choice for u was 3.0 and the initial region r was taken as 7.0. The choice of larger values

of ε produced faster convergence as shown in *Fig. 1*, where with $t=0.4$ convergence to 0.11937 was obtained in 9 iterations requiring 16 sec of CPU time.

The effect of the number of time stages on the performance index and CPU time is shown in *Table 1*. Reduction factor of 0.7 ($\varepsilon=0.3$) was used throughout and 20 iterations were specified. For $P=14$ and $P=30$ instead of $N=21$, we used 41. The CPU time for 20 iterations is increased by a bit more than a factor of 2.

It is interesting to note that the performance index is improved as P increases, but not monotonically. Amongst the entries $P=28$ gave the best result. The values of the performance index in *Table 1* were checked by ROSEN [6], using

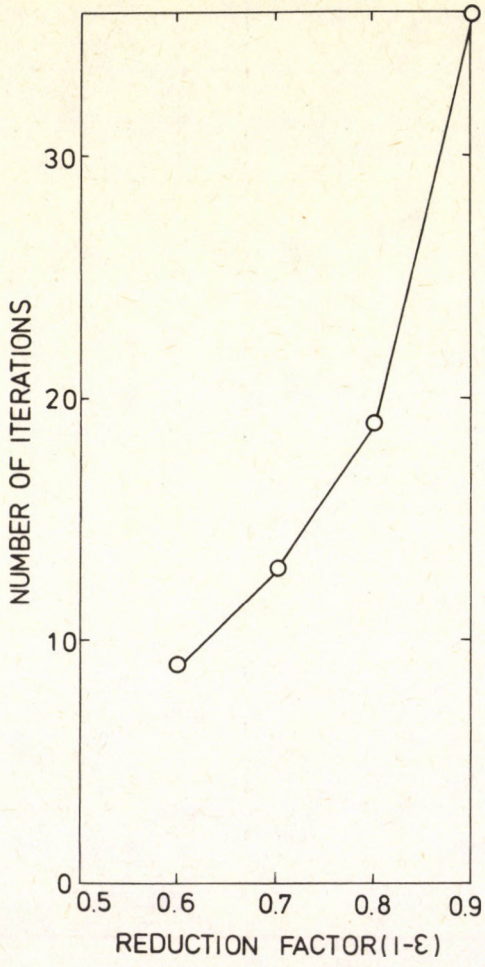

Figure 1
Effect of Reduction Factor on Convergence to $I^0=0.11937$ with $P=25$

Table 1.
Effect of Number of Stages on the Performance Index and CPU time. N = 21, M = 3, $\Theta = 0.3$.

Number of Time Stages P	Optimal Performance Index	Number of Iterations to reach optimum	CPU time for 20 iterations s
10	0.12011	16	11
11	0.11957	13	14
12	0.11952	16	15
13	0.11975	17	16
14	0.11973	13	40*
15	0.11954	12	18
16	0.11951	12	21
17	0.11961	14	21
18	0.11960	13	24
19	0.11948	14	26
20	0.11944	12	26
21	0.11947	12	28
22	0.11944	13	29
23	0.11937	12	34
24	0.11934	13	37
25	0.11937	13	34
26	0.11936	13	37
27	0.11934	14	40
28	0.11933	18	43
29	0.11936	17	46
30	0.11934	12	118*
31	0.11935	13	52

* N = 41 was used

nonlinear programming and DVERK subroutine for integration as outlined by ROSEN and LUUS [7]. The only differences that were found were that for $N = 29$ he obtained 0.11935 instead of 0.11936 and for $N = 13$ he obtained 0.11976 instead of 0.11975. Therefore, there is no doubt about the convergence. It is also interesting to note that here a better result of 0.12011 was obtained for $P = 10$, than reported by LUUS [3].

The optimal control policy for $P = 28$ is given in *Fig. 2*. To obtain further improvement, the number of time stages was doubled to 56. A most surprising result was obtained. Instead of getting an improved result, convergence to 0.11958 resulted in 18 iterations with a CPU time of 110 sec for 20 iterations. This was the first sign of difficulty in convergence, since it is obvious that the result should not be worse than 0.11933 obtained with $P = 28$. The run was repeated by taking $N = 41$ rather than 21. With this value convergence to $I = 0.11927$ resulted in 13 iterations. CPU time for 20 iterations was 296 s. The resulting optimal control policy is shown in *Fig. 3*. The control policy is quite similar to the one shown in *Fig. 2*, but, besides refinement, there is a significantly longer section where the control is zero and the control in the interval $0.64 < t < 0.75$ is quite different.

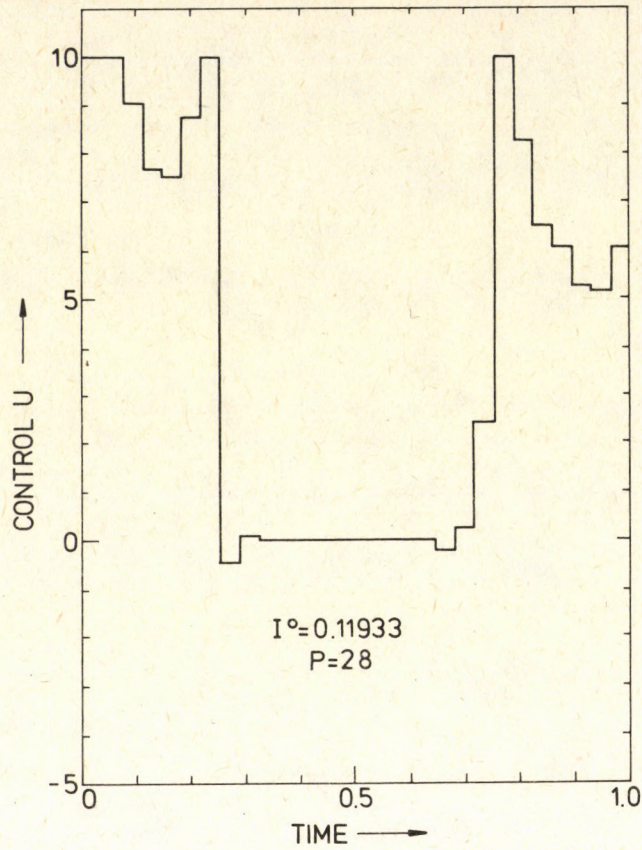

Figure 2
Optimal Control Policy for Example 1 with $P=28$

Example 2

We choose next the tubular reactor problem of ROSENBROCK and STOREY [8] where the mass balance equations are:

$$\frac{dx_1}{dt} = -(k_1+k_2+k_3)x_1 \tag{17}$$

$$\frac{dx_2}{dt} = k_1x_1 - k_4x_2 \tag{18}$$

$$\frac{dx_3}{dt} = k_4x_2 - k_5x_3 \tag{19}$$

with the initial condition:

$$\mathbf{x}(0) = \begin{bmatrix} 1 \\ 0 \\ 0 \end{bmatrix} \tag{20}$$

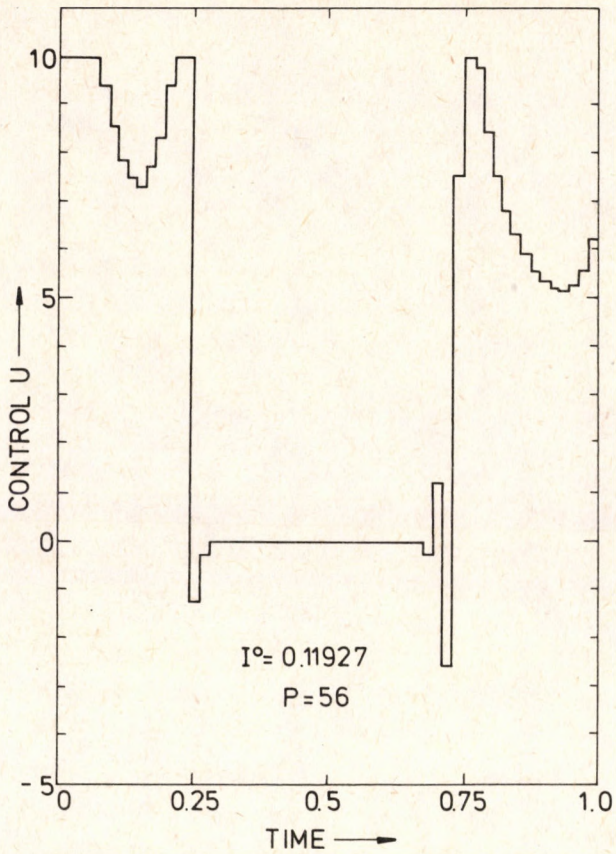

Figure 3
Optimal Control Policy for Example 1 with $P=56$

The rate constants, k_1 to k_5 are given by:

$$k_i = k_{i0} \exp\left\{-\frac{E_i}{R}\left[\frac{1}{T} - \frac{1}{658}\right]\right\} \tag{21}$$

where k_{i0} and E_i are given in *Table 2*. The objective is to maximize $x_3(t_f)$, the outlet concentration of species C by choosing the temperature profile along the reactor, so that:

$$623.16 \leqq T \leqq 823.16 \tag{22}$$

The final time t_f was taken as 1.0 s.

To solve this problem we shall take 21 values of T inside the region assigned to T and integrate the state equations to generate the **x**-grid. After every iteration the region is contracted as before, so the grid becomes finer close to the best trajectory. For the control variable T, we give only 3 allowable values

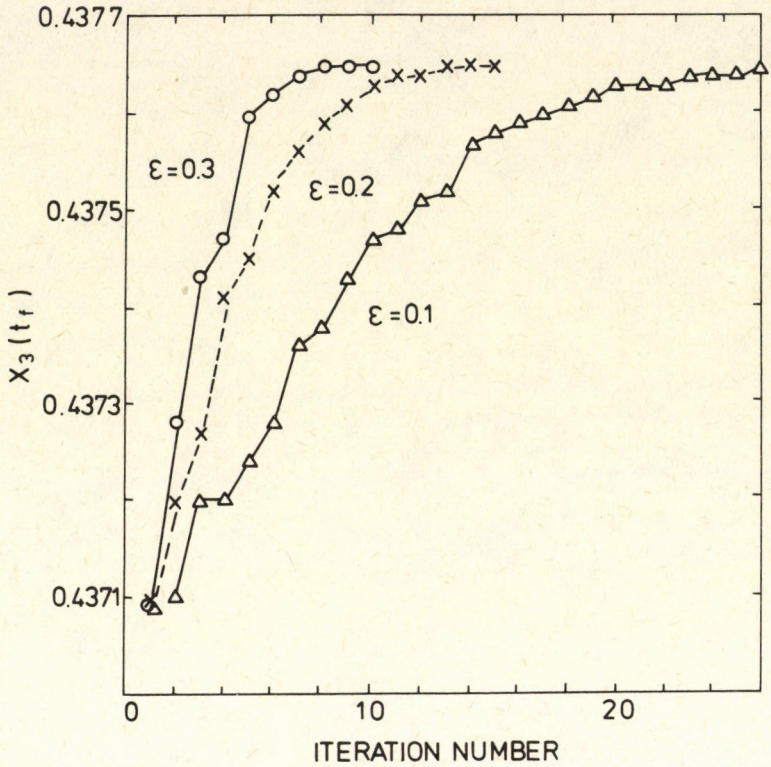

Figure 4
Convergence to the Optimum for Example 2 with $P=15$

Table 2.
Values for k_{i0} and E_i for Example 2

i	1	2	3	4	5
k_{i0}	1.02	0.93	0.386	3.28	0.084
E_i	16000	14000	15000	10000	15000

as before, and clipping is used if Eq. (22) is violated. This means that there are 63 integrations to be performed at each time step.

The initial value of T was taken as 723.16 and the initial region for T was chosen as 100 to span the entire range given by Eq. (22). For integration a step-size of 0.01 or smaller was used to obtain reliable results. For example when $P=15$ was chosen then the integration step-size was taken as 0.01/1.05 so that the final time is reached exactly after 105 integrations steps.

As in Example 1, the convergence to the optimum was quite rapid and systematic a shown in *Fig. 4* where $P=15$ was used. As the reduction factor was decreased, the rate of convergence increased as shown in *Fig. 5* where conver-

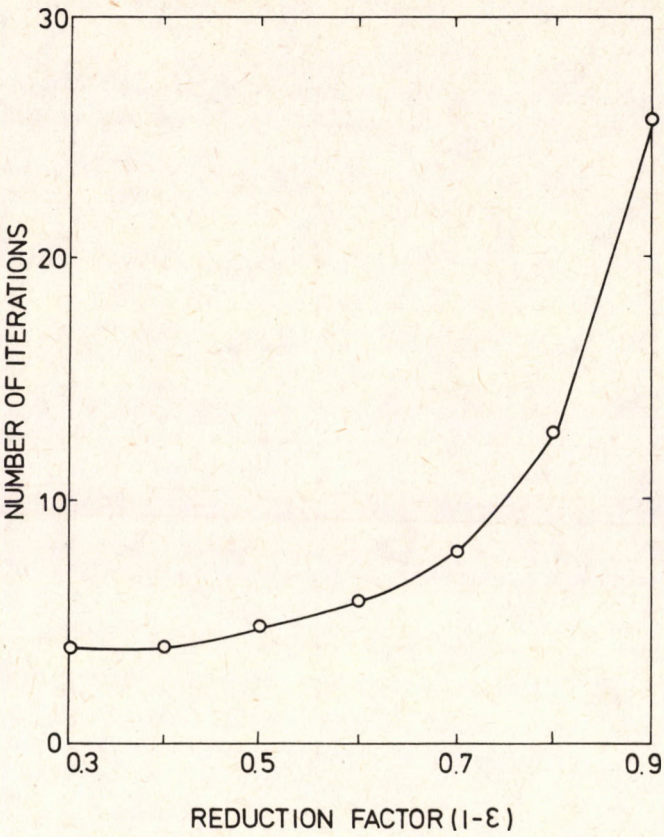

Figure 5
Effect of Reduction Factor on Convergence to $x_3(t_f)=0.43765$; $P=15$

gence to 0.43765 was obtained in only 4 iterations when ε was chosen to be 0.6 and 0.7. The computation time for 20 iterations was 48 s. The resulting concentration profile for x_2 is shown in *Fig. 6*. It is seen that x_3 increases steadily, reaching a maximum value of 0.43765 at $t=1$.

The listing of the computer program is given in *Appendix 1* and the output for the first ten iterations is given in *Appendix 2* for $\varepsilon=0.4$ corresponding to reduction factor of 0.6.

Using $\varepsilon=0.4$, we refined the optimal solution by choosing $P=45$. Convergence to $x_3(t_f)=0.43767$ resulted in 8 iterations. The CPU time for 20 iterations was 206 sec. The optimal temperature profile is very close to the one obtained for $P=15$ as is shown in *Fig. 7*.

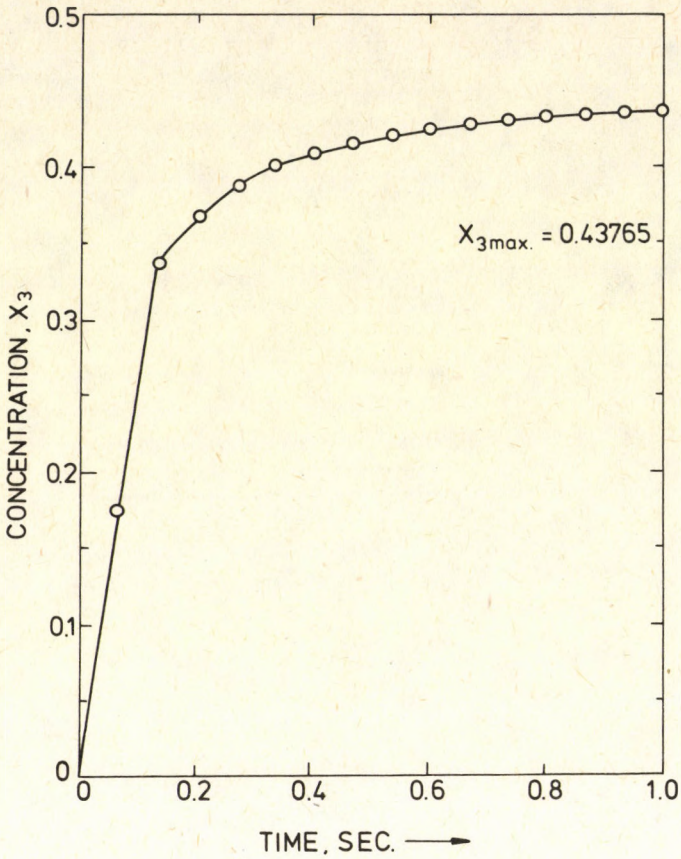

Figure 6
Concentration Profile for Example 2

The optimum obtained here is better than was obtained by ROSENBROCK and STOREY [8] and is just slightly better than the 0.437 obtained by RAO and LUUS [5] using control vector iteration procedure. Although the difference is small, the interpretation from the design point of view is important. ROSENBROCK and STOREY concluded that the maximum value possible for x_3 occurs for t_f less than 1, whereas the present work indicates that t_f greater than 1 should be examined. In fact, a run was made with $t_f = 1.5$ to give a maximum x_3 of 0.4406 which is greater than possible for $t_f = 1.0$. No attempt, however, was made to find the value for t_f that gives the maximum $x_3(t_f)$. It was interesting to observe that the resulting optimal temperature profile with $t_f = 1.5$ and $P = 45$ was completely bang-bang. The temperature was at 823.16 from $t = 0$ to $t = 0.1333$ (first four time stages) and then switched to 623.16 and kept there until $t = 1.5$.

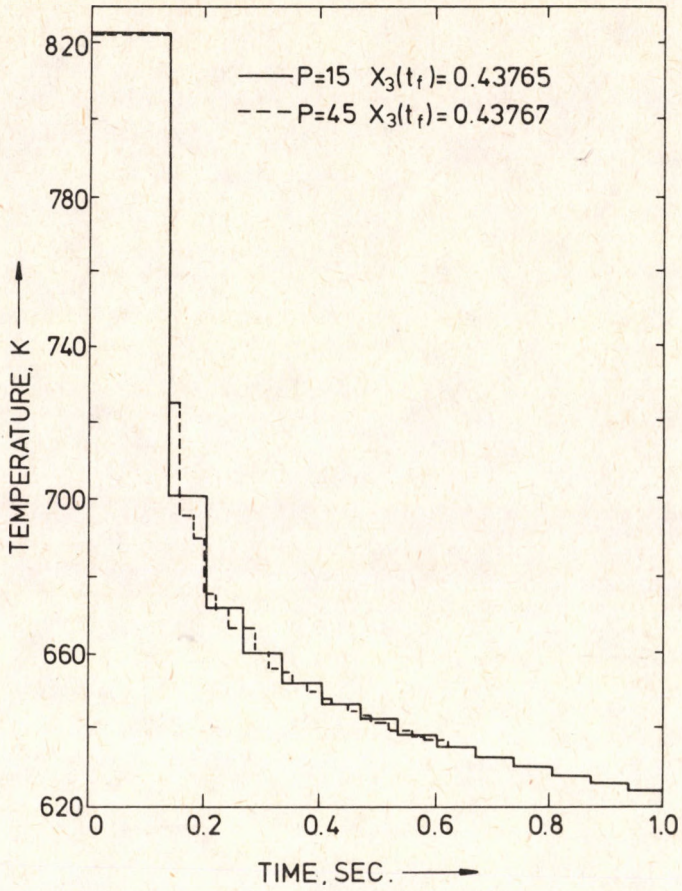

Figure 7
Optimal Temperature Profile for Example 2

Discussion and Conclusions

Dynamic programming with systematic reduction in grid size is easy to program and provides a reliable means of obtaining piecewise constant control policy for nonlinear optimal control problems. The use of only accessible states for the **x**-grid permits the use of relatively few grid points even if the dimension of **x** is high. For the two examples chosen here the use of 21 points for **x**-grid was quite adequate when the number of time stages was of the order of 30 or less. For the first example a larger number (41) yielded a better answer when 56 stages were used. Another approach is to use the results obtained for a small P as a starting point for larger P.

The convergence properties of the present procedure have not been examined in detail. What is surprising, however, is that only 3 allowable values of control worked so well. Also what is surprising is that the reduction factor as low as 0.5 yielded very rapid convergence to the optimal solution. This gives encouragement to try this method in a system of very high dimensions with numerous controls.

Acknowledgements

Financial support from the Natural Sciences and Engineering Research Council of Canada grant A–3515 is gratefully acknowledged. Computations were carried out on the Cray *X*–MP/24 digital computer.

SYMBOLS

E	activation energy, cal/g mole
f	vector of n functions of $\mathbf{x}$ and u
I	performance index to be maximized or minimized
k	index used to denote time interval; rate constant
L	length of a time stage
M	number of allowable values for control at each time stage
n	dimension of state vector
N	number of grid points taken for $\mathbf{x}$
P	number of time stages
r	region allowed for the control
R	gas constant; 1.9872 cal/g mole K
t	time
u	control variable
$\mathbf{x}$	state vector of n variables

Greek letters

α	lower bound on control u
β	upper bound on control u
ε	amount by which the allowable region is contracted after every iteration
$1-\varepsilon$	contraction factor
Φ	final state performance index

Subscripts

f	final
i	index pertaining to chemical species, or entry in vector
0	preexponential factor as in Eq. (21)

Superscripts

(j)	iteration number
0	optimal

REFERENCES

1. DeTremblay, M. and Luus, R.: Can. J. Chem. Engng., *1989,* 67, 494–502.
2. Lapidus, L. and Luus, R.: Optimal Control of Engineering Processes. Blaisdell, Waltham, Mass., 1967, pp. 75–87.
3. Luus, R.: "Optimal Control by Dynamic Programming Using Systematic Reduction in Grid Size", presented at North American/German Workshop on Chemical Engineering Mathematics and Computation, Göttingen, West Germany, July 18–23, 1989.
4. Luus, R. and Jaakola, T. H. I.: AIChE J., *1973,* 19, 760–766.
5. Rao, S. N. and Luus, R.: Can. J. Chem. Engng., *1972,* 50, 777–784.
6. Rosen, O.: Private Communication, 1989.
7. Rosen, O. and Luus, R.: Chem. Engng. Sci., *1989,* in press.
8. Rosenbrock, H. H. and Storey, C.: "Computational Techniques for Chemical Engineers", Pergamon Press, N. Y., 1966. pp. 241–277.
9. Waller, K.; Jonasson, D. and Gustafsson, T.: Kemia-Kemi, 1977, *4,* 113–117, 243–246, 477–480.
10. Yeo, B. P.: Int. J. Control, *1980,* 32, 723–730.
11. Aris, R.: "Discrete Dynamic Programming", Blaisdell, New York, 1964.
12. Bellman, R. E. and Dreyfus, S. E.: "Applied Dynamic Programming", Princeton Univ. Press, Princeton, N. J., 1962.

APPENDIX 2

Output of the Computer Program given in Appendix 1

INITIAL CONDITIONS ARE

	0.00000	0.00000	0.00000	0.00000
1	0.06667	0.64414	0.13221	0.03331
2	0.13333	0.41491	0.17068	0.10053
3	0.20000	0.26726	0.16527	0.17254
4	0.26667	0.17215	0.14225	0.23662
5	0.33333	0.11089	0.11478	0.28846
6	0.40000	0.07143	0.08891	0.32784
7	0.46667	0.04601	0.06696	0.35622
8	0.53333	0.02964	0.04940	0.37564
9	0.60000	0.01909	0.03587	0.38805
10	0.66667	0.01230	0.02573	0.39519
11	0.73333	0.00792	0.01827	0.39843
12	0.80000	0.00510	0.01287	0.39887
13	0.86667	0.00329	0.00900	0.39732
14	0.93333	0.00212	0.00626	0.39437
15	1.00000	0.00136	0.00433	0.39047

PASS NUMBER = 1

P	T	X1	X2	X3	U
1	0.06667	0.20589	0.21931	0.17463	823.16000
2	0.13333	0.04239	0.12468	0.33639	823.16000
3	0.20000	0.02730	0.08626	0.37620	723.16000
4	0.26667	0.01759	0.05941	0.40144	723.16000
5	0.33333	0.01620	0.05206	0.40818	623.16000
6	0.40000	0.01493	0.04564	0.41392	623.16000
7	0.46667	0.01376	0.04003	0.41879	623.16000
8	0.53333	0.01267	0.03513	0.42290	623.16000
9	0.60000	0.01168	0.03085	0.42635	623.16000
10	0.66667	0.01076	0.02711	0.42921	623.16000
11	0.73333	0.00991	0.02384	0.43157	623.16000
12	0.80000	0.00913	0.02097	0.43348	623.16000
13	0.86667	0.00841	0.01847	0.43501	623.16000
14	0.93333	0.00775	0.01627	0.43620	623.16000
15	1.00000	0.00714	0.01435	0.43709	623.16000

PASS NUMBER = 2

P	T	X1	X2	X3	U
1	0.06667	0.20589	0.21931	0.17463	823.16000
2	0.13333	0.04239	0.12468	0.33639	823.16000
3	0.20000	0.02730	0.08626	0.37620	723.16000
4	0.26667	0.02303	0.07007	0.39192	663.16000
5	0.33333	0.01815	0.05433	0.40643	683.16000
6	0.40000	0.01672	0.04766	0.41249	623.16000
7	0.46667	0.01541	0.04184	0.41764	623.16000
8	0.53333	0.01420	0.03675	0.42199	623.16000
9	0.60000	0.01308	0.03231	0.42566	623.16000
10	0.66667	0.01205	0.02841	0.42872	623.16000
11	0.73333	0.01110	0.02501	0.43126	623.16000
12	0.80000	0.01023	0.02202	0.43333	623.16000
13	0.86667	0.00942	0.01941	0.43500	623.16000
14	0.93333	0.00868	0.01712	0.43632	623.16000
15	1.00000	0.00800	0.01511	0.43732	623.16000

PASS NUMBER = 3

P	T	X1	X2	X3	U
1	0.06667	0.20589	0.21931	0.17463	823.16000
2	0.13333	0.04239	0.12468	0.33639	823.16000
3	0.20000	0.02730	0.08626	0.37620	723.16000
4	0.26667	0.02303	0.07007	0.39192	663.16000
5	0.33333	0.02025	0.05889	0.40246	647.16000
6	0.40000	0.01728	0.04835	0.41197	659.16000
7	0.46667	0.01474	0.03973	0.41933	659.16000
8	0.53333	0.01257	0.03268	0.42491	659.16000
9	0.60000	0.01158	0.02872	0.42802	623.16000
10	0.66667	0.01067	0.02526	0.43060	623.16000
11	0.73333	0.00983	0.02225	0.43271	623.16000
12	0.80000	0.00906	0.01958	0.43441	623.16000
13	0.86667	0.00835	0.01725	0.43575	623.16000
14	0.93333	0.00769	0.01522	0.43677	623.16000
15	1.00000	0.00709	0.01343	0.43752	623.16000

PASS NUMBER = 4

P	T	X1	X2	X3	U
1	0.06667	0.20589	0.21931	0.17463	823.16000
2	0.13333	0.04239	0.12468	0.33639	823.16000
3	0.20000	0.03083	0.09213	0.37017	701.56000
4	0.26667	0.02415	0.07119	0.39077	684.76000
5	0.33333	0.02124	0.05987	0.40152	647.16000
6	0.40000	0.01812	0.04919	0.41124	659.16000
7	0.46667	0.01627	0.04218	0.41743	637.56000
8	0.53333	0.01461	0.03619	0.42250	637.56000
9	0.60000	0.01292	0.03069	0.42685	644.76000
10	0.66667	0.01142	0.02604	0.43025	644.76000
11	0.73333	0.01052	0.02293	0.43246	623.16000
12	0.80000	0.00970	0.02021	0.43425	623.16000
13	0.86667	0.00893	0.01782	0.43568	623.16000
14	0.93333	0.00823	0.01572	0.43678	623.16000
15	1.00000	0.00758	0.01389	0.43760	623.16000

PASS NUMBER = 5

P	T	X1	X2	X3	U
1	0.06667	0.20589	0.21931	0.17463	823.16000
2	0.13333	0.04239	0.12468	0.33639	823.16000
3	0.20000	0.03083	0.09213	0.37017	701.56000
4	0.26667	0.02531	0.07348	0.38858	671.80000
5	0.33333	0.02153	0.06021	0.40212	660.12000
6	0.40000	0.01898	0.05078	0.40989	646.20000
7	0.46667	0.01656	0.04251	0.41718	650.52000
8	0.53333	0.01487	0.03649	0.42230	637.56000
9	0.60000	0.01315	0.03094	0.42671	644.76000
10	0.66667	0.01194	0.02686	0.42981	631.80000
11	0.73333	0.01075	0.02317	0.43238	636.12000
12	0.80000	0.00968	0.02000	0.43436	636.12000
13	0.86667	0.00871	0.01729	0.43585	636.12000
14	0.93333	0.00803	0.01526	0.43688	623.16000
15	1.00000	0.00740	0.01347	0.43764	623.16000

PASS NUMBER = 6

P	T	X1	X2	X3	U
1	0.06667	0.20589	0.21931	0.17463	823.16000
2	0.13333	0.04239	0.12468	0.33639	823.16000
3	0.20000	0.03083	0.09213	0.37017	701.56000
4	0.26667	0.02531	0.07348	0.38858	671.80000
5	0.33333	0.02153	0.06021	0.40212	660.12000
6	0.40000	0.01863	0.05001	0.41055	653.97600
7	0.46667	0.01654	0.04249	0.41720	642.74400
8	0.53333	0.01461	0.03596	0.42269	645.33600
9	0.60000	0.01313	0.03092	0.42673	636.98400
10	0.66667	0.01174	0.02649	0.43003	639.57600
11	0.73333	0.01057	0.02284	0.43254	636.12000
12	0.80000	0.00966	0.01997	0.43438	628.34400
13	0.86667	0.00882	0.01748	0.43582	628.34400
14	0.93333	0.00813	0.01542	0.43687	623.16000
15	1.00000	0.00749	0.01362	0.43765	623.16000

PASS NUMBER = 7

P	T	X1	X2	X3	U
1	0.06667	0.20589	0.21931	0.17463	823.16000
2	0.13333	0.04239	0.12468	0.33639	823.16000
3	0.20000	0.03083	0.09213	0.37017	701.56000
4	0.26667	0.02531	0.07348	0.38858	671.80000
5	0.33333	0.02153	0.06021	0.40212	660.12000
6	0.40000	0.01863	0.05001	0.41055	653.97600
7	0.46667	0.01637	0.04212	0.41750	647.40960
8	0.53333	0.01446	0.03564	0.42292	645.33600
9	0.60000	0.01287	0.03039	0.42707	641.64960
10	0.66667	0.01162	0.02624	0.43017	634.91040
11	0.73333	0.01055	0.02281	0.43256	631.45440
12	0.80000	0.00964	0.01994	0.43440	628.34400
13	0.86667	0.00881	0.01745	0.43582	628.34400
14	0.93333	0.00805	0.01529	0.43689	627.82560
15	1.00000	0.00742	0.01351	0.43765	623.16000

PASS NUMBER = 8

P	T	X1	X2	X3	U
1	0.06667	0.20589	0.21931	0.17463	823.16000
2	0.13333	0.04239	0.12468	0.33639	823.16000
3	0.20000	0.03083	0.09213	0.37017	701.56000
4	0.26667	0.02507	0.07300	0.38904	674.59936
5	0.33333	0.02133	0.05981	0.40157	660.12000
6	0.40000	0.01845	0.04967	0.41084	653.97600
7	0.46667	0.01622	0.04183	0.41772	647.40960
8	0.53333	0.01441	0.03558	0.42296	642.53664
9	0.60000	0.01291	0.03049	0.42700	638.85024
10	0.66667	0.01165	0.02633	0.43012	634.91040
11	0.73333	0.01058	0.02289	0.43252	631.45440
12	0.80000	0.00962	0.01992	0.43441	631.14336
13	0.86667	0.00878	0.01743	0.43583	628.34400
14	0.93333	0.00807	0.01534	0.43689	625.02624
15	1.00000	0.00743	0.01355	0.43765	623.16000

PAS NUMBER = 9

P	T	X1	X2	X3	U
1	0.06667	0.20589	0.21931	0.17463	823.16000
2	0.13333	0.04239	0.12468	0.33639	823.16000
3	0.20000	0.03083	0.09213	0.37017	701.56000
4	0.26667	0.02522	0.07329	0.38876	672.91974
5	0.33333	0.02145	0.06005	0.40135	660.12000
6	0.40000	0.01864	0.05004	0.41052	652.29638
7	0.46667	0.01638	0.04215	0.41747	647.40960
8	0.53333	0.01456	0.03585	0.42277	642.53664
9	0.60000	0.01303	0.03072	0.42685	638.85024
10	0.66667	0.01176	0.02653	0.43000	634.91040
11	0.73333	0.01065	0.02300	0.43247	633.13402
12	0.80000	0.00968	0.02002	0.43437	631.14336
13	0.86667	0.00885	0.01752	0.43581	628.34400
14	0.93333	0.00810	0.01538	0.43688	626.70586
15	1.00000	0.00746	0.01358	0.43765	623.16000

PASS NUMBER = 10

P	T	X1	X2	X3	U
1	0.06667	0.20589	0.21931	0.17463	823.16000
2	0.13333	0.04239	0.12468	0.33639	823.16000
3	0.20000	0.03083	0.09213	0.37017	701.56000
4	0.26667	0.02522	0.07329	0.38876	672.91974
5	0.33333	0.02145	0.06005	0.40135	660.12000
6	0.40000	0.01859	0.04994	0.41061	653.30415
7	0.46667	0.01634	0.04206	0.41754	647. 40960
8	0.53333	0.01452	0.03578	0.42282	642.53664
9	0.60000	0.01300	0.03066	0.42690	638.85024
10	0.66667	0.01171	0.02643	0.43006	635.91817
11	0.73333	0.01061	0.02291	0.43251	633.13402
12	0.80000	0.00966	0.01998	0.43439	630.13559
13	0.86667	0.00882	0.01748	0.43582	628.34400
14	0.93333	0.00809	0.01537	0.43688	625.69809
15	1.00000	0.00745	0.01355	0.43765	624.16777

HUNGARIAN JOURNAL
OF INDUSTRIAL CHEMISTRY
VESZPRÉM
Vol. 17. pp. 545–561 (1989)

THERMAL SENSITIVITY OF MULTI–TUBE REACTORS

An Example for the Use of the VEKRON-I Test Problem.*

A. Govil, E.K. Kazanjian, R. Rastogi, A. Saraf, T F. Spero, Chien Sze, and V. M. Voruganti**

Received: July 13, 1989

A statistical study is made to understand the effect of non–uniformity in the catalyst packing densites among the parallel tubes of a multi–tube reactor on its thermal sensitivity and performance. Simulated experiments are conducted for three levels of variations in the packing density distribution at various tube wall temperatures. It was observed that as the reactor approaches the runaway conditions, the number of tubes suffering runaway increases gradualllly, due to non–uniform performance of the tubes. Also for a given set of initial conditions and tube wall temperature, the fraction of tubes suffering runaway was found to be sensitive to the degree of non–uniformity in catalyst packing density distribution. The study also showed that complete uniformity of tubes may not always be advantageous.

Introduction

Many theoretical and a few experimental studies on thermal sensitivity and stability of cooled tubular reactors have been reported in literature [1, 2]*. Most of these studies assume that the knowledge of performance of one tube can be extrapolated for modelling a multi–tube reactor. In reality the tubes are not uniform in their performance. One of the reasons for this is the small variations in catalyst packing density from tube to tube, which results in flow differences. This study is a statistical investigation of the effect of variation in catalyst packing density on thermal sensitivity and productivity of a reactor operating close to thermal runaway conditions. A set of one hundred tubes was used as

* The VEKRON-I Test Problem was developed by the Veszprem University of Chemical Engineering in Hungary from the UCKRON-I Test Problem that in turn was created by the University of Akron, in Akron, OH, USA in cooperation with Union Carbide Corporation, South Charleston, WV USA.

** Participants in Dr. Jozsef M. Berty's Advanced Reaction Engineering course, Summer 1987. Correspondence should be sent to Dr. Berty, 100 Lincoln St., Akron, OH 44308–1708, USA

a representative sample of the 3,000 tubes of the methanol synthesis reactor described by BERTY et al. [3]. A one–dimensional model was used to simulate the tubes of this reactor. Runs were made at different coolant temperatures and catalyst packing density distributions to study their effect on the reactor performance.

The Mathematical Model

The basic one–dimensional model used in this study considers transport in the axial direction by plug flow. The mathematical model is developed by carrying out mass, energy and force balances on a differential volume of the tube, which is essentially a plug flow reactor. The kinetic equations used in this study are based on the "VERKON–I" rate expression, proposed by SZEIFERT and ÁRVA [4]. The "VERKON–I" Test Problem gives a hypothetical, but thermodynamically consistent, reaction mechanism for the Methanol Synthesis reaction coupled with the Reverse Water–Gas Shift reaction. The overall reactions are:

$2H_2 + CO \rightleftharpoons CH_3OH$ (Methanol Synthesis Reaction, r_1)
$CO_2 + H_2 \rightleftharpoons CO + H_2O$ (Reverse Water–Gas Shift Reaction, r_2)

From the stoichiometry, the following component rate expressions (R_j) can be obtained:

rate for H_2 $(j=1) \equiv R_1 = -2r_1 - r_2$
rate for CO $(j=2) \equiv R_2 = -r_1 - r_2$
rate for CH_3OH $(j=3) \equiv R_3 = r_1$
rate for CO_2 $(j=4) \equiv R_4 = -r_2$
rate for H_2O $(j=5) \equiv R_5 = r_2$.

Component Material Balance

The component material balance can be expressed as:

$$\frac{d(F'c_j)}{dx} = R_j V, \text{ where } x = z/L \tag{1}$$

Due to the two reactions, the number of moles, axial temperature and the pressure change along the tube. Therefore, using the ideal gas law ($c_j = p_j/RT$) and expanding the differential (see *Appendix A*), the component material balance equation can be expressed as:

$$\frac{dp_j}{dx} = \frac{RTV}{F'} R_j - \frac{p_j}{F'} \frac{dF'}{dx} + \frac{p_j}{T} \frac{dT}{dx} \text{ where, } j = 1 \text{ to } 5 \tag{2}$$

* At the completion of the work on 1987 the paper of LEE et al. [6] was published, that contains additional references and treats the simplest zero–order kinetics in adiabatic tubes.

Thermal Energy Balance

At steady state the thermal energy balance for the system can be written as (see Appendix B):

$$\frac{dT}{dx} = \{(-\Delta H_1)r_1 + (-\Delta H_2)r_2\}\frac{V}{\varrho c_p F'} - \frac{4UV(T-T_w)}{d_t \varrho c_p F'} \tag{3}$$

Further, one can assume that the wall temperature, T_w, equals the coolant (boiling water) temperature, because the shell side heat transfer coefficient is much greater than the tube side coefficient and also since the temperature drop in the tube wall is negligible.

Overall Material Balance

Summing Equation (2) for all the components results in the following material balance equation (see *Appendix C*):

$$\frac{dF'}{dx} = \frac{RTV(-2r_1)}{P} - \frac{F'}{PT}\left[T\frac{dP}{dx} - P\frac{dT}{dx}\right] \tag{4}$$

Pressure Drop Equation

The pressure drop equation used in this model is:

$$\frac{dP}{dx} = \frac{2\varrho g L f}{d_p} \cdot \frac{16F'^2}{\pi^2 d_t^4} \tag{5}$$

in this equation P is in N/m^2 and f, the friction factor, is estimated using Ergun's equation:

$$f = \frac{1-\epsilon}{\epsilon^3}\left[1.75 + 150 \cdot \frac{1-\epsilon}{Re'}\right] \qquad \text{where, } Re' = \frac{\psi d_p G}{\mu}. \tag{6}$$

The reactor model used for this study consists of 7 independent equations, namely, equation (2) for $j = 1$ to 4; equation (3); equation (4); and equation (5). Also, equation (2) for $j = 1$ to 5 used to calculate the partial pressure of each of the components, which can then be used to check the condition of $\sum p_j = P$

Internation and Numerical Technique

Since the thermal sensitivity of the reactor is of primary interest to this study, it is necessary for the integration procedure to calculate the first and the second derivatives of reactor temperature with respect to the axial length of the reactor at every step. This is needed to indicate the onset of thermal runaway when the

second derivative of temperature turns positive ($d^2T/dx^2 > 0$), while the first derivative is still greater than zero ($dT/dx > 0$) [5]. The forward difference method was used to estimate the second derivative, which has an error of $1/(\text{stepsize})^2$ and hence, limits the stepsize. The system of first order differential equations described above was integrated using the Euler method and a fourth order Runge–Kutta algorithm. The two methods produced similar results. The results provided below are from the Runge–Kutta algorithm.

Results and Discussion

A set of one hundred tubes with a randolmy distributed variation on catalyst packing was used to simulate a multi–tube industrial reactor and account for any differences in the packing density among the various tubes.

To begin with, simulation runs were made on a single tube, which showed that the incipient runaway first sets in at a wall temperature of 487.5K ($T_{w,\,critical}$). Next, six simulated experiments were carried out on one hundred tubes at wall temperatures ranging from 485 to 490K and with five percent normally distributed variation in the catalyst packing density in order to study the effect of wall temperature on number of tubes suffering thermal runaway. It was seen that at 485K, only 1% of the tubes suffered thermal runaway, at 488K, 48% of the tubes, and at 490K all of the tubes had thermal runaway. These results demonstrate the high thermal sensitivity of the reactor tubes towards the wall temperature. It can also be seen that runaway sets in gradually as the runaway conditions are approached and that there is no fixed temperature at which the reactor suddenly runs away.

Finally, the effect of different levels of variations in packing density on thermal sensitivity of a multi-tube reactor was studied. Packing variations may result from non-uniformity caused during the charging of the catalyst and due to aging. Aging causes gradual plugging of the tubes or entrainment of small catalyst particles with the reaction mixture. Three levels of variations in packing density – 2.5%, 5.0% and 10.0%, were studied at temperatures of 486K, 488K and 489K (*Figures 1* to *9*). The experiments showed that as the packing density distribution becomes wider, the number of tubes suffering runaway increases at 486K, but decreases at 489K. This phenomenon can be explained by referring to *Figure 10*. At 486K, as the distribution in the packing density becomes wider, the distribution of the difference between the wall temperature and the catalyst particle temperature, $(\Delta T)_{max}$, also becomes wider. Since the $(\Delta T)_{max}$ at which runaway occurs is almost constant, the number of tubes suffering runaway, therefore, increases. At 489K, the reverse occurs. The number of tubes suffering runaway decrease when the packing density distribution becomes wider. This is because most of the tubes suffer runaway when the onset runaway temperature ($\Delta T_{w,\,critical}$) is less than the average $(\Delta T)_{max}$ temperature. Also, as expected the number of tubes suffering runaway remains almost constant at 488K where about half the tubes display thermal runaway for all the three levels of packing density distribution.

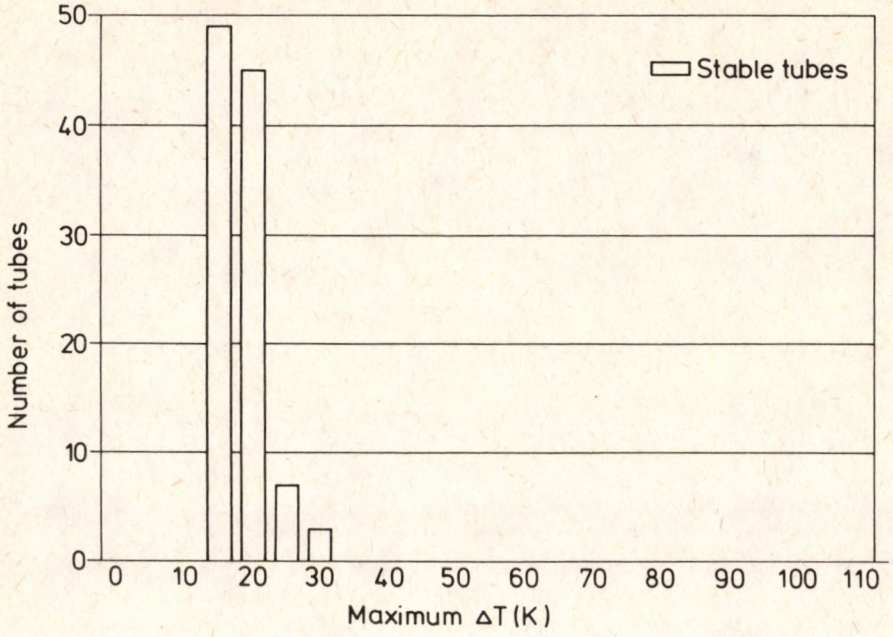

Figure 1,
The effect of packing density on the number of runaway tubes at 486K with 2.5% random packing variation

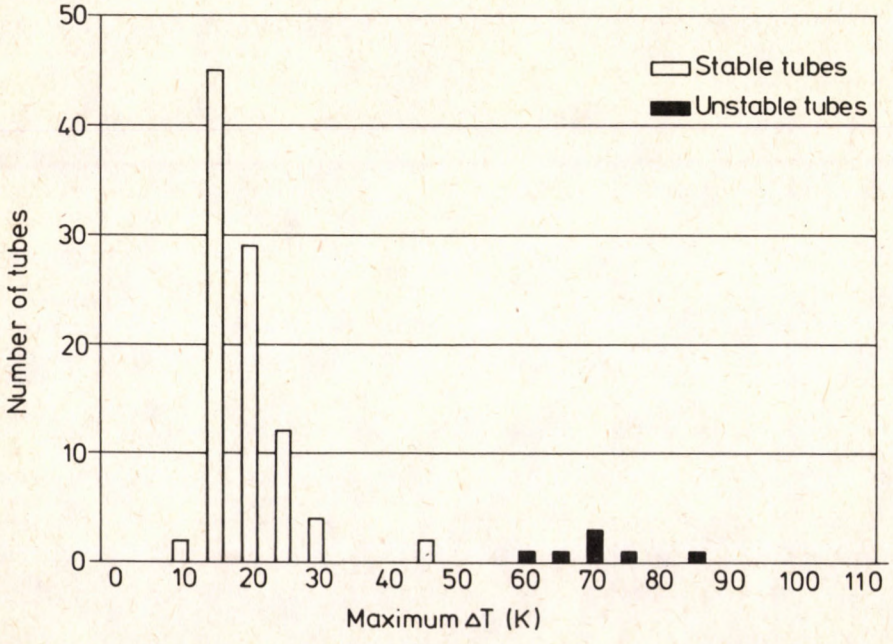

Figure 2.
The effect of packing density on the number of runaway tubes at 486K with 5.0% random packing variation

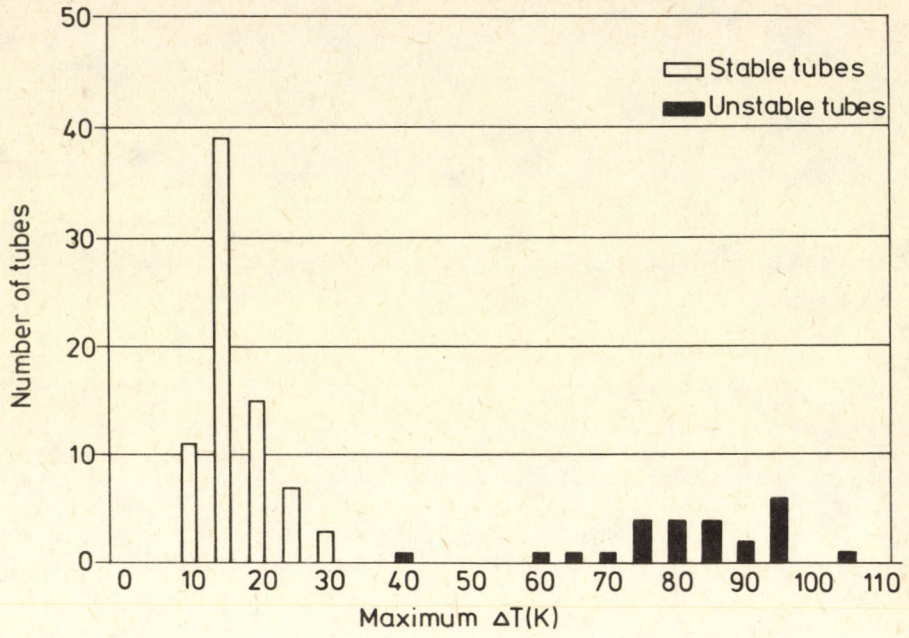

Figure 3.
The effect of packing density on the number or runaway tubes at 486K with 10% random packing variation

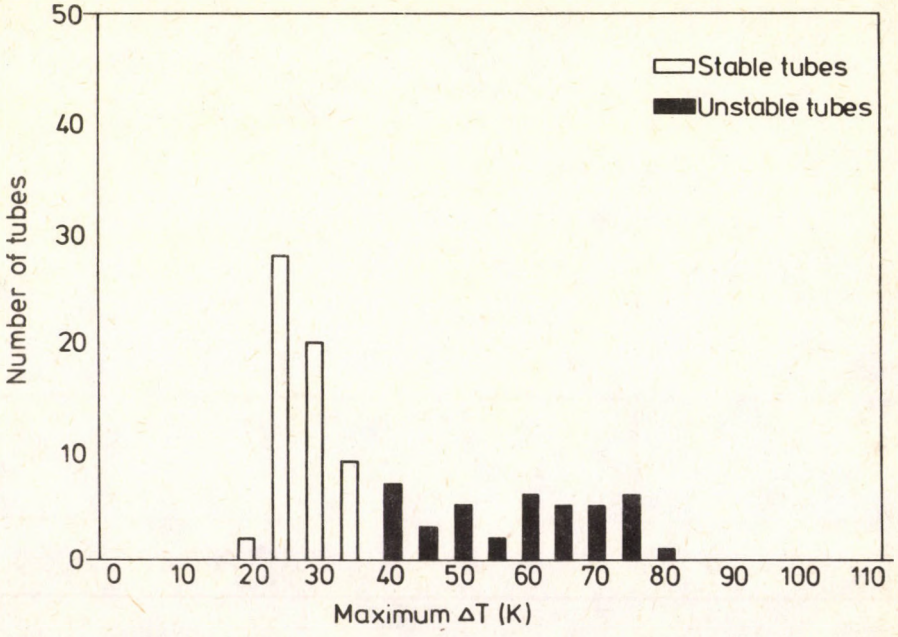

Figure 4.
The effect of packing density on the number or runaway tubes at 488K with 2.5% random packing variation

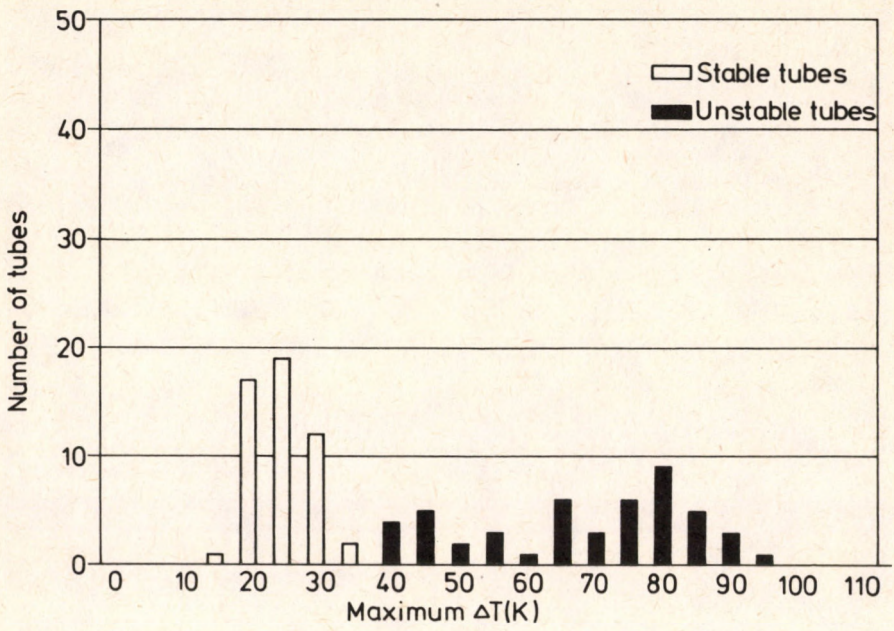

Figure 5.
The effect of packing density on the number or runaway tubes at 488K with 5.0% random packing variation

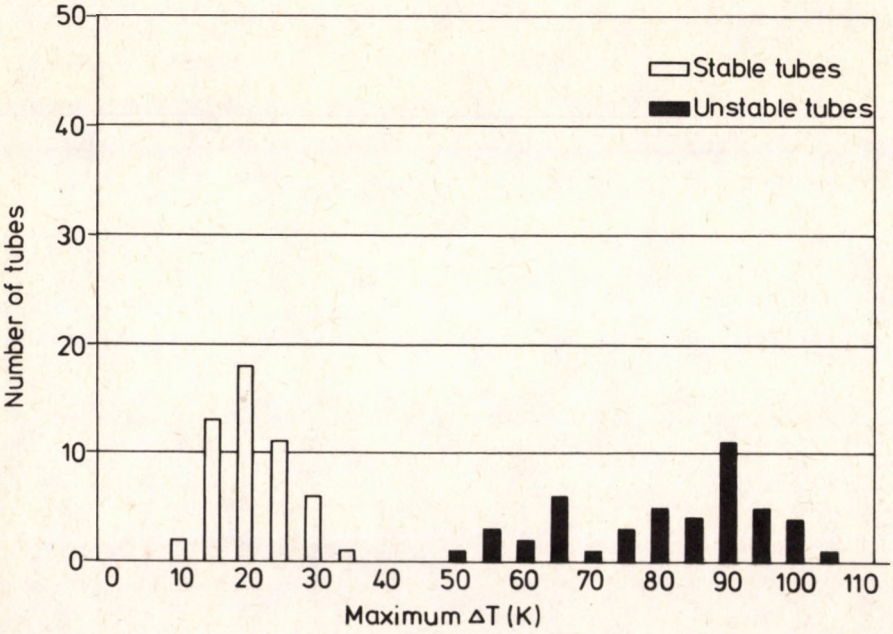

Figure 6.
The effect of packing density on the number or runaway tubes at 488K with 10% random packing variation

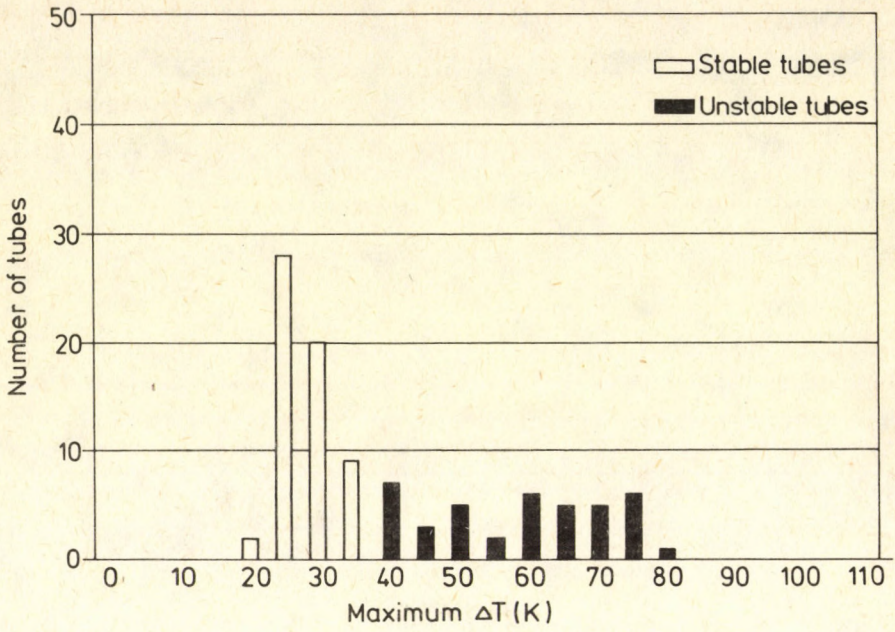

Figure 7.
The effect of packing density on the number of runaway tubes at 489K with 2.5% random packing variation

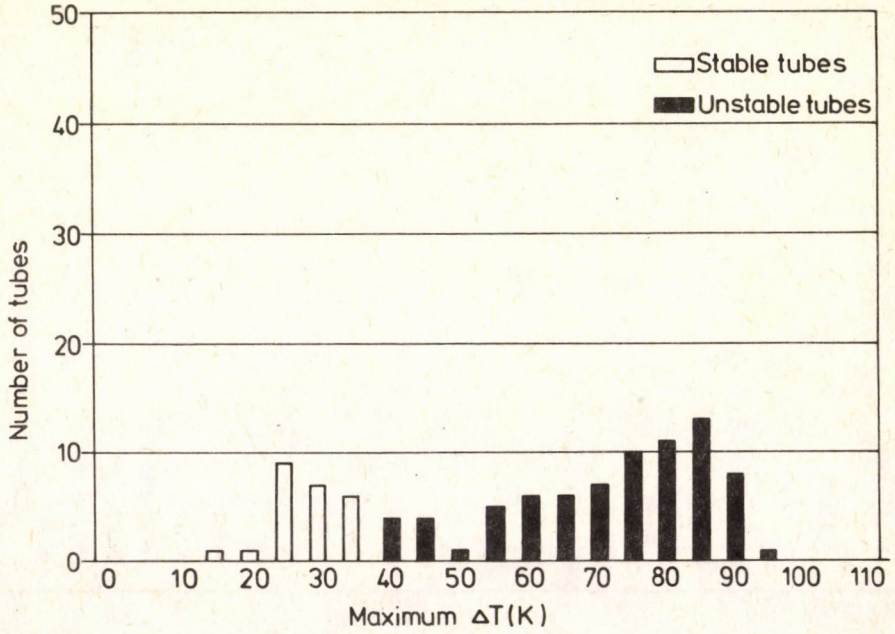

Figure 8.
The effect of packing density on the number of runaway tubes at 489K with 5.0% random packing variation

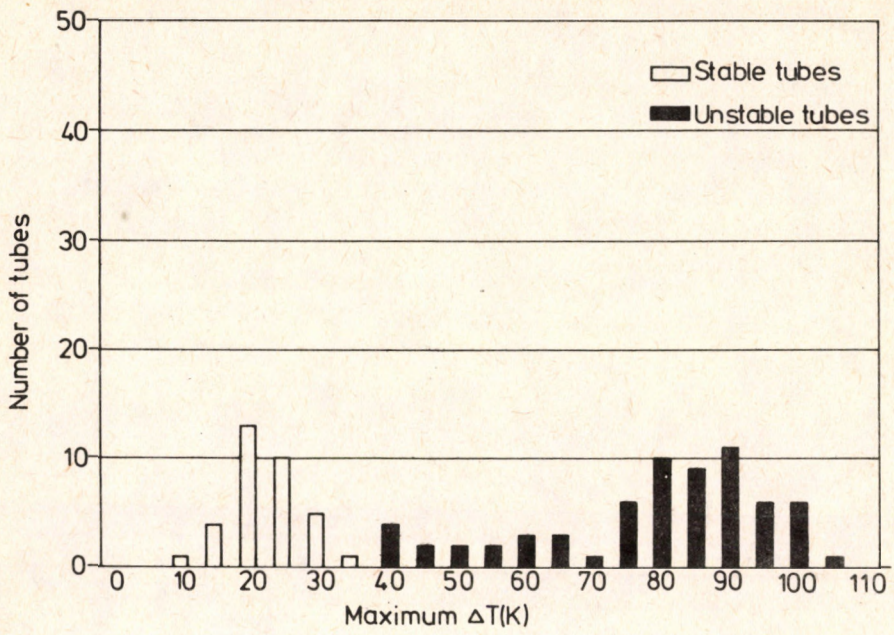

Figure 9.
The effect of packing density on the number of runaway tubes at 489K with 10% random packing variation

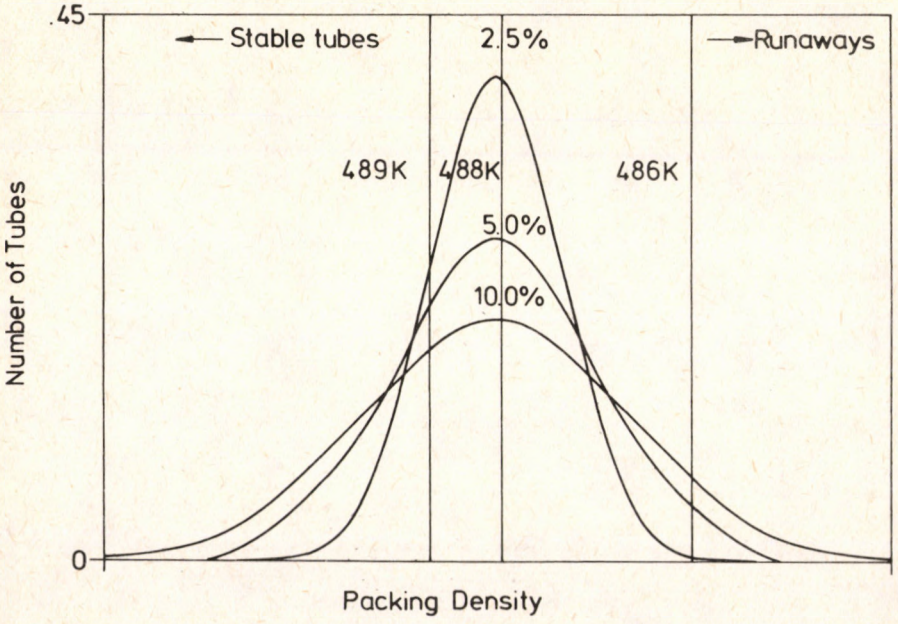

Figure 10.
The effect of packing density variation on the number or runaway tubes at 486K, 488K and 489K

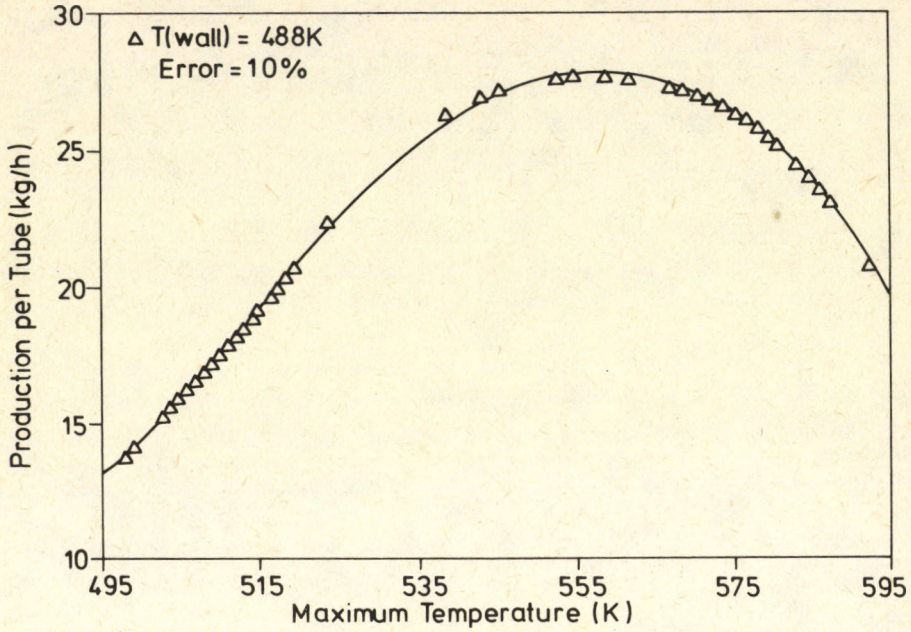

Figure 11.
The effect of runaway on production rate at 488K and 10% variation in packing density

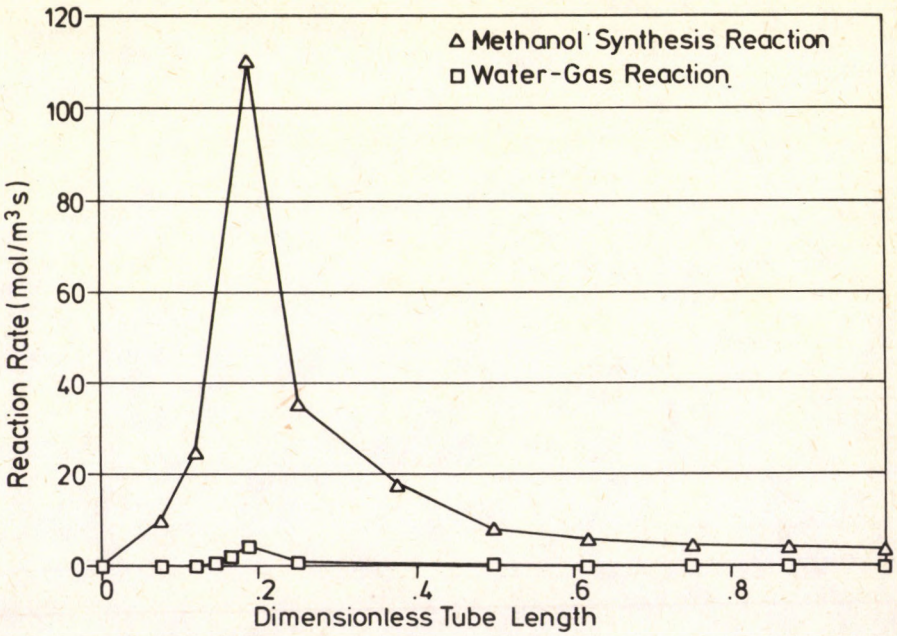

Figure 12.
The comparison of the methanol synthesis and the water-gas shift reaction rates in a tube suffering runaway versus dimensionless length

In most of the experiments, it was observed that the production rate was higher in the tubes having higher $(\Delta T)_{max}$. However, it was noticed on *Figure 11* that in runs with wider packing density distributions at 488K and 489K, the tubes with the highest $(\Delta t)_{max}$ did not have the highest production rates. This occurs because the tubes with the highest $(\Delta T)_{max}$ also had the highest packing density, and hence the lowest flow rates. *Figure 12* shows that the reaction attains equilibrium within the first half of the tubes with almost no conversion taking place thereafter, resulting in low production rates.

In conclusion, the tube wall temperature should be set at a value corresponding to the expected level of variation in packing density. For a high packing density variation (e.g. 10.0%) the tube wall temperature should be set sufficiently lower than the $T_{w,\,critical}$ so that no tube suffers runaway. Similarly, if the packing density variation is low (2.5%) then the tube wall temperature can be set at a correspondingly higher value in order to achieve a higher production rate. Thus, we see that the perfomance of the multi-tube reactor is sensitive to the catalyst packing distribution and this factor should be taken into account when scaling-up a reactor from pilot plant data.

Due to the non-uniform performance of the tubes, the number of tubes suffering runaway gradually increases as the runaway conditions are approached. This, in a way, moderates the overall sensitivity of the reactor since small upsets in the operating conditions cause hot spotting in only a few tubes rather than a simultaneous run away of all of them. Although runaway in a few tubes may cause uneven stresses, the resulting damage is much less than that can be caused by a sudden runaway of all the tubes. The partial runaway indicates that perfect uniformity of tubes is not necessarily desirable for some reactions.

Acknowledgements

The authors greatly appreciate the motivation and guidance of DR. JOZSEF M. BERTY of the Department of Chemical Engineering and the advice of Dr. Dale S. Borowiak, of the Department of Mathematics.

Appendix A

Derivation of the Material Balance

Let A, be the cross–section area of the tube and L be tube length. Then for the differential volume shown in *Figure A1*, one can write the following mass balance:

$$(F'c_j)\,|_z + R_j A\,dz = (F'c_j)\,|_{z+\Delta z}.$$

Therefore:

$$R_j A = \lim_{dz \to} \frac{(F'c_j)\,|_{z+\Delta z} - (F'c_j)\,|_z}{dz}$$

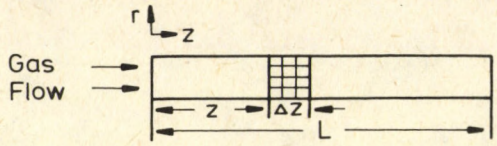

Figure A1.
Reactor tube differential volume

or:

$$\frac{d}{dz}(F'c_j) = R_j A.$$

In dimensionaless terms, since x = z/L:

$$\frac{d}{dx}(F'c_j) = R_j V$$

Since $c_j = p_j/RT$, the material balance may be written as:

$$\frac{d}{dx}\left(\frac{F'P_j}{RT}\right) = R_j V \qquad \text{(a1)}$$

If F', p_j, and T are all taken as functions of x then, differentiating with respect to x gives:

$$\frac{dp_j}{dx} = \frac{RTV}{F'}R_j - \frac{p_j}{F'}\frac{dF'}{dx} + \frac{p_j}{T}\frac{dT}{dx} \qquad \text{where j = 1 to 5.}$$

Appendix B

Derivation of the Energy Balance

Let A_w be the tube wall surface area. Therefore, at steady state, the energy balance for the differential volume can be written as:

$$F'\varrho c_p dT + UA_w(T - T_w) = (-\Delta H)R''dV$$

where: $(-\Delta H)R'' = (-\Delta H_1)r_1 + (-\Delta H_2)r_2$
Substituting x = z/L, $A_w = \pi d_t L$ ($dA_w = \pi d_t dL$), dV = A · dL, and dx = dz/L, and multiply by $L/(\varrho c_p F' dx)$, we get:

$$\frac{dT}{dx} = \{(-\Delta H_1)r_1 + (-\Delta H_2)r_2\}\frac{V}{\varrho c_p F'} - \frac{4UV(T - T_w)}{d_t \varrho c_p F'}$$

Appendix C

Derivation of the Ideal Flow Equation

From the ideal gas law:

$$c_j = \frac{p_j}{RT}$$

Summing concentratoins of all five components, we get:

$$\sum_{j=1}^{5} c_j = c_T = \frac{P}{RT} \tag{c1}$$

Also summing Equation (a1) for all five components gives:

$$\frac{d}{dx}(F'\sum c_j) = V(-2r_1)$$

Substituting Equation (c1) for $\sum c_j$, gives:

$$\frac{d}{dx}\left(\frac{F'P}{RT}\right) = V(-2r_1)$$

Since P, F′, and T are functions of x, by differentiating, then using the product and the quotient rules, the flow balance equation is obtained:

$$\frac{dF'}{dx} = \frac{VRT(2r_1)}{P} - \frac{F'}{PT}\left[T\frac{dP}{dx} - P\frac{dT}{dx}\right]$$

SYMBOLS

c_p	heat capacity
c_j	concentration for the j^{th} species
d_p	particle diameter
d_t	tube diameter
f	friction factor
F'	volumetric flow rate
ΔH	heat of reaction
L	reactor length
p_j	component partial pressure
P	pressure
r_i	overall reaction rate for the methanol synthesis (i = 1) or the reverse water-gas shift reaction (i = 2).
R	universal gas constant
R_j	reaction rate for j^{th} species
Re	Reynold's number
T	temperature
ΔT	temperature difference between tube wall and catalyst particle
U	heat transfer coefficient
V	volume
x	dimensionaless length

Greek letters

ϵ bed porosity
ψ shape factor
μ viscosity
ϱ density

REFERENCES

1. FROMENT, G. F. and BISCHOFF, K. B.: Chemical Reactor Analysis and Design, John Wiley and Sons, New York, 1979.
2. SMITH, J. M.: Chemical Engineering Kinetics, 2nd Ed., McGraw-Hill, New York, 1970.
3. BERTY, J. M., LEE, S., SZEIFERT, F. and CROPLEY, J. B.: Special Issue of Chemical Engineering Communication, *1989*, 76, 9–33.
4. ÁRVA, P. and SZEIFERT, F.: Special Issue of Chemical Engineering Communication, *1989*, 76, 195–206.
5. BERTY, J. M., BRICKER, J. H. and HAMBRICK, J. O.: "Stability of Staged Adiabatic Reactors with Interstage Coolers", Preprint 10 E, AIChE Meeting, St. Louis, February 1968.
6. LEE, J. P., BALAKOTAIAH, V. and LUSS, D.: AIChE Journal, *1987*, 33, (7) 1136–1154.

APPENDIX 1.

Listing of Computer Program for Example 2.

```
      EXTERNAL CSTR
      DIMENSION X (5), DX (5), XG (3,
      100, 21), UG (100, 21), US (100, 21)
      DIMENSION XIN (5), FACT1 (21),
      FACT2 (21), UIN (100), UR (100)
      COMMON U
      N=3
      NX=3
      RED=0.60
      XIN (1)=1.0
      XIN (2)=0.0
      XIN (3)=0.0
      WRITE (6,23) T, (XIN (J), J=1, N)
   23 FORMAT (//1X, 'INITIAL CON-
      DITIONS ARE', 8F 10.5)
      DO 25 I=1, N
   25 X (I)=XIN (I)
      UMAX=823.16
      UMIN=623.16
      NT=15
      NGX=21
      NGU=3
      NINT=7
      AINT=NINT
      DT=0.01*100./105
      DO 49 I=1, NT
      UIN (I)=723.16
   49 CONTINUE
      DO 50 I=1, NT
      UR (I)=100.
      U=UIN (I)
      DO 111 JK=1, NX
  111 XG (JK, I, 1)=X (JK)
      DO 11 INT=1, NINT
      CALL RUNGK (T, X, N, DT, DX,
      CSTR)
      T=T+DT
   11 CONTINUE
      WRITE (6, 56) I, T, (X (J), J=1, N)
   50 CONTINUE
      NGXX=NGX/2+1
      ANP=NGX-1
      DO 41 I=1, NGX
      A2=2* (I-1)
```

```
 41 FACT1 (I)=A2/ANP
    FACT1 (NGXX)=FACT1 (1)
    BNP=NGU-1
    DO 42 J=1, NGU
    A3=2* (J-1)
 42 FACT2 (J)=A3/BNP
    DO 99 LOOP=1.20
    WRITE (6, 100) LOOP
    WRITE (6.110)
100 FORMAT (//10X, 'PASS NUMBER
    =', I5)
110 FORMAT (5X, 'P', 7X, 'T', 8X, 'X1',
    8X, 'X2', 8X, 'X3', 8X, 'U')
    DO 52 I=2, NGX
    DO 117 II=1, N
117 X (II)=XIN (II)
    T=O.
    DO 51 K=1, NT
    U=UIN       (K)-UR(K)+FACT1
    (I)*UR(K)
    IF (U. GT. UMAX) U=UMAX
    IF (U. LT. UMIN) U=UMIN
    DO 159 KJ=1, NX
159 XG (KJ, K, I)=X (KJ)
    DO 59 INT=1, NINT
    CALL RUNGK (T, X, N, DT, CSTR)
    T=T+DT
 59 CONTINUE
 51 CONTINUE
 52 CONTINUE
    DO 53 K=1, NT
    DO 53 J=1, NGU
    UG (K, J)=UIN (K)-UR
    (K)+FACT2 (J)*UR (K)
    IF (UG. (K, J). LT. UMIN) UG (K,
    J)=UMIN
    IF (UG. (K, J). GT. UMAX) UG (K,
    J)=UMAX
 53 CONTINUE
 56 FORMAT (1X, I5, 11F10.5)
    K=NT
    DO 60 I=1, NGX
    TESTP=3000.
    DO 60 L=1, NGU
    DO 160 J=1, NX
160 X(J)=XG(J, K, I)
    U=UG (NT, L)
    T=NT-1
    T=DT*T*AINT
    DO 12 INT=1, NINT
    CALL RUNGK (T, X, N, DT, DX,
    CSTR)
    T=T+DT
 12 CONTINUE
    PERF=-X (3)
    IF (PERF. GT. TESTP) GO TO 30
    US (NT, I)=UG (NT, L)
    TESTP=PERF
 30 CONTINUE
 60 CONTINUE
    K1=NT-2
    DO 63 LL=1, K1
    K=NT-LL
    KL=K+1
    DO 61 I=1, NGX
    TESTP=3000.
    DO 64 L=1, NGU
    DO 164 J=1, NX
164 X (J)=XG (J, K, I)
    T=K-1
    T=DT*T*AINT
    U=UG (K, L)
    DO 13 INT=1, NINT
    CALL RUNGK (T, X, N, DT, DX,
    CSTR)
    T=T+DT
 13 CONTINUE
    DO 33 KK=KL, NT
    TESTD=3000.
    DO 62 II=1, NGX
    T1=0.
    DO 162 JJ=1, NX
162 T1=T1+(X (JJ)-XG (JJ, KK,
    II))**2
    IF (T1. GT. TESTD) GO TO 31
    TESTD=T1
    IB=II
 31 CONTINUE
 62 CONTINUE
    T=KK-1
    T=T*DT*AINT
    U=US (KK, IB)
    DO 14 INT=1, NINT
    CALL RUNGK (T, X, N, DT, DX,
    CSTR)
    T=T+DT
 14 CONTINUE
 33 CONTINUE
    PERF=-X(3)
    IF (PERF. GT. TESTP) GO TO 32
    TESTP=PERF
    US (K, I)=UG (K, L)
 32 CONTINUE
 64 CONTINUE
 61 CONTINUE
 24 FORMAT (1X, 11F10.5)
 63 CONTINUE
    K=1
    KL=2
    TESTP=3000.
    DO 74 L=1, NGU
    X (1)=XIN (1)
    X (2)=XIN (2)
    X (3)=XIN (3)
```

```
      T=O.
      U=UG (K, L)
      DO 15 INT=1, NINT
      CALL RUNGK (T, X, N, DT, DX,
      CSTR)
      T=T+DT
   15 CONTINUE
      DO 93 KK=KL, NT
      TESTD=3000.
      DO 92 II=1, NGX
      T1=O.
      DO 192 JJ=1, NX
  192 T1=T1+(X (JJ)-XG (JJ, KK,
      II))**γ
      IF (T1. GT. TESTD) GO TO 91
      TESTD=T1
      IB=II
   91 CONTINUE
   92 CONTINUE
      T=KK-1
      T=T*DT*AINT
      U=US (KK, IB)
      DO 16 INT=1, NINT
      CALL RUNGK (T, X, N, DT, DX,
      CSTR)
      T=T+DT
   16 CONTINUE
   93 CONTINUE
      PERF=-X (3)
      IF (PERF. GT. TESTP) GO TO 94
      TESTP=PERF
      US (K, 1)=UG (K, L)
   94 CONTINUE
   74 CONTINUE
      X (1)=XIN (1)
      X (2)=XIN (2)
      X (3)=XIN (3)
      T=O.
      U=US (1, 1)
      UIN (K)=U
      DO 18 INT=1, NINT
      CALL RUNGK (T, X, N, DT, DX,
      CSTR)
      T=T+DT
   18 CONTINUE
      WRITE (6,56) K, T, (X(I), I=1, N), U
      DO 96 K=2, NT
      TESTD=3000.
      DO 97 II=1, NGX
      T1=O.
      DO 197 JJ=1, NX
  197 T1=T1+(X (JJ)-XG (JJ, K, II))**2
      IF (T1. GT. TESTD) GO TO 98
      TESTD=T1
      IB=II
   98 CONTINUE
   97 CONTINUE
      T=K-1
      T=T*DT*AINT
      DO 119 KJ=1, NX
  119 XG (KJ, K, 1)=X (KJ)
      U=US (K, IB)
      UIN (K)=U
      DO 19 INT=1, NINT
      CALL RUNGK (T, X, N, DT, DX,
      CSTR)
      T=T+DT
   19 CONTINUE
      WRITE (6,56) K, T, (X(I), I=1, N), U
   96 CONTINUE
      DO 10 I=1, NT
      UR (I)=UR (I)*RED
   10 CONTINUE
   99 CONTINUE
  101 CONTINUE
      STOP
      END
      SUBROUTINE CSTR (N, T, X, DX)
      DIMENSION X (5), DX (5)
      COMMON U
      UINV=1.0/(U*1.9872)
      TIN=1.0/(658.*1.9872)
      FACT=TIN-UINV
      AK1=1.02*EXP (16 000.*FACT)
      AK2=0.93*EXP (14 000.*FACT)
      AK3=0.386*EXP (15 000.*FACT)
      AK4=3.28*EXP (10 000.*FACT)
      AK5=0.084*EXP (15 000.*FACT)
      DX (1)=-(AK1+AK2+AK3)*X
      (1)
      DX (2)=AK1*X (1)-AK4*X (2)
      DX (3)=AK4*X (2)-AK5*X (3)
      RETURN
      END
      SUBROUTINE RUNGK (TSTART,
      Y, N, H, DY, DIFEQS)
      DIMENSION Y (N), DY (N)
      DIMENSION AK0 (10), AK1 (10),
      AK2 (10), AK3 (10), Y1 (10), Y2 (10),
      Y3 (10)
      T=TSTART
      CALL DIFEQS (N, T, Y, DY)
      DO 10 I=1, N
      AKO (I)=H*DY (I)
   10 Y1 (I)=Y (I)+0.5*AKO (I)
      T1=T+0.5*H
      CALL DIFEQS (N, T1, Y1, DY)
      DO 14 I=1, N
      AK1 (I)=H*DY (I)
```

```
14 Y2 (I)=Y (I)+0.5*AK1 (I)
   CALL DIFEQS (N, T1, Y2, DY)
   DO 15 I=1, N
   AK2 (I)=H*DY (I)
15 Y3 (I)=Y (I)+AK2 (I)
   T2=T+H
   CALL DIFEQS (N, T2, Y3, DY)
   DO 16 I=1, N
   AK3 (I)=H*DY (I)
   Y (I)=Y (I)+(AKO (I)+2.* (AK1
   (I)+AK2 (I))+AK3 (I))/6.
16 CONTINUE
   RETURN
   END
```

Egyetemi Nyomda – 897590 Budapest, 1990. Felelős vezető: Sümeghi Zoltán igazgató

Guide for authors

The "Hungarian Journal of Industrial Chemistry" is a joint publication of the Veszprém scientific institutions of the chemical industry that deals with the results of applied and fundamental research in the field of chemical processes, unit operations and chemical engineering in the form of original articles written in English.

In addition to the scientific workers of the institutions at Veszprém, the Editorial Board of this publication also welcomes articles for inclusion in this periodical, which are written by authors who are engaged in the above mentioned fields.

1. Manuscripts should be sent – in duplicate – to the Editor-in-Chief:

Dr. Endre Bodor
Veszprém University of Chemical Engineering (VVE), P.O.B. 158
H-8201, Veszprém, Hungary

2. *In a brief letter attached to the manuscripts, authors should declare that:*
   a) their work is *original* and *has not previously been published elsewhere in its present format,* and
   b) for the purposes of correspondence, they can be contacted at the address and telephone number which they give.
3. Manuscripts should be typed on paper of A/4 size.

The first page should give the title, the author's name, place of work and a brief summary of the article (maximum of 15 lines).

If possible the article should be presented with an introduction, experiments carried out, conclusions and discussion. Tables and Figures must be presented on separate sheets and their position in the text should be noted on the margin. A summary of the symbols used, and captions of the Figures should be attached separately to the manuscripts.

It is regretted that photographs cannot be included in the periodical.

The Tables and Figures should not exceed an A/4 size. If diagrams are presented, only the explanation and dimensions of the ordinate and abscissa, and marking numbers are required, while further explanatory texts can be given in the captions of the Figures. The equations used should be numbered, and Tables and Figures should be numbered and noted on the margin.

With regard to units, it is essential that an SI (Système International d'Unités) should be used.

4. References should be prepared in the following manner:
   a) Publications which have appeared in periodicals; e.g.

   WAKAO, N. and SCHWARTZ, J. M.: Chem. Eng. Sci. *1962,* 17 (3), 825–827.

   b) Books; e.g.

   SATTERFIELD, C. N.: Mass Transfer in Heterogeneous Catalysis. MTI Press, Cambridge, Mass., 1951. pp. 26–32.

   c) Patents; e.g.

   U.S. Pat. 3,425,442 Brit. Pat. 997,665 Hung. Pat. 553,243

   d) Published lectures; e.g.

   HIH, S., HHU, C. and LEECH, W. J.: A Discrete Method to Heat Conduction Problems. 5th International Heat Transfer Conference, Tokyo, 1975. Co. 2.4.
5. Authors receive 50 complimentary copies of their paper.

Editorial Board
Hungarian Journal of Industrial Chemistry

Ára: 300,– Ft

CONTENTS